# ELECTROMAGNETIC FIELD DISTRIBUTIONS IN A TRAVELLING-WAVE INDUCTION HEATER

by

Q.I.M. BULAND AKHTAR, B.Sc.(Eng)., M.Sc.

A Thesis submitted for the degree of Doctor of Philosophy

Department of Electrical Engineering,
University of Aston in Birmingham,
England.

March, 1977

## SUMMARY

As an improvement to the non-uniform induction-heating method using wrap-around coil and pulsating field, Davies and Bowden[5] suggested use of travelling magnetic fields for inductively heating solid-iron plates from both sides, the primary excitations being provided by 3-phase distributed windings. This thesis presents a study of electromagnetic fields in such a travelling-wave induction heater.

Electromagnetic field solutions for corresponding poles of similar and of opposite instantaneous polarity on the two primaries form two parallel developments throughout this thesis. A plate of finite-thickness, and subsequently of finite-width, is considered subjected to travelling fields and expressions for electromagnetic field quantities are obtained for magnetically linear and non-linear plates; these expressions are functions of plate-thickness, but agree with published works[30,40] for large plate-thicknesses. In electromagnetically thick plates, the power loss is the same for either pole-arrangements, whereas in thin plates, power loss for poles of opposite polarity is shown to be much greater than that for poles of similar polarity[4]. Despite finite plate-thickness, the magnetic field in the plate is predominantly one-dimensional for both pole-arrangements. In the non-linear theory, a new function is introduced as a solution to the diffusion equation to account for the additional boundary condition due to finite plate-thickness. Electromagnetic field quantities in the

plate are expressed in terms of primary excitation by equating field solutions at the air-iron interface.

The effects of finite plate-width are accounted for by introducing a finite-width factor; the two-dimensional solution developed assumes weak eddy-current reaction, includes effects of magnetic non-linearity and shows that finite-width effect is more significant for poles of opposite polarity than for poles of similar polarity. Beyond the active width, plate-currents are shown to be predominantly cross-thickness or cross-pole in nature depending on the pole-arrangement and plate-thickness.

The non-linear theory and the finite-width effect were verified by measuring power loss, flux/pole and surface curent-densities on EN1A steel plates subjected to travelling magnetic fields; agreement between theoretical and experimental results was good.

Indexing terms: Heater, Induction, Travelling-wave, Electromagnetic field distribution.

To

my mother

and

those who loveth me.

## ACKNOWLEDGEMENTS

The author wishes to express his sincere thanks and gratitude to Dr. A.L. Bowden, supervisor of this work, for his continual help and guidance, kind permission to use data from his thesis and for meticulously going through the manuscript. The author also wishes to sincerely thank Professor E.J. Davies, advisor of this work, for his keen interest and constructive criticisms from time to time. Thanks are also due to Mr. B. James for scrutinising part of this work. The author is grateful to his friend, and colleague in research, Dr. S. Das, for his continual inspiration and close co-operation in many fruitful discussions. Special thanks are due to the many laboratory technicians who helped with the preparation of the experimental rig. Particular mention must be made of Mr. B. Harrison and Mr. J. Partlow of Electrical Machines Centre, for their welcome assistance. The author thanks Dr. S. Sarkar and Messrs. M.A. Rahman, R.K. Chakravorty and G.P. Gogue, for their help with the preparation of the thesis. Many thanks are due to Miss Freeman and Mrs. Turner for their careful preparation of the typescript.

The author wishes to thank the Association of Commonwealth Universities who financed part of this work. The author gratefully acknowledges the help of Dr. G. Mustafa in providing with financial guarantee for one year of this work. Sincere thanks are also due to Mr. S.R. Ghosh for his help in this respect.

The author wishes to thank the authorities of the Bangladesh University of Engineering and Technology for granting him study-leave for the period of this research work.

The author is grateful to his many friends and relatives in Bangladesh and elsewhere for their continual encouragement and well wishes.

## LIST OF SYMBOLS

Throughout this thesis rationalised MKSA units are used.

$A$ = Magnetic vector potential (Chapter 3), T.m.

$a$, $b$ = Constants used in the parabolic representation of the normal B-H curve ($B=aH^b$), numeric.

$A$ = 1.25a (Chapter 5), numeric

$B$ = Magnetic flux density, T.

$\dot{C}_p$ = Function showing influence of primary permeability, numeric.

$C_1$ = Constant in the current-density expressions for the plate (Chapter 7), $A/m^2$.

$C_2$ = Constant in the current-density expressions for the end-strips (Chapter 7), $A/m^2$.

$c_1$ = $\sqrt{2}\cos\{(\pi/4) - (\theta_h/2)\}$, numeric

$c_2$ = $\sqrt{2}\sin\{(\pi/4) - (\theta_h/2)\}$, numeric

$\dot{D}_s$ = $(\mu_r q - k)/(\mu_r q + k)$, numeric

$d$ = Half-thickness of the plate, m.

$d_c$ = Thickness near the plate surface over which the current density is assumed uniform (Chapter 7), m.

$d_e$ = Width of conducting end-strips (Chapter 7), m.

$d_m$ = Half-thickness of the plate for optimum loss, m.

$E$ = Electric field strength, V/m.

$F$ = Force density in the plate, $N/m^3$.

$F_c$ = Primary m.m.f., At/pole.

$F_r$ = Eddy-current reaction m.m.f., At/pole.

$f$ = Constant in equation (5.17), $m^{-1}$.

$g$ = Air-gap length, m.

$H$ = Magnetic field strength, A/m.

$h$ = Constant in equation (5.17), $m^{-1}$.

$J$ = Current density, $A/m^2$.

$j$ = $\pi/2$ operator.

$K_f$ = Finite-width factor, numeric.

$K_z$ = Line density of primary current sheet, A/m.(*)

$k$ = $(q^2 + j2\alpha^2)^{\frac{1}{2}}$, $m^{-1}$

$k_b$ = Function of b, numeric

$k_h$ = $(q^2 + j2\alpha_h^2)^{\frac{1}{2}}$, $m^{-1}$

$k_1$ = $(q\rho\lambda^2 \tanh qg)/\{2d\mu_o\omega(\lambda-1)\}$, numeric

$k_2$ = $[q\rho\{(2/d) + \alpha_t\} \tanh qg]/\mu_o\omega$.

$L$ = Active width of the plate, m.

$\dot{M}$ = Given by equations (3.42) or (3.78), numeric

$m$ = $\mu_r q/\alpha$, numeric

$P$ = Total eddy-current loss in the plate and end-strips, W.

$P_c$ = Eddy-current loss in the solid-iron plate, W.

$P_e$ = Eddy-current loss in conducting end-strips, W.

$P_o$ = Eddy-current loss in the active width of a plate fitted with zero-resistivity end-strips, W.

---

* While it is realised that the symbol for the density of current sheet should be A (B.S. 1991, Pt. 6, 1975), the symbol K is used in this thesis to avoid confusion with the magnetic vector potential which has A as its symbol.

$P_y$ or $\mathcal{P}_y$ = Eddy-current loss in the plate per unit of surface area, $W/m^2$

$p$ = Number of pairs of pole, numeric.

$Q$ = Ratio of wave impedances at the surface of the plate (Chapter 6, Non-linear theory), numeric

$Q_\ell$ = Ratio of wave impedances at the surface of the plate (Chapter 4, linear theory), numeric.

$q$ = $\pi/\tau$, $m^{-1}$

$R$ = Function of b, numeric

$r$, $s$ = Constants in equation (5.17), numeric

$\dot{T}$ = Ratio of the y-component of the magnetic field strength to the x-component of the magnetic field strength at the surface of the plate, numeric.

$t$ = Time, s

$V$ = R.M.S. Voltage, V.

$x,y,z$ = Cartesian co-ordinates, x is in the direction of travel of the magnetic field and is along the length of the plate, y is measured into the depth of the plate, z is measured across the width of the plate, m.

$Z$ = Wave impedance, $\Omega$.

$\alpha$ = $(\mu_o \mu_r \omega/2\rho)^{\frac{1}{2}}$, $m^{-1}$

$\alpha$ = $\alpha_x k_b$, $m^{-1}$

$\alpha_h$ = $\alpha.\exp(-j\theta_h/2)$, $m^{-1}$

$\alpha_x$ = Given by equation (5.25) or (5.53), $m^{-1}$.

$\beta$ = $2/(1-b)$, numeric

$\gamma$ = Given by equation (5.33) or (5.58), numeric

$\Delta$ = Function of Q (Chapter 6), numeric

$\Delta_\ell$ = Function of $Q_\ell$ and plate-thickness (Chapter 4), numeric

$\delta$ = $1/\alpha$, depth of penetration, m.

$\delta_e$ = Depth of penetration in end-strips, m

$\delta_t$ = A limiting depth of penetration, equation (5.61), m.

$\varepsilon$ = $(\cosh 2\alpha d + \cos 2\alpha d)/(\cosh 2\alpha d - \cos 2\alpha d)$, numeric

$\eta$ = $\rho d_e/\rho_e d_c$, numeric

$\theta$ = Phase angle with depth, rad.

$\theta_h$ = Hysterisis angle, rad.

$\lambda$ = $(1+2\alpha d) + (1+4\alpha^2 d^2)^{\frac{1}{2}}$, numeric

$\mu_e$ = Equivalent constant permeability, H/m.

$\mu_o$ = Permeability of free space, $4\pi \times 10^{-7}$ H/m

$\mu_r (=\mu_3)$ = Relative permeability of the material of the plate, numeric.

$\mu_1$ = Relative permeability of the primary member, numeric

$\rho$ = Resistivity of the material of the plate, $\Omega$.m.

$\rho_e$ = Resistivity of the material of the end-strips, $\Omega$.m.

$\tau$ = Pole-pitch of excitation current sheet, m.

$\phi$ = Magnetic flux, Wb.

$\phi_p$ = Magnetic flux/pole, Wb.

$\phi$ = Impedance angle, rad.

$\psi_1$ = $(\sin 2\alpha d - \sin 2\alpha d)/(\cosh^2 2\alpha d - \cos^2 2\alpha d)^{\frac{1}{2}}$, numeric

$\psi_2$ = $(\sinh 2\alpha d + \sin 2\alpha d)/(\cosh^2 2\alpha d - \cos^2 2\alpha d)^{\frac{1}{2}}$, numeric

$\omega$ = Angular frequency of current sheet variation, rad/s.

SUBSCRIPTS

av = Average value

d = On the surface of the plate, i.e. at y=d.

e = In the end-strips.

h = Effect of hysteresis.

i = Any of the three regions, i=1 represents the primary member, i=2 represents the air-gap, i=3 represents the solid-iron plate.

$\ell$ = Longitudinal flux arrangement.

m = At maximum loss.

max = Maximum value

o = In a thin plate or in the presence of zero-resistivity end-strips.

t = Transverse flux arrangement.

x = Along the direction of travel of the magnetic fields, i.e. along the length of the plate.

y = Into the depth of the plate.

z = Across the width of the plate.

$\infty$ = In an infinitely thick plate.

SUPERSCRIPTS

. = Complex quantity.

* = Complex conjugate or footnote.

^ = Peak value of an alternating quantity.

~ = Sinusoidal quantity.

ABBREVIATIONS

| | |
|---|---|
| exp | = Exponential of |
| $\|G\|$ | = Absolute value of G. |
| . | = Multiplication. |
| LFA | = Longitudinal flux arrangement. |
| Re | = Real part of. |
| TFA | = Transverse flux arrangement. |
| $\equiv, \cong, \simeq,$ | = Approximately equal to. |

LIST OF CONTENTS

Page No.

# CHAPTER 1

# INTRODUCTION TO THIS THESIS

## 1.1 INTRODUCTION

Electro-heat techniques are by far the most efficient of various heating methods and induction heating is one of the most widely used. In the first part of this Chapter various heating methods are briefly discussed. The problems associated with inductively heating a metallic plate or slab are discussed and a new travelling-wave induction heating system is introduced as a probable alternative to existing induction heaters. In the rest of this Chapter, various aspects of the travelling-wave induction heater are discussed and those aspects which are the concern of this thesis are defined.

After a brief reference to the continued interest in the effects of eddy-currents, the various approaches to the solution of electromagnetic fields in solid iron are outlined and the approach used in this thesis is defined. The work of this thesis is then briefly introduced.

In a travelling-wave induction heater, a plate is subjected to travelling magnetic fields on both sides. The arrangement of poles on the two sides of the plate (Fig. 1.1) may be of similar or opposite instantaneous polarity and the significance of these are discussed in section 1.4.2. For each of these pole arrangements, two-dimensional linear theories are proposed for magnetically linear plates. In

order to account for the effects of magnetic non-linearity in a solid-iron plate, non-linear one-dimensional theories have been developed. The effects of finite plate width and the nature of end-current distribution are discussed in Chapter 7. The work of this Chapter concludes with a brief reference to the experimental investigation undertaken.

## 1.2 BACKGROUND OF THIS THESIS

### 1.2.1 General

Various existing heating methods, particularly electrical induction heating, and their limitations are discussed in this section and, from this background, the travelling-wave induction heating method is introduced.

### 1.2.2 Methods of Heating Flat Metal Plates

Various methods of heating a flat metal plate have been used in industry. Some of these methods use coal, oil or gas as the source of heat energy. Because the heating is indirect, these methods have a low rate of heat transfer and their efficiency is low. Since heat has to diffuse into the metal, heating is non-uniform and slow.

The use of electricity for heating purposes is, perhaps, as old as the discovery of it, since the passage of electric current results in heat. Because heat can be generated directly within the workpiece, system efficiencies are greater and as a result electro-heat techniques are widely adopted.

### 1.2.3 Electro-heat Techniques

Electrical heating is the method of converting electrical energy into heat energy by restricting the free flow of electric current. Different heating methods[1,2] have been developed and since electrical and magnetic phenomena are complementary, some of these methods are electro-magnetic.

There are four main methods of electrical heating:

(i) Resistance heating

(ii) Induction heating

(iii) Dielectric heating, and

(iv) Electric arc heating

Other electrical heating methods (e.g. microwave heating, electron beam heating, glow discharge heating etc.) have rather limited areas of application and are not discussed here.

Resistance heating (direct and indirect) is an efficient method; but it is expensive and the heating pattern cannot be varied. Moreover for the direct method, there is the problem of providing low contact-resistance terminals connecting the supply to the workpiece and the indirect method heats up surrounding structures in addition to the workpiece. Dielectric heating needs high frequencies and high electrode voltages and is used, generally, for non-metals and poor conductors. Electric arc heating is not a very efficient heating method, since it relies on radiation, and has limited use (e.g. steelmaking).

Electrical resistance heating, dielectric heating, electric arc heating and the other forms of electrical heating all use one or more of the three principles of heat-transfer, namely, conduction, convection and radiation.

Electrical induction heating, on the other hand, does not utilise any of these heat-transfer methods, but produces heat directly in the workpiece due primarily to the eddy-currents induced by an alternating magnetic field.

1.2.4 Induction Heating Method

Induction heating is an efficient method and is used for a variety of applications, e.g. heating metal billets, metal melting, soldering, brazing, welding etc. It has many advantages over other electrical heating methods, namely, high heating rates, heating confined to workpiece, precise control of heating sequence, ease of automation, minimum workpiece distortion, in-line operation etc.

However, in this method heat generated in the workpiece is not uniform over the cross-section due to the concentration of alternating current at the surface of the conductor (skin effect). Most of the heat, approximately 87%[3], is generated within a depth of penetration, $\delta$, defined by

$$\delta = \sqrt{\frac{\text{Resistivity}}{\pi . (\text{Permeability} \times \text{Frequency})}} \qquad (1.1)$$

Thus, magnetic materials, rather than non-magnetic, are more easily heated. Frequency of supply is an important

variable, since its choice allows the depth of the heated layer to be controlled. Frequencies varying from 50Hz to 1MHz are used, although frequencies higher than power frequencies involve extra cost.

Although induction heating of steel slabs is a long established industrial process, it has its limitations which are dependent on the method of application. In induction heating method, generally a wrap-around coil is used (Figure) and heating is achieved by a pulsating field (rather than travelling) due to the use of single phase supply. The necessity to permanently tailor the induction coil to the workpiece drastically limits its scope of application. Since the flux path is totally axial in the coil and workpiece and since the return path of the flux is usually a high reluctance one (being in air), induction heating by this method is not very effective.

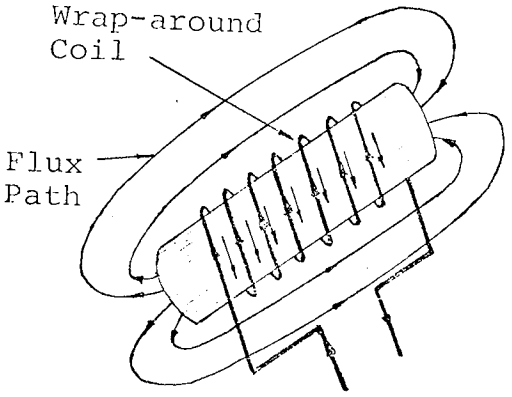


Thus there was considerable need for improvement in induction heating methods. Higher heating efficiencies in slabs may be obtained by winding the coil around the slabs largest dimensions[3] (Figure), although the

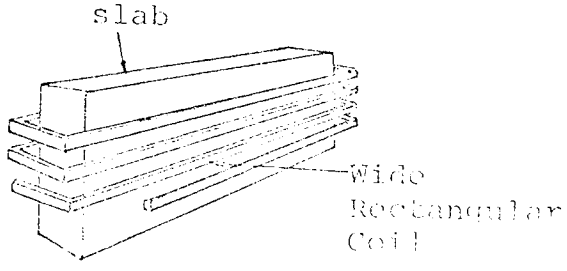

return flux path is still in the air. Many of the deficiencies of induction heating method may, however, be overcome in a split arrangement as shown in Fig. 1.1. Jackson[4] has used this arrangement for directing flux through the workpiece and hence the name transverse flux heating. But his concept applies to essentially thin plates and since single phase supply is used, the heating is non-uniform across the plate width.

The essential features of Fig. 1.1 are described in the following section.

1.2.5 Introduction of Travelling Wave Induction Heating

The travelling-wave induction heater, like other induction heating systems, produces heat by periodically varying electromagnetic fields within the workpiece.

The essential features of a travelling-wave induction heater are shown in the model of Fig. 1.1. It consists of two laminated-iron primary members each of which houses a three phase winding for the production of travelling magnetic field. The workpiece (or the plate) is placed in the air-gap between the two members. When the windings are energised

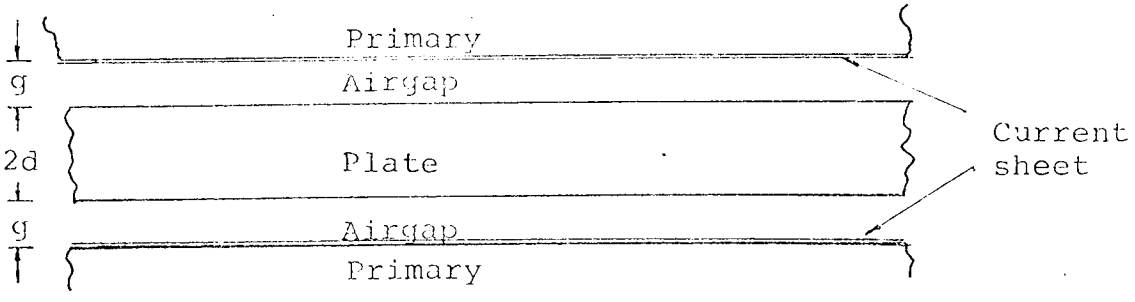


Fig. 1.1: The essential features of a travelling-wave induction heater and the model used in analysis

from a balanced three phase supply, the workpiece is subjected to travelling magnetic fields on both sides. It is possible to have opposite or like polarities on the two sides of the workpiece.

The travelling-wave induction heating differs from the conventional (i.e. using wrap-around coil) induction heating method in four major ways:

(i) The travelling magnetic field is produced by supplying the primary from a balanced three-phase source, as against single-phase supply for conventional method resulting in pulsating field. As a consequence a more uniform heating is produced by travelling-wave induction heaters. Also, for large heating requirements (of the order of MW), the three phasing balances the load demand on the industrial supply system.

(ii) The split arrangement of travelling-wave heaters offers much greater flexibility since no induction coil of fixed dimensions is involved; the same travelling-wave induction heater may be used for heating plates and slabs of various thicknesses.

(iii) In travelling-wave heating, the return flux path is a low reluctance one, being mostly in the primary iron, and thus higher effective flux densities may be obtained.

(iv) The ability of travelling-wave heaters to have

opposite or like poles offers the flexibility of obtaining different eddy-current flow patterns in the workpiece, which can result in a reduction of end-region loss (due to concentration of end currents).

Since a travelling-wave induction heater is an electromagnetic heating device, electromagnetic and thermal distributions are interactive. In addition, the essential discontinuities would introduce entry and exit problems at the ends of the effective length. These are discussed in the following section with a view to introducing the area of interest in this work.

## 1.3 ELECTROMAGNETIC FIELD DISTRIBUTION OF TRAVELLING-WAVE INDUCTION HEATERS

### 1.3.1 Electromagnetic Field Distribution

The travelling-wave induction heating, it is believed, is a new concept proposed by Davies and Bowden[5] and although it is introduced here as an electro-heat device its electromagnetic field distribution needs to be carefully analysed before the heating aspect can be considered. Whilst it is recognised that a complete analysis would involve simultaneous solution of electromagnetic field equation and the heat transfer equation, it is difficult to achieve in practice, although some efforts have been made in this direction[6]. The difficulty arises from the fact that the heat transfer

equation contains many ill-defined quantities (e.g. specific heat, thermal conductivity etc.) which are themselves functions of temperature. The presence of all three modes of heat transfer (viz, conduction, convection and radiation) further complicates the situation. However, for the travelling-wave heaters a great deal needs to be done (theoretically as well as experimentally) to understand the electromagnetic nature of the device. For example, it was felt that it would be instructive to study the distribution of electromagnetic field quantities in both magnetically linear and non-linear plates and to study the effect of finite plate width and thickness on them. It is realised that even the electromagnetic field distribution itself would have such temperature sensitive quantities as resistivity and permeability; their effects on theoretical predictions have been neglected, although approximate allowances have been made in experimental investigations for the variation of resistivity.

In addition to the temperature effect, the problems of entry and exit edges at the ends of the active length are inherent in the device due to essential discontinuities. At these positions the windings are faced with a larger air-gap than in the central part of the machine* and the plate itself passes through a transition because the travelling-

---

* The word 'machine' has sometimes been used in this thesis in place of 'travelling-wave induction heating device'.

wave either starts or finishes its travel along the plate length. The entry and exit effects manifest themselves in lower current and flux densities at the ends of the active length. However, some experimental investigations made at the start of this project showed that these effects were very small and did not occur except at the extreme ends of the active length. Also due to multipole excitation the effects of entry and exit edges are usually small. Thus in this thesis the entry and exit edge effects are also neglected,

The contents of this thesis may, therefore, be stated as a study of electromagnetic field distribution within an idealised model of a travelling-wave induction heating device as shown in Fig. 1.1, in which the current sheet considered for the primary excitation is not influenced by the finite-width or the entry and exit effects.

In the following sections reference is made to the interest in the problems associated with electromagnetic fields in ferromagnetic bodies and to the various approaches adopted for the solution of the problems.

### 1.3.2 Interest in Eddy-current Problems

Early interest in eddy-current and associated electromagnetic phenomena dates back to the nineteenth century[7]. In early twentieth century, the works of Rudenberg[8] and Rosenberg[9] are outstanding.

The considerable interest in eddy-currents since that time are due partly to historical necessities, but mostly to the following reasons:

(i) the occurrence of eddy current in a very wide range of electrical engineering apparatus.

(ii) the recognition of its occurrence as desirable [10,11] or detrimental[9].

(iii) the ever pressing need of the designer to know more accurately the effects of eddy currents, due, mostly, to the non-linear magnetisation in solid iron, and

(iv) the advances made in experimental techniques[12] and the high speed digital computers.

Depending on the source of its occurrence and the body in which it occurs, the eddy-current effects may be very complicated and difficult to solve. Various approaches are thus found in literature for their solution. Some of these approaches and the approach adopted in this thesis are discussed in the following sections.

1.3.3 Various Approaches to the Solution of Eddy-current Fields

The flow of eddy-current is associated not only with the generation of heat but also with the production of eddy-current reaction field and forces of electromagnetic origin. None of these is easy to measure and a sound theoretical basis is necessary to appreciate the effects of

each of them. Various approaches for the solution of eddy-current problems are available in published works. Accordingly, taking data from a previous similar set-up is a long established design practice, but is limited when a considerable change in size and design is involved. Making a prototype or experimental model is also widely practiced, but the questions of cost and its applicability become very important in such cases. The approach to the problem is accomplished rather easily by an analogue or a mathematical model, although numerical methods are presently being widely used. Numerical methods may be quite accurate, but are costly in terms of labour and computer time and storage. Also they lack generality. Although the analogue model simulates the performance through a network of electrical resistors, capacitors, diodes etc., it is the mathematical model that results, despite necessary approximations, in algebraic solutions in which the machine parameters appear as the variables. Thus the effect of varying one or more of these parameters is easily visualised and this, in turn, helps the design of the system.

1.3.4 Approach Adopted in this Thesis

In this thesis, an analytic approach based on an idealised model is used. Such idealisations are necessary for the problem to be amenable to analytic solutions and for taking into account the finite geometry of the arrangement. Thus, several assumptions are made at the beginning

of the theory. Either these assumptions or the mathematical model or both are later modified to incorporate the particular case being considered.

## 1.4 THE WORK OF THIS THESIS

### 1.4.1 General

Clearly, the work of this thesis recognises the presence of eddy current as desirable and studies the electromagnetic fields in a solid-iron plate subjected to travelling magnetic fields from both sides. The arrangement is shown in the model of Fig. 1.1. It consists of a plate of finite thickness, 2d, and is separated from the primary members by air-gaps each of length g. The primary excitations are represented by current sheets on the surfaces.

The work of this thesis has two parallel developments, one for each of the two different pole arrangements (section 1.4.2). For each of these, the work has three distinct aspects:

(i) a linear two-dimensional theory for the electromagnetic field components in the plate and in the air-gap.

(ii) a non-linear one dimensional theory for field components in the plate; and

(iii) finite-width effect on loss calculation including magnetic non-linearity and end-current distribution.

Aspects (ii) and (iii) of this work are experimentally

verified on a test rig.

1.4.2 The Pole Arrangements

The frequency and the direction of travelling fields on the two primary members are the same, so that poles of the two travelling fields are stationary with respect to each other. Thus, it is possible to have two different pole arrangements on the two sides of the plate.

1.4.2.1 The Longitudinal Flux Arrangement

In this arrangement, Fig. 1.2, the corresponding poles on the two sides of the plate are of similar instantaneous polarity, i.e. a north pole on the top primary member is always accompanied by another north pole on the bottom primary member. This arrangement of poles results in the

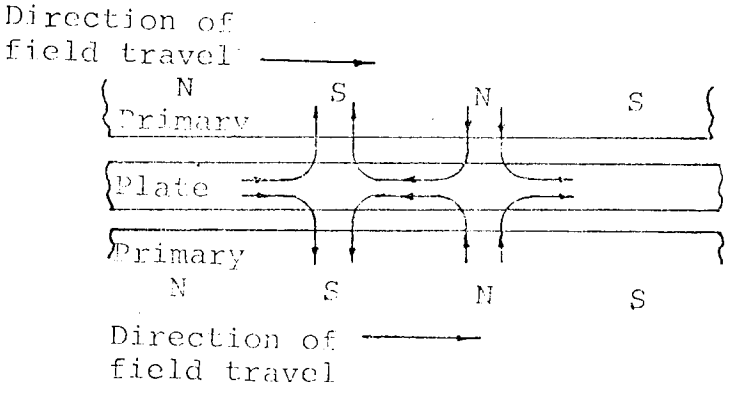


Figure 1.2: Longitudinal Flux Arrangement

flux being predominantly directed along the length of the plate and is termed the Longitudinal Flux Arrangement (or LFA for brevity) throughout this thesis.

1.4.2.2 The Transverse Flux Arrangement

In this arrangement, Fig. 1.3, the corresponding poles on the two sides of the plate are of opposite instantaneous

polarity, i.e. a north pole on the top primary member is

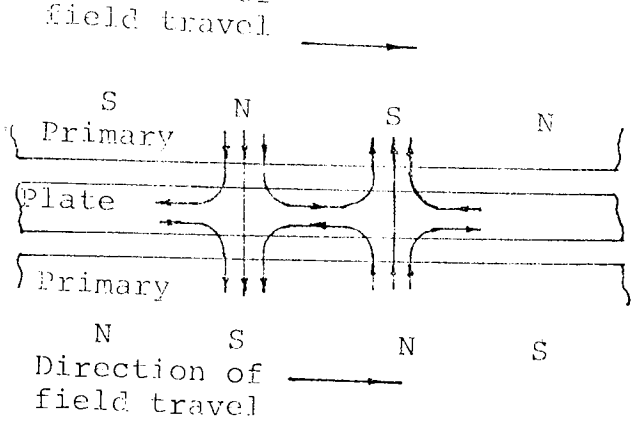


Figure 1.3: Transverse Flux Arrangement

always accompanied by a south pole on the bottom primary member. This arrangement of poles may be thought to give rise to the flux being predominantly directed across the plate thickness. (As will be shown in Chapter 3, this is far from true; but the idea is retained here only to differentiate from the LFA). This is termed the Transverse Flux Arrangement (or TFA for brevity) throughout this thesis.

1.4.3 Linear Two Dimensional Theory

Linear two-dimensional theories have been developed in Chapter 3 for the idealised double-sided arrangement shown in Fig. 1.1. Although such two-dimensional linear theories are well known[13], few studies published so far consider both a finite plate-thickness and a double-sided arrangement.

Linear theories have been developed for both longitudinal and transverse flux arrangements. The two theories differ in respect of (i) the representations of the current sheets on the surfaces of the two primary members and (ii) the boundary condition at the centre plane of the plate.

Equations have been obtained for the electromagnetic field quantities inside the plate and in the air-gap region and expressions are obtained for power loss and forces developed. Certain criteria have been obtained for considering the plate electrically thick and thin. Penetration curves have been obtained for electromagnetic field quantities inside the plate and variation of power loss through the transition from electrically thin to thick plates has been studied in some detail. The one-dimensional nature of magnetic field strength has been investigated in the presence of double-sided arrangement and finite plate thickness.

In Chapter 4, field equations have been obtained on the plate surface and are used to study the effects of eddy-current reaction field. Criteria for optimum loss in the plate are defined and expressions are obtained for optimum plate thickness. A comparative study has also been made of the electromagnetic field quantities for the two different arrangements of poles.

1.4.4 Non-linear One Dimensional Theory

In order to account for the magnetic non-linearity in the plate, one-dimensional non-linear theories have been developed in Chapter 5. $B = aH^b$ has been used for the representation of the magnetisation curve, but a new double function has been introduced as a solution to the diffusion equation. Equations have been obtained for electromagnetic field quantities, power loss and forces.

These are expressed in Chapter 6 in terms of primary excitation by equating the field solutions at the air-iron interface.

The solutions obtained clearly show the combined effects of finite thickness and magnetic non-linearity. Conditions for maximum loss in the plate are obtained and optimum plate-thickness is defined.

1.4.5 Finite-width Effects

In order to account for the effects of finite plate width on power loss, finite-width factors have been introduced in Chapter 7. Two dimensional theories have been developed for considering finite plate width. These theories are related to the linear and non-linear theories, through a new loss-invariance concept, in defining equivalent thicknesses over which the current densities have been assumed uniform.

By considering the magnitude of current densities at the end of the active width, the preferred directions of end currents for the two different pole arrangements are studied for various plate thicknesses.

1.4.6 Experimental Investigation

Experimental investigations have been undertaken in order to verify the non-linear theories proposed in Chapters 5 and 6 of this thesis. The investigation also included finite width effect and the nature of end-current distribution (Chapter 7). For this purpose two identical

primary members and three ENIA steel plates were used. These were properly instrumented for measuring surface current density, flux/pole and temperature. One of the plates used had width equal to the width of active region and was used for the investigation of finite width effect and current-density distribution at the end of the plate width.

## 1.5 CONCLUSIONS

In this Chapter an induction heating device, utilising travelling magnetic fields, is introduced. It is believed that this device offers considerable improvement and flexibility over the conventional induction heating method. In this device, a solid-iron plate is subjected to travelling fields on both of its sides and induced eddy currents produce heat in it. Although heating effects by this method are quite important, the work of this thesis is concerned with electromagnetic field distribution only. In the development of the solutions for electromagnetic fields, temperature effect and entry and exit effects are neglected and a mathematical model approach is adopted.

The longitudinal and transverse flux arrangements define two important parallel developments of the whole study. For each of these pole arrangements, the thesis has the following aspects:

(i) a linear two-dimensional theory for the electromagnetic field components in the plate and in the air-gap.

(ii) a non-linear one-dimensional theory for the field components in the plate.

(iii) effect of finite width on loss calculation including magnetic non-linearity and end-current distribution, and

(iv) an experimental verification of the non-linear theories and finite-width effect.

# CHAPTER 2

# A SURVEY OF LITERATURE

## 2.1 INTRODUCTION

As stated in Chapter 1, this thesis is concerned with the study of the distribution of electromagnetic fields and the power loss in a linear double-sided travelling wave induction heating arrangement as shown in Fig. 1.1. Heating of the plate occurs due to eddy currents induced by the travelling magnetic fields and in this chapter a brief description of the nature of eddy-current problems in relation to the above arrangement precedes the survey of published works.

The remainder of this chapter consists of three distinct parts. In the first part published works using a model similar to Fig. 1.1 are discussed with a view to defining the need and the scope of the present work. In the second part (section 2.4.4) some of the published works using linear B-H relationship are discussed. This forms the basis of the linear analysis presented in this thesis. For a ferromagnetic material, a solution is made more difficult by the non-linearity of B-H relationship and various efforts (analytic and otherwise) are made to include its effect in the solution. In the third part of this Chapter, some published analytic works including the effects of magnetic non-linearity are discussed and justification has been sought for the present treatment. Because of its relevance

to the present work, the parabolic B-H relationship has been discussed in some detail. In addition to these, various other approaches (e.g. numerical) for including the effects of magnetic non-linearity have been briefly referred to for completeness.

Published works including the important effect of finite width are not included in this Chapter and will be discussed in Chapter 7.

## 2.2 NATURE OF EDDY CURRENT PROBLEMS IN RELATION TO THE MODEL OF FIG. 1.1

Eddy currents are generated in a solid ferromagnetic material when it is subjected to a time-varying (pulsating or travelling) magnetic field. In so far as they form a closed path within the body itself, the flow of eddy currents is always associated with the production of power loss within the body and is manifested by a rise in the body's temperature, the production of an eddy-current reaction field and forces of electromagnetic origin.

The study of eddy-current phenomena in a body is very much dependent on the magnetic field strength to which it is subjected and the resulting magnetic flux density throughout the body. In a magnetically linear media, the flux density is directly proportional to the magnetic field strength and the calculation of electromagnetic field quantities in such a case is mathematically tractable; the configuration of the model determines the particular nature of the solution. In a magnetically non-linear media, the

study of eddy-current problem is complicated by magnetic saturation; this affects the electromagnetic field quantities occuring in the media and the solution obtained depends very much on the analytic (or other) relationship between flux density and the magnetic field strength.

When a solid-iron body is subjected to high magnetic field strength, not only does it bring about the problem of magnetic non-linearity, but also the increase in temperature, in turn, means that the increase in the values of resistivity and permeability of the material needs to be considered. This has been discussed in section 1.3.1. Thus, although it is recognised that the idea of producing eddy currents in a body, as in the model of Fig. 1.1, is one of producing as high a power loss as possible, the work of this thesis is concerned with the study of electromagnetic field quantities only and the effect of temperature is an important area where further work may be carried out.

Since eddy currents are confined to flow within the body in which they are generated, they have to close their paths in the end-regions where they need to be driven at the expense of the e.m.f. induced in the active region. This, in turn, means that the loss occuring in the plate will be reduced. In relation to the configuration of Fig. 1.1, this effect depends largely on the pole arrangement (section 1.4.2) and the thickness of the plate in addition to the ratio of plate-width to pole-pitch. This effect, termed finite width effect, is discussed in detail in Chapter 7.

Determination of eddy-current effects is further complicated by the occurrence of hysteresis. This occurs because the flux density in the material, on the reduction of magnetic field strength, does not retrace its own path. However, the effect of hysteresis is generally small, especially for the high magnetic field strength used in travelling wave heating, and as found in the literature, it is very often neglected. In the work of this thesis also, hysteresis is neglected, although an approximate analysis to include its effect is given in Appendix 1.

In the literature concerned with eddy current problems, only a few authors use a model like the one shown in Fig. 1.1 and in the following section published works on this model are discussed. In the subsequent sections, other works using a model similar in certain respects to that of Fig. 1.1 (single-sided arrangement with a semi-infinite body) are also included.

## 2.3 SOME PUBLISHED WORKS USING THE MODEL OF FIG. 1.1

### 2.3.1 General

The distinctive feature of the model of Fig. 1.1 is its double-sided arrangement resulting in two air-gaps, a finite plate thickness and a plane of symmetry at the centre of the plate thickness. Many double-sided eddy-current treatments consider no air-gaps, since they pertain to the loss in the steel laminations and, as such, consider the magnetic field strength on the plate surface as a known quantity. Thomson's[7] classic work is one such example.

Baker[14], Jackson[4] and Davies and Bowden[5] used the model of Fig. 1.1 (i.e. include air gaps) and Gibson et al[15] considered heating effect in some details. Two arrangements are used for this model, namely, transverse flux heaters[4,14,15] and travelling wave heaters[5] differentiated by the arrangement of poles on the two sides of the plate. These are discussed in the following sections. Reference is also made to the use of the above model for linear induction motors.

### 2.3.2 Transverse Flux Heaters

Transverse flux heaters utilise a configuration shown in Fig. 1.3 (p.15). The poles on the two primary structures are of opposite polarity and since the plate being considered is thin and non-magnetic, the air-gap flux passes normally through it i.e. in a transverse direction to that of the plane of the plate (hence the name of the heater).

Baker[14] first suggested the transverse flux induction heating method. He argued that, with the usual single solenoidal coil, the magnetic flux was longitudinal i.e. axial and the small cross-section of a non-magnetic strip contained only a small percentage of the flux through the inducing coil. Improvement was in fact achieved by using transverse-flux technique, but only for thin non-magnetic strips. The equations obtained by Baker would not apply to thick ferromagnetic plates. The strip was considered to be in motion, thus averaging out the power

loss over most of the strip length. However, heating was not uniform over the width of the strip and due to current crowding at the edges, excessive heating of the edges occured and Baker found it necessary to attach U-shaped Copper shields at the edges. While this was found satisfactory for preventing physical distortion and magnetic non-uniformity, significant electrical losses were believed to occur in the shield.

An improvement was later suggested by Lackner[16] in which the current and directions of strip motion were inclined to one another (i.e. not at $90^{o}$). Jackson[4] and Gibson et al[15] used this skewed arrangement which resulted in a reduction of edge heating. However, the distribution of current and power density across the width of the plate was not uniform, resulting in non-uniform heating.

Jackson[4] has carried out extensive theoretical and experimental work on transverse flux heaters and this method of heating is claimed to offer a rapid rate of heating at high strip speeds. Jackson showed that for a given excitation the loss occuring in electrically thin plates had a maximum value for transverse flux heating. This is also substantiated in the present work (Chapter 3). Very high theoretical efficiencies were obtained by Jackson for transverse flux heating. Jackson also considered resistance-limited and reactance-limited cases of eddy-current distribution, the former occuring in thin plates and the latter in thick plates. However, transverse flux

heating was found unsuitable for thick ferromagnetic plates, although it was suitable for non-magnetic plates of low resistivity. The author recognised that longitudinal flux heating was better suited for magnetic strips or plates. Although Jackson considered heating of electrically thin plates, he did not consider transition modes from thin to thick plates. Gibson et al[15] reported experimental results for transverse flux heating of thin stainless steel sheets and close agreement with computed results was obtained.

Transverse flux heaters have limitations of their own. As has been suggested by the authors, this heating system was useful mainly for electrically thin strips and the idea originated from the necessity of directing the magnetic flux in the low reluctance path across the plate thickness for non-magnetic materials. Nevertheless, these strips are subjected to electromagnetic fields and hence, unless the plate is electrically thin*, the magnetic flux density in it would have longitudinal, in addition to transverse, component even in the transverse flux configuration. For electrically thick* plates, the longitudinal component of flux density becomes the dominant one and the transverse flux concept becomes invalid.

---

* A plate or strip may be considered thin or thick depending on whether its half-thickness is less or greater than the depth of penetration in that material, respectively.

Transverse flux heaters utilise a single-phase supply and this results in non-uniform heating. For moving strips, this effect may be reduced, but cannot be eliminated altogether. Since in the transverse flux heaters poles in the half inductors are of opposite polarity, eddy currents circulate only in planes parallel to the air-gap surface and considerable reduction in power loss can take place due to the impedance of current paths which do not link active flux.

Thus, there is a need to improve on the existing heating arrangement utilising transverse flux technique, and yet retain the advantages and flexibilities of the split arrangement. One such arrangement was suggested by Davies and Bowden[5].

### 2.3.3 Travelling Wave Induction Heaters

As an improvement to the transverse flux heaters, Davies and Bowden[5] suggested travelling wave induction heaters, where, more uniform heating was obtained by the use of a balanced three phase supply, instead of single phase. Their travelling-wave induction heater envisaged similar instantaneous polarity* for the corresponding poles of each half inductor and was shown to result in a much higher power loss in the plate, compared with the same when the opposite instantaneous polarity** for the

---

* Longitudinal flux arrangement of the present work.
** Transverse flux arrangement of the present work.

corresponding poles was considered. This higher loss was due, primarily, to the cross-thickness rather than cross-pole distribution of end currents.

Their work, which did not include any analytic treatment of the travelling wave heating arrangement, was, it is believed, a pioneering piece of work in this field and pointed to the necessity of carrying out extensive theoretical and experimental studies of the two different pole arrangements.

### 2.3.4 Other Literature

The bulk of the treatments for the model of Fig. 1.1 is , however, in connection with a different class of problem, namely, the theory of linear induction motors[17-22] where a developed linear arrangement is considered for the conventional cylindrical induction motor. These studies are mainly concerned with the thrust exerted on a linearly moving part by travelling magnetic fields and these moving parts may not necessarily be of ferromagnetic material[22]. In the present arrangement, however, essentially ferromagnetic material is considered and although no motion of the plate is envisaged, due consideration is given to the forces of electromagnetic origin. Many linear induction motor applications are single-sided, whereas the present work necessarily considers a double-sided arrangement. In a linear induction motor, the problem of heat developed is particularly unwelcome. In the present arrangement,

however, heating effect of eddy currents is very desirable. Also, due to essential discontinuities, short rotor or short stator effects do arise in linear induction motors and part of the whole machine is in a transient state at all times. The problem of edge-effect[20] both at entry and exit edges of the plate and the effect of finite width of the moving part[19,21,22] further complicates the treatment of linear induction motors.

Thus, although these works consider a model like the one shown in Fig. 1.1, they have very little in common with the present work, but are included here for completeness. However, these linear induction motors were considered to be suitable for the production of travelling magnetic fields (i.e. primary members) in the model and two identical linear induction motor units were actually used for the experimental investigations (Chapter 8).

### 2.3.5 Observations

It may be observed from the study in this section that transverse flux heating has many shortcomings and these may be overcome by the use of a travelling-wave induction heating system. It may also be observed that there is a need for extensive study (theoretical and experimental) of electromagnetic fields in such a system. However, any such study would have to consider various aspects of magnestisation (e.g. analytic B-H relationship, effect of magnetic non-linearity etc.) and in the following sections of this Chapter, some published works on these aspects are discussed.

## 2.4 A SURVEY OF LITERATURE ON EDDY-CURRENT PROBLEMS

### 2.4.1 General

In this section, some published works on electromagnetic effects in cases of magnetically linear and non-linear plates are considered. Most of the works included here are analytic; other works (e.g. graphical) are briefly included for completeness.

### 2.4.2 Early Works

In considering means for reducing eddy-current loss in transformer laminations, Thomson[7] (1892) related mathematically the loss in thick and thin plates to the number of laminae, frequency and permeability. Thomson's analysis is basically one-dimensional; although similarity of expressions with the present linear theory (Chapter 3) is notable. Also, he considered a known surface magnetic field strength instead of primary excitation.

Following the early work of Thomson, Rudenberg[8] (1906) solved the diffusion equation for a two-dimensional model of eddy-current coupling. He considered the applied field and the reaction fields of eddy currents. Even though he considered constant permeability, Rudenberg's work was a major contribution of his time and formed the basis of some subsequent works (e.g. Glazenko[23]).

The effects of magnetic non-linearity are implicit in Rosenberg's[9] (1923) work carried out for the flux in an iron core. The flux density into the depth of iron was

taken as constant over a depth of penetration and negligible at greater depths. Current density was taken as maximum on the surface and decreased uniformly to zero over the same depth of penetration. Power loss/area was shown to vary approximately to the exponent 1.5 of the magnetic field strength (compared with 2.0 in the linear case). In his one-dimensional analysis, Rosenberg considered a pulsating field. His assumption of uniform flux density over the depth of penetration and neglect of phase shift with depth resulted in smaller calculated depth of penetration and lower loss values. Despite these limitations, good agreement between predicted and experimental values of loss were obtained and this showed the need to consider the effects of magnetic non-linearity.

### 2.4.3 Dependence of Analyses on Assumed B-H Relations

In all the analyses of the electromagnetic effects of eddy-current, it is necessary to assume some kind of relationship between B, the magnetic flux density obtained in the media and H, the magnetic field strength producing the flux density. This applies irrespective of whether magnetic non-linearity is considered or not. Depending on the kind of B-H relation, a solution particular to the problem being considered is obtained. Some published works depending on linear B-H relation are discussed below, while others are discussed later.

### 2.4.4 Linear Analyses

Linear B-H relationship is the simplest and considers the magnetic field intensity, H, as being directly proportional to the flux density, B, i.e.

$$B = \mu H \qquad (2.1)$$

where the constant of proportionality, $\mu$, is the permeability of the material.

All published works considering a linear B-H relationship use a model for the analysis. The model considered in the works discussed here are similar to Fig. 1.1 in so far as excitation is produced by a primary member and the body in which eddy current occurs is separated from the primary member by an air-gap. The linear analyses on the basis of these models bring out the aspects that must be considered in the present treatment. Some published works considering linear B-H relationship are discussed below.

In connection with their analysis for a synchronous machine with cylindrical solid-iron rotor, Concordia and Poritsky[24] developed a rigorous mathematical treatment from field distribution theory. Their work made a worthwhile contribution in predicting the performance of synchronous machines under transient and sub-transient conditions. They considered a surface current sheet for excitation and also assumed that the magnetic field did not vary in the axial direction. Although their paper presented a means of considering the effect of eddy currents in solid iron, no eddy-current loss expression was given; it also neglected end effects and considered infinite stator permeability without justification.

Kuyper[25] presented a two-dimensional linear analysis in determining pole-face losses in solid-rotor turbine generator. He carried out an analysis in terms of a current sheet and obtained that the tangential component of magnetic field strength in the rotor was greater than the radial component. Contribution of higher m.m.f. harmonics was considered in his loss calculations. However, Kuyper neglected end-effects and considered infinite stator permeability from the beginning.

Mukherji[25] presented a linear solution for a rotor subjected to an alternating field and considered the reaction of eddy-current (induced in the rotor) on the inducing field. He, however, did not consider the presence of a ferromagnetic medium for the location of the source of excitation. Mukherji, in a later paper[27], introduced a stator with finite permeability and resistivity. He showed that the field at the air-gap/rotor interface was a component of stator excitation, which attenuated over the air-gap length in an exponential manner. His consideration of finite stator core permeability is a more realistic approach. He showed that for large values of stator permeability and air-gap length, expressions obtained[27] for electromagnetic field quantities were consistent with those obtained previously[26]. However, his work is a case of single-sided excitation and he did not consider the occurrence of eddy currents in a finite thickness of the media.

Based on Mukherji's work, Stoll and Hammond[28] considered eddy-current loss in a plate of finite thickness. The paper considers the problem of a current sheet carrying a sinusoidally distributed current parallel to a conducting magnetic surface. The paper makes the distinction between the total (or resultant) and the applied magnetic fields and recognises that it is the total field that satisfies the complete field equations. Their observations about the criteria of plate thickness, one-dimensional nature of magnetic fields for the calculation of current density and power loss and their use of the method of images are also commendable.

Although Stoll and Hammond considered eddy currents in a plate of finite thickness, theirs' is also a case of single-sided excitation. However, their model resembles that of the present work in so far as a current sheet, separated by an air-gap causes eddy current in the solid conducting medium. Thus, some similarity of observations and also of expressions may be expected especially when the plate thickness is large.

Lammeraner and Stafl[29] have also dealt in detail with linear theory. Their work clearly showed how the skin effect of eddy current influences the resistance of the body in which it flows. Although their analysis concerned thin laminations, the equations obtained were, nevertheless, applicable to a plate of finite thickness. The assumed distributions of flux and current densities over the plate

thickness (Fig. 6 of reference 29) are similar to those considered for longitudinal flux arrangement (Chapter 3) of the present work. Similarity of the nature of equations is also notable. The authors have also analysed the penetration of a plane electromagnetic wave in a thick plate. However, their work envisages a known surface magnetic field strength, which, very often forms an unknown component of a known primary excitation .

Elaborate studies of one and two-dimensional electromagnetic fields considering linear magnetisation was also undertaken by Stoll[13]. His study of eddy currents in a plate subjected to uniform applied field parallel to its surfaces (section 2.2 - 2.4, reference 13), in effect, utilises a one-dimensional study of the longitudinal flux case (Chapter 3) of this thesis. The similar nature of curves obtained for loss by Stoll (Fig. 2.2 of reference 13) and in the present work (Fig. 3.6, firm lines) shows that the eddy-current loss in the plate is determined by one-dimensional fields irrespective of plate-thickness. His observations about power loss in electrically thick and thin plates are also similar to those obtained in the present work. However, Stoll considered one-dimensional eddy-current flow and his work being concerned with eddy-current loss in laminations also considered the magnetic field strength on the plate surface as a known quantity. In his two-dimensional study later, Stoll considered a known primary excitation, instead of surface magnetic field strength.

Bowden's[30] study of linear magnetisation considers a

semi-infinite solid-iron medium. Bowden considers a primary current sheet rather than unknown surface magnetic field strength. He considers finite permeability of the primary members from the beginning and later justified its being considered infinite. His contributions to published eddy current theories include the treatment of impedance matching principle, recognition of eddy current reaction field and analysis in terms of a dimensionless parameter, Q. He obtained expressions for loss, torque and flux/pole and defined the conditions when these would be maximum. The one-dimensional nature of eddy current loss in a two-dimensional model was also obtained.

### 2.4.5 Effect of Magnetic Non-linearity

For the case of linear magnetisation, the flux density in the material increases linearly with increase in the magnetic field strength. This, however, applies to non-ferromagnetic materials and approximately for low excitation (below the knee point of the magnetisation curve) applications in ferromagnetic materials. For very high temperature applications of ferromagnetic materials (above Curie point), the linear theory applies.

In general, the ferromagnetic materials exhibit marked non-linearity with increase in magnetic field strength; although it is realised that even at low excitations, the assumption of linear magnetisation for solid iron is not strictly justified. Nevertheless, it is the saturation effect at higher excitation (above knee point

of the magnetisation curve) that is of interest in most practical applications.

The effect of magnetic non-linearity is that the permeability of the material (apart from the effect of temperature) is no longer constant, but is a function of magnetic field strength. With increase in magnetic field strength, the permeability increases at first and then decreases. A unique permeability may, therefore, be defined at each layer inside the solid-iron plate.

In addition to the permeability being a variable, magnetic saturation results in a much higher loss in the body in which the eddy-currents flow. It has been shown[30] that due to magnetic saturation eddy-current loss may be as high as 1.47 times of the same in the linear case and hence it is important to consider magnetic non-linearity.

Various efforts have been made in the past in order to account for the effects of magnetic non-linearity. These include analytic, graphical and numerical approaches. Some analytic approaches are considered below.

Of the various analytic treatments of magnetic non-linearity, one relation between B and H is the limiting non-linear case (Fig. 2.1) and it is briefly discussed in the following section. Other analytic approaches are discussed later.

2.4.6 Analyses Depending on Limiting Non-linear B-H Relation

The limiting non-linear (or step function) B-H relation is shown in Fig. 2.1. The magnetic flux density

in the solid-iron body is supposed to have only one value $\pm B_s$, called saturation flux density, for all values of magnetic field intensity $\pm H$ except $H = 0$ when the flux changes instantly from one direction to the other.

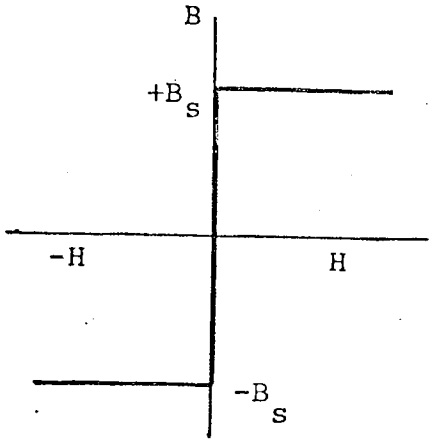


The B-H relation may be expressed in this case as

$$B = B_s(\text{Sig. } H) \qquad (2.2)$$

Where 'Sig. H' stands for 'Sign of H'.

Figure 2.1: Step function B-H curve

Many authors[31-34,36] have considered this case and the result is one of a moving wave-front of flux density with distorted wave-fronts of induced e.m.f., flux and magnetic field intensity inside the body, depending on whether H is considered sinusoidal or $\Phi$ is considered sinusoidal.

Haberland and Haberland[31] offered the first treatment of limiting non-linear case in 1936. McConnell[32] presented the diminishing magnitudes and phase shift of flux density with depth for linear and limiting non-linear theories in a logical manner. After discussing the shortcomings of Rosenberg's theory[9], McConnell showed that the limiting non-linear theory included the effects of both time

harmonics of current density and phase shift in the magnetic field strength. He made specific reference to the use of non-linear theory in calculations of inductive and conductive heating. McConnell[32] assumed a sinusoidal flux. In contrast, MacLean[33] considered sinusoidal magnetic field strength and showed that the loss on the surface calculated on the basis of step-function B-H curve was $16/3\pi$ times higher than that of linear theory and $\pi/4$ times that obtained by Rosenberg[9].

Agarwal[34], like MacLean[33], also assumed sinusoidal magnetic field on the surface; but considered penetration of the wave from both sides of a plate of finite thickness. Depending on whether the half-thickness of the plate was greater than the depth of penetration or otherwise, Agarwal obtained theoretical waveforms for electric field and magnetic flux on the surface and inside of the plate. These were substantiated by extensive experimental work. Loss values obtained by his theory was higher than those obtained experimentally and in order to provide good agreement between theory and test results, Agarwal found it necessary to reduce the saturation flux density, $B_s$, at the surface corresponding to peak impressed mmf, by an empirical factor of 0.75. The logical basis of this empirical factor has since been proved by Bowden[30] and Ellett[35].

Davies and Bowden[36] used step function B-H curve for direct resistance heating problem of a cylindrical body. The theory considered constant voltage and constant current

modes and dealt with the penetration of e.m.f. wave into a cylindrical body. They introduced a concept of saturation depth which was verified by experimental results.

### 2.4.7 Analyses based on Other Analytic Representations of B-H Curve

It has been shown that, by comparison with experimental results, the linear theory underestimates the loss in solid-iron, whilst the limiting non-linear theory overestimates it; a more realistic representation of B-H relation must be somewhere in between. Various attempts have been made to represent this relation analytically and Fisher and Moser[37] made a survey of many such functions. They showed that while the Frohlich equation, $B=H/(a+bH)$, and the equation of the form $B=a-b/H$, where a and b are constants, are most suitable for the representation of B-H relation at and around the knee of the magnetisation curve, they are less accurate at higher magnetic field strengths. Alternately, the simple parabolic representation, $B=aH^b$ is less accurate for very low magnetising field strength, but is most suitable for representing the saturated region of the curve (typically 1.5 - 30.0 kA/m for mild steel). Because of its especial relation to this work, the parabolic representation of the magnetisation curve is discussed in the following section.

### 2.4.8 The Parabolic Representation ($B=aH^b$) of the Magnetisation Curve

2.4.8.1 The Nature of $B = aH^b$ Representation

In the parabolic representation of the magnetisation curve, the peak value of magnetic field intensity, H, and the peak value of the resulting magnetic flux density, B, are related by

$$B = aH^b \qquad (2.3)$$

where a and b are constants. This pre-supposes that a sinusoidal H-field results in a sinusoidal B-field, which is, of course, not so in practice due to magnetic non-linearity. Depending on the type of analysis, however, one or both of B and H may be sinusoidal. Equation (2.3) above relates the peak values of two sinusoidal quantities which may be fundamental components of distorted B and/or H wave.

The function $B = aH^b$ may be used to represent B-H curve of any shape by the appropriate choice of the parameters a and b. For the linear case b = 1 and the limiting non-linear case may be obtained by putting b = o. Thus, as shown in Fig. 2.2, the parabolic function may be used to represent any shape of B-H curve and the constant b may be recognised as a shape factor. The constant a represents either the permeability of the material (linear case) or the saturation flux density (limiting non-linear case). For the general case of non-linear

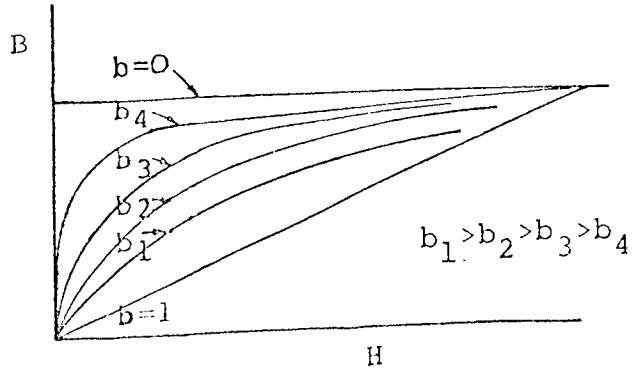


Figure 2.2: Variation of B-H curve in $B=aH^b$ equation with the exponent b

magnetisation, however, the constants a and b may be obtained from the log-log plot of normal B-H curve of the material, b being the slope of the then linear portion of the curve and a is obtained by substituting the value of b in the equation. It is clear from Fig. 2.2 that the value of the exponent b should be between 0 and 1, closer for a ferromagnetic material to 0 than 1.

Not only is the $B = aH^b$ type representation suitable for values of H well into saturation, it offers even a better fit when the material temperature rises above room temperature. The permeability $\mu$ obtained as

$$\mu = aH^{b-1} \qquad (2.4)$$

however, approaches very high values at very low values of magnetic field strength, as against small values obtained from the actual B-H curve. Although this is recognised as a shortcoming, it has been shown[30] to have much less effect on loss than it at first appears.

Because of its simplicity of form, accuracy of representation, flexibility of analytic treatment and logical similarity to the B-H curve on a log-log plot, it was decided to use parabolic function for representing B-H relation in the non-linear theory (Chapter 5).

2.4.8.2 Analyses Using $B = aH^b$ Type Analytic Function

Many authors[30,38-46] have used the parabolic function for representing the magnetisation wave. Nejman[38] assumed a spatial variation of permeability of the form

$$\mu = 1/(c-dy)^2 \qquad (2.5)$$

where c and d were constants. Using equation (2.5) in Maxwell's one-dimensional equation, he obtained an expression for magnetic field strength. The constants c and d were, however, obtained by equating the arbitrary function (equation (2.5)) to the permeability defined from $B=aH^b$ relation. Lasocinski[39] developed his theory on the basis of constant permeability at first and later accounted for its variation according to Nejman's[38] method. Thus both the above works lack merit in so far as an arbitrary spacial variation of permeability was initially assumed.

In connection with his work on eddy-current couplings, Davies[40], following Gibb's[11] work, started with a linear analysis, but discovered that the upper part of the magnetisation curve for his loss drum followed a relation $(\mu_r\mu_o)^{\frac{1}{4}} H = kH^m$, where k and m were constants. He later modified this in the form of equation (2.3) and produced a generalised theory[41]. In his extensive experimental and theoretical work, Davies obtained eddy-current reaction mmf, and its relation to the surface magnetic field strength. He also developed normalised torque-slip curve, the flux/pole and the relation between torque and applied mmf. Davies, however, allowed for magnetic non-linearity in his final expression and the permeability did not vary with depth. For a more appropriate appreciation of this function to represent magnetic non-linearity, this B-H relation (i.e. $B = aH^b$) needs to be substituted at an early stage. This was done by Bowden[30].

Pillai[42], using parabolic B-H relation, obtained eddy-current loss density, flux/pole, magnetic field strength and induced emf in a solid-rotor induction motor. Pillai[43], in part 2 of his paper, extended his own work for a hollow rotor (i.e. a rotor having a finite radial thickness). Results obtained were given in graphical form and good agreement was obtained between experimental and predicted values. However, Pillai's assumption that the tangential components of flux density, $B_x$, and the magnetic field strength, $H_x$, were related by equation (2.3), whereas the relation between the radial components of the same (i.e. $B_y$ and $H_y$) was linear, needs more justification. Whilst it is correct that $H_x >> H_y$ and consequently, the component flux densities may well be into non-linear and linear regions respectively, permeabilities may not be chosen in different directions independent of each other and the component flux densities are obtained from a resultant B, which may be well into saturation. In effect, Pillai tried to offer a two-dimensional non-linear analytic solution which is known to be difficult. He got expressions for loss for the limiting non-linear case, although the linear case was not considered. While the effect of temperature rise was included in a simple and useful way, very little has been mentioned about the quantity, 'thermal conductivity' which is a function of temperature, and about the effect of temperature on the variation of air-gap length.

Davies et al[44] used the parabolic B-H relation for the experimental verification of the generalised theory of

eddy-current coupling and good agreement was obtained between predicted and experimental values. The authors suggested the use of equation (2.3) for design purposes.

Woolley[45] and Chalmers and Woolley[46], in connection with a general theory for solid-rotor induction motors, have used the parabolic B-H relation together with limiting non-linear function and another function of the form $\mu_i H = B/(1-B/B_s)$ where $\mu_i$ was the initial permeability and $B_s$ was the value of B at very high H. Compared with the results of other forms of B-H relation, they obtained, using $B = aH^b$ representation, consistently good agreement between predicted and experimental values of torque-slip and current-slip characteristics for a wide range of motors (6 W, 250 W and 1.5 kW).

All these published works suggest that in studying the effects of magnetic non-linearity analytically, the parabolic B-H relationship is most suitable and accurate.

2.4.8.3 Bowden's Work Using $B = aH^b$

It is believed that Bowden's non-linear analysis[30] was the only one of its kind in so far as the function $B = aH^b$ was inserted into the diffusion equation at an initial stage and expressions for loss, armature reaction and flux/pole were obtained in terms of primary excitation and the constants a and b. In his solution, Bowden considered a one-dimensional magnetic field strength ($H_x >> H_y$) inside the rotor and obtained a new expresssion for the peripheral component of magnetic field intensity, $H_x$.

He extended his work to two-dimensional analysis by equating current densities at the air-iron interface, and hence obtained loss in terms of primary excitation. The ratio of wave impedances in the iron and in air-gap surface of the rotor was introduced as a dimensionless parameter, $Q_n$, and was fruitfully exploited for performance calculations. Depending on whether $Q_n$ was much smaller than, equal to and greater than unity, the eddy-current loss was shown to be proportional to $1/\rho$ (approximately), independent of $\rho$, and proportional to $\sqrt{\rho}$ respectively, thereby, recognising three distinct modes of machine operation. His work successfully included linear and non-linear magnetisations as special cases. He obtained expressions for generalised loss and torque and the variation of flux/pole with torque. Bowden substantiated his theory by extensive experimental investigation.

### 2.4.9 Other Non-linear Solutions

Various other approaches for the representation of the magnetisation curve are available in literature. Some of these utilise an assumed variation of permeability with depth, some utilise a graphical approach, while others use finite-element and finite-difference solutions.

#### 2.4.9.1 Assumed Permeability Distribution

Ollendorf[47] and Gonen and Stricker[48] assumed that permeability varied with depth, y, according to the relation

$$\mu(y) = \mu_s \exp(y/y_s) \qquad (2.6)$$

where $\mu_s$ is the surface value of permeability and $y_s$ is the decay depth of permeability. Increase in permeability with depth, predicted by equation (2.6) is justified in so far as H decreases with depth. Fig. (2.3) shows the actual variation of $\mu$ with H together with the above function. As shown in this figure, however, for very weak H-field (i.e. below the knee point) permeability actually decreases, so that equation (2.6) is only approximately true. The other disadvantage of using this function is that even with no air-gap assumption, the loss and torque equations are in terms of complicated Hankel functions, which are not well tabulated.

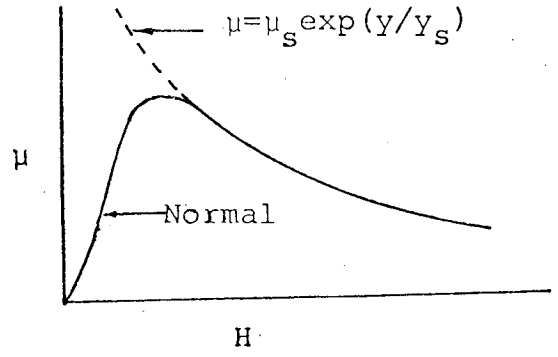


Figure 2.3: $\mu$-H curve

Nejman[38] also assumed a spatial permeability variation and is given by equation (2.5). This has been discussed in section 2.4.7.2.

2.4.9.2 Graphical Solution

In the graphical method of solution, the whole of the ferromagnetic body is divided into thin layers each, say $\delta y$, and a linear solution is obtained for each layer. The values of magnetic and electric field strengths and hence the flux density are assumed on the surface of the material

and their values at the depth $\delta y$ are obtained from linear theory. These values now determine the starting point for obtaining the electromagnetic field quantities in the next layer, which now has a new permeability (determined by the magnetic field strength at the depth $\delta y$ below the surface). The process is continued till the magnetisation phenomena in the whole body is obtained. Pohl[49] and later Kesavamurthy et al[50,51] have used this step-by-step solution of this graphical method. The graphical method of solution could offer a high degree of accuracy because of the very nature of the procedure, but it is a very laborious and a rather lengthy technique. Although similar to piecework linearisation of the magnetisation curve, the graphical solution is the less accurate one, since the permeability is obtained from B/H rather than dB/dH.

2.4.9.3 Finite-element Method

In the finite-element method of solution, the problem is discretised in such a way that the field variable has a simply defined variation over a number of elements which may be triangular, rectangular or of any other convenient form which together covers the region. This variational method is based on calculus of variations and seeks to approximate the field function. The advantages of the method are that the inclusion of boundary conditions is inherent in the method and that the sub-division of the elements may be graded to give small elements where it is anticipated that the field is varying rapidly and large elements elsewhere

for economy. Also a high degree of accuracy may be obtained in this method. Disadvantages of this method are that it is conceptually difficult and that resulting matrix equation requires compact storage and Gaussian elimination for solution.

The finite-element method of solution has not been applied to eddy-current problems to any great extent, although Binns, Jabbar and Bernard[52] have used it for computing the magnetic fields of permanent magnets.

2.4.9.4 Finite-difference Method

The finite-difference method is simpler to apply than the finite-element method. In this method of numerical solution, the equation of an electromagnetic field component is written in the algebraic form in which the differential forms are expanded by Taylor series. Because of the development of high-speed digital computers, it is possible to replace the differential equations with difference equations having very small increments. The problems of convergence and hence, of efficient use of computer-time, however, do arise. Also the accuracy of finite difference method is limited by the discretisation error due to the truncation of higher order terms in Taylor series, although the error is generally small.

Gillot and Calvert's[53] finite-difference solution for electromagnetic fields inside a solid-iron plate considered sinusoidal mmf., sinusoidal flux and total conduction current and used the normal B-H curve rather than any usual

approximations to it. Computed loss agreed well with test results. While they neglected hysteresis, Gillot and Abrams[54] considered it in their finite-difference calculation. They too obtained good agreement between calculated and measured values of loss.

While the finite-difference solutions are very accurate, they cannot be presented in a way in which the machine dimensions and other parameters appear as variable (as they do in analytic solutions). In the finite-difference solutions of Lim and Hammond[55,56], this disadvantage has been partly overcome by expressing various machine dimensions and parameters as dimensionless variables. The authors[55] have produced universal loss charts from which the power loss for a wide range of surface magnetic values and a variety of steels may be obtained after simple calculations. Their work thus has the merit of an analytic solution; although, as the name suggests, only loss values can be obtained. Lim and Hammond[56] have obtained electromagnetic field components on the surface and at depths inside the plate and compared with those obtained by Agarwal's theory[34]. Their work showed that the contribution of the fundamental component of eddy-current to the loss was high even at high levels of saturation. However, the accuracy of both of their treatments is limited by the Fröhlich approximation to B-H curve, which, as has been mentioned in section 2.4.7, offers good approximations at and around the knee of normal magnetisation curve and diverges at high H.

## 2.5 CONCLUSIONS

In this Chapter, a survey has been made of some published literature on eddy current and associated electromagnetic and thermal problems in a model of Fig. 1.1 and in some similar models.

It may be observed from this survey that most of the published works on eddy currents consider its occurrence in a semi-infinite body due necessarily to a single-sided excitation. Some works that consider a finite thickness of the body and a double-sided excitation consider no air-gaps and also the magnetic field on the plate surface as a known quantity. Others consider non-uniform heating effects due to pulsating transverse flux in essentially thin plates. Many of the shortcomings of a transverse flux heater may be overcome by the use of travelling magnetic fields in its split arrangement. However, no published work is available on such a system. Thus there is a gap in the literature where a study may be made of eddy currents and associated electromagnetic phenomena in a solid-iron plate of finite thickness, subjected to travelling magnetic fields on both sides. An idealised model for such a study is shown in Fig. 1.1, in which the magnetic field strengths on the plate surface constitute unknown components of a known primary excitation. Further, two different arrangements of poles of travelling fields on the two sides of the plate may be considered in such a study.

The survey of literature on eddy-current problems shows that many published works consider linear magnetisation only and are, thus, strictly limited to low excitations or to non-magnetic materials. Others consider the limiting non-linear magnetisation where a saturation flux density is obtained at all excitations and thus, overestimates the effects of saturation. Some authors try to incorporate the effect of magnetic non-linearity by functional representations. While such a representation of magnetisation curve has its own limitations, it offers good compromise between underestimating (as in linear case) and overestimating (as in the limiting non-linear case) the effects of magnetic non-linearity on loss. After considering its advantages and limitations, the parabolic B-H curve has been chosen in this thesis to represent the normal magnetisation curve of the material.

A two-dimensional linear theory for the model of Fig. 1.1 is given in Chapters 3 and 4 of this thesis, where due consideration has been given to the reaction fields of eddy current. A non-linear theory (assuming $B = aH^b$) for the same model is developed in Chapters 5 and 6 where a new function has been introduced for the solution of diffusion equation.

# CHAPTER 3

# LINEAR TWO DIMENSIONAL THEORIES FOR (a) LONGITUDINAL FLUX ARRANGEMENT AND (b) TRANSVERSE FLUX ARRANGEMENT

## 3.1 INTRODUCTION

In this chapter a two-dimensional linear theory is developed for both longitudinal and transverse flux arrangements for the model configuration given in Fig. 1.1. As explained in Chapter 1, the linear induction heater consists of an iron plate subjected to travelling magnetic fields from both sides. For the longitudinal flux arrangement, the corresponding poles on both sides of the plate are of similar instantaneous polarity, while for the transverse flux arrangement, they are of opposite instantaneous polarity.

The primary excitation is assumed to consist of a z-directed current sheet only and the flux density is taken as directly proportional to the magnetic field intensity. Analysis is carried out in terms of the magnetic vector potential A and expressions are given for the magnetic field strengths and current densities within the plate. The general expressions obtained are modified to suit the condition of pole-pitch being much greater than the depth of penetration. Expressions for power loss and force are also given.

The solutions obtained show that the effect of primary iron on the electromagnetic fields inside the plate is influenced by the finite plate thickness.

Equations are obtained for the components of magnetic field strengths on the surface of the plate and by considering their relative magnitudes, thickness criteria (i.e. for the plate to be considered electromagnetically thick and thin) are established. The one-dimensional nature of electromagnetic field quantities is investigated for a plate of finite thickness and also for the two different pole arrangements. Variation of power loss in the plate through the transition from electromagnetically thin to thick plates is considered for the two different arrangements. When the plate is thick, expressions for the electromagnetic field quantities are checked against those previously published.

The mathematical model assumed is explained in Section 3.2. The assumptions made are also summarised in Section 3.2 and the solutions for electromagnetic field quantities are given in Section 3.3. Analysis is then carried out for the two different pole arrangements being considered.

## 3.2 THE MATHEMATICAL MODEL

### 3.2.1 General

The mathematical model chosen for the analysis and the associated co-ordinate system are shown in Fig. 3.1 (p.57) It consists of a solid-iron secondary plate of thickness 2d which is separated from the two primary members by air-gaps of length g each. The current sheets are assumed to be located on the surfaces of the two primaries. Since

a flat linear arrangement is being considered, rectangular co-ordinates have been used. The three co-ordinates x, y, z, are used to represent the following directions:

x : the length of the plate and also the direction of travel for the magnetic fields.

y : the plate thickness, and

z : the plate width (i.e. perpendicular to the plane of Fig. 3.1).

Fig. 3.1 consists of three regions, namely, the laminated-iron primary, the air-gap and the solid-iron secondary. Each of these regions and the associated assumptions will be explained in the following sub-sections. However, it may be noted in Fig. 3.1 that y = 0 is a plane of symmetry and the analysis may be carried out for either half of the plate only. The solution obtained would, of course, be subject to clearly defined boundary conditions at this plane, so that with due regard to the sign, the same solution will be applicable to the other half of the secondary. Thus in the following analysis only the upper half of the secondary will be considered, i.e. for y varying from y = 0 to y = d.

The model will be assumed to be extending from $z = -\infty$ to $z = +\infty$ and also from $x = -\infty$ to $x = +\infty$, so that finite-width effect and entry and exit-edge effect are ignored. It is customary to make such assumptions[13,28,29,30,40], so that the current density

in the secondary may be assumed purely along the width (i.e. z-directed), and the problem becomes amenable to analytic treatments. However, in a practical machine z will be finite and the finite width effect will be dealt with in detail in Chapter 7. Because of the discontinuity in the x-direction inherent in the present model, entry and exit-edge effects will arise. However, such effects do not arise except at the two extreme ends and are generally small. This will be referred to again in Chapter 9.

3.2.2 The Laminated-iron Primary

Two identical primaries extend from $y = \pm (d + g)$ to $y = \pm \infty$. However, in the present analysis, details of the primary extending from $y = (d + g)$ to $\infty$ will be given, it being understood that the same applies for the other primary as well.

The primary consists of infinitely thin laminations each placed in the x-y plane. Each of the laminations are insulated so that the resistivity of the primary in the z-direction, $\rho_1$, is infinite. The relative permeability of the primary is finite and equal to $\mu_1$.

The primary excitation is represented by an infinitely thin current sheet in which the current varies sinusoidally both in space and time. The current flows only in the z-direction and its line density $\tilde{K}_z$ A/m may be represented by:

$$\tilde{K}_z = \hat{K}_z \cos(\omega t - qx)$$

$$= \text{Re}\ \hat{K}_z \exp j(\omega t - qx) \qquad (3.1)$$

where,

$\hat{K}_z$ = peak value of $\tilde{K}_z$, A/m

$\omega$ = angular frequency of current sheet variation, rad/s

$t$ = time, s.

$q$ = $\pi/\tau$, $m^{-1}$

$\tau$ = pole-pitch of spatial current variation, m

Re stands for 'real part of'.

A '~' sign on the top signifies sinusoidal and '^' sign on the top signifies peak quantities.

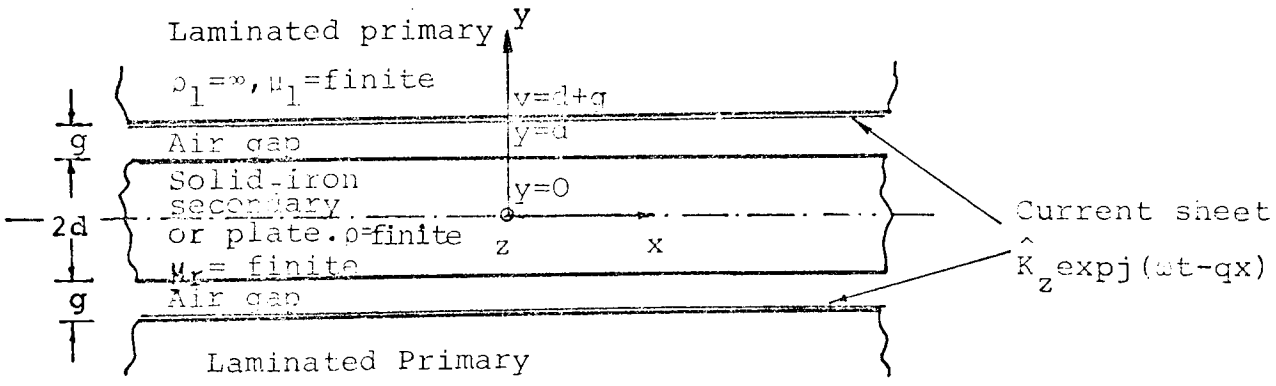


Fig. 3.1 Two-dimensional model used in analysis.

A current sheet may be considered to be obtained by the merging of infinitely thin conductors carrying current. The m.m.f.s may be obtained from current sheets by integration. Slotting or other discontinuities have not been included in the model.

Equation (3.1)represents a sinusoidally distributed wave travelling at a velocity of $\omega/q$ m/s in the x-direction. Whilst it is noted that a more realistic representation would assume a current sheet at some depth into the primary, thereby, affecting its leakage reactance, its effect on the field in air-gap and the secondary member is negligible; and hence current sheets on the surface of the primaries may be assumed.

3.2.3 The Air-gap

Two identical air-gaps, each of length g, exist between $y = \pm d$ and $y = \pm (d + g)$ and separate the primary members from the secondary. They are situated symmetrically at equal distances from the $y = 0$ plane and, as before, analysis will be confined to the air-gap existing between $y = d$ and $y = (d + g)$.

The permeability of the air-gap is that of free space and equal to $\mu_o$ and the resistivity is infinite.

3.2.4 The Solid-iron Secondary

The secondary member is a solid-iron plate and is assumed to be composed of isotropic homogeneous, ferromagnetic material. It has a finite thickness of 2d, and the plane of symmetry, $y = 0$, is its centre plane. Once again the analysis will be confined to only half the thickness, d, of the plate, i.e. for y varying from 0 to d.

The secondary member has a constant restivity, $\rho$,

and a constant relative permeability, $\mu_r (= \mu_3)$. The currents in the secondary are z-directed only and this gives rise to magnetic field components in the x and y directions.

3.2.5 Assumptions

Assumptions made for the model of Fig. 3.1, have been discussed in detail in the preceding sections, but are summarised here for clarity.

(i) The permeabilities of both the primary and secondary members are constant in time and space.

(ii) The resistivity of the primary member is infinite in the z-direction and that of the secondary is finite and constant. The resistivity of the air-gap is also infinite.

(iii) The surfaces of all the regions are smooth, flat and parallel to the z-x plane.

(iv) Only the z-directed component of current exists in the current sheet and in the solid-iron secondary.

(v) The solid-iron secondary is composed of isotropic homogeneous ferromagnetic material and has a finite thickness, 2d.

(vi) The model extends to $\pm \infty$ in both z and x directions, so that finite width effect and exit and entry effects may be ignored.

(vii) y = 0 is a plane of symmetry and analysis may be confined to y =+ve side only.

(viii) Both primary and secondary members are stationary.

(ix) Hysteresis is neglected in this analysis.

## 3.3 ANALYTIC DERIVATION OF ELECTROMAGNETIC FIELD COMPONENTS

### 3.3.1 The Field Equations

The mathematical model assumed consists of a linear conducting medium. Maxwell's equations for such a medium, where displacement currents can be neglected at low frequencies, are given by:

$$\text{curl } \bar{H} = \bar{J} \tag{3.2}$$

and

$$\text{curl } \bar{E} = -\frac{\partial \bar{B}}{\partial t} \tag{3.3}$$

where

H = Magnetic field strength, A/m

J = Current density, $A/m^2$

E = Electric field, V/m

B = Magnetic flux density, T

and the bar on top signifies vector quantities.

In terms of the resistivity, $\rho$, and relative permeability, $\mu_r$,

$$\bar{E} = \rho \bar{J} \tag{3.4}$$

and

$$\bar{B} = \mu_o \mu_r \bar{H} \tag{3.5}$$

Also, the magnetic flux density and electric current density must satisfy the continuity conditions,

$$\text{div } \bar{B} = 0 \tag{3.6}$$

and

$$\text{div } \bar{J} = 0 \tag{3.7}$$

### 3.3.2 The Magnetic Vector Potential, A.

For analysis, a magnetic vector potential, $\bar{A}$, may be defined by the equations

$$\text{curl } \bar{A} = \bar{B} \qquad (3.8)$$

and $$\text{div } \bar{A} = 0 \qquad (3.9)$$

Analysis in terms of a magnetic vector potential is preferred, because in all the three regions the electromagnetic field quantities may easily be evaluated in terms of $\bar{A}$ alone, thus eliminating the necessity of finding various components from first principles. By concentrating on variation of one vector quantity as against three (e.g. $J_z$, $H_x$ and $H_y$), variations in all the three regions are comparatively easily visualised. Consideration of the vector potential offers simple continuity conditions at the boundaries between different regions and thus, makes computation easy. For two dimensional analytic methods in case of linear conductors, the use of the vector potential has been found advisable, since it is parallel to the current density and may be conveniently obtained by surface integral.

Because the line current is z-directed, $\bar{A}$ has only one component, namely, $A_z$, and the suffix will be omitted for the rest of this analysis. Also A does not vary in the z-direction and we have, in equation (3.9)

$$\frac{\partial A}{\partial z} = 0 \qquad (3.10)$$

As the current sheet varies sinusoidally in space and time, and the resistivities in all the regions are constant, then A also varies sinusoidally and may be described by

$$\tilde{A} = \text{Re}\ \hat{A} \exp(j\omega t) \tag{3.11}$$

Expanding equation (3.8) and using equation (3.5), the x and y components of magnetic field strength, $H_x$ and $H_y$, respectively, are given by

$$H_{xi} = \frac{1}{\mu_o \mu_i} \cdot \frac{\partial A_i}{\partial y} \tag{3.12}$$

$$H_{yi} = \frac{-1}{\mu_o \mu_i} \cdot \frac{\partial A_i}{\partial x} \tag{3.13}$$

where the suffix i refers to any one of the three regions, so that i = 1 signifies primary member

i = 2 signifies air-gap

and i = 3 signifies secondary member.

The current density may be obtained from equations (3.8), (3.3), (3.4) and (3.11) as

$$J_{zi} = \frac{-j\omega}{\rho_i} A_i \tag{3.14}$$

The current density could also be obtained from equation (3.2) as

$$J_{zi} = \frac{\partial H_{yi}}{\partial x} - \frac{\partial H_{xi}}{\partial y} \tag{3.15}$$

Both equations (3.14) and (3.15) give the same result, as they must, while much less labour is needed

if equation (3.14) is used.

3.3.3 Laplace's Equation in Two Dimensions

Taking curl of equation (3.8)

$$\text{grad } (\text{div } \bar{A}) - \nabla^2 \bar{A} = \text{curl } \bar{B} \qquad (3.16)$$

where $\nabla^2 = \frac{\partial^2}{\partial x^2} + \frac{\partial^2}{\partial y^2} + \frac{\partial^2}{\partial z^2}$ is the Laplacian operator.

Using equations (3.9), (3.5), (3.2) and (3.14) and the assumptions (i) and (ii) of section 3.2.5, it is obtained that

$$\nabla^2 A = 0 \quad \text{for primary and air-gap regions}$$

and $$\nabla^2 A = \frac{j\mu_o \mu_r \omega}{\rho} A \quad \text{for the secondary member}$$

Using equation (3.10), the Laplacian operator in two dimensions has the form

$$\nabla^2 = \frac{\partial^2}{\partial x^2} + \frac{\partial^2}{\partial y^2}$$

so that for the primary member and the air-gap

$$\frac{\partial^2 A}{\partial x^2} + \frac{\partial^2 A}{\partial y^2} = 0 \qquad (3.17)$$

and for the secondary member

$$\frac{\partial^2 A}{\partial x^2} + \frac{\partial^2 A}{\partial y^2} = \alpha^2 (1+j)^2 A \qquad (3.18)$$

where $$\alpha^2 = \frac{\mu_o \mu_r \omega}{2\rho} \qquad (3.19)$$

Equations (3.17) and (3.18) are the required Laplace's equations and describe the variations of the

magnetic vector potential in two dimensions. Equations (3.17) and (3.18) have the general form of solution

$$\dot{A}_i = \left[ C_i \exp(ky) + D_i \exp(-ky) \right] \exp(-jqx) \qquad (3.20)$$

where $C_i$ and $D_i$ are the constants to be obtained from the boundary conditions, and

$$k^2 = q^2 + j2\alpha^2 \qquad (3.21)$$

$\therefore$ $k = q$ for primary member and air-gap.

The boundary conditions for evaluating $C_i$ and $D_i$ will be outlined in the following section.

3.3.4 The Boundary Conditions

Since the vector potential in the primary member cannot be infinite, i.e. has to be finite when y tends to infinity, therefore the constant $C_1 = 0$. The remaining constants may be evaluated from boundary conditions at $y = (d + g)$, $y = d$ and $y = 0$.

(i) At the boundary $y = (d + g)$, $A_1 = A_2$

(ii) At the boundary $y = d$, $A_2 = A_3$

(iii) At the boundary $y = (d + g)$

$$\frac{1}{\mu_o} \cdot \frac{\partial A_2}{\partial y} - \frac{1}{\mu_o \mu_1} \cdot \frac{\partial A_1}{\partial y} = \hat{K}_z \exp(-jqx)$$

(iv) At the boundary $y = d$

$$\frac{1}{\mu_o \mu_r} \cdot \frac{\partial A_3}{\partial y} - \frac{1}{\mu_o} \cdot \frac{\partial A_2}{\partial y} = 0$$

In addition to these, another boundary condition may be established at y = 0. This condition, however, depends on the particular pole arrangement being considered and may be obtained by considering the attenuation of the vector potential $A_3$ from the surface to the inside of the plate.

3.3.4.1 Longitudinal Flux Arrangement

For this arrangement, since corresponding poles on the primaries are of similar instantaneous polarity, $A_3$ is an even function of y, i.e. $A_3(y) = -A_3(-y)$. Since $A_3$ is continuous at all values of y, therefore, at the boundary y = 0,

$$A_3 = 0$$

Thus for longitudinal flux arrangement, the relation between the constants $C_3$ and $D_3$ is given by

$$C_{3\ell} = - D_{3\ell} \qquad (3.22)$$

(A further subscript $\ell$ signifies longitudinal flux arrangement).

3.3.4.2 Transverse Flux Arrangement

For this arrangement, since the corresponding poles on the primaries are of opposite instantaneous polarity, $A_3$ is an odd function of y, i.e. $A_3(y) = A_3(-y)$. Since $A_3$ is continuous at all values of y, it must pass through a minimum at y = o. Therefore, at the boundary y = o,

$$\frac{\partial A_3}{\partial y} = 0$$

Thus for transverse flux arrangement, the relation between the constants $C_3$ and $D_3$ is given by

$$C_{3t} = D_{3t} \tag{3.23}$$

(A further subscript t signifies transverse flux arrangement).

## 3.4 FIELD EQUATIONS FOR LONGITUDINAL FLUX ARRANGEMENT

### 3.4.1 General

In order to represent the longitudinal flux arrangement, a further suffix $\ell$ will be used with all suffixed quantities. The equations for the magnetic vector potential in the three regions are now given by

$$\dot{A}_{1\ell} = \left[D_{1\ell}\exp(-qy)\right]\exp(-jqx) \tag{3.24a}$$

$$\dot{A}_{2\ell} = \left[C_{2\ell}\exp(qy) + D_{2\ell}\exp(-qy)\right]\exp(-jqx) \tag{3.24b}$$

$$\dot{A}_{3\ell} = \left[C_{3\ell}\sinh ky\right]\exp(-jqx) \tag{3.24c}$$

The four constants may now be evaluated from the four boundary conditions of section 3.3.4. Since the field equations in the air-gap and the secondary member are only of concern, the values of $A_{2\ell}$ and $A_{3\ell}$ are only given.

$$\dot{A}_{2\ell} = \frac{-\mu_o \hat{K}_z}{q.\dot{C}_{p\ell}}\Big[\{\exp(kd)-\dot{D}_s\exp(-kd)\}\exp\{q(y-d)\}-$$

$$\{\exp(-kd)-\dot{D}_s\exp(kd)\}\exp\{-q(y-d)\}\Big]\exp\{-(kd+qg+jqx)\} \tag{3.25}$$

and

$$\dot{A}_{3\ell} = \frac{-4\mu_o\mu_r \hat{K}_z}{\dot{C}_{p\ell}(\mu_r q + k)}\left[\sinh ky\right]\exp\{-(kd+qg+jqx)\} \qquad (3.26)$$

where

$$\dot{C}_{p\ell} = \frac{\mu_1+1}{\mu_1}\left[\{\dot{D}_s\exp(-2kd)-1\}+\frac{\mu_1-1}{\mu_1+1}\{\dot{D}_s-\exp(-2kd)\}\exp(-2qg)\right] \qquad (3.27)$$

and $$\dot{D}_s = \frac{\mu_r q-k}{\mu_r q+k} \qquad (3.28)$$

3.4.2 Field Equations in the Air-gap and Secondary

The equations for magnetic field strengths and current densities may be obtained from equations (3.25) and (3.26) in conjunction with equations (3.12), (3.13), and (3.14). Thus for the air-gap region the magnetic field components are given by

$$\dot{H}_{x2\ell} = \frac{-\hat{K}_z}{\dot{C}_{p\ell}}\left[\{\exp(kd)-\dot{D}_s\exp(-kd)\}\exp\{q(y-d)\}+\{\exp(-kd)-\dot{D}_s\exp(kd)\}\exp\{-q(y-d)\}\right]\exp\{-(kd+qg+jqx)\} \qquad (3.29)$$

$$\dot{H}_{y2\ell} = \frac{-j\hat{K}_z}{\dot{C}_{p\ell}}\left[\{\exp(kd)-\dot{D}_s\exp(-kd)\}\exp\{q(y-d)\}-\{\exp(-kd)-\dot{D}_s\exp(kd)\}\exp\{-q(y-d)\}\right]\exp\{-(kd+qg+jqx)\} \qquad (3.30)$$

For the secondary member, i.e. the solid-iron plate, the magnetic field strength and the current density are given by

$$\dot{H}_{x3\ell} = \frac{-4\hat{K}_z}{\dot{C}_{p\ell}} \left[\frac{k}{\mu_r q+k}\text{coshky}\right]\exp\{-(kd+qg+jqx)\} \quad (3.31)$$

$$\dot{H}_{y3\ell} = \frac{-j4\hat{K}_z}{\dot{C}_{p\ell}} \left[\frac{q}{\mu_r q+k}\text{sinhky}\right]\exp\{-(kd+qg+jqx)\} \quad (3.32)$$

and

$$\dot{J}_{z3\ell} = \frac{j8\hat{K}_z}{\dot{C}_{p\ell}} \left[\frac{\alpha^2}{\mu_r q+k}\text{sinhky}\right]\exp\{-(kd+qg+jqx)\} \quad (3.33)$$

3.4.3 The Effect of Primary Member

The relative permeability $\mu_1$ of the primary member appears in the expression for $\dot{C}_{p\ell}$, which is given by

$$\dot{C}_{p\ell} = \frac{\mu_1+1}{\mu_1}\left[\{\dot{D}_s\exp(-2kd)-1\}+\frac{\mu_1-1}{\mu_1+1}\{\dot{D}_s-\exp(-2kd)\}\exp(-2qg)\right] \quad (3.27)$$

The effect of variation in the permeability of primary iron can, therefore, be studied from equation (3.27). Two extreme cases may be considered:

(i) $\mu_1 = 1$

In this case, equation (3.27) becomes

$$\dot{C}_{p\ell} = 2\{\dot{D}_s\exp(-2kd)-1\} \quad (3.34)$$

The expression $\frac{\mu_1-1}{\mu_1+1} = 0$ and this shows that there is no reflection of the current sheet and the image current

sheet disappears.

(ii) $\mu_1 = \infty$

In this case, equation (3.27) becomes

$$\dot{C}_{p\ell\infty} = \{\dot{D}_s \exp(-2kd) - 1\} + \{\dot{D}_s - \exp(-2kd)\}\exp(-2qg) \quad (3.35)$$

The expression $\frac{\mu_1 - 1}{\mu_1 + 1} \to 1$, which shows complete reflection.

Equations (3.27), (3.34) and (3.35) clearly show how the finite thickness of the secondary member affects the contribution of the primary. For the case of d being large (i.e. $d >> 1/k$), all these equations tend to the standard expressions available in published literature [30].

The effect of varying $\mu_1$ is shown in Fig. 3.2, where $\left|\frac{\dot{C}_{p\ell\infty}}{\dot{C}_{p\ell}}\right|$ has been plotted against $\mu_1$, for various values of half-thickness, d. Bowden [30] plotted the same function for an infinitely thick plate with various values of qg and $\frac{\mu_r q}{\alpha}$. Fig. 3.2 has been plotted for one value of qg and $\frac{\mu_r q}{\alpha}$, while curves of the same nature may be obtained for various values of them. It can be observed from these curves also that for $\mu_1 \geq 500$, $\dot{C}_{p\ell} \cong \dot{C}_{p\ell\infty}$. The point to note here is that the half-thickness d has very little effect on such an observation. It may be seen that for $\mu_1$ as small as 100, the variation of thickness has very little effect on the ratio $\left|\frac{\dot{C}_{p\ell\infty}}{\dot{C}_{p\ell}}\right|$. The same may be observed for curves drawn for other values of qg & $\frac{\mu_r q}{\alpha}$.

Since for practical cases $\mu_1$ is very high (i.e. > 500), it can be reasonably concluded that, the primary permeability may be taken as infinite. Few authors seem to offer such reasoning for assuming $\mu_1 = \infty$ at the outset.

Thus, in the rest of the analysis, $\mu_1 = \infty$ and $\dot{C}_{p\ell} = \dot{C}_{p\ell\infty}$. Based on these and some further modifications, the equations for electromagnetic field quantities in the secondary will be simplified in section 3.4.4.

3.4.4 Fields in the Secondary and Some Further Modifications

In section 3.4.2, the field equations were given for both air-gap and secondary member for ease of comparison and completeness of analysis. However, since the electromagnetic phenomena in the plate only is of interest here, the field equations in the secondary member will be of concern in the following analysis. Thus, the subscript 3 in the equations (3.31) to (3.33) may be omitted. While the field equations in the air-gap may still retain 2 in the subscript, field equations in the secondary will not contain 3 in the subscript and $H_{y\ell}$, for example, will signify the y-component of the magnetic field strength in the secondary.

As has been pointed out in section 3.4.3, the permeability of the primary iron may be reasonably assumed infinite, so that $\dot{C}_{p\ell}$ is given by $\dot{C}_{p\ell\infty}$ as in equation (3.35).

In most practical cases, the pole-pitch of the machine, $\tau$ $(= \pi/q)$ is very much greater than the

depth of penetration, $\delta (= \frac{1}{\alpha})$. (At least it may be made so at the designer's discretion). Thus in equation (3.21), it is assumed that:

$$2\alpha^2 >> q^2 \tag{3.36}$$

so that

$$k \equiv (1 + j)\alpha \tag{3.37}$$

Based on the above modifications and using equation (3.37), equations (3.31), (3.32) and (3.33) become

$$\dot{H}_{x\ell} = \frac{-2\hat{K}_z(1+j)}{\dot{M}_\ell} \left[\cosh\alpha(1+j)y\right]\exp(-jqx) \tag{3.38}$$

$$\dot{H}_{y\ell} = \frac{-j2\hat{K}_z q}{\alpha\dot{M}_\ell} \left[\sinh\alpha(1+j)y\right]\exp(-jqx) \tag{3.39}$$

and

$$\dot{J}_{z\ell} = \frac{j4\hat{K}_z\alpha}{\dot{M}_\ell} \left[\sinh\alpha(1+j)y\right] \exp(-jqx) \tag{3.40}$$

where

$$\dot{M}_\ell = -2\cosh qg \cosh\alpha d \cos\alpha d \left[\{(m\tanh qg - \tan\alpha d)\tanh\alpha d + 1\} + j\{(m\tanh qg + \tanh\alpha d)\tan\alpha d + 1\}\right] \tag{3.41}$$

$$|M_\ell| = \sqrt{2}\cosh qg\{m^2\tanh^2 qg(\cosh 2\alpha d - \cos 2\alpha d) + 2m\tanh qg(\sinh 2\alpha d + \sin 2\alpha d) + 2(\cosh 2\alpha d + \cos 2\alpha d)\}^{\frac{1}{2}} \tag{3.42}$$

$$\text{and } m = \frac{\mu_r q}{\alpha} \tag{3.43}$$

In the secondary being considered for this analysis, y varies from d to 0, and equations (3.38), (3.39) and (3.40) show that electromagnetic field quantities attenuate with

depth in terms of hyperbolic functions. When the secondary is infinitely thick (i.e. d is large), then, allowing for the fact that these quantities cannot become infinite when $y \to \infty$, the nature of attenuation with depth may be recognised as exponential.

The attenuation of the magnetic field strengths $H_{x\ell}$ and $H_{y\ell}$ for half the plate thickness are shown by firm lines in Figs. 3.3 and 3.4 respectively. Different ratios of half-thickness of the plate to the depth of penetration ($= d/\delta$) are considered, viz 0.25, 1.0, 2.0, 3.0 and 4.0. The value of the magnetic field strength on the plate surface is taken as unity and the half-thickness of the plate is expressed in fractions of d.

In Fig. 3.3, it may be seen that the attenuation of $H_{x\ell}$ is small when the half-thickness is small (e.g. $\frac{d}{\delta} = 0.25$), whereas for thicker plates (e.g. $\frac{d}{\delta} = 4.0$), the attenuation is quite marked because of the boundary condition at the centre of the plate (i.e. y = 0). It may be observed that at the depth of penetration, the attenuation of $H_{x\ell}$ is only 77% when the ratio of $d/\delta = 1.0$, as against 37% when the ratio $d/\delta = 4.0$, i.e. the plate may be considered infinitely thick. In Fig. 3.4, although the boundary condition requires that $H_{y\ell} = 0$ at y = 0, the attenuation of $H_{y\ell}$ is again greater for large values of the ratio $d/\delta$ compared with that for small values of the same ratio.

It may be noted that the surface values of magnetic field strengths $H_{y\ell}$ in Fig. 3.4 are very much smaller

compared with those of Fig. 3.3 (table insets in the Figures) This, together with the fact that the attenuation of the curves of Fig. 3.4 is more pronounced, shows that on the surface and also in the inside of the plate the x-component of magnetic field strength is the dominant one.

Fig. 3.4 also shows the attenuation of $(\frac{\partial H_{x\ell}}{\partial y})$ and $(\frac{\partial H_{y\ell}}{\partial x})$ in the plate. Both are coincident with the curves of $H_{y\ell}$. The surface value of $(\frac{\partial H_{x\ell}}{\partial y})$ is, however, very much greater than that of $(\frac{\partial H_{y\ell}}{\partial x})$, (table inset in Fig.3.4). This shows that the current density on the surface and in the inside of the plate is due predominantly to $(\frac{\partial H_{x\ell}}{\partial y})$ only.

3.4.5 Field Components at the Secondary Surface

The field components on the surface of the secondary may be obtained from equations (3.38) to (3.40) by putting y = d. After some manipulations this gives

$$H_{x\ell d} = \frac{-2\hat{K}_z}{|M_\ell|} (\cosh 2\alpha d + \cos 2\alpha d)^{\frac{1}{2}} \exp(-jqx) \angle H_{x\ell d} \tag{3.44}$$

$$H_{y\ell d} = \frac{-\sqrt{2}\hat{K}_z q}{\alpha |M_\ell|} (\cosh 2\alpha d - \cos 2\alpha d)^{\frac{1}{2}} \exp(-jqx) \angle H_{y\ell d} \tag{3.45}$$

$$J_{z\ell d} = \frac{2\sqrt{2}\hat{K}_2 \alpha}{|M_\ell|} (\cosh 2\alpha d - \cos 2\alpha d)^{\frac{1}{2}} \exp(-jqx) \angle -H_{y\ell d} \tag{3.46}$$

where $|M_\ell|$ is given by equation (3.42).

$$\underline{/^{H}x\ell d} = \tan^{-1}\left[\frac{m\tanh qg(\sinh 2\alpha d-\sin 2\alpha d)}{m\tanh qg(\sinh 2\alpha d+\sin 2\alpha d)+2(\cosh 2\alpha d+\cos 2\alpha d)}\right]$$

and (3.47)

$$\underline{/^{H}y\ell d} = \tan^{-1}\left[\frac{m\tanh qg(\cosh 2\alpha d-\cos 2\alpha d)+(\sinh 2\alpha d+\sin 2\alpha d)}{(\sinh 2\alpha d-\sin 2\alpha d)}\right]$$

(3.48)

For the case when $\alpha d$ is large, (i.e. $d>>\frac{1}{\alpha}$) equations (3.47) and (3.48) become,

$$\underline{/^{H}x\ell d}\Big]_{\alpha d \text{ large}} = \tan^{-1}\left[\frac{m\tanh qg}{m\tanh qg+2}\right] \qquad (3.47a)$$

and

$$\underline{/^{H}y\ell d}\Big]_{\alpha d \text{ large}} = \tan^{-1}[m\tanh qg+1] \qquad (3.48a)$$

Equations (3.47a) and (3.48a) are the same as those obtained by Bowden[30] for an infinitely thick plate. It may also be seen that for the condition of these equations, $\underline{/^{H}y\ell d}$ leads $\underline{/^{H}x\ell d}$ by $\pi/4$.

When d is very small, however, both equations (3.47) and (3.48)give very small values for the phase angles, approaching zero.

Thus equations (3.47) and (3.48) help establish the well known fact that when the plate is sufficiently thick, the nature of eddy current is inductance-limited, whereas when the plate is sufficiently thin the nature is resistance-limited.

Fig. 3.5 shows in firm lines, the variation of the

surface magnetic field strengths $H_{x\ell d}$ and $H_{y\ell d}$ with the ratio of half-thickness to depth of penetration. The value of magnetic field strengths for an infinitely thick plate is taken as unity and the curves are drawn for two relative permeability values (viz, 250 and 1000) for the plate.

The figure shows that for very small thicknesses of the plate, $H_{x\ell d}$ is higher than its value for an infinitely thick plate. The reverse is true for $H_{y\ell d}$. Physically this means that the eddy-current reaction field is small for such thin plates and because of the essential boundary condition at the centre (y=0) of the plate, the small flux is constrained to take the path along the length of the plate. In transition from thin to thick plates, $H_{x\ell d}$ passes through a minimum and $H_{y\ell d}$ a maximum; the flux passing into the plate is increasing, but the reaction field is now becoming increasingly significant.

The curves for $H_{y\ell d}$ also represent the variation of the surface values of $(\frac{\partial H_{x\ell}}{\partial y})$ and $(\frac{\partial H_{y\ell}}{\partial x})$.

3.4.6 A Thickness Criterion

Most studies in literature consider a plate of infinite thickness from the beginning and as such, little justification is necessary for its thickness so long as it is greater than the depth of penetration. In the present case, however, a plate of finite thickness, 2d is being considered from the beginning. This leaves one with the option of defining the conditions or criteria

which determine whether a plate is electrically thick or thin. For the cases of thick and thin plates, the general nature of eddy currents has been mentioned in Section 3.4.5. Thus it is necessary to determine the criteria which makes the plate look like thick or thin, for, the eddy-current phenomena are governed by certain distinct formulae in each case.

It is well known that when the secondary is sufficiently thick, $|H_{x\ell d}|$ is much greater than $|H_{y\ell d}|$ and the conditions which make it so will be studied. From equations (3.44) and (3.45),

$$\frac{|H_{x\ell d}|}{|H_{y\ell d}|} = \frac{\sqrt{2}\alpha}{q} \cdot \left[\frac{\cosh 2\alpha d + \cos 2\alpha d}{\cosh 2\alpha d - \cos 2\alpha d}\right]^{\frac{1}{2}} \qquad (3.49)$$

When d is sufficiently large (i.e. $d >> 1/\alpha$), this reduces to $\frac{\sqrt{2}\alpha}{q}$. But since by assumption $\frac{\sqrt{2}\alpha}{q} >> 1$, $|H_{x\ell d}| >> |H_{y\ell d}|$, when the plate is very thick.

Equation (3.49) also reduces to $\frac{\sqrt{2}\alpha}{q}$ when $\cos 2\alpha d = 0$ i.e. when $d = \frac{\pi}{4} \cdot (\frac{1}{\alpha})$. This means that for the plate to be considered thick its half-thickness should be at least equal to $\pi/4$ times the depth of penetration.

When d is sufficiently small the right hand side of equation (3.49) is given by,

$$\frac{\sqrt{2}\alpha}{q} \cdot \left[\frac{2}{4\alpha^2 d^2}\right]^{\frac{1}{2}} = \frac{1}{qd}$$

Thus a plate may also be deemed as thick when its half-thickness is greater than $1/q$ (i.e. $1/\pi$ times the pole-pitch), for, in this case, the x-component becomes the dominant component of magnetic field strength in the plate.

It may, therefore, be summarised that a plate may be considered electrically thick if its half-thickness is greater than $\pi/4$ times the depth of penetration. The plate may also be considered electrically thick, if its half-thickness is greater than $1/\pi$ times the pole-pitch.

Stoll and Hammond[28] also obtained similar condition for plate thickness. Their work has shown that for a plate to be considered thick, the second condition is sufficient but not necessary.

3.4.7 One-dimensional Nature of Magnetic Fields in the Plate

The one-dimensional nature of the magnetic field in the secondary may be obtained by studying the relative contributions of the two terms on the right hand side of equation (3.15).

From equation (3.38),

$$\frac{\partial \dot{H}_{x\ell}}{\partial y} = \frac{-j4\hat{K}_z \alpha}{\dot{M}_\ell} \left[\sinh\alpha(1+j)y\right]\exp(-jqx) \qquad (3.50)$$

From equation (3.39),

$$\frac{\partial \dot{H}_{y\ell}}{\partial x} = \frac{-2\hat{K}_z q^2}{\alpha \dot{M}_\ell} \left[\sinh\alpha(1+j)y\right]\exp(-jqx) \qquad (3.51)$$

$$\therefore \quad \frac{|\partial H_{x\ell}/\partial y|}{|\partial H_{y\ell}/\partial x|} = \frac{2\alpha^2}{q^2} \qquad (3.52)$$

which is much greater than unity (Section 3.4.4). Thus $\left|\frac{\partial H_{x\ell}}{\partial y}\right| >> \left|\frac{\partial H_{y\ell}}{\partial x}\right|$ and as far as the current density in the plate is concerned, the magnetic field is approximately such that only the $H_{x\ell}$ component exits.

Equation (3.52) has been obtained by previous authors[13,28], for a single-sided arrangement. The point to note here is that the same condition applies not only for the double-sided arrangement, but also for the finite thickness of the plate. It may also be noted that equation (3.52) is independent of y, so that this condition applies at all depths and for any thickness of the plate.

Attenuation of $\partial H_{x\ell}/\partial y$ and $\partial H_{y\ell}/\partial x$ inside the plate is shown in the firm lines in Fig. 3.4. Nature of variation of both at per unit of the surface value is the same in both the cases, although the former is of much higher magnitude.

3.4.8 Eddy-Current Loss

The eddy-current loss per unit of surface area in half the thickness of the plate is given by the complex Poynting vector, $\wp_{y\ell}$, where

$$\wp_{y\ell} = -\frac{1}{2} \mathrm{Re}(\dot{E}_{z\ell} \times H^*_{x\ell}) \qquad (3.53)$$

where $H^*_{x\ell}$ is the complex conjugate of $\dot{H}_{x\ell}$ and $\dot{E}_{z\ell} = \rho \dot{J}_{z\ell}$.

Using equation (3.38) and (3.40), then, this becomes,

$$\rho_{y\ell} = \frac{2\hat{K}_z^2 \rho\alpha}{|M_\ell|^2}(\sinh 2\alpha y - \sin 2\alpha y) \qquad (3.54)$$

The loss expression, therefore, contains $2\alpha y$ in hyperbolic terms as against $\alpha y$ in case of electric or magnetic fields. The total loss in the iron per unit of surface area is obtained by letting y=d in equation (3.54). This gives, using equation (3.42), the total loss per unit area as

$$\rho_{y\ell d} = \frac{\hat{K}_z^2 \rho\alpha}{\cosh^2 qg}\left[\frac{(\sinh 2\alpha d - \sin 2\alpha d)}{m^2\tanh^2 qg(\cosh 2\alpha d - \cos 2\alpha d) + 2m\tanh qg(\sinh 2\alpha d + \sin 2\alpha d) + 2(\cosh 2\alpha d + \cos 2\alpha d)}\right] \qquad (3.55)$$

When d is large (i.e. $d >> \frac{1}{\alpha}$), the hyperbolic terms are much greater than the trigonometric terms and since $\cosh 2\alpha d \simeq \sinh 2\alpha d$, the loss for an infinitely thick plate is given by

$$\rho_{y\ell\infty} = \frac{\hat{K}_z^2 \rho\alpha}{\cosh^2 qg} \cdot \left[\frac{1}{m^2\tanh^2 qg + 2m\tanh qg + 2}\right] \qquad (3.56)$$

Equation (3.56) is the same as the loss expression obtained by Bowden [30]. The loss per unit of its value for an infinitely thick plate may be obtained by dividing equation (3.55) by equation (3.56) and has been plotted as a function of the ratio $d/\delta$ in firm lines in Fig. 3.6.

Stoll[13] also obtained similar curves. These curves show that when the plate is sufficiently thin, the loss is greatly reduced, although $H_{x\ell}$ increases. This is because for very thin plates both the flux and the eddy-current loss are small. With increase in plate thickness, both the flux in the plate and the eddy-current reaction increases causing the loss to pass through a maximum value.

When d is small (i.e. $d << \frac{1}{\alpha}$), equation (3.55) reduces to the form,

$$P_{y\ell o} = \frac{2\hat{K}_z^2 \rho \alpha^4 d^3}{3\cosh^2 qg} \cdot \frac{1}{(\alpha d m \tanh qg + 1)^2} \qquad (3.57)$$

which shows that the loss is greatly reduced.

3.4.9 Time-average Force Density

Because of the presence of flux and current densities in the steel plate, forces of electromagnetic nature are developed. The x-component of the time average force density, $F_{x\ell}$, may be obtained as

$$F_{x\ell} = -\frac{1}{2} \mathrm{Re}(\dot{J}_{z\ell} \times B^*_{y\ell}) \qquad (3.58)$$

where $B^*_{y\ell}$ is the complex conjugate of $\dot{B}_{y\ell} = \mu_o \mu_r \dot{H}_{y\ell}$. The y-component of the same, $F_{y\ell}$, is, likewise, given by

$$F_{y\ell} = -\frac{1}{2} \mathrm{Re}(\dot{J}_{z\ell} \times B^*_{x\ell}) \qquad (3.59)$$

where $B^*_{x\ell}$ is the complex conjugate of $\dot{B}_{x\ell} = \mu_o \mu_r \dot{H}_{x\ell}$.

Substituting the values of $\dot{J}_{z\ell}$, $\dot{B}_{x\ell}$ and $\dot{B}_{y\ell}$ from equations (3.40), (3.38), (3.39) and (3.5),

$$F_{x\ell} = \frac{2\mu_o \mu_r \hat{K}_z^2 q}{|M_\ell|^2} (\cosh 2\alpha y - \cos 2\alpha y) \qquad (3.60)$$

and

$$F_{y\ell} = \frac{2\mu_o \mu_r \hat{K}_z^2 \alpha}{|M_\ell|^2} (\sinh 2\alpha y - \sin 2\alpha y) \qquad (3.61)$$

where the value of $|M_\ell|$ is given by equation (3.42).

Equation (3.60) is a force of translation while equation (3.61) is a force of attraction. They vary at different depths of the plate as may be seen from the equations. At the centre of the plate both forces are reduced to zero. At the surface of the secondary, the ratio of the two forces is given by,

$$\frac{F_{y\ell d}}{F_{x\ell d}} = \frac{\alpha}{q} \cdot \left[\frac{\sinh 2\alpha d - \sin 2\alpha d}{\cosh 2\alpha d - \cos 2\alpha d}\right] \qquad (3.62)$$

Thus, at the surface of an infinitely thick plate (i.e. $d >> 1/\alpha$), the force of attraction, $F_{y\ell d}$, is greater than, equal to or less than the force of translation, $F_{x\ell d}$, according to whether the pole-pitch is greater than, equal to or less than $\pi$ times the depth of penetration, respectively. For a thin (i.e. $d << 1/\alpha$) secondary, on the other hand, equation (3.62) reduces to

$\frac{2\alpha^2 d}{3q}$ which shows that the ratio can be very small. Thus, for thin plates the force of translation can be greater than the force of attraction.

In general the pole-pitch should be large compared with the depth of penetration, so that the force of attraction is the dominant one and whose effect may be reduced because of the double sided arrangement.

## 3.5 FIELD EQUATIONS FOR TRANSVERSE FLUX ARRANGEMENT

### 3.5.1 Gèneral

In order to represent the transverse flux quantities, a further suffix t is used with all suffixed expressions. The equations for magnetic vector potential in the three different regions may now be obtained from equation (3.20), together with the boundary conditions outlined in Section 3.3.4, as

$$\dot{A}_{1t} = [D_{1t}\exp(-qy)]\exp(-jqx) \qquad (3.63a)$$

$$\dot{A}_{2t} = [C_{2t}\exp(qy)+D_{2t}\exp(-qy)]\exp(-jqx) \qquad (3.63b)$$

and

$$\dot{A}_{3t} = [C_{3t}\cosh ky]\exp(-jqx) \qquad (3.63c)$$

The four constants may now be obtained from the four boundary conditions given in Section 3.3.4. Since the field equations in the air-gap and the secondary member are required, the values of $A_{2t}$ and $A_{3t}$ only are given.

$$\dot{A}_{2t} = \frac{\mu_o \hat{K}_z}{q\dot{C}_{pt}} \cdot \left[ \{\exp(kd) + \dot{D}_s \exp(-kd)\} \exp\{q(y-d)\} + \{\dot{D}_s \exp(kd) + \exp(-kd)\} \right.$$
$$\left. \exp\{-q(y-d)\} \right] \exp\{-(kd+qg+jqx)\} \qquad (3.64)$$

and

$$\dot{A}_{3t} = \frac{4\mu_o \mu_r \hat{K}_z}{\dot{C}_{pt}(\mu_r q + k)} \cdot [\text{coshky}] \exp\{-(kd+qg+jqx)\} \qquad (3.65)$$

where

$$\dot{C}_{pt} = \frac{\mu_1+1}{\mu_1} \left[ \{\dot{D}_s \exp(-2kd) + 1\} - \frac{\mu_1-1}{\mu_1+1} \{\dot{D}_s + \exp(-2kd)\} \exp(-2qg) \right] \qquad (3.66)$$

and $\dot{D}_s$ is given by equation (3.28).

### 3.5.2 Field Equations in the Air-gap and the Secondary

The field equations in the air-gap may be obtained from equation (3.64) in conjunction with equations (3.12) and (3.13). Thus the magnetic field strengths for the air-gap region are given by

$$\dot{H}_{x2t} = \frac{\hat{K}_z}{\dot{C}_{pt}} \cdot \left[ \{\exp(kd) + \dot{D}_s \exp(-kd)\} \exp\{q(y-d)\} - \{\dot{D}_s \exp(kd) + \exp(-kd)\} \right.$$
$$\left. \exp\{-q(y-d)\} \right] \exp\{-(kd+qg+jqx)\} \qquad (3.67)$$

and

$$\dot{H}_{y2t} = \frac{j\hat{K}_z}{\dot{C}_{pt}} \cdot \left[ \{\exp(kd) + \dot{D}_s \exp(-kd)\} \exp\{q(y-d)\} + \{\dot{D}_s \exp(kd) + \exp(-kd)\} \right.$$
$$\left. \exp\{-q(y-d)\} \right] \exp\{-(kd+qg+jqx)\} \qquad (3.68)$$

The equations for magnetic field strengths and current density in the secondary member may be, similarly, obtained from equations (3.65) together with equations

(3.12), (3.13) and (3.14). Thus for the secondary member i.e. solid-iron plate, the field equations are given by

$$\dot{H}_{x3t} = \frac{4\hat{K}_z}{\dot{C}_{pt}} \left[\frac{k}{\mu_r q+k} \sinh ky\right] \exp\{-(kd+qg+jqx)\} \qquad (3.69)$$

$$\dot{H}_{y3t} = \frac{j4\hat{K}_z}{\dot{C}_{pt}} \left[\frac{q}{\mu_r q+k} \cosh ky\right] \exp\{-(kd+qg+jqx)\} \qquad (3.70)$$

and

$$\dot{J}_{z3t} = \frac{-j8\hat{K}_z}{\dot{C}_{pt}} \left[\frac{\alpha^2}{\mu_r q+k} \cosh ky\right] \exp\{-(kd+qg+jqx)\} \qquad (3.71)$$

3.5.3 The Effect of Primary Member

The relative permeability of the primary member occur in the expression of $\dot{C}_{pt}$, equation (3.66), only, so that the effect of the primary member may be studied from this equation. The expression for $\dot{C}_{pt}$ is given by

$$\dot{C}_{pt} = \frac{\mu_1+1}{\mu_1}\left[\{\dot{D}_s \exp(-2kd)-1\} - \frac{\mu_1-1}{\mu_1+1}\{\dot{D}_s+\exp(-2kd)\}\exp(-2qg)\right] \qquad (3.66)$$

Two extreme cases of variation of primary permeability may be studied from equation (3.66):

Case 1, $\mu_1 = 1$

In this case, equation (3.66) becomes

$$\dot{C}_{pt1} = 2\{\dot{D}_s \exp(-2kd)+1\} \qquad (3.72)$$

The expression $\frac{\mu_1-1}{\mu_1+1} = 0$ showing that there is no reflection of the current sheet and the image current sheet disappears.

Case 2, $\mu_1=\infty$

In this case, equation (3.66) becomes

$$\dot{C}_{pt} = \{\dot{D}_s \exp(-2kd)+1\}-\{\dot{D}_s+\exp(-2kd)\}\exp(-2qg) \tag{3.73}$$

The expression $\frac{\mu_1-1}{\mu_1+1} \to 1$, showing complete reflection of current sheet.

The influence of the finite thickness, 2d, of the secondary member on the contribution of the primary member is clearly demonstrated in equations(3.66), (3.72) and (3.73). When the secondary thickness is very large (i.e. $d >> 1/k$), these equations reduce to standard expressions available in the literature.

The effect of varying $\mu_1$ is shown in Fig. 3.7, where $\left|\frac{C_{pt\infty}}{C_{pt}}\right|$ has been plotted against $\mu_1$ for various values of d. The curves obtained are of similar nature as those for $\frac{|C_{p\ell\infty}|}{|C_{p\ell}|}$, Fig. 3.2. Thus the observations made in Section 3.4.3, are also applicable for curves of Fig. 3.7. Bowden observed that for $\mu_1 \geq 500$, this ratio tends to unity, i.e. the primary permeability may reasonably be assumed infinite over this value. This observation also holds in Fig. 3.7, irrespective of the secondary thickness. For very small secondary thicknesses, ($\alpha d << 0.1$), however, this observation needs to be modified. Such small thicknesses would, perhaps, not be used in practice or even if it does,

this observation will hold good at a higher value of $\mu_1$.

Thus, it will be assumed that $\mu_1 = \infty$ for the rest of the analysis. The field equations in the secondary will be modified in the following section on the basis of this and some further assumptions.

3.5.4 Modified Forms of Field Equations in the Plate

As observed in Section 3.4.4, the three modifications may be outlined as:

(i) the secondary quantities will, henceforth, occur without the further subscript of 3 , e.g. $H_{xt}$ for $H_{x3t}$, etc.

(ii) the relative permeability of the primary will be taken as infinite so that $\dot{C}_{pt} = \dot{C}_{pt\infty}$ given by equation (3.73), and

(iii) the pole-pitch of exciting current sheet will be assumed much greater than the depth of penetration, $\delta$ $(= 1/\alpha)$, so that $2\alpha^2 >> q^2$ and $k = (1+j)\alpha$.

In terms of the above modifications, equations (3.69), (3.70) and (3.71) are given by

$$\dot{H}_{xt} = \frac{2\hat{K}_z(1+j)}{\dot{M}_t}\cdot[\sinh\alpha(1+j)y]\exp(-jqx) \qquad (3.74)$$

$$\dot{H}_{yt} = \frac{j2\hat{K}_z q}{\alpha\dot{M}_t}\cdot[\cosh\alpha(1+j)y]\exp(-jqx) \qquad (3.75)$$

and

$$\dot{J}_{zt} = \frac{-j4\alpha\hat{K}_z}{\dot{M}_t}[\cosh\alpha(1+j)y]\exp(-jqx) \qquad (3.76)$$

where

$$\dot{M}_t = 2\cosh qg\cosh\alpha d\cos\alpha d[\{m\tanh qg+\tanh\alpha d-\tan\alpha d\}+j\{(m\tanh qg\tanh\alpha d+1)\tan\alpha d+\tanh\alpha d\}] \qquad (3.77)$$

The absolute value of $\dot{M}_t$ is given by

$$|M_t| = \sqrt{2}\cosh qg\left[m^2\tanh^2 qg(\cosh 2\alpha d+\cos 2\alpha d)+2m\tanh qg(\sinh 2\alpha d-\sin 2\alpha d)+2(\cosh 2\alpha d-\cos 2\alpha d)\right]^{\frac{1}{2}} \qquad (3.78)$$

The attenuation of the magnetic field strengths $H_{xt}$ and $H_{yt}$ for half of the plate thickness is shown in dotted lines in Figs. 3.3 and 3.4. The construction of these graphs has been described in Section 3.4.4.

In these figures it may be seen that the nature of attenuation of $H_{xt}$ is the same as that of $H_{y\ell}$ and the nature of attenuation of $H_{yt}$ is the same as that of $H_{x\ell}$. But like in longitudinal flux arrangement, here also $|H_{xt}| >> |H_{yt}|$, in spite of the boundary condition which requires $H_{xt} = 0$ at $y = 0$. (Table insets in the figures).

In these figures, the attenuation of both $H_{xt}$ and $H_{yt}$ is seen to be very small for small thicknesses (e.g. $d/\delta = 0.25$) and rather pronounced for large thicknesses, (e.g. $d/\delta = 3.0$). The surface value of $H_{xt}$ in Fig. 3.3 is much higher than that of $H_{yt}$ in Fig. 3.4 and this shows that under transverse flux arrangement also, the x-component

of magnetic field strength is the dominant one.

The dotted lines in Fig. 3.4 also represent the attenuation of $(\frac{\partial H_{xt}}{\partial y})$ and $(\frac{\partial H_{yt}}{\partial x})$, although the surface value of the former is much higher than that of the latter (table inset in the figure). This shows that the current density on the plate surface and also in the inside of the plate is due predominantly to $(\frac{\partial H_{xt}}{\partial y})$.

3.5.5 The Field Components at the Secondary Plate Surface

The field components on the surface of the secondary may be obtained from equations (3.74) to (3.76) by putting y = d. After some further calculations, this gives,

$$H_{xtd} = \frac{2\hat{K}_z}{|M_t|}(\cosh 2\alpha d - \cos 2\alpha d)^{\frac{1}{2}}\exp(-jqx)\ \angle H_{xtd} \tag{3.79}$$

$$H_{ytd} = \frac{\sqrt{2}\hat{K}_z q}{\alpha|M_t|}(\cosh 2\alpha d + \cos 2\alpha d)^{\frac{1}{2}}\exp(-jqx)\ \angle H_{ytd} \tag{3.80}$$

and

$$J_{ztd} = \frac{2\sqrt{2}\alpha\hat{K}_z}{|M_t|}(\cosh 2\alpha d + \cos 2\alpha d)^{\frac{1}{2}}\exp(-jqx)\ \angle -H_{ytd} \tag{3.81}$$

where,

$$\angle H_{xtd} = \tan^{-1}\left[\frac{m\tanh qg(\sinh 2\alpha d+\sin 2\alpha d)}{m\tanh qg(\sinh 2\alpha d-\sin 2\alpha d)+2(\cosh 2\alpha d-\cos 2\alpha d)}\right] \tag{3.82}$$

and

$$\angle H_{ytd} = \tan^{-1}\left[\frac{m\tanh qg(\cosh 2\alpha d+\cos 2\alpha d)+(\sinh 2\alpha d-\sin 2\alpha d)}{(\sinh 2\alpha d+\sin 2\alpha d)}\right] \tag{3.83}$$

For the case when $\alpha d$ is large i.e. $d >> 1/\alpha$, equations (3.82) and (3.83) become

$$\left.\angle H_{xtd}\right]_{\alpha d \text{ large}} = \tan^{-1}\left[\frac{m\tanh qg}{m\tanh qg+2}\right] \qquad (3.82a)$$

and

$$\left.\angle H_{ytd}\right]_{\alpha d \text{ large}} = \tan^{-1}[m\tanh qg+1] \qquad (3.83a)$$

Equations (3.82a) and (3.83a) are the same as the corresponding equations, i.e. equations (3.46a) and (3.47a) respectively, of the longitudinal flux case, and of course, the same as were obtained by Bowden[30], for an infinitely thick plate.

When d is very small, however, $\angle H_{xtd}$ and $\angle H_{ytd}$ tend to $\pi/4$ and $\pi/2$ respectively.

Fig. 3.5 shows in dotted lines the variations of the surface magnetic field strengths $H_{xtd}$ and $H_{ytd}$ with the ratio of half-thickness of the plate to depth of penetration. The construction of the graphs has been described in Section 3.4.5.

Unlike the longitudinal flux case, here $H_{xtd}$ decreases and $H_{ytd}$ increases for very thin plates. For thin plates, this implies that the eddy current reaction field is small and more and more of the flux is allowed to pass through the plate thickness. With increase in plate thickness however, $H_{xtd}$ soon becomes significant. In transition from thin to thick plates $H_{xtd}$ goes through a maximum and $H_{ytd}$ through a minimum.

The curves of $H_{ytd}$ also represent the variations

of the surface values of $(\frac{\partial H_{xt}}{\partial y})$ and $(\frac{\partial H_{yt}}{\partial x})$, although the former is always much greater than the latter.

3.5.6 A Thickness Criterion

As in the longitudinal flux arrangement, Section 3.4.6, a thickness criterion may be established for the transverse flux arrangement. From equations (3.79) and (3.80),

$$\left|\frac{H_{xtd}}{H_{ytd}}\right| = \frac{\sqrt{2}\alpha}{q} \cdot \left[\frac{\cosh 2\alpha d - \cos 2\alpha d}{\cosh 2\alpha d + \cos 2\alpha d}\right]^{\frac{1}{2}} \qquad (3.84)$$

When d is very large, i.e. the plate is very thick, this reduces to $\frac{\sqrt{2}\alpha}{q}$. But since by assumption $\frac{\sqrt{2}\alpha}{q} >> 1$, therefore $|H_{xtd}| >> |H_{ytd}|$ which is obtained for a thick plate. Equation (3.84) also reduced to $\frac{\sqrt{2}\alpha}{q}$ when $\cos 2\alpha d = 0$, i.e. when $d = \frac{\pi}{4}(1/\alpha)$. This means that for a plate to be considered thick, its half thickness should be at least equal to $\pi/4$ times the depth of penetration.

When d is small, on the other hand, equation (3.84) reduces to

$$\frac{\sqrt{2}\alpha}{q} \cdot \left[\frac{4\alpha^2 d^2}{2}\right]^{\frac{1}{2}} = \frac{2\alpha^2 d}{q}$$

Thus a plate may also be considered thick if $d > \frac{q}{2\alpha^2}$, i.e. if its half-thickness is greater than $\pi/2$ times $\frac{(\text{depth of penetration})^2}{\text{pole-pitch}}$, for, then the x-component of

surface magnetic field strength becomes the dominant one.

3.5.7 One-Dimensional Nature of Magnetic Fields in the Secondary Plate

From equation (3.74) and (3.75)

$$\frac{\partial \dot{H}_{xt}}{\partial y} = \frac{j4\hat{K}_z \alpha}{\dot{M}_t}[\cosh\alpha(1+j)y] \exp(-jqx) \qquad (3.85)$$

and

$$\frac{\partial \dot{H}_{yt}}{\partial x} = \frac{2\hat{K}_z q^2}{\alpha \dot{M}_t}[\cosh\alpha(1+j)y] \exp(-jqx) \qquad (3.86)$$

$\therefore$ From equations (3.85) and (3.86) therefore,

$$\frac{|\partial H_{xt}/\partial y|}{|\partial H_{yt}/\partial x|} = \frac{2\alpha^2}{q^2} \qquad (3.87)$$

Since by assumption $\frac{2\alpha^2}{q^2} >> 1$, (Section 3.4.4), therefore $|\partial H_{xt}/\partial y| >> |\partial H_{yt}/\partial x|$. Equations (3.85) and (3.86) form the two terms in the current density expression of equation (3.15), so that the current density obtained is approximately such that only the $H_{xt}$ component of the magnetic field existed in the plate. The equation (3.87) is obtained irrespective of the plate thickness and in spite of the presence of a boundary condition at y = 0 plane. This equation also holds at any depth in the plate.

Attenuations of $(\frac{\partial H_{xt}}{\partial y})$ and $(\frac{\partial H_{yt}}{\partial x})$ inside the plate for one half of plate thickness have been shown in Fig.3.4, (dotted lines). Although the nature of variations of both at per unit of the surface value is the same, the former is much higher than the latter in magnitude.

3.5.8 Eddy-Current Loss

The eddy-current loss per unit of surface area in half the thickness of the plate is given by the complex Poynting vector, $\rho_{yt}$ where

$$\rho_{yt} = -\frac{1}{2} \mathrm{Re}(\dot{E}_{zt} \times H^*_{xt}) \tag{3.88}$$

$H^*_{xt}$ is the complex conjugate of $\dot{H}_{xt}$ and $\dot{E}_{zt} = \rho \dot{J}_{zt}$. Using equation (3.74) and (3.76), this becomes,

$$\rho_{yt} = \frac{2\hat{K}_z^2 \alpha \rho}{|M_t|^2}(\sinh 2\alpha y + \sin 2\alpha y) \tag{3.89}$$

where $|M_t|$ is given by equation (3.78).

The total loss from one side is obtained by putting y=d as

$$\rho_{ytd} = \frac{\hat{K}_z^2 \alpha \rho}{\cosh^2 qg} \cdot \left[ \frac{(\sinh 2\alpha d + \sin 2\alpha d)}{m^2 \tanh^2 qg (\cosh 2\alpha d + \cos 2\alpha d) + 2m \tanh qg (\sinh 2\alpha d - \sin 2\alpha d) + 2(\cosh 2\alpha d - \cos 2\alpha d)} \right] \tag{3.90}$$

when d is sufficiently large (i.e. $\alpha d >> 1$), equation (3.90) becomes

$$\rho_{yt\infty} \equiv \frac{\hat{K}_z^2 \alpha \rho}{\cosh^2 qg} \cdot \left[ \frac{1}{m^2 \tanh^2 qg + 2m \tanh qg + 2} \right] \tag{3.91}$$

which is the same as was obtained by Bowden.

When d is small (i.e. $\alpha d << 1$), equation (3.90) becomes

$$P_{yto} \equiv \frac{2\hat{K}_z^2.\alpha^2.\rho.d}{\cosh^2 qg} \cdot \left[\frac{1}{m^2.\tanh^2 qg + \frac{8\alpha^3 d^3}{3}.m.\tanh qg + 4\alpha^2 d^2}\right] \tag{3.92}$$

i.e. $$P_{yto} \equiv \frac{2\hat{K}_z^2.\alpha^2.\rho.d}{m^2.\sinh^2 qg} \tag{3.92a}$$

Thus the loss becomes very small.

The loss per unit of its value for an infinitely thick plate has been plotted in dotted lines in Fig. 3.6. These curves confirm the observation by Jackson [4], that for thin plates the loss in transverse flux arrangement may be many times higher than that obtained in longitudinal flux arrangement.

For very thin plates, the reaction field is weak and the flux passes through the plate. The eddy-current distribution over the plate thickness is uniform, as may be observed from attenuation curves (Figs. 3.3 and 3.4), and the loss increases. With increase in plate thickness, the x-component of magnetic field gradually comes into prominence, the total flux reduces and a greater proportion of the flux passes along the plate length. The loss thus reduces, and goes to a minimum. When the plate is very thick, the reaction field governs the loss, which becomes the same as that in the longitudinal flux arrangement.

### 3.5.9 Time Average Force Density

The x and y-components of time average force densities $F_{xt}$ & $F_{yt}$ may be obtained from

$$F_{xt} = -\frac{1}{2} \mathrm{Re}(\dot{J}_{zt} \times B^*_{yt}) \tag{3.93}$$

and

$$F_{yt} = -\frac{1}{2} \mathrm{Re}(\dot{J}_{zt} \times B^*_{xt}) \tag{3.94}$$

where, $B^*_{yt}$ and $B^*_{xt}$ are the complex conjugates of $\dot{B}_{yt}$ $(=\mu_r\mu_o\dot{H}_{yt})$ and $\dot{B}_{xt}$ $(=\mu_r\mu_o\dot{H}_{xt})$ respectively.

Substituting from equations (3.74), (3.75) and (3.76) into equations (3.93) and (3.94),

$$F_{xt} = \frac{2\mu_r\mu_o q\hat{K}_z^2}{|M_t|^2} (\cosh 2\alpha y + \cos 2\alpha y), \quad 0 \leq y \leq d \tag{3.95}$$

and

$$F_{yt} = \frac{2\mu_r\mu_o \alpha\hat{K}_z^2}{|M_t|^2} (\sinh 2\alpha y + \sin 2\alpha y), \quad 0 \leq y \leq d \tag{3.96}$$

where $|M_t|$ is given by equation (3.78).

Thus both the forces of translation, $F_{xt}$, and of attraction, $F_{yt}$, vary with the depth, y. At the centre of the plate, however, only $F_{xt}$ exists. At the surface of the plate, their relative magnitudes are given by

$$\frac{F_{ytd}}{F_{xtd}} = \frac{\alpha}{q} \cdot \left[\frac{\sinh 2\alpha d + \sin 2\alpha d}{\cosh 2\alpha d + \cos 2\alpha d}\right] \tag{3.97}$$

Thus, at the surface of an infinitely thick ($\alpha d >> 1$) plate, $F_{yt}$ will be greater than, equal to or less than $F_{xt}$,

according to whether the pole-pitch is greater than, equal to or less than, $\pi$ times the depth of penetration, respectively. When the plate thickness is very small equation (3.97) reduces to $\frac{2\alpha^2 d}{q}$ which shows that $F_{xt}$ may be much greater than $F_{yt}$ at the surface.

Thus, in general the pole-pitch should be greater than the depth of penetration for the transverse flux arrangement also, so that the force of attraction becomes the dominant one, and whose effect may be reduced due to the double-sided arrangement.

## 3.6 CONCLUSIONS

In this chapter, linear two-dimensional theories have been developed as applied to a plate being subjected to travelling magnetic fields on either side. The cases of poles on opposite sides being of the same, (i.e. longitudinal flux), and opposite (i.e. transverse flux), instantaneous polarity have been considered in detail. Analysis has been carried out for one-half of the plate thickness, it being assumed that the same applies to the other half of the plate through matching boundary conditions at the centre of the plate.

Expressions have been obtained for magnetic field strengths and current density in the plate. The contribution of primary iron, equations (3.27) and (3.66), has been shown to be affected by the finite thickness of the plate. It is shown that for primary relative permeability of 500 and over, the influence of finite thickness is negligible.

Surface values of different electromagnetic quantities and their associated phase angles have been obtained and verified against standard expressions available in the literature[30], when the plate thickness has been taken as being very large. A thickness criterion has been established by considering the relative magnitudes of the x and y-components of surface magnetic fields. They help establish the criterion as to when a plate may be considered electrically thick or thin.

It has been established that the magnetic fields in the secondary are predominantly one-dimensional in nature, irrespective of pole arrangements, plate thickness and the presence or otherwise of boundary conditions at the plate centre. Loss expressions have been obtained which agree for $d \to \infty$, with those obtained for a thick plate. It has been shown that for the transverse flux case the loss in thin plates may be many times greater than that for longitudinal flux case. In transition from electromagnetically thin to thick plates $((d/\delta) > 1)$ the loss for the transverse flux arrangement goes through a minimum and the loss for the longitudinal flux case passes through a maximum. Equations for electromagnetic forces developed in the plate have been obtained and used to show the prominence or otherwise of the force of attraction against the force of translation. Conditions have been obtained to determine when one force is greater than the other.

For the case of the plate being very thick, the two different pole arrangements become the same, for both reduce to the case of studying electromagnetic fields in an infinitely thick plate. Thus the different expressions for electromagnetic fields and loss become the same for thick plate as may be seen from curves of Fig. 3.5 and 3.6.

As mentioned in Section 3.2.5, the effect of hysteresis has been neglected in this chapter. However, an approximate allowance for hysteresis was made on the basis of elliptical B-H curve. The electromagnetic field quantities obtained in this chapter are modified in order to allow for hysteresis. The detailed derivation of these are given in Appendix 1.

# CHAPTER 4

# THE FIELD EQUATIONS ON THE PLATE AND PRIMARY SURFACES AND A COMPARATIVE STUDY OF THE TWO POLE-ARRANGEMENTS

## 4.1 INTRODUCTION

The linear two-dimensional theories developed in Chapter 3 have been extended further in this chapter, which is divided into two different, though related, parts.

In the first part, the field equations have been developed at the surface of the primary (y=d+g) and at the surface of the plate (y=d). These equations have been used to investigate the nature of the eddy-current reaction field for various operating conditions. The resulting magnetic flux densities are also considered. The wave impedances at the plate surface are obtained and their ratio is defined as an important dimensionless parameter, Q. The study also includes power loss and electromagnetic force expressions. The two different pole-arrangements are considered in detail.

In the second part of this chapter, a comparative study has been made of the linear theories developed for the two different pole-arrangements. The advantage of considering a finite thickness of the plate in the analysis is that the specific cases of infinitely thick and thin plates may be obtained from the resulting equations; the comparative study considers the two cases in some detail. The study includes

the eddy-current distribution pattern in the plate, the magnetic field strengths on the plate surface, the eddy-current loss, the reaction field of eddy currents and the impedances at the plate surface. For this purpose, the results obtained in Chapter 3 have been used. The study also includes an investigation of the various assumed inequalities which were used to simplify many of the expressions obtained.

## 4.2 THE FIELD EQUATIONS ON THE PLATE AND PRIMARY SURFACES

### 4.2.1 General

The equations for field quantities in the plate and in the air-gap region are given in Chapter 3. The quantities at the surface of the plate may be obtained by putting y=d in these equations. For each of the arrangements of poles, it is possible to study the reaction field of eddy currents in the plate, its dominance or otherwise on the magnetic field in the absence of eddy currents, the flux density at different parts in the air-gap region, etc. By studying the input impedances on the plate surface, it is possible to define certain dimensionless parameters; the loss and force expressions may be obtained in terms of these parameters.

As has been shown in Chapter 3, the magnetic field strength is predominantly one-dimensional in the plate when $2\alpha^2 >> q^2$. Thus in the study of the magnetic field strength in the plate, only the x-component is considered. In the following section the longitudinal flux arrangement is

considered and the transverse flux arrangement is considered in section 4.2.3.

### 4.2.2 Longitudinal Flux Arrangement

#### 4.2.2.1 Eddy-Current Reaction Field

The magnetic field strength obtained in the plate consists of two components, $\dot{H}_c$, the magnetic field strength of the current sheet, and $\dot{H}_r$, the reaction field of eddy current. Thus, the resultant magnetic field, $\dot{H}$ is given by

$$\dot{H} = \dot{H}_c + \dot{H}_r \tag{4.1}$$

Since only x-component of magnetic field strength is being considered, then for the LFA and at the surface of the plate (i.e. y=d), equation (4.1) may be written as,

$$\dot{H}_{x\ell d} = \dot{H}_{cx\ell d} + \dot{H}_{rx\ell d} \tag{4.2}$$

The analysis so far has assumed only the resultant fields, so that $\dot{H}_{x\ell d}$ may be obtained from equations (3.38) and (3.41) as,

$$\dot{H}_{x\ell d} = \frac{\hat{K}_z (1+j)\,(1+j\tanh\alpha d\,\tan\alpha d).\exp(-jqx)}{\cosh qg\left[\{(m\tanh qg-\tan\alpha d)\tanh\alpha d+1\}+j\{(m\tanh qg+\tanh\alpha d)\tan\alpha d+1\}\right]}$$

$$\begin{cases} \dfrac{2\alpha^2}{q^2} >> 1 \\ \mu_1 \to \infty \end{cases} \tag{4.3}$$

In order to obtain $\dot{H}_{cx\ell d}$, it is necessary to define the

condition when the surface current density in the plate becomes zero for any plate thickness. As may be seen from equation (3.40) or (3.46), this condition is obtained when $\alpha \to 0$. Since the relative permeability of the solid-iron plate is quite large and sinusoidal alternating fields are being considered, $\alpha \to 0$ implies that $\rho \to \infty$. Thus, for determining the magnetic field of the current sheet, $\rho \to \infty$ and $\alpha \to 0$ and from equation (3.21)

$$k = q \tag{4.4}$$

At the plate surface (i.e. y=d), therefore, $\dot{H}_{cx\ell d}$ may be obtained from equation (3.31) or (3.29) as,

$$\dot{H}_{cx\ell d} = \frac{\hat{K}_z . \exp(-jqx)}{\cosh qg\,(1+\mu_r \tanh qg \tanh qd)} \tag{4.5}$$

The reaction field at the surface $\dot{H}_{rx\,\ell d}$ may be obtained by substituting equations (4.3) and (4.5) in equation (4.2). Clearly, the resulting expression is complicated and three specific cases about the reaction field may be studied from the above equations as they are.

Dividing equation (4.3) by equation (4.5),

$$\frac{\dot{H}_{x\ell d}}{\dot{H}_{cx\ell d}} = \frac{\{(1-\tan\alpha d . \tanh\alpha d)+j(1+\tan\alpha d . \tanh\alpha d)\}.(1+\mu_r \tanh qg . \tanh qd)}{\{(m\tanh qg \tan\alpha d)\tanh\alpha d+1\}+j\{(m\tanh qg+\tanh\alpha d)\tan\alpha d+1\}} \tag{4.6}$$

If in equation (4.6), $m.\tanh qg << \tanh \alpha d$ and also $m.\tanh qg << \tan \alpha d$, then it reduces to

$$\frac{\dot{H}_{x\ell d}}{\dot{H}_{cx\ell d}} \cong (1+\mu_r.\tanh qg.\tanh qd), \quad \begin{cases} m.\tanh qg << \tanh \alpha d \\ m.\tanh qg << \tan \alpha d \end{cases} \qquad (4.7)$$

$m.\tanh qg << \tanh \alpha d$ is believed to be the general case of the assumption $m.\tanh qg << 1$ in Bowden's work [30], and, likewise, also implies that the eddy-current field is strong. $m.\tanh qg << \tan \alpha d$ is another restriction brought in due to the finite thickness of the plate. In general, however, $m.\tanh qg << \tanh \alpha d$ is the necessary condition.

Three specific cases may be identified from equation (4.7).

Case 1 $\mu_r.\tanh qg.\tanh qd >> 1$

This means that $\dot{H}_{x\ell d} >> \dot{H}_{cx\ell d}$ and hence, $\dot{H}_{x\ell d} \rightarrow \dot{H}_{rx\ell d}$. Thus under this condition the eddy-current reaction field is almost equally as strong as the resultant field. This applies to solid-iron plates having high permeability and/or to heaters having large ratios of plate-thickness to pole-pitch and air-gap to pole-pitch.

Case 2 $\mu_r.\tanh qg.\tanh qd << 1$

This means that $\dot{H}_{x\ell d} \rightarrow \dot{H}_{cx\ell d}$ and hence $\dot{H}_{rx\ell d} \rightarrow 0$. Under this condition, thererfore, the reaction field is very weak and this signifies a complete reflection of applied field in the secondary. This condition may be obtained with rather

thin plates of low permeability, e.g. Copper, and with a low value of the ratio of air-gap length to pole-pitch.

Case 3 $\mu_r \tanh qg.\tanh qd=1$

This means that $\dot{H}_{cx\ell d} \rightarrow \dot{H}_{rx\ell d} \rightarrow \dot{H}_{x\ell d}/2$. In this case, the plate may be of solid iron or copper. In the former, the plate-thickness and the ratio of air-gap to pole-pitch are both relatively unimportant, while in the latter these should be as large as possible.

The above study defines the conditions when the eddy-current reaction field may be equally as strong, half as strong or very weak compared with the resultant field. They are shown to depend on such factors as the relative permeability of the plate, its thickness, the air-gap length and the pole-pitch.

4.2.2.2 The y-Component of Flux Density at the Surfaces

4.2.2.2.1 At the Plate Surface, y=d

The y-component of the total flux density at the surface of the plate (i.e. y=d) may be obtained from equations (3.39), (3.41) and (3.5) as,

$$\dot{B}_{y\ell d} = \frac{jm\mu_o \hat{K}_z (\tanh\alpha d + j\tan\alpha d)\ \exp(-jqx)}{\cosh qg\left[\{m\tanh qg - \tan\alpha d)\tanh\alpha d + 1\} + j\{(m\tanh qg - \tanh\alpha d)\tan\alpha d + 1\}\right]}$$

(4.8)

The y-component of the flux density at the plate surface due to the applied field of the current sheet, $\dot{B}_{cy\ell d}$, may be obtained from equations (3.5), (3.32) and (4.4) as,

$$\dot{B}_{cy\ell d} = \frac{j\mu_o \mu_r \hat{K}_z \tanh qd \cdot \exp(-jqx)}{\cosh qg\,(1+\mu_r \tanh qg \tanh qd)} \qquad (4.9)$$

$$\therefore \dot{B}_{cy\ell d} = \frac{j\mu_o \hat{K}_z \cdot \exp(-jqx)}{\sinh qg} \quad \text{if} \quad \mu_r \tanh qg \tanh qd >> 1 \qquad (4.9a)$$

$\mu_r \tanh qg \tanh qd >> 1$ will be assumed to hold, so that the simplified expression of equation (4.9a), instead of equation (4.9), will be used in further analysis.

Since magnetically linear media are being considered here, equation (4.1) applies to the y-component of the magnetic field strength, and for that matter, to the magnetic flux density also. Thus, using the relation $\dot{B}_{y\ell d} = \dot{B}_{cy\ell d} + \dot{B}_{ry\ell d}$, the reaction flux density at the plate surface, $\dot{B}_{ry\ell d}$, is obtained as,

$$\dot{B}_{ry\ell d} = \dot{B}_{y\ell d} - \dot{B}_{cy\ell d} \qquad (4.10)$$

Putting the values from equation (4.8) and (4.9a), equation (4.10) becomes,

$$\dot{B}_{ry\ell d} = \frac{-j\mu_o \hat{K}_z (1+j)(1+j\tan\alpha d \cdot \tanh\alpha d) \cdot \exp(-jqx)}{\sinh qg\left[\{(m\tanh qg - \tan\alpha d)\tanh\alpha d + 1\} + j\{(m\tanh qg - \tanh\alpha d)\tan\alpha d + 1\}\right]}$$

(4.11)

Comparing equation (4.11) with equation (4.3), it may be seen that

$$\dot{B}_{ry\ell d} = \frac{-j\mu_o}{\tanh qg}\cdot\dot{H}_{x\ell d} \qquad \text{if} \begin{cases} \sqrt{2}\alpha >> q, \ \mu_1 \to \infty \\ \mu_r . \tanh qg . \tanh qd >> 1 \end{cases} \tag{4.12}$$

4.2.2.2.2. At the Surface of the Primary, y=d+g

An equation of the form (4.12) may be obtained for the y-component of the flux density at the primary surface (i.e. y=d+g) when there is no eddy current. Thus putting k=q in equation (3.30) and using equation (3.5) again, the y-component of flux density at y=d+g in the absence of eddy current, $\dot{B}_{cy\ell(d+g)}$ is given by

$$\dot{B}_{cy\ell(d+g)} = \frac{j\mu_o \hat{K}_z (\mu_r \tanh qd + \tanh qg)\cdot \exp(-jqx)}{(1 + \mu_r \tanh qg \tanh qd)} \tag{4.13}$$

$$\dot{B}_{cy\ell(d+g)} = \frac{j\mu_o}{\tanh qg}\cdot\hat{K}_z \qquad \text{if} \quad \begin{cases} \mu_r \tanh qd >> \tanh qg \\ \mu_r \tanh qg \tanh qd >> 1 \end{cases} \tag{4.13a}$$

The condition $\mu_r \tanh qg \tanh qd >> 1$ was already assumed to hold and if this condition is satisfied the other condition, viz. $\mu_r \tanh qd >> \tanh qg$, will also be satisfied. Thus two conditions of equation (4.13a) actually amounts to one.

In equation (4.13a), $\hat{K}_z$ is the actual line current density obtained at the primary surface. Thus comparing equation (4.13a) with equation (4.12), it may be seen that the total effect of eddy current may be represented by an

equivalent current sheet on the plate surface whose line density is equal to $-\dot{H}_{x\ell d}$.

4.2.2.3 The Input Impedances at the Plate Surface

The input impedance at the plate surface (i.e. y=d) is given by

$$\dot{Z}_{y\ell d} = \frac{\dot{E}_{z\ell d}}{\dot{H}_{x\ell d}} = \frac{\rho \dot{J}_{z\ell d}}{\dot{H}_{x\ell d}} \qquad (4.14)$$

From equations (3.38) and (3.40), then,

$$\dot{Z}_{y\ell d} = -(1+j)\alpha\rho\tanh\alpha(1+j)d \qquad (4.15)$$

The impedance due to the reaction field of the eddy current at the plate surface is given by

$$\dot{Z}_{ry\ell d} = \frac{\dot{E}_{rz\ell d}}{\dot{H}_{x\ell d}} \qquad (4.16)$$

where $\dot{E}_{rz\ell d}$ is the electric field obtained at the surface of the plate due to the reaction field of eddy current, and is given by

$$\dot{E}_{rz\ell d} = \int \frac{\partial B_{ry\ell d}}{\partial t}\, dx \qquad (4.17)$$

Using equation (4.12), this becomes,

$$\dot{E}_{rz\ell d} = \frac{j\mu_o\omega}{q\tanh qg} \cdot \dot{H}_{x\ell d} \qquad (4.17a)$$

so that the impedance $\dot{Z}_{ry\ell d}$, equation (4.16), becomes,

$$\dot{Z}_{ry\ell d} = \frac{j\mu_o\omega}{q\tanh qg} \qquad (4.18)$$

It may be seen that the input impedance has a real and an imaginary part i.e.it has a resistive and a reactive component while the impedance due to the reaction field has only an imaginary part i.e. it is wholly reactive. The input impedance is dependent on the finite thickness of the plate while the impedance due to the reaction field is independent of it. In fact equation (4.18) is the same as was obtained for an infinitely thick plate [30].

#### 4.2.2.4 The Dimensionless Parameter, $Q_{\ell\ell}$

In order that maximum power transfer may take place between the primary and the solid-iron plate, the two impedances given by equations (4.15) and (4.18) must be equal. In general, however, a dimensionless parameter, $Q_{\ell\ell}$, may be defined as the ratio of the moduli of the two impedances. For the case of maximum loss, therefore, this parameter will become unity, i.e. for maximum loss, $Q_{\ell\ell} = 1$.

From equations (4.15) and (4.18), therefore,

$$Q_{\ell\ell} = \frac{|\dot{Z}_{r\ell 1d}|}{|\dot{Z}_{y\ell d}|} = \frac{\sqrt{2\varepsilon}}{m\,t\,anhqg} \tag{4.19}$$

where

$$\varepsilon = \left[\frac{\cosh 2\alpha d + \cos 2\alpha d}{\cosh 2\alpha d - \cos 2\alpha d}\right] \tag{4.20}$$

From equations (4.8) and (4.11), it may be seen that

$$\frac{\dot{B}_{y\ell d}}{\dot{B}_{ry\ell d}} = \frac{-m\,t\,anhqg(\tanh\alpha d + j\tan\alpha d)}{(1+j)(1+j\tanh\alpha d.\tan\alpha d)}$$

After some simplifications,

$$\frac{|\dot{B}_{y\ell d}|}{|\dot{B}_{ry\ell d}|} = \frac{m\,t\,anhqg}{\sqrt{2\varepsilon}} = \frac{1}{Q_{\ell\ell}} \tag{4.21}$$

so that for maximum loss, $|\dot{B}_{y\ell d}| = |\dot{B}_{ry\ell d}|$.

It is interesting to note that when the plate is infinitely thick, the value of $\varepsilon$ given by equation (4.20) tends to unity and the present definition of $Q_{\ell\ell}$ becomes the same as was given by Bowden[30]. Using equations (3.43) and (3.19) for the value of m in equation (4.19), the expression for $Q_{\ell\ell}$ may be obtained as,

$$Q_{\ell\ell} = \frac{1}{q\,t\,anhqg} \cdot \left[\frac{\mu_o \omega \varepsilon}{\rho \mu_r}\right]^{\frac{1}{2}} \tag{4.22}$$

Clearly, $Q_{\ell\ell}$ is a function of the machine dimensions and the

thickness of the plate. Thus it is possible to define the optimum half-thickness, $d_{m\ell}$, at which maximum loss will be obtained. Such a value of $d_{m\ell}$ is obtained, by putting $Q_{\ell\ell}=1$ in equation (4.19) and using equation (4.20), as,

$$\frac{\cosh 2\alpha d_{m\ell}}{\cos 2\alpha d_{m\ell}} = \frac{m^2 \tanh^2 qg+2}{m^2 \tanh^2 qg-2} \qquad (4.23)$$

Equation (4.23) shows that for a given set of machine dimensions a thickness of the plate may be so chosen that maximum loss is obtained. Conversely, for a given plate thickness, equation (4.23) may be used to define machine dimensions for maximum loss.

In general, $Q_{\ell\ell}$ is obtained as a number e.g. 12.58 and is indicative of the fact whether the loss obtainable under a given arrangement is very well exploited or not. A value of $Q_{\ell\ell}$ as close to unity as possible is highly desirable, because in that case loss close to the maximum possible is being obtained.

4.2.2.5 Loss In Terms of $Q_{\ell\ell}$

The loss expression, equation (3.55), may be obtained in terms of the dimensionless parameter and such a form of equation makes it easy to visualise when the maximum loss occurs. Also, expressing the loss as per unit of the maximum loss one can see how best the obtainable loss is

being exploited.

From equation (4.19).

$$m\tanh qg = \frac{\sqrt{2\varepsilon}}{Q_{\ell\ell}} \tag{4.19a}$$

Using equation (4.19a) in equation (3.55), the loss expression is finally obtained as,

$$\rho_{y\ell d} = \frac{\hat{K}_z^2 \mu_o \omega \psi_1 \Delta_{\ell\ell}}{2\sqrt{2} q \sinh qg . \cosh qg} \tag{4.24}$$

where

$$\psi_1 = \frac{\sinh 2\alpha d - \sin 2\alpha d}{(\cosh^2 2\alpha d - \cos^2 2\alpha d)^{\frac{1}{2}}} , \tag{4.25a}$$

$$\Delta_{\ell\ell} = \frac{1}{Q_{\ell\ell} + Q_{\ell\ell}^{-1} + \sqrt{2}\psi_2} \tag{4.25b}$$

and

$$\psi_2 = \frac{\sinh 2\alpha d + \sin 2\alpha d}{(\cosh^2 2\alpha d - \cos^2 2\alpha d)^{\frac{1}{2}}} \tag{4.25c}$$

For the case of maximum loss, $\Delta_{\ell\ell}$ is obtained by putting $Q_{\ell\ell}=1$ in equation (4.25b) and, thus, the loss expressed at per unit of its maximum value is given by,

$$\frac{\rho_{y\ell d}}{\rho_{y\ell dm}} = \frac{\Delta_{\ell\ell}}{\Delta_{\ell\ell}\Big]_{Q_{\ell\ell}=1}} = \frac{2+\sqrt{2}\psi_2}{Q_{\ell\ell} + Q_{\ell\ell}^{-1} + \sqrt{2}\psi_2} \tag{4.26}$$

4.2.2.6 Force Densities in Terms of $Q_{\ell\ell}$

Using equation (4.19a) in equations (3.60) and (3.61), the time average force densities at the plate surface may be obtained in terms of $Q_{\ell\ell}$. Thus the x-component, $F_{x\ell d}$, is given by,

$$F_{x\ell d} = \frac{\hat{K}_z^2 \mu_o \alpha \Delta_{\ell\ell}}{\sqrt{2}\varepsilon \sinh qg \cosh qg} \qquad (4.27)$$

and the y-component, $F_{y\ell d}$, is given by

$$F_{y\ell d} = \frac{\hat{K}_z^2 \mu_o \alpha^2 \psi_1 \Delta_{\ell\ell}}{\sqrt{2} q \sinh qg \cosh qg} \qquad (4.28)$$

In equations (4.27) and (4.28), $\Delta_{\ell\ell}$ is given by equation (4.25b). The forces will also have their maximum when $Q_{\ell\ell}=1$ and equation (4.26) also gives the forces per unit of their maximum values.

i.e. $$\frac{F_{x\ell d}}{F_{x\ell dm}} = \frac{F_{y\ell d}}{F_{y\ell dm}} = \frac{P_{y\ell d}}{P_{y\ell dm}} \qquad (4.29)$$

4.2.3 Transverse Flux Arrangement

4.2.3.1 Eddy-Current Reaction Field

Equation (4.1) also applies for transverse flux arrangement and in terms of the plate-surface (i.e. y=d) quantities for the TFA, equation (4.1) is given by,

$$\dot{H}_{xtd} = \dot{H}_{cxtd} + \dot{H}_{rxtd} \qquad (4.30)$$

where $\dot{H}_{cxtd}$ is the magnetic field strength of the current sheet, $\dot{H}_{rxtd}$ is the magnetic field strength of the eddy-current reaction field and $\dot{H}_{xtd}$ is the resultant field.

$\dot{H}_{xtd}$ is obtained from equation (3.74) together with equation (3.77) and is given by,

$$\dot{H}_{xtd} = \frac{\hat{K}_z.(1+j)(\tanh\alpha d + j\tan\alpha d).\exp(-jqx)}{\cosh qg\left[\{m\tanh qg+\tan\alpha d-\tan\alpha d\}+j\{(m\tanh qg.\tanh\alpha d+1)\tan\alpha d+\tanh\alpha d\}\right]} \qquad (4.31)$$

$\dot{H}_{cxtd}$ is obtained, as in section 4.2.2.1, by putting k=q in equation (3.69). And this give, after some steps,

$$\dot{H}_{cxtd} = \frac{\hat{K}_z.\exp(-jqx)}{\cosh qg\ (1 + \mu_r.\tanh qg.\coth qd)} \qquad (4.32)$$

Once again, the effect of the reaction field may be obtained by finding the ratio $\frac{\dot{H}_{xtd}}{\dot{H}_{xctd}}$ and from equations (4.31) and (4.32)

$$\frac{\dot{H}_{xtd}}{\dot{H}_{cxtd}} = \frac{\{(\tanh\alpha d-\tan\alpha d)+j(\tanh\alpha d+\tan\alpha d)\}(1+\mu_r\tanh qg.\coth qd)}{\left[\{m\tanh qg+\tanh\alpha d-\tan\alpha d\}+j\{(m\tanh qg.\tanh\alpha d+1)\tan\alpha d+\tanh\alpha d\}\right]} \qquad (4.33)$$

If $m\tanh qg << |(\tanh\alpha d - \tan\alpha d)|$ and $m\tanh qg.\tanh\alpha d << 1$, then equation (4.33) reduces to the form,

$$\frac{\dot{H}_{xtd}}{\dot{H}_{cxtd}} \cong (1 + \mu_r \tanh qg.\coth qd), \begin{cases} m\tanh qg << |(\tanh\alpha d - \tan\alpha d)| \\ m\tanh qg.\tanh\alpha d << 1 \end{cases} \qquad (4.34)$$

$m\tanh qg.\tanh\alpha d << 1$ (i.e. $m\tanh qg << \coth\alpha d$) is believed to be another form of the general expression in place of $m\tanh qg << 1$ used by Bowden[30] and implies that the eddy-current field is strong. $m\tanh qg << |(\tanh\alpha d - \tan\alpha d)|$ is another restriction due to the finite plate thickness. In general, however, $m\tanh qg.\tanh\alpha d << 1$ is the necessary condition.

Three specific cases may be studied, as before, from equation (4.34).

Case 1 $\mu_r \tanh qg.\coth qd >> 1$

In this case, $\dot{H}_{xtd} >> \dot{H}_{cxtd}$, so that $\dot{H}_{xtd} \rightarrow \dot{H}_{rxtd}$. Thus the reaction field is nearly equal to the total field. This condition is obtained, for a given pole-pitch in a machine having large air-gaps and with plates of high permeability and any thickness.

Case 2 $\mu_r \tanh qg.\coth qd << 1$

This means, $\dot{H}_{xtd} \rightarrow \dot{H}_{cxtd}$ and hence $\dot{H}_{rxtd} \rightarrow 0$. Thus, the total field is nearly the same as the field of the applied current sheet and since $\dot{H}_{rxtd} \rightarrow 0$, this implies complete reflection of eddy-current field in the plate. For a given

pole-pitch, this condition applies to machines having small air-gaps and a thick plate of low permeability, e.g. Copper.

Case 3 $\mu_r.\tanh qg.\coth qd=1$

This means $\dot{H}_{cxtd} \rightarrow \dot{H}_{rxtd} \rightarrow \frac{\dot{H}_{xtd}}{2}$. Thus the field of the current sheet and the reaction field of the eddy current are approximately equal in magnitude. This applies to plates of high (e.g. solid iron) or low (e.g. solid copper) permeability. For given values of air-gap length and pole-pitch, the plate thickness could be large with a high permeability plate, and small with a low permeability plate.

4.2.3.2 The y-Components of Flux Density at the Surfaces

4.2.3.2.1 At the Plate Surface, y=d

The y-component of total flux density at the plate surface (i.e. y=d), $\dot{B}_{ytd}$, may be obtained from equations (3.75), (3.77) and (3.5) as,

$$\dot{B}_{ytd} = \frac{j\hat{K}_z m\mu_o (1+j\tanh\alpha d.\tan\alpha d).\exp(-jqx)}{\cosh qg[\{m\tanh qg+\tanh\alpha d-\tan\alpha d\}+j\{(m\tanh qg.\tanh\alpha d+1)\tan\alpha d+\tanh\alpha d\}]} \qquad (4.35)$$

The y-component of flux density at plate surface (i.e. y=d) due to the field of applied current sheet, $\dot{B}_{cytd}$, is obtained by putting k=q in equation (3.70), together with equation (3.5), as,

$$\dot{B}_{cytd} = \frac{j\mu_r.\mu_o.\hat{K}_z.\exp(-jqx)}{\cosh qg\{\mu_r.\tanh qg + \tanh qd\}} \qquad (4.36)$$

$$\therefore \quad \dot{B}_{cytd} \cong \frac{j\mu_o.\hat{K}_z.\exp(-jqx)}{\sinh qg}, \text{ if } \mu_r.\tanh qg >> \tanh qd \qquad (4.36a)$$

Since $\mu_r \tanh qg >> \tanh qd$ will be obtained in most cases, the simplified form of equation (4.36a) will be used. At the plate surface, therefore, the magnetic field strength due to the reaction field of eddy currents, $\dot{B}_{rytd}$, may be obtained from the relation $\dot{B}_{ytd} = \dot{B}_{cytd} + \dot{B}_{rytd}$ and equations (4.35) and (4.36a) as,

$$\dot{B}_{rytd} = \frac{-j\mu_o.\hat{K}_z.(1+j)\,(\tanh\alpha d+\tan\alpha d)\,\exp(-jqx)}{\sinh qg\left[\{m\tanh qg+\tanh\alpha d-\tan\alpha d\}+j\{(m\tanh qg.\tanh\alpha d+1)\tan\alpha d+\tanh\alpha d\}\right]} \qquad (4.37)$$

Comparing equation (4.37) with equation (4.31),

$$\dot{B}_{rytd} = \frac{-j\mu_o}{\tanh qg}.\dot{H}_{xtd} \qquad \text{if} \begin{cases} \sqrt{2}\alpha >> q, \ \mu_1 \to \infty \\ \mu_r.\tanh qg >> \tanh qd \end{cases} \qquad (4.38)$$

4.2.3.2.2 At the Primary Surface, y=d+g

The y-component of flux density at the surface of the primary (i.e. y=d+g), due to the field of the applied current sheet $\hat{K}_z$ is obtained by putting k=q in equation (3.68) and using equation (3.5). This flux density $\dot{B}_{cyt(d+g)}$ is, thus, given by,

$$\dot{B}_{cyt(d+g)} = \frac{j\mu_o \hat{K}_z.(\mu_r + \tanh qd.\tanh qg)}{(\mu_r \tanh qg + \tanh qd)} \qquad (4.39)$$

In general $\mu_r >> \tanh qd.\tanh qg$ and by assumption in the previous sub-section $\mu_r.\tanh qg >> \tanh qd$, so that equation (4.39) may be approximated as,

$$\dot{B}_{cyt(d+g)} \cong \frac{j\mu_o}{\tanh qg}.\hat{K}_z \quad \text{if} \begin{cases} \mu_1 \to \infty \\ \mu_r >> \tanh qd.\tanh qg \\ \mu_r.\tanh qg >> \tanh qd \end{cases} \qquad (4.40)$$

But $\hat{K}_z$ is the actual line current density assumed at the primary surface. Thus, comparing equation (4.40) with equation (4.38), it may be concluded that the total effect of eddy currents may be represented by an equivalent current sheet on the plate surface whose line density is equal to $-H_{xtd}$.

4.2.3.3 The Input Impedances at the Plate Surface

The input impedance at the plate surface, $\dot{Z}_{ytd}$, is given by,

$$\dot{Z}_{ytd} = \frac{\dot{E}_{ztd}}{\dot{H}_{xtd}} = \frac{\rho \dot{J}_{ztd}}{\dot{H}_{xtd}} \qquad (4.41)$$

From equations (3.76) and (3.74) at y=d, then,

$$\dot{Z}_{ytd} = -(1+j)\alpha\rho \coth\alpha(1+j)d \qquad (4.42)$$

The impedance $\dot{Z}_{rytd}$ due to the reaction field of the eddy current is obtained from,

$$\dot{Z}_{rytd} = \frac{\dot{E}_{rytd}}{\dot{H}_{xtd}} \tag{4.43}$$

where $\dot{E}_{rytd}$ is the electric field at the plate surface induced by the reaction field in the plate and is given by,

$$\dot{E}_{rytd} = \int \frac{d\dot{B}_{rytd}}{dt}\, dx \tag{4.44}$$

Using equation (4.38), this becomes,

$$\dot{E}_{rytd} = \frac{j\mu_o \omega}{q \tanh qg} \cdot \dot{H}_{xtd} \tag{4.44a}$$

Thus $\dot{Z}_{rytd}$ in equation (4.43) is given by,

$$\dot{Z}_{rytd} = \frac{j\mu_o \omega}{q \tanh qg} \tag{4.45}$$

Once again, the input impedance due to the total field has resistive and reactive parts and is influenced by the finite plate-thickness while the impedance due to the reaction field of eddy currents is purely inductive and independent of plate-thickness.

4.2.3.4 The Dimensionless Parameter, $Q_{\ell t}$

As in section 4.2.2.4, a dimensionless parameter, $Q_{\ell t}$, may

be defined in this case also as the ratio of the moduli of the two impedances, and hence for maximum loss $Q_{\ell t}=1$. From equations (4.42) and (4.45), therefore

$$Q_{\ell t} = \frac{|\dot{Z}_{rytd}|}{|\dot{Z}_{ytd}|} = \frac{\sqrt{2}}{\sqrt{\varepsilon} m t \tanh qg} \tag{4.46}$$

where $\varepsilon$ is given by equation (4.20).

From equations (4.35) and (4.37),

$$\frac{\dot{B}_{ytd}}{\dot{B}_{rytd}} = \frac{-mt\tanh qg(1 + j\tanh\alpha d.\tan\alpha d)}{(1 + j)(\tanh\alpha d + j\tan\alpha d)} \tag{4.47}$$

$$\therefore \frac{|\dot{B}_{ytd}|}{|\dot{B}_{rytd}|} = \frac{mt\tanh qg.\sqrt{\varepsilon}}{\sqrt{2}} = \frac{1}{Q_{\ell t}} \tag{4.48}$$

Thus for maximum loss, $|\dot{B}_{ytd}| = |\dot{B}_{rytd}|$.

For the case of a thick plate, the value of $\varepsilon$, equation (4.20), tends to unity and the definition of $Q_{\ell t}$ is the same as the definition given by Bowden[30]. Putting the value of m, equation (4.46) finally becomes,

$$Q_{\ell t} = \frac{1}{qt\tanh qg}\left[\frac{\mu_o \omega}{\rho \mu_r}\right]^{\frac{1}{2}} \tag{4.49}$$

Once again an optimum half-thickness $d_{mt}$ may be defined for the plate for which maximum loss will be obtained. This is given by,

$$\frac{\cosh 2\alpha d_{mt}}{\cos 2\alpha d_{mt}} = \frac{2 + m^2 \tanh^2 qg}{2 - m^2 \tanh^2 qg} \qquad (4.50)$$

In general, the value of $Q_{\ell t}$ should be as close to unity as possible, and the observations made in connection with equation (4.23) also apply here.

4.2.3.5 Loss in Terms of $Q_{\ell t}$

The loss per unit of surface area from one side of the plate may be obtained in terms of $Q_{\ell t}$ from equations (3.90) and (4.46) as,

$$P_{ytd} = \frac{\hat{K}_z^2 \mu_o \omega \psi_2 \Delta_{\ell t}}{2\sqrt{2} q \sinh qg . \cosh qg} \qquad (4.51)$$

where

$$\Delta_{\ell t} = \frac{1}{Q_{\ell t} + Q_{\ell t}^{-1} + \sqrt{2}\psi_1} \qquad (4.52)$$

and $\psi_1$ and $\psi_2$ are given by equations (4.25a) and (4.25c) respectively. The maximum loss, $P_{ytdm}$, is obtained when $Q_{\ell t}=1$ and the loss expressed at per unit of the maximum value is given by

$$\frac{P_{ytd}}{P_{ytdm}} = \frac{\Delta_{\ell t}}{\Delta_{\ell t}\Big]_{Q_{\ell t}=1}} = \frac{2 + \sqrt{2}\psi_1}{Q_{\ell t} + Q_{\ell t}^{-1} + \sqrt{2}\psi_1} \qquad (4.53)$$

4.2.3.6 Force Densities in Terms of $Q_{\ell t}$

The force densities at the surface from one side is obtained from equations (3.95), (3.96) and (4.46) in terms of $Q_{\ell t}$, as,

$$F_{xtd} = \frac{\hat{K}_z^2 . \mu_o . \alpha . \varepsilon^{\frac{1}{2}} . \Delta_{\ell t}}{\sqrt{2} \sinh qg . \cosh qg} \qquad (4.54)$$

and

$$F_{ytd} = \frac{\hat{K}_z^2 . \mu_o . \alpha^2 . \psi_2 . \Delta_{\ell t}}{\sqrt{2} q \sinh qg . \cosh qg} \qquad (4.55)$$

where $\Delta_{\ell t}$ is given by equation (4.52).

The forces expressed at per unit of their maximum values both have the form given by equation (4.53).

## 4.3 A COMPARATIVE STUDY OF THE TWO POLE-ARRANGEMENTS ON THE BASIS OF LINEAR THEORY

### 4.3.1 General

The equations describing the electromagnetic field quantities in and around a solid-iron plate subjected to travelling magnetic fields from both sides have been obtained in Chapter 3, and earlier in this chapter. Both longitudinal and transverse flux arrangements have been discussed in some detail, but few comparisons have been made. In this section a comparative study of the two different pole-arrangements is undertaken.

The current-density distribution in the plate is essentially different in the two cases and thus forms the basis

of the two particular pole arrangements. So the study begins with a discussion of the current density distribution and goes on to consider the magnetic field strengths and flux densities on the plate surface, the eddy-current losses and reaction fields, the wave impedances and the various inequalities assumed in the study.

### 4.3.2 Current-Density Distribution

Physically the two arrangements of the poles are such that the eddy-current paths are very clearly defined. With the longitudinal flux arrangement, the current density is an even function of depth into the plate, y. Therefore, the currents flowing across one face of the plate find a return path on the other, particularly when the plate is thin. With the transverse flux arrangement, on the other hand, the current density is an odd function of depth into the plate, so that the currents flowing across one face of the plate do not find a return path on the other. The return paths of the currents in the latter case are, therefore, under the adjacent poles on the same surface.

The above observations do not necessarily mean that in the end region all the currents flow across the thickness in the LFA and across the pole (i.e. currents are cross-pole only) in the TFA. In fact their distribution is a little different and this fact has been dealt with in detail in Chapter 7, in connection with the finite-width effects.

It may, however, be noted that the above pattern of current-density distribution is generally true and forms a very basic point of distinction between the two cases. This point of distinction is very pronounced in thin ($d<<1/\alpha$) plates but not so much with a thick ($d>>1/\alpha$) one. This is because with a thick plate, the currents flow so that they are doing so in a semi-infinite plate and the situation in one-half of the plate is unaffected by that in the other half. Consequently, the currents would tend to flow in the now low-resistivity cross-pole paths.

### 4.3.3 The Surface Magnetic Field Strengths

The magnetic field strenths on the surface of the plate (i.e. $y=d$) are given for longitudinal flux arrangement by equations (3.44) and (3.45) and for transverse flux arrangement by equations (3.79) and (3.80). The consideration of the x and y-components reveals someinteresting aspects.

#### 4.3.3.1 The x-Components of the Magnetic Field Strength

When the plate is infinitely thick ($d>>1/\alpha$), equations (3.44) for LFA and (3.79) for TFA both tend to

$$\left|H_{x\ell d\omega}\right| = \left|H_{xtd\omega}\right| = \frac{\sqrt{2}\hat{K}_z}{\cosh qg}\cdot\left[\frac{1}{m^2\tanh^2 qg + 2m\tanh qg + 2}\right]^{\frac{1}{2}} \quad (4.56)$$

which is the same as was obtained by Bowden[30].

When the plate is very thin ($d<<1/\alpha$), equation (3.44) for LFA reduces to,

$$|H_{x\ell do}| \cong \frac{\hat{K}_z}{\cosh qg(1 + \mu_r qd\tanh qg)} \qquad (4.57)$$

and equation (3.79) for TFA becomes,

$$|H_{xtdo}| \cong \frac{2\alpha d\hat{K}_z}{\cosh qg} \cdot \left[\frac{1}{m^2\tanh^2 qg + \frac{8\alpha^3 d^3}{3} m\tanh qg + 4\alpha^2 d^2}\right]^{\frac{1}{2}}$$

Neglecting higher powers of d, this becomes

$$|H_{xtdo}| \cong \frac{2\alpha^2 d\hat{K}_z}{\mu_r q\sinh qg} \qquad (4.58)$$

Thus it can be seen that when the plate is thin, the x-components of the magnetic field strength on the plate surface are quite different. Since d, which is assumed small, appears in the numerator of equation (4.58), therefore, generally, for thin plates the x-component of the surface magnetic field strength under longitudinal flux arrangement is greater than that under transverse flux arrangement. This is to be expected in practice, because with a thin plate more and more flux would tend to go through the low reluctance path across the plate thickness rather than pole-to-pole under the transverse flux arrangement.

### 4.3.3.2 The y-Components of the Magnetic Field Strength

As in the previous case, when the plate is infinitely

thick (i.e. $d \gg 1/\alpha$), the y-components of the magnetic field strength at its surface, given by equations (3.45) and (3.80) for LFA and TFA respectively, reduce to,

$$|H_{y\ell d\infty}| = |H_{ytd\infty}| \cong \frac{\hat{K}_z q}{\alpha \cosh qg}\left[\frac{1}{m^2 \tanh^2 qg + 2m \tanh qg + 2}\right]^{\frac{1}{2}} \tag{4.59}$$

When the plate is thin, however, these two equations tend to, respectively,

$$|H_{y\ell do}| \cong \frac{\hat{K}_z qd}{\cosh qg(1 + \mu_r qd \tanh qg)} \tag{4.60}$$

and

$$|H_{ytdo}| \cong \frac{\hat{K}_z q}{\alpha \cosh qg}\left[\frac{1}{m^2 \tanh^2 qg + \frac{8\alpha^3 d^3}{3} m \tanh qg + 4\alpha^2 d^2}\right]^{\frac{1}{2}}$$

Neglecting $d^2$ and $d^3$ terms in the denominator, this becomes

$$|H_{ytdo}| \cong \frac{\hat{K}_z}{\mu_r \sinh qg} \tag{4.61}$$

As seen from equation (4.61), the y-component of magnetic field strength on the surface of a thin plate under transverse flux arrangement is practically independent of d. But from equation (4.60), the same under longitudinal flux arrangement contains d in the numerator. Thus it may be reasonably concluded that when the plate is thin $|H_{ytd}| > |H_{y\ell d}|$.

These observations are confirmed by the plots of $H_{x\ell d}$ and

and $H_{ytd}$ in Fig. 3.5. This study of the magnetic field strengths on the surface of the plate, thus, helps establish the fact that when the plate is thin, the flux tends to pass through the plate for the transverse flux arrangement more than for the longitudinal flux arrangement.

It may, however, be remembered that, as has been shown in Chapter 3, the magnetic field in the plate is predominantly one dimensional and whatever the observation of this comparative study, the fact remains that the y-component of magnetic field strength on the plate surface is negligibly small compared with the x-component if $\sqrt{2}\alpha >> q$.

### 4.3.4 The Eddy-Current Loss

The eddy current loss per unit of surface area of the plate for the LFA is given by equation (3.55) and for the TFA by equation (3.90). The forms of these equations for the cases of the plate being infinitely thick (i.e. $d >> 1/\alpha$) and very thin (i.e. $d << 1/\alpha$) are given by equations (3.56), (3.57) and (3.91), (3.92) respectively. It may be seen from these equations that for a thick plate the loss in both the cases are equal. For a thin plate, however, the loss in the longitudinal flux arrangement is much smaller (being proportional to $d^3$) than that in the transverse flux arrangement (being proportional to d).

Fig. 4.1 shows the plot of the ratio $P_{y\ell}/P_{yt}$ obtained

from Fig. (3.6) and confirms the above observations. It may be seen in this figure that for thin plates, the power loss under transverse flux arrangement can in fact be many times greater than that under the longitudinal flux arrangement. This observation has been reported before[4]. As the plate thickness increases, the loss in the transverse flux arrangement goes through a minimum while that in the longitudinal flux arrangement goes through a maximum.

In order to obtain the greatest possible power loss, therefore, it is advisable to use the TFA when the plate is thin ($d<<1/\alpha$). For plate half-thicknesses of between 1.5 and 2.5 times the depth of penetration, the LFA is the more effective arrangement. When the plate is infinitely thick ($d>>1/\alpha$), either arrangement of poles may be used. With the provision that one of the two primary members is movable, the same heater may be used for both pole-arrangements.

### 4.3.5 Eddy-Current Reaction Field on Plate Surface

At the plate surface, the ratio of the resultant magnetic field strength to the field of applied current sheet are given for the LFA by equation (4.7) and forthe TFA by equation (4.34). Both are of the form (1+x), and the influence of the eddy-current reaction field in the plate depends on how big or small x is compared with 1.

When the plate is infinitely thick (i.e. $d>>1/\alpha$, $d>>1/q$), both of these equations reduce to,

$$\frac{\dot{H}_{x\ell d\infty}}{\dot{H}_{cx\ell d\infty}} = \frac{\dot{H}_{xtd\infty}}{\dot{H}_{cxtd\infty}} \cong 1 + \mu_r.\tanh qg, \quad m.\tanh qg << 1 \qquad (4.62)$$

Equation (4.62) is the same as was obtained by Bowden[30] for the same study.

It is interesting to note that for a thin plate equation (4.7) reduces to

$$\frac{\dot{H}_{x\ell do}}{\dot{H}_{cx\ell do}} \cong 1 + \mu_r qd.\tanh qg, \quad m.\tanh qg << \alpha d \qquad (4.63)$$

and the equation (4.34) becomes,

$$\frac{\dot{H}_{xtdo}}{\dot{H}_{cxtdo}} \cong 1 + \frac{\mu_r}{qd}.\tanh qg, \quad \begin{cases} m.\tanh qg << \dfrac{2\alpha^3.d^3}{3} \\ \mu_r.qd.\tanh qg << 1 \end{cases} \qquad (4.64)$$

From the equations (4.63) and (4.64), it may be seen that for thin plates, the reaction field of eddy current is very weak under the longitudinal flux arrangement, while under the transverse flux arrangement the reaction field is quite strong. This is to be expected in practice, since with a thin plate, the eddy current paths for the TFA are more restricted than for the LFA.

### 4.3.6 The Impedances at the Plate Surface

Under both the pole arrangements, the input impedances to the plate surface, equations (4.15) and (4.42), are functions of thickness. While for an infinitely thick plate

the impedances are expressed by the same equation, they are quite different when the plate is thin. From equation (4.15) the magnitude $|\dot{Z}_{y\ell do}|$ of the input impedance under LFA for a thin plate ($(d/\delta)<<1$) may be obtained as,

$$|\dot{Z}_{y\ell do}| \cong 2\rho\frac{d}{\delta^2} , \quad (\delta = 1/\alpha) \tag{4.65}$$

From equation (4.42) the same under TFA is obtained as

$$|\dot{Z}_{ytdo}| \cong \frac{\rho}{d} \tag{4.66}$$

Thus it may be seen that for a thin plate, the input impedance for the longitudinal flux arrangement exhibits a reactance-limited nature (being a function of $\delta$), while the input impedance for the transverse flux arrangement exhibits a resistance-limited nature (being independent of $\delta$). This is indicative of the fact that for the LFA, currents flow in opposite directions in the two halves of the plate and the flux is constrained to pass through zero at the plate centre. For the TFA, on the other hand, currents flow in the same direction in the two halves of the plate and are more uniformly distributed, since the flux passes straight through the plate with little or no attenuation. The impedance given by equation (4.66) is, however, larger than that given by equation (4.65).

The impedances due to the reaction fields, equations (4.18) and (4.45), for longitudinal and transverse flux arrangements respectively, are equal and unaffected by the plate thickness.

### 4.3.7 The Parameters $Q_{\ell\ell}$ and $Q_{\ell t}$

The parameters $Q_{\ell\ell}$ and $Q_{\ell t}$, for longitudinal and transverse flux arrangements respectively, both become for an infinitely thick plate ($d>>1/\alpha$)

$$Q_{\ell\ell\infty} = Q_{\ell t\infty} = \frac{\sqrt{2}}{m\pm\tanh qg} \tag{4.67}$$

Equation (4.67) is obtained from equations (4.19) and (4.46) together with equation (4.20), by making d large and , as expected, is the same as the definition of Q obtained by Bowden[30].

For a thin plate ($d<<1/\alpha$), equation (4.19) for longitudinal flux arrangement reduces to

$$Q_{\ell\ell o} \cong \frac{1}{\mu_r qd\pm\tanh qg} \tag{4.68}$$

and equation (4.46) for transverse flux arrangement becomes,

$$Q_{\ell to} \cong \frac{2\alpha^2 d}{\mu_r q\pm\tanh qg} \tag{4.69}$$

For a thin plate, although both $Q_{\ell\ell o}$ and $Q_{\ell to}$ are greater than one, $Q_{\ell\ell o} > Q_{\ell to}$. This shows that for a thin plate, the TFA is better 'tuned' than is the LFA; the current-density distribution in the plate is more uniform in the TFA and this results in higher loss.

### 4.3.8 The Assumed Inequalities

In this chapter, certain assumptions have been made with various equations for the two different pole-arrangements. These assumptions were made to facilitate the understanding of the point. However, these equations contain d, the half-thickness of the plate, and while the assumptions may hold when the plate is infinitely thick, it may not when the plate is thin, and vice versa. Table 4.1 makes a comparative study of these assumptions with a view to pointing out their applicability or otherwise.

The table shows that not only are the assumed inequalities of different form for the two different pole-arrangements, but in most cases, they retain these differences for thick and thin plates. Some of these inequalities are applicable only for certain plate-thicknesses, and thus it is necessary to practice caution when using them.

## 4.4 CONCLUSIONS

The occurrence of eddy currents is always accompanied by its own reaction fields. The work in this chapter clearly defines the conditions of dominance or otherwise of this field. It has been shown that for a given pole-pitch, the reaction field depends on the relative permeability of the plate in which it occurs, the air-gap length and the plate-thickness. For either arrangement of poles, the total effect of the eddy currents have been shown to be represented by an equivalent

TABLE 4.1

AN INVESTIGATION INTO THE NATURE OF ASSUMED INEQUALITIES

| The Assumed Inequality | Equn. No. where occurs | LFA or TFA | Form of the Inequality when | | Comment |
|---|---|---|---|---|---|
| | | | d is large $d \gg 1/\alpha; d \gg 1/q$ | d is small $d \ll 1/\alpha; d \ll 1/q$ | |
| $m_t \tanh qg \ll \tan\alpha d$ | 4.7 | LFA | $m_t \tanh qg \ll 1$ | $m_t \tanh qg \ll \alpha d$ | May not hold when d is small |
| $m_t \tanh qg \ll \tan\alpha d$ | 4.7 | LFA | $m_t \tanh qg \ll \tan\alpha d$ | $m_t \tanh qg \ll \alpha d$ | May not necessarily hold when d is small. When d is large, holds only for values of $\alpha d$ in the range of $\pi/4$ and $3\pi/4$ or any odd multiple of it |
| $\mu_r \tanh qg . \tanh qd \gg 1$ | 4.9a 4.12 4.13a | LFA | $\mu_r \tanh qg \gg 1$ | $\mu_r q_d \tanh qg \gg 1$ | May not hold when d is small |
| $\mu_r \tanh qd \gg \tanh qg$ | 4.13a | LFA | $\mu_r \gg \tanh qg$ | $\mu_r q_d \gg \tanh qg$ | In all probability holds for all thicknesses |
| $m_t \tanh qg \ll \lvert \tanh\alpha d - \tan\alpha d \rvert$ | 4.34 | TFA | $m_t \tanh qg \ll \lvert (1-\tan\alpha d) \rvert$ | $m_t \tanh qg \ll \frac{2\alpha^3 d^3}{3}$ | May hold most of the time when d is large, but not necessarily when d is small |
| $m_t \tanh qg . \tanh\alpha d \ll 1$ | 4.34 | TFA | $m_t \tanh qg \ll 1$ | $\mu_r q_d \tanh qg \ll 1$ | Will hold more when d is small than when it is large |
| $\mu_r \tanh qg \gg \tanh qd$ | 4.36a 4.40 | TFA | $\mu_r \tanh qg \gg 1$ | $\mu_r \tanh qg \gg q_d$ | Holds for all thicknesses |
| $\mu_r \gg \tanh qg . \tanh qd$ | 4.40 | TFA | $\mu_r \gg \tanh qg$ | $\mu_r \gg q_d \tanh qg$ | |

current sheet on the plate surface, whose line density is equal in magnitude to the surface magnetic field strength.

The input impedance on the plate surface has been shown to be dependent on the plate-thickness while the impedance due to the reaction field is not. The ratio of their moduli ($Q_{\ell\ell}$ or $Q_{\ell t}$) has been introduced as an important parameter and it has been shown that the loss and force equations may be obtained in terms of this quantity. The maximum values of loss and force occurs when Q (i.e. $Q_{\ell\ell}$ or $Q_{\ell t}$) becomes unity. For a given set of machine dimensions it has been shown that, a plate thickness, $2d_m$ may be chosen so that maximum power loss occurs.

The comparative study of the longitudinal and transverse flux arrangements help establish the very different patterns of current-density distributions all over the plate. The study of the plate surface magnetic field strengths, the eddy-current losses in the two cases, the reaction fields and the impedances all establish one fact beyond doubt, namely, when the plate is infinitley thick (i.e. $d>>1/\alpha$, $d>>1/q$), the longitudinal and transverse flux arrangements both become the same. This is so because both arrangements reduce to the case of the study of electro-magnetic fields in a semi-infinite plate and because the field equations in one half of the plate are unaffected by the same in the other half. For a finite thickness the equations for the electro-magnetic field qunatities have their own individual forms and these forms

may be drastically different when the plate is thin .

An investigation into the assumed inequalities in this work has shown that while some of these inequalities will hold good for any thickness, others may not. Thus it is necessary to practice caution in using them.

# CHAPTER 5

## ONE-DIMENSIONAL NON-LINEAR THEORIES FOR (a) LONGITUDINAL FLUX ARRANGEMENT AND (b) TRANSVERSE FLUX ARRANGEMENT

### 5.1 INTRODUCTION

It has been shown in Chapters 3 and 4 that the magnetic flux penetration in solid-iron plates, subjected to travelling magnetic fields on both sides, is predominantly one-dimensional if $2\alpha^2 >> q^2$. This is obtained irrespective of the pole arrangements and of the finite plate thickness. In so far as the pole-pitch of the winding is generally much greater than the depth of penetration, the condition $2\alpha^2 >> q^2$ is satisfied.

In this chapter, one-dimensional theories, including magnetic non-linearity, for the penetration of electromagnetic field quantities in solid-iron plate are developed (the air-gap will be included in Chapter 6). Both longitudinal and transverse flux cases have been considered in some detail. A plate of finite thickness is considered from the beginning and its magnetisation curve is represented by the parabolic form $B = aH^b$. Starting from the Maxwell's equations applied to the plate, the B-H relation is substituted at an early stage in the analysis. A new function for the attenuation of magnetic field strength from the surface to the inside of the plate has been assumed and is evaluated by substitution in the final form of diffusion equation. Having obtained the magnetic field strength inside the plate, the current density,

the impedance and the loss density values are obtained.

The work of this chapter is believed to be original.

## 5.2 ONE-DIMENSIONAL ANALYSIS

In the linear analyses of Chapters 3 and 4, it has been shown that the x-component of magnetic field strength, $H_x$, in the plate is very much greater than the y-component, $H_y$, if $2\alpha^2 >> q^2$. This condition implies that only $H_x$ needs to be considered in solid-iron plate for determining the electromagnetic field quantities.

In the non-linear analysis, use of this condition is even more desirable since a two-dimensional analysis is mathematically intractable due to the variation of permeability with magnetic field strength. Since the magnetic field strength decreases with depth inside the iron, the permeability increases with depth, provided the surface magnetic field strength is greater than the value at the knee of the magnetisation curve. Thus, if the condition $2\alpha^2 >> q^2$ holds on the surface, it also holds at any depth. Many previous researchers [30,48,63] have found this to be so.

Since $2\alpha^2 >> q^2$ is obtained in most practical cases, it is assumed in the following analysis that $H_x >> H_y$ and the electromagnetic field distribution in the solid-iron plate is the same as that of a one-dimensional, or plane electromagnetic wave. The non-linear theories developed in this chapter are related (by equating fields at the air-iron interface) to the fields in the air-gap in Chapter 6.

In the following section, Maxwell's equations applied to the model of Fig. 3.1, together with the assumptions, are developed. In sections 5.4 and 5.5, the particular cases of longitudinal and transverse flux arrangements, respectively, are considered.

## 5.3 ELECTROMAGNETIC FIELD EQUATIONS APPLIED TO SOLID-IRON PLATE

### 5.3.1 Analytical Model

The analysis is carried out for a plate of finite thickness, 2d, and the arrangements are shown in Fig. 5.1a and Fig. 5.1b. The arrows indicate the attenuation of x-component of magnetic field strength, $H_x$, over the plate

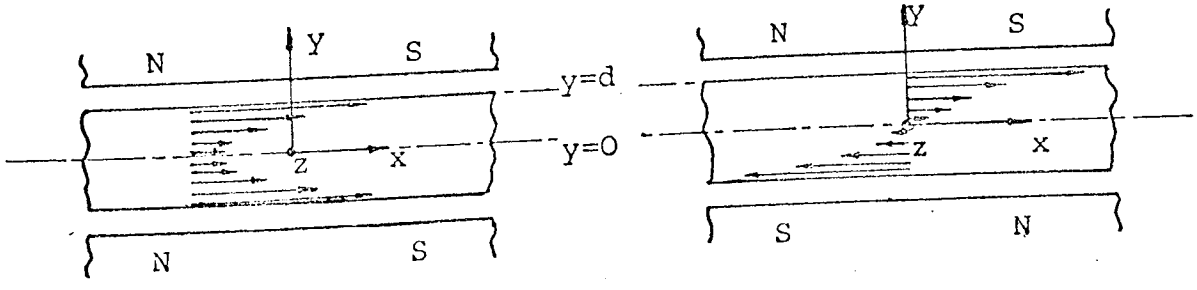


Fig. 5.1a
Longitudinal Flux Case

Fig. 5.1b
Transverse Flux Case

thickness. The two different distributions of $H_x$ over the

thickness is the basic distinction between the two cases*.

The rectangular co-ordinate axes are as shown in Fig. 5.1. The plate is assumed to extend to infinity in both x and z- directions, so that entry and exit- edge and finite width effects may be neglected. Because of the symmetry of the field distribution about the y=0 plane, only one half of the plate need be considered. As has been done in the linear case, (Chapter 3), analysis is carried out for the upper half of the plate i.e. for y varying from 0 to +d.

The magnetic field strength has been considered as having only an x-component and the resulting current density only a z-component. The magnetic field strength and the flux density are taken as being distributed sinusoidally, both in space and time and their peak values are related through the assumed hyperbolic form. Thus, the analysis is basically confined to the fundamental sinusoids of flux density and magnetic field strength, for, a sinusoidal H would not result in a sinusoidal B due to magnetic non-linearity in the plate.

### 5.3.2 The Assumptions

The assumptions made for the theory are discussed in the

---

* It is noted that, in Fig. 5.1b, the nomenclature of "transverse flux" may be somewhat misleading, since the transverse or the y- component of flux has been neglected altogether. However, the term "transverse flux" is retained to differentiate from the term "longitudinal flux" and to maintain continuity throughout this thesis. Justifications for retaining these terms have been given in Chapter 1.

preceding section, but are summarised here for convenience.

(i) The magnetic field strength everywhere in the plate is x-directed only (i.e. $H_y = H_z = 0$).

(ii) The current density everywhere in the plate is z-directed only (i.e. $J_x = J_y = 0$).

(iii) Neither $H_x$ nor $J_z$ vary in the z-direction.

(iv) The magnetic field strength and the resulting flux density are sinusoidally distributed both in space and time.

(v) The peak value of magnetic field strength, $\hat{H}_x$, is related to the peak value of the magnetic flux density, $\hat{B}_x$, by $\hat{B}_x = a\hat{H}_x^{\,b}$ where a and b are constants.

(vi) The plate is composed of homogeneous isotropic material, has a finite thickness and extends to infinity both in the z- and x-directions.

(vii) The surfaces of all regions are smooth, flat and parallel to the z-x plane.

(viii) y = 0 is a plane of symmetry and the analysis may be confined to y = +ve side only.

(ix) Both the primary members and the plate are stationary.

(x) Hysteresis is neglected.

### 5.3.3 Field Equations Applied to the Solid-Iron Plate

Since electromagnetic fields do not vary in the z-direction, from curl H = J, therefore,

$$J_z = -\frac{\partial H_x}{\partial y} = -\frac{dH_x}{dy} \qquad (5.1)$$

From the relation curl $E = -\frac{\partial B}{\partial t}$ and Ohm's Law,

$$\frac{\partial J_z}{\partial y} = -\frac{1}{\rho}.\frac{\partial B_x}{\partial t} \qquad (5.2)$$

From equations (5.1) and (5.2),

$$\frac{d^2 H_x}{dy^2} = \frac{1}{\rho}.\frac{\partial B_x}{\partial t} \qquad (5.3)$$

Equation (5.3) is the diffusion equation governing the penetration of magnetic flux density in iron.

At the surface of the plate i.e. at $y = d$, the fundamental sinusoids of magnetic field strength, $H_{xd}$, and flux density, $B_{xd}$, are given by

$$H_{xd} = \hat{H}_{xd} \cos(\omega t - qx) \qquad (5.4)$$

and

$$B_{xd} = \hat{B}_{xd} \cos(\omega t - qx) \qquad (5.5)$$

where $\hat{H}_{xd}$ and $\hat{B}_{xd}$ are the peak values at the plate surface, $q = \pi/\tau$ and $\tau$ = pole-pitch of primary excitation. Equations (5.4) and (5.5) constitute travelling magnetic fields having a velocity of $\omega/q$ m/s in the x direction.

At any depth in the plate both $B_x$ and $H_x$ attenuate and shift in phase with respect to the surface values and

since hysteresis is neglected, both magnetic field strength and the flux density shift in phase by the same amount. Thus, let $\theta$ represent the phase-shift with depth of both flux density and magnetic field strength, so that at any depth $y' = (y - d)$ i.e. inside the secondary, these quantities are given by

$$H_x = \hat{H}_x \cos(\omega t - qx + \theta) \tag{5.6}$$

and

$$B_x = \hat{B}_x \cos(\omega t - qx + \theta) \tag{5.7}$$

where $\hat{H}_x$ , $\hat{B}_x$ and $\theta$ all are functions of y.

In the analysis so far, the peak value of magnetic flux density is taken as related to the peak value of magnetic field strength by the normal B-H curve. But in order to account analytically for magnetic non-linearity, a mathematical relation between these two quantities are a pre-requisite and in the rest of the analysis, they would be assumed to be related by the equation

$$\hat{B}_x = a\hat{H}_x^{\,b} \tag{5.8}$$

where a and b are constants.

Now, from equations (5.6) and (5.7)

$$\frac{d^2 H_x}{dy^2} = \left[\frac{d^2 \hat{H}_x}{dy^2} - \hat{H}_x \left(\frac{d\theta}{dy}\right)^2\right] \cos(\omega t - qx + \theta) - \left[\hat{H}_x \frac{d^2\theta}{dy^2} + 2\frac{d\hat{H}_x}{dy} \cdot \frac{d\theta}{dy}\right] \times \sin(\omega t - qx + \theta) \tag{5.9}$$

and

$$\frac{\partial B_x}{\partial t} = -\omega B_x \sin(\omega t - qx + \theta) \tag{5.10}$$

But equations (5.9) and (5.10) are related through equation (5.3), so that, equating the co-efficients of 'sin' and 'cos' terms from both sides

$$\frac{d^2\hat{H}_x}{dy^2} - \hat{H}_x\left(\frac{d\theta}{dy}\right)^2 = 0 \qquad (5.11)$$

and

$$\hat{H}_x \cdot \frac{d^2\theta}{dy^2} + 2\frac{d\hat{H}_x}{dy} \cdot \frac{d\theta}{dy} = \frac{\omega}{\rho} \cdot \hat{B}_x \qquad (5.12)$$

From equation (5.11)

$$\frac{d\theta}{dy} = \left(\frac{1}{\hat{H}_x} \cdot \frac{d^2\hat{H}_x}{dy^2}\right)^{\frac{1}{2}} \qquad (5.13)$$

From equations (5.12) and (5.13) and using the relation of equation (5.8),

$$\frac{\omega a}{\rho} \cdot \hat{H}_x^{(b+1)} = \frac{d}{dy}\left[\hat{H}_x^{3/2}\left(\frac{d^2\hat{H}_x}{dy^2}\right)^{\frac{1}{2}}\right] \qquad (5.14)$$

Equation (5.14) is the final form of the differential equation concerning $\hat{H}_x$ and y. Clearly a mathematical solution of this differential equation is intractable, and hence a particular function regarding attenuation of $\hat{H}_x$ from the plate surface to inside the iron has to be considered.

### 5.3.4 A Solution to the Field Equation

Bowden[30] obtained equation (5.14) and considered a

solution of the form $\hat{H}_x = \hat{H}_{xd}(1+hy')^r$, $hy' < -1$, where h and r were constants and y' varied from zero at the surface of the plate increasing (negatively) inside, i.e. $y' = y-d$ in the present model. Bowden considered the case of a semi-inifinite slab and, essentially, one-sided excitation and hence the use of the above function was appropriate. But in the present case because of the double-sided arrangement and of the finite thickness of the plate, there are further restrictions to the solution.

In both longitudinal and transverse flux cases, $\hat{H}_x$ has the maximum value at the plate surface and decreases inside the plate. In the case of longitudinal flux arrangement, $\hat{H}_x$ reaches a minimum at the centre plane, i.e. at y=0, and then increases again as shown in Fig. 5.1a and curve (i) of Fig. 5.2. In other words $\hat{H}_x$ is an even function of y, and since $\hat{H}_x$ is continuous inside the plate,

$$\frac{d\hat{H}_{x\ell}}{dy} = 0 \quad \text{at} \quad y=0 \tag{5.15}$$

(The suffix $\ell$ signifies longitudinal flux arrangement).

Similarly, for transverse flux arrangement, $\hat{H}_x$ is an odd function of y inside the plate (Fig. 5.1b and curve (ii) of Fig. 5.2) and the boundary condition at the plate centre is given by

$$\hat{H}_{xt} = 0 \quad \text{at} \quad y=0 \tag{5.16}$$

(The suffix t signifies transverse flux arrangement).

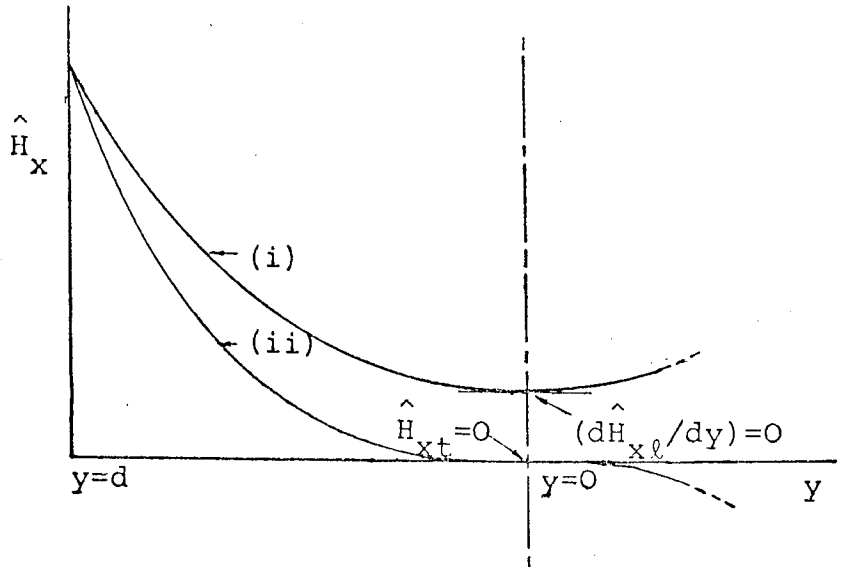


Fig. 5.2 Assumed attenuation of $\hat{H}_x$ from the surface to the inside of the plate. Curve (i):Longitudinal flux arrangement, Curve (ii): Transverse flux arrangement.

To satisfy the equations (5.15) and (5.16), the use of Bowden's function for $\hat{H}_x$ gives h = 1/d. This is an extremely undesirable restriction for three reasons:

(i) h = 1/d implies that h can have only one value determined by the plate thickness, whereas in a practical situation h should be a function of surface magnetic field strength.

(ii) Conversely, d=1/h means that a solution may be obtained only for a plate thickness equal to 2/h, whereas a solution must be obtained for the general case of a plate thickness equal to 2d without any restrictions.

(iii) Use of h = 1/d specifies that $\hat{H}_x$ must be zero at the plate centre. While this is the case in transverse flux arrangement, this may not necessarily be so in longitudinal flux arrangement.

Thus a new function must be found as a solution to equation (5.14) in order to satisfy both conditions given by (5.15) and (5.16).

Allowing for the attenuation of $\hat{H}_x$ with depth a solution of the form*

$$\hat{H}_x = \hat{H}_{xd}(1 + hy')^r(1 + fy')^s, \quad hy'<-1, \quad fy'<-1 \qquad (5.17)$$

where h,r and f,s are positive constants and y' = (y-d), was found to satisfy the boundary conditions at y=0.

From y' = (y-d), dy'=dy, so that differentiating with respect to y' is the same as differentiating with respect to y.

In the following sections longitudinal and transverse flux cases are considered and equation (5.17) is used as a solution in both cases.

---

* Probably a more general solution would have the form

$$\hat{H}_x = \hat{H}_{xd} \prod_{i=1}^{\infty} (1 + h_i y')^{r_i}, \qquad h_i y'<-1 \qquad (5.17a)$$

This equation would definitely give a more accurate solution, but is not easily ammenable to analytic solution. In fact very little is gained at the expense of mounting complexity. Equation (5.17), while being simple gives sufficiently accurate results.

## 5.4 A NON-LINEAR THEORY FOR LONGITUDINAL FLUX ARRANGEMENT

### 5.4.1 Equation for Magnetic Field Strength in the Plate

The longitudinal flux arrangement, in which the corresponding poles on the two sides of the plate are of the same instantaneous polarity, has been shown in Fig. 5.1a and the resulting magnetic field distribution in curve (i) of Fig. 5.2. A further subscript $\ell$ is used to represent the longitudinal flux quantities, so that equation (5.17) may be written as

$$\hat{H}_{x\ell} = \hat{H}_{x\ell d}(1 + h_\ell y')^{r_\ell}(1 + f_\ell y')^{s_\ell},\ h_\ell y' < -1,\ f_\ell y' < -1 \qquad (5.18)$$

According to the condition of equation (5.15), therefore

$$\hat{H}_{x\ell d}(1-h_\ell d)^{r_\ell - 1}(1-f_\ell d)^{s_\ell - 1}\{s_\ell f_\ell (1-h_\ell d) + r_\ell h_\ell (1-f_\ell d)\} = 0 \qquad (5.19)$$

Since neither $h_\ell$ or $f_\ell$ can be equal to $1/d$ for reasons given in section 5.3.4, equation (5.19), therefore, implies that

$$s_\ell f_\ell + r_\ell h_\ell = f_\ell h_\ell d(s_\ell + r_\ell) \qquad (5.20)^*$$

---

* Equation (5.20) shows that when $d$ becomes large (i.e. plate tends to a semi-infinite one)

$$f_\ell h_\ell (r_\ell + s_\ell) = \frac{1}{d}(s_\ell f_\ell + r_\ell h_\ell) \to 0$$

so that either $f_\ell \to 0$ or $h_\ell \to 0$. Letting $f_\ell \to 0$, equation (5.18) tends to

$$\hat{H}_{x\ell} = \hat{H}_{x\ell d}(1 + h_\ell y')^{r_\ell}$$

which is of the same form of equation as used by Bowden.

Equation (5.18) may be substituted in equation (5.14) and using the condition of equation (5.20), this results in an identity, from which

$$\hat{H}^{2}_{x\ell d}(f_\ell h_\ell)(s_\ell+r_\ell)^{\frac{1}{2}}(s_\ell+r_\ell-1)^{\frac{1}{2}}(1-h_\ell d)(1-f_\ell d)3$$

$$(1+h_\ell y')^{(2r_\ell-2)}(1+f_\ell y')^{(2s_\ell-2)} = \frac{\omega a}{\rho}.\hat{H}^{(b+1)}_{x\ell d}(1+h_\ell y')^{r_\ell(b+1)}(1+f_\ell y')^{s_\ell(b+1)} \qquad (5.21)$$

Both sides of equation (5.21) are of the form $K(1+h_\ell y')^{p}(1+f_\ell y')^{q}$ so that the indices and the constant terms may be equated. Therefore, $2r_\ell-2 = r_\ell(b+1)$ and $2s_\ell-2 = s_\ell(b+1)$, so that

$$r_\ell = s_\ell = \frac{2}{(1-b)} = \beta_\ell, \text{ say} \qquad (5.22)$$

and

$$\hat{H}^{2}_{x\ell d} f_\ell h_\ell (s_\ell+r_\ell)^{\frac{1}{2}}(s_\ell+r_\ell-1)^{\frac{1}{2}}(1-h_\ell d)(1-f_\ell d)\ 3$$

$$= \frac{\omega a}{\rho}.\hat{H}^{b+1}_{x\ell d}$$

which, using equation (5.22), becomes

$$f_\ell h_\ell (1-h_\ell d)(1-f_\ell d) = \alpha_\ell^{2} \qquad (5.23)$$

where

$$\alpha_\ell^{2} = \alpha^{2}_{x\ell d}.k^{2}_{b\ell} \qquad (5.24)$$

and

$$\alpha^2_{x\ell d} = \frac{\omega a \hat{H}^{(b-1)}_{x\ell d}}{2\rho} \qquad (5.25)$$

$$k^2_{b\ell} = \frac{(1-b)}{3(3+b)^{\frac{1}{2}}} \qquad (5.25)$$

Using equation (5.22), equation (5.20) gives

$$f_\ell = \frac{-h_\ell}{1-2h_\ell d} \qquad (5.27)$$

Substituting the value of $f_\ell$ from equation (5.27) into (5.23) and taking magnitudes only, a quadratic equation in $h_\ell$ is obtained, the solution of which is

$$h_\ell = \frac{\lambda}{2d} \qquad (5.28)$$

where

$$\lambda = (1+2\alpha_\ell d) \pm (1+4\alpha^2_\ell d^2)^{\frac{1}{2}} \qquad (5.29a)$$

Taking the positive sign in equation (5.29a) it is seen that when d is large, $\lambda \cong 4\alpha_\ell d$ and therefore $h_\ell \to 2\alpha_\ell$ and $f_\ell \to \frac{1}{2d}$ ; and when d is small $\lambda \cong 2(1+\alpha_\ell d)$, i.e. $h_\ell \to 1/d$ and $f_\ell \to 1/d$.

Taking the negative sign in equation (5.29a), it is seen that when d is large, $\lambda \cong 0$, so that $h_\ell \to f_\ell \to 0$; and when d is small, $\lambda \cong 2\alpha_\ell d$, i.e. $h_\ell \to \alpha_\ell$ and $f_\ell \to \frac{-\alpha_\ell}{1-2\alpha_\ell d} \to -\alpha_\ell$.

Thus only the positive sign in equation (5.29a) is of importance, so that

$$\lambda = (1+2\alpha_\ell d) + (1+4\alpha^2_\ell d^2)^{\frac{1}{2}} \qquad (5.29\ )$$

From equations (5.29), (5.28) and (5.27)

$$f_\ell = \frac{\lambda}{2d(\lambda-1)} \tag{5.30}$$

Equation (5.18) for the peak magnetic field strength can now be written as

$$\hat{H}_{x\ell} = \hat{H}_{x\ell d}\left[\{1+\frac{\lambda}{2d}\,y'\}\{1+\frac{\lambda}{2d(\lambda-1)}\,y'\}\right]^{\beta_\ell} \tag{5.31}$$

The phase angle $\theta_\ell$ is obtained by substituting equation (5.31) in equation (5.13) and integrating with respect to y. The constant of integration is determined from the boundary condition that at the surface of the plate (i.e. at y'=0), $\theta_\ell$ =0. Thus,

$$\theta_\ell = \gamma_\ell \ln\left[(1+\frac{\lambda}{2d}\,y')\{1+\frac{\lambda}{2d(\lambda-1)}\,y'\}\right] \tag{5.32}$$

where

$$\gamma_\ell = \pm\ \frac{\sqrt{2(1+b)}}{(1-b)} \tag{5.33}$$

Substituting equations (5.31) and (5.33) in equation (5.6), the value of magnetic field strength, $H_{x\ell}$, inside the plate is given by

$$H_{x\ell} = \hat{H}_{x\ell d}\left[(1+\frac{\lambda}{2d}y')\{1+\frac{\lambda}{2d(\lambda-1)}y'\}\right]^{\beta_\ell}\cos$$

$$\left[\omega t - qx + \gamma_\ell \ln\{(1+\frac{\lambda}{2d}\,y')(1+\frac{\lambda}{2d(\lambda-1)}\,y')\}\right] \tag{5.34}$$

or

$$H_{x\ell} = \text{Re } \hat{H}_{x\ell d}\left[\left(1+\frac{\lambda}{2d}y'\right)\left\{1+\frac{\lambda}{2d(\lambda-1)}y'\right\}\right]^{\beta_\ell+j\gamma_\ell}\exp j(\omega t-qx) \qquad (5.35)$$

## 5.4.2 Limiting Depth of Penetration

From equation (5.35) it may be seen that $H_{x\ell}$ becomes zero at $y_1' = -\frac{2d}{\lambda}$ and also at $y_2' = -\frac{2d(\lambda-1)}{\lambda}$. For a thick plate $\lambda \to 4\alpha_\ell d$ and the $y_1'$ tends to $-\frac{1}{2\alpha_\ell}$ while $y_2'$ tends to $-2d$ and hence only $y' = -\frac{2d}{\lambda}$ is applicable so far as the determination of a limiting penetration depth is concerned. $y_1'$ is also smaller than $y_2'$; for a thick plate no magnetic field strength exists beyond $y=y_1'$, so that $y_2'$ has no signficiance. For a thin plate, however, $y_2'$ is effective in modifying the attenuation and satisfying equation (5.15).

It may, however, be noted that $H_x$ does not necessarily go to zero inside the plate (curve (i) of Fig. 5.2) and thus the concept of a limiting penetration depth may only be retained with particular regards to plate-thickness, the surface magnetic field strength, the frequency and the resistivity and magnetisation curve of the material of the plate.

## 5.4.3 The Current-Density Distribution and the Impedance Angle

The distribution of current density inside the plate may be obtained from equations (5.1) and (5.35) and is given by,

$$J_{z\ell}=-\mathrm{Re}\hat{H}_{x\ell d}\frac{\lambda^2 y(\beta_\ell+j\gamma_\ell)}{2d^2(\lambda-1)}\left[(1+\frac{\lambda y'}{2d})\{1+\frac{\lambda y'}{2d(\lambda-1)}\}\right]^{\beta_\ell-1+j\gamma_\ell}\mathrm{expj}(\omega t-qx) \tag{5.36}$$

At the surface of the plate, y=d and y'=0, so that the amplitude of the surface current density is given by,

$$\hat{J}_{z\ell d}=\frac{\hat{H}_{x\ell d}\lambda^2(\beta_\ell+j\gamma_\ell)}{2d(\lambda-1)} \tag{5.37a}$$

i.e.

$$\hat{J}_{z\ell d}=\frac{\hat{H}_{x\ell d}\lambda^2 R_\ell}{2d(\lambda-1)}\ \angle\ \phi_\ell \tag{5.37}$$

where

$$R_\ell=(\beta_\ell^2+\gamma_\ell^2)^{\frac{1}{2}}=\frac{\sqrt{2(3+b)}}{(1-b)} \tag{5.38}$$

and

$$\tan\phi_\ell=\frac{\gamma_\ell}{\beta_\ell}=\left(\frac{1+b}{2}\right)^{\frac{1}{2}} \tag{5.39}$$

$\phi_\ell$, being the angle between the surface values of magnetic field strength and the current density, may be termed impedance angle. As may be seen from equation (5.39) this angle tends to $\pi/4$ for linear case, i.e. when b=1.

### 5.4.4 The Impedance of the Solid-Iron Plate

The impedance of the solid-iron plate is given by

$$Z_{y\ell}=\frac{E_{z\ell}}{H_{x\ell}}=\frac{\rho J_{z\ell}}{H_{x\ell}}$$

Using equations (5.35) and (5.36), this becomes

$$Z_{y\ell} = \frac{\rho\lambda^2 R_\ell y}{2d^2(\lambda-1)(1+\frac{\lambda y'}{2d})\{1+\frac{\lambda y'}{2d(\lambda-1)}\}} \angle \phi_\ell \qquad (5.40)$$

At the surface of the plate y=d and y'=0 and the magnitude of the impedance at the surface is given by

$$|Z_{y\ell d}| = \frac{\rho\lambda^2 R_\ell}{2d(\lambda-1)} \qquad (5.41)$$

The impedance increases with depth inside the plate tending to $\infty$ at $y' = -\frac{2d}{\lambda}$, the limiting depth of penetration.

## 5.4.5 Eddy-Current Loss in the Plate

The mean power per unit area from any one side into the solid iron at any depth is given by the complex Poynting vector, $\mathcal{P}_{y\ell}$, as

$$\mathcal{P}_{y\ell} = -\tfrac{1}{2}\mathrm{Re}(E_{z\ell} \times H_{x\ell}^*) \qquad (5.42a)$$

where $H_{x\ell}^*$ denotes complex conjugate of $H_{x\ell}$.

Substituting for $H_{x\ell}$ and $E_{z\ell}(=\rho J_{z\ell})$ from equations (5.35) and (5.36), respectively,

$$\mathcal{P}_{y\ell} = \frac{\hat{H}_{x\ell d}^2 \rho\beta_\ell\lambda^2 y}{4d^2(\lambda-1)}\left[(1+\frac{\lambda y'}{2d})\{1+\frac{\lambda y'}{2d(\lambda-1)}\}\right]^{2\beta_\ell-1} \qquad (5.42)$$

The total loss per unit of surface area due to excitation from any one side only is given by the power crossing the air-gap and may be obtained by putting y=d i.e. y'=0 in equation (5.42). This is given by

$$\mathcal{P}_{y\ell d} = \mathcal{P}_{y\ell}\Big]_{y=d} = \frac{\hat{H}^2_{x\ell d}\rho\beta_\ell\lambda^2}{4d(\lambda-1)} \qquad (5.43)$$

When the plate is thick, i.e. d is large, $\lambda$ is large and tends to $4\alpha d$, so that equation (5.43) becomes

$$\mathcal{P}_{y\ell d\infty} \cong \hat{H}^2_{x\ell d}\rho\beta_\ell\alpha_\ell \qquad (5.44)$$

Using equations (5.24) and (5.25) for $\alpha_\ell$ it can be seen that the true exponent of $\hat{H}_{x\ell d}$ in equation (5.44) is (b+3)/2. Other researchers [30,40] have also found it to be so.

When d is very small $\lambda \to 2(1+\alpha_\ell d) \to 2$ and equation (5.43) becomes

$$\mathcal{P}_{y\ell do} \cong \frac{\hat{H}^2_{x\ell d}\rho\beta_\ell}{d} \qquad (5.45)$$

Here the true exponent of $\hat{H}_{x\ell d}$ is 2. Also, compared with equation (5.44), it may be seen from equation (5.45) that with thin plates higher loss densities may be obtained.

Thus it may be concluded that in transition from electrically thin to thick plates, not only does the loss

density go on decreasing,but also the exponent of $\hat{H}_{x\ell d}$ reduces from approximately 2 to (b+3)/2. In general, therefore, the exponent of $\hat{H}_{x\ell d}$ in the expression of loss density is between 2 and (b+3)/2.

Fig. 5.3 shows the plot of $P_{y\ell d}$ as a function of $\hat{H}_{x\ell d}$ for various thicknesses.

## 5.5 A NON-LINEAR THEORY FOR TRANSVERSE FLUX ARRANGEMENT

### 5.5.1 Equation for Magnetic Field Strength in the Plate

The transverse flux arrangement has been shown in Fig.5.1b and the resulting distribution of magnetic field strength inside the plate has been shown by curve (ii) of Fig. 5.2 . A further subscript t is used to represent the transverse flux quantities. Equation (5.17) for transverse flux case may be written as

$$\hat{H}_{xt} = \hat{H}_{xtd}(1+h_t y')^{r_t}(1+f_t y')^{s_t}, \quad h_t y'<-1, \quad f_t y'<-1 \tag{5.46}$$

According to the condition of equation (5.16), therefore,

$$\hat{H}_{xtd}(1-h_t d)^{r_t}(1-f_t d)^{s_t} = 0 \tag{5.47}$$

$r_t$ and $s_t$ are both positive quantities, since a negative value for them would mean (Equation (5.46)) that $H_{xt}$ increases with depth inside the plate, which cannot be true. Equation (5.47), therefore, implies that either $h_t = 1/d$

or $f_t = 1/d$. Let $f_t = 1/d^*$, so that equation (5.46) reduces to

$$\hat{H}_{xt} = \hat{H}_{xtd}\,(1+h_t y')^{r_t}(y/d)^{s_t} \qquad (5.48)$$

Equation (5.48) may now be substituted in equation (5.14) and this finally results in an identity, from which

$$\frac{\hat{H}^2_{xtd}}{d^2}\, s_t^{\frac{1}{2}}(s_t-1)^{\frac{1}{2}}(2s_t-1)(1-h_t d)^2 (1+h_t y')^{(2r_t-2)} (y/d)^{(2s_t-2)}$$

$$= \frac{\omega a}{\rho}.\hat{H}^{(b+1)}_{xtd}\; (1+h_t y')^{r_t(b+1)} (y/d)^{s_t(b+1)} \qquad (5.49)$$

Both sides of this equation are of the form $K(1+h_t y')^m (y/d)^n$ so that the indices and the constant terms may be equated. Thus,

$(2r_t-2)=r_t(b+1)$ and $(2s_t-2)=s_t(b+1)$, so that

$$r_t = s_t = \frac{2}{(1-b)} = \beta_t, \text{ say,} \qquad (5.50)$$

and

$$\frac{\hat{H}^2_{xtd}}{d^2}.s_t^{\frac{1}{2}}(s_t-1)^{\frac{1}{2}}(2s_t-1)(1-h_t d)^2 = \frac{\omega a}{\rho}.\hat{H}^{(b+1)}_{xtd}$$

which, using equation (5.50), becomes

---

* When d is large, $f_t \to 0$ and equation (5.46) reduces to $H_{xt}=\hat{H}_{xtd}(1+h_t y')^{r_t}$ which is of the same form as used by Bowden.

$$(1-h_t d)^2 = \alpha_t^2 . d^2 \tag{5.51}$$

where

$$\alpha_t^2 = \alpha_{xtd}^2 \cdot K_{bt}^2 \tag{5.52}$$

and

$$\alpha_{xtd}^2 = \frac{\omega a \hat{H}_{xtd}^{(b-1)}}{2\rho} \tag{5.53}$$

and

$$K_{bt}^2 = \frac{\sqrt{2}(1-b)^2}{(3+b)(1+b)^{\frac{1}{2}}} \tag{5.54}$$

From equation (5.51),

$$h_t = \frac{(1 \pm \alpha_t d)}{d} \tag{5.55a}$$

$y' = (y-d)$ varies from 0 to $-d$ inside the plate and hence is always negative inside the plate. Thus, for $(1+h_t y')$ to decrease with depth $h_t$ must always be positive. If $h_t = \frac{1-\alpha_t d}{d} = \frac{1}{d} - \alpha_t$, then for large values of d, $h_t$ becomes negative. Hence

$$h_t = \frac{(1+\alpha_t d)}{d} \tag{5.55}$$

Equation (5.48) now becomes

$$\hat{H}_{xt} = \hat{H}_{xtd}\left[\{1+(1+\alpha_t d)y'/d\}y/d\right]^{\beta_t} \tag{5.56}$$

The phase angle $\theta_t$ is obtained by substituting equation (5.56) in equation (5.13) and integrating with respect to y. The constant of integration may be obtained from the boundary condition that at y=d (i.e. y'=0), $\theta_t$=0. Thus

$$\theta_t = \gamma_t \ln\left[\{1+(1+\alpha_t d)y'/d\}y/d\right] \tag{5.57}$$

where

$$\gamma_t = \pm \frac{\sqrt{2(1+b)}}{(1-b)} \tag{5.58}$$

Thus, the complete solution for the magnetic field strength inside the secondary is given by

$$H_{xt} = \hat{H}_{xtd}\left[\{1+(1+\alpha_t d)y'/d\}y/d\right]^{\beta_t} \cos\left[\omega t - qx + \gamma_t \ln\{1+(1+\alpha_t d)y'/d\}y/d\right] \tag{5.59}$$

or

$$H_{xt} = \text{Re}\ \hat{H}_{xtd}\left[\{1+(1+\alpha_t d)y'/d\}y/d\right]^{\beta_t + j\gamma_t} \exp j(\omega t - qx) \tag{5.60}$$

## 5.5.2 Limiting Depth of Penetration

From equation (5.56), a value of y' may be defined as

$$y' = -\delta_t = \frac{-d}{1+\alpha_t d} \tag{5.61}*$$

when $H_{xt}$ becomes zero. It may, thus, be termed as a 'limiting

* As may be expected, equation (5.61) reduces to Bowden's definition of a limiting depth of penetration when d is large.

depth of penetration'. Clearly, the value of y' given by equation (5.61) is less than -d, so that $H_{xt}$, in fact becomes zero at a depth less than the half-thickness of the plate and remains so equally beyond in the other half of the plate (as the symmetry requires). The depth at which $H_{xt}$ becomes zero is determined by $\alpha_t$, i.e. by such quantities as, the surface magnetic field strength, the frequency, the resistivity and the magnetisation curve of the material.

### 5.5.3 The Current-Density Distribution and the Impedance Angle

The current-density distribution, $J_{zt}$, inside the plate may be obtained from equations (5.1) and (5.60) as

$$J_{zt}=-\mathrm{Re}\hat{H}_{xtd}(\beta_t+j\gamma_t)\frac{1}{d}\{2(1+\alpha_t d)y/d-\alpha_t d\}\left[\{1+(1+\alpha_t d)y'/d\}y/d\right]^{\beta_t-1+j\gamma_t} \tag{5.62}$$

At the surface of the plate y=d and y'=0 and the amplitude of the surface current density is given by

$$\hat{J}_{ztd} = (\beta_t+j\gamma_t)(\frac{2}{d} + \alpha_t)\hat{H}_{xtd} \tag{5.63a}$$

$$\hat{J}_{ztd} = R_t(\frac{2}{d} + \alpha_t)\hat{H}_{xtd}\,\angle\phi_t \tag{5.63}$$

where

$$R_t = (\beta_t^{\,2}+\gamma_t^{\,2})^{\frac{1}{2}} = \frac{\sqrt{2(3+b)}}{(1-b)} \tag{5.64}$$

and

$$\tan \phi_t = \frac{\gamma_t}{\beta_t} = \left(\frac{1+b}{2}\right)^{\frac{1}{2}} \qquad (5.65)$$

$\phi_t$ is the angle between the surface values of magnetic field strength and the current density and, as such, may be termed the impedance angle. As may be seen from equation (5.65), the angle becomes $\pi/4$ for the case of linear magnetisation. It may be seen that

$$\cos \phi_t = \frac{\beta_t}{R_t} = \left(\frac{2}{3+b}\right)^{\frac{1}{2}} \qquad (5.66)$$

and

$$\sin \phi_t = \frac{\gamma_t}{R_t} = \left(\frac{1+b}{3+b}\right)^{\frac{1}{2}} \qquad (5.67)$$

### 5.5.4 The Impedance of the Solid-Iron Plate

The impedance of the solid-iron plate, $Z_{yt}$, is given by

$$Z_{yt} = \frac{E_{zt}}{H_{xt}} = \frac{\rho J_{zt}}{H_{xt}}$$

which, using the equation (5.62) and (5.60), becomes

$$Z_{yt} = \frac{\rho . R_t . \{2(1+\alpha_t d)y/d - \alpha_t d\}}{\{1+(1+\alpha_t d)y'/d\}y} \angle \phi_t \qquad (5.68)$$

At the surface of the plate y=d and y'=0 and the magnitude of the surface impedance, $|Z_{ytd}|$, is given by

$$|Z_{ytd}| = \rho . R_t . \left(\frac{2}{d} + \alpha_t\right) \qquad (5.69)$$

The impedance increases inside the plate, tending to $\infty$ at $y' = \frac{-d}{1+\alpha_t d}$, the limiting depth of penetration.

5.5.5 Eddy-Current Loss in Solid Iron

The mean power flow per unit area from any one side into the solid iron at any depth is given by the complex Poynting vector, $\mathcal{P}_{yt}$,

$$\mathcal{P}_{yt} = -\frac{1}{2} \mathrm{Re}(E_{zt} \times H_{xt}^*) \tag{5.70}$$

where $H_{xt}^*$ is the complex conjugate of $H_{xt}$.

Substituting for $E_{zt}$ $(=\rho J_{zt})$ and $H_{xt}$ from equation (5.62) and (5.60), respectively,

$$\mathcal{P}_{yt} = \frac{1}{2} \cdot \frac{\hat{H}_{xtd}^2}{d} \rho\beta_t \{2(1+\alpha_t d)y/d - \alpha_t d\} [\{1+(1+\alpha_t d)y'/d\}y/d]^{2\beta_t - 1} \tag{5.71}$$

The total loss per unit of surface area due to excitation from any one side only, is given by the power crossing the air-gap and may be obtained by putting y=d in equation (5.71). This is given by

$$\mathcal{P}_{ytd} = \mathcal{P}_{yt}\Big]_{y=d} = \frac{1}{2} \cdot \hat{H}_{xtd}^2 \cdot \rho\beta_t \left(\frac{2}{d} + \alpha_t\right) \tag{5.72}$$

When d is large, (i.e. $d >> \frac{2}{\alpha_t}$), equation (5.72) becomes

$$\mathcal{P}_{ytd\infty} \cong \frac{1}{2} \cdot \hat{H}_{xtd}^2 \rho\beta_t \alpha_t \tag{5.73}$$

Using equation (5.52) and (5.53), it can be seen that the

true exponent of $\hat{H}_{xtd}$ in equation (5.73) is $\frac{(b+3)}{2}$ .

When d is small (i.e. $d<<\frac{2}{\alpha_t}$), equation (5.72) becomes

$$P_{ytdo} \cong \frac{\hat{H}^2_{xtd}\rho.\beta_t}{d} \qquad (5.74)$$

Here the true exponent of $\hat{H}_{xtd}$ is 2. Also the loss density given by equation (5.74) is higher than that given by equation (5.72).

Thus for transverse flux arrangement, the true exponent of $\hat{H}_{xtd}$ in the loss equation is between 2 and (b+3)/2. When the plate-thickness is small, the exponent tends to 2, while for a thick plate, it tends to (b+3)/2.

Fig. 5.4 shows the plot of $P_{ytd}$ as a function of $\hat{H}_{xtd}$ for various thicknesses of the plate.

## 5.6 CONCLUSIONS

In this chapter, one-dimensional non-linear theories have been developed for the penetration of electromagnetic field quantities in a solid-iron plate under both longitudinal and transverse flux arrangements. The variations of these quantities inside the plate depend on the surface magnetic field strength, the frequency of the current sheet excitation, the resistivity and the magnetisation curve of the material.

A salient feature of the work of this chapter is that a plate of finite thickness was considered from the beginning. This together with the two pole-arrangements give rise

to special boundary conditions at the centre of the plate-thickness. This necessitated the introduction of a new function (equation (5.17)) as a solution of the diffusion equation. The resulting expressions obtained for electromagnetic field quantities clearly show how these are influenced by finite plate thickness. The expressions for an infinitely thick plate are obtained as a special case by letting the thickness become very large.

It has been shown that the magnetic field strength for both arrangements of the poles are confined mainly near the plate surfaces. For both pole arrangements the impedance angles are independent of plate-thickness and are functions of the magnetisation curve of the material of the plate. In both cases, the impedance of solid-iron plate increases from the surface inwards, although the natures of their variation are different.

The loss densities obtained in both cases are of the same general nature, being higher for thin plates than thick, and the exponent of the surface magnetic field strength in the loss expression being between 2 and (b+3)/2. It has been shown that for thin plates, the exponent tends to 2, while for thick plates, the exponent tends to (b+3)/2.

# CHAPTER 6

# TWO-DIMENSIONAL ANALYSIS INCLUDING MAGNETIC NON-LINEARITY

## 6.1 INTRODUCTION

In Chapter 5, non-linear one-dimensional theories were developed for the penetration of electromagnetic field quantities in a solid-iron plate; fields in the air-gap were not included in the analysis.

In the air-gap, linear theory applies and the fields are essentially two dimensional. In this chapter, field equations in the air-gap are obtained and related to the quantities defined in Chapter 5 in terms of the surface current density. It is assumed that the current density on the plate surface is due totally to one-dimensional non-linear theory, and is equated to that obtained considering two-dimensional fields in the air-gap.

The magnetic field strength on the surface of the plate is obtained in terms of the primary current sheet. A non-dimensional design parameter Q is introduced as the ratio of the wave impedances at the surface of the plate. The magnetic field intensity at the surface of the plate and the loss per unit of surface area of the plate are obtained in terms of this parameter. By letting Q become unity the maximum value of loss is obtained. Expressions have also been obtained for force density and the flux per pole, and these are also given in terms of the same parameter. Both longitudinal and transverse

flux arrangements have been considered in detail.

In the concluding section different aspects of the two different pole-arrangements are discussed. These include Q, the plate-surface values of magnetic field strength, the current densities, the impedances, the losses/area, the flux/pole, and the forces developed.

## 6.2 FIELDS IN THE AIR-GAP

As has been shown in Section 3.3.2, Laplace's equation in two dimensions for the linear air-gap region (Figure 3.1) is given by

$$\nabla^2 A = 0 \tag{6.1}$$

where $\nabla^2 = \frac{\partial^2}{\partial x^2} + \frac{\partial^2}{\partial y^2}$ is the Laplacian operator and A is the vector potential.

The solution of equation (6.1) is given by

$$\dot{A}_2 = \{C_2 \exp(qy) + D_2 \exp(-qy)\} \exp(-jqx) \tag{6.2}$$

where the subscript 2 indicates air-gap quantities and $q = \frac{\pi}{\tau}$, $\tau$ being the pole-pitch of the spatial current variation.

Equation (6.2) describes the magnetic field components in the air-gap region once the constants $C_2$ and $D_2$ are known. The x and y-components of the magnetic field strength would then be given by

$$\dot{H}_{x2} = \frac{1}{\mu_o} \cdot \frac{\partial \dot{A}_2}{\partial y} \tag{6.3}$$

and

$$\dot{H}_{y2} = - \frac{1}{\mu_o} \cdot \frac{\partial \dot{A}_2}{\partial x} \qquad (6.4)$$

It has been shown in Sections 3.4.3 and 3.5.3 that in the model of Fig. 3.1, the primary member may be assumed to have infinite permeability. Thus at the primary surface, i.e. at y = (d+g),

$$\left.\frac{\partial \dot{A}_2}{\partial y}\right]_{y=(d+g)} = \mu_o \hat{K}_z \exp(-jqx) \qquad (6.5)$$

At the surface of the plate, i.e. at y=d, let the x and y components of magnetic field strength be related by

$$\dot{H}_{y2d} = - \dot{T} \dot{H}_{x2d} \qquad (6.6a)$$

where $\dot{T}$ is a complex quantity.

Using equations (6.3) and (6.4), equation (6.6a) becomes,

$$\left.\frac{\partial \dot{A}_2}{\partial x}\right]_{y=d} = \dot{T} \left.\frac{\partial \dot{A}_2}{\partial y}\right]_{y=d} \qquad (6.6)$$

From equations (6.2), (6.5) and (6.6), the unknown constants $C_2$ and $D_2$ may be evaluated. The values of $\dot{A}_2$, $\dot{H}_{x2}$ and $\dot{H}_{y2}$ may then be obtained from equations (6.2), (6.3) and (6.4), respectively. The values of these quantities at the surface of the plate may be obtained by putting y=d in these expressions. Thus the x-component of magnetic field strength on the surface of the plate $\dot{H}_{x2d} = \dot{H}_{xd}$ is given by

$$\dot{H}_{xd} = H_{x2}\Big]_{y=d} = \frac{\hat{K}_z \exp(-jqx)}{\cosh qg\,(1+j\dot{T}\tanh qg)} \qquad (6.7)$$

Likewise, the surface value of the magnetic vector potential $\dot{A}_{2d} = \dot{A}_d$ is given by

$$\dot{A}_d = \dot{A}_2\Big]_{y=d} = j\frac{\mu_o \dot{T}}{q}\cdot\dot{H}_{xd} \qquad (6.8)$$

where $\dot{H}_{xd}$ is given by equation (6.7).

The magnetic vector potential $\dot{A}_2$ in the linear air-gap region varies sinusoidally in both space and time and induces on the surface of the plate an electric field, $\dot{E}_{z2d} = \dot{E}_{zd}$, given by

$$\dot{E}_{zd} = -\frac{\partial \dot{A}_2}{\partial t}\Big]_{y=d}$$

$$\therefore \quad \dot{E}_{zd} = -j\omega\dot{A}_2\Big]_{y=d} \qquad (6.9a)$$

Using equation (6.8) then, equation (6.9a) becomes

$$\dot{E}_{zd} = \frac{\mu_o \omega \dot{T}}{q}\cdot\dot{H}_{xd} \qquad (6.9)$$

## 6.3 MEANS TO EVALUATE THE COMPLEX QUANTITY, $\dot{T}$

Equations (6.7) to (6.9) are applicable to both longitudinal and transverse flux cases, although the values of $\dot{T}$ are different. To obtain the field equations at the surface of the plate, it is necessary to evaluate $\dot{T}$ first.

The complex dimensionless quantity $\dot{T}$ may be obtained by using the one-dimensional non-linear solutions

for the solid iron developed in Chapter 5. This, however, presupposes that the current-density distribution in the plate is dependent only on the x-component of magnetic field strength. This has been discussed in Sections 3.4.7, 3.5.7 and 5.2, where it was shown that this assumption is valid if $2\alpha^2 >> q^2$ at the surface of the plate.

Thus, in the following analysis the condition $2\alpha^2 >> q^2$ (which is obtained in most cases) is assumed to hold and the current density obtained at the plate surface from the consideration of linear theory in the air-gap is equated to that obtained from the non-linear solution (Chapter 5) in order to evaluate $\dot{T}$.

## 6.4 FIELD EQUATIONS AT THE PLATE SURFACE UNDER LONGITUDINAL FLUX ARRANGEMENT

As in all previous cases, the longitudinal flux arrangement is represented by a further suffix $\ell$ with all quantities.

### 6.4.1 The Value of $\dot{T}_\ell$

Under longitudinal flux arrangement, the current density at the surface of the plate is given by equation (5.37), so that using equation (3.4), the electric field is given by

$$\hat{E}_{z\ell d} = - \frac{\rho \hat{H}_{x\ell d} . \lambda^2 . (\beta_\ell + j\gamma_\ell)}{2d(\lambda - 1)} \qquad (6.10)$$

It has been assumed in Chapter 5 that, the electromagnetic field quantities vary sinusoidally in time and space, and hence, the distribution of these quantities in the x-direction is also sinusoidal. Thus, in terms of the notations of Chapter 3

$$\dot{E}_{z\ell d} = \frac{-\rho\lambda^2(\beta_\ell + j\gamma_\ell)}{2d.(\lambda-1)} \cdot \dot{H}_{x\ell d} \qquad (6.11)$$

where $\dot{H}_{x\ell d} = \hat{H}_{x\ell d} \exp(-jqx)$, and is the same as given in equation (6.7).

From equations (6.9) and (6.11), therefore

$$\dot{T}_\ell = \frac{-q\rho}{\mu_o \omega} \cdot \frac{(\beta_\ell + j\gamma_\ell)\lambda^2}{2d.(\lambda-1)} \qquad (6.12)$$

Having obtained the complex non-dimensional quantity $\dot{T}_\ell$, other electromagnetic field equations at the surface of the plate may now be obtained.

### 6.4.2 Surface Magnetic Field Strength in Terms of Primary Excitation

Substituting the value of $\dot{T}_\ell$ in equation (6.7), the magnitude of the magnetic field strength on the surface of the plate, $|\dot{H}_{x\ell d}|$, is given by

$$\left|\dot{H}_{x\ell d}\right| = \frac{\hat{K}_z}{\text{coshqg}\left[1+k_1^2.R_\ell^2+2k_1.R_\ell.\sin\phi_\ell\right]^{\frac{1}{2}}} \qquad (6.13)$$

where $R_\ell^2 = \beta_\ell^2 + \gamma_\ell^2$ is a function of b only and

$$k_1 = \frac{q\rho\lambda^2.\tanh qg}{2d\mu_o\omega.(\lambda-1)} \qquad (6.14)$$

Equation (6.13) defines the magnetic field strength on the surface of the plate in terms of the primary excitation, the machine dimensions and the resistivity and the magnetisation curve of the material. $|\dot{H}_{x\ell d}|$ may also be obtained in terms of a dimensionless parameter, $Q_\ell$, to be introduced in the next section.

6.4.3 The Dimensionless Parameter, $Q_\ell$

As in the linear theory, a non-dimensional parameter, $Q_\ell$, may be defined in the non-linear theory as the ratio of the impedance due to eddy-current reaction field, $|\dot{Z}_{ry\ell d}|$, to the input impedance $|\dot{Z}_{y\ell d}|$ at the surface of the plate. Clearly $Q_\ell = 1$ is the condition when the maximum loss occurs in the plate. Other electromagnetic field equations may also be obtained in terms of $Q_\ell$ and thus define the nature of these equations under the conditions of maximum loss.

$Q_\ell$ is defined by

$$Q_\ell = \frac{|\dot{Z}_{ry\ell d}|}{|\dot{Z}_{y\ell d}|} \qquad (6.15)$$

$|Z_{y\ell d}|$ is given by equation (5.41). $|Z_{ry\ell d}|$ may be obtained from equation (4.18) if the permeabilities of both primary and the plate are high and if $\mu_r \tanh qg \tanh qd \gg 1$, i.e. the eddy-current field is strong. While the permeabilities are generally high, this condition applies for moderate values of qg and qd. Thus, equation (4.18),

which does not contain solid-iron parameters, may be used for $\dot{Z}_{ry\ell d}$, so that equation (6.15) becomes

$$Q_\ell = \frac{2d\mu_o\omega(\lambda-1)}{q\rho\lambda^2 R_\ell \tanh qg} \qquad (6.16)$$

This expression of $Q_\ell$ is used in defining plate thickness for optimum loss in the following section. Equation (6.16) is used also in obtaining other electromagnetic field quantities on the surface of the plate.

6.4.4 Plate Thickness for Optimum Loss

Since $Q_\ell = 1$ represents the maximum loss, a plate thickness may be so defined that maximum loss will occur. Such a value for half-thickness, $d_{\ell m}$, may be obtained from equations (6.16) and (5.29) by putting $Q_\ell = 1$.

$$|d_{\ell m}| = \frac{2\mu_o\omega q\rho R_\ell \tanh qg}{\mu_o^2\omega^2 - 4\alpha_\ell^2 q^2\rho^2 R_\ell^2 \tanh^2 qg} \qquad (6.17)$$

It may be seen from equation (6.17) that the plate-thickness for optimum loss depends on (i) the magnitude (included in $\alpha_\ell$) and frequency of primary excitation, (ii) the machine dimensions, and (iii) the resistivity and the magnetisation curve of the material of the plate. For given values of these quantities, therefore, there exists a plate thickness, which if used would result in maximum power loss. Conversely, for a given value of the plate thickness, equation (6.17) may be used to define machine dimensions for maximum loss.

6.4.5 $|\dot{H}_{x\ell d}|$ and m.m.f. Expressions in terms of $Q_\ell$

From equations (6.14) and (6.16)

$$R_\ell k_1 = \frac{1}{Q_\ell}$$

so that the relation between the magnetic field strength on the plate surface and the primary current sheet, equation (6.13), may be written as

$$|\dot{H}_{x\ell d}| = \frac{\hat{K}_z Q_\ell^{\frac{1}{2}}}{\text{coshqg}(Q_\ell + Q_\ell^{-1} + 2\sin\phi_\ell)^{\frac{1}{2}}} \qquad (6.18)$$

$|\dot{H}_{x\ell d}|$ may also be expressed in terms of the m.m.f.s obtained at the primary and the plate surfaces. This relation may later be used in loss, force and flux expressions to obtain these in terms of the primary m.m.f.

It is shown in Appendix II that the eddy-current reaction m.m.f. in the plate $|\dot{F}_{r\ell}|$ is related to $|\dot{H}_{x\ell d}|$ by the equation

$$|\dot{F}_{r\ell}| = \frac{|\dot{H}_{x\ell d}|}{q} \qquad (6.19)$$

and that the primary m.m.f., $\dot{F}_{c\ell}$, is related to $\hat{K}_z$ by

$$|\dot{F}_{c\ell}| = \frac{|\hat{K}_z|}{q} \qquad (6.20)$$

From equations (6.18), (6.19) and (6.20), therefore

$$\dot{H}_{x\ell d} = \frac{q|F_{c\ell}|Q_\ell^{\frac{1}{2}}}{\text{coshqg}(Q_\ell + Q_\ell^{-1} + 2\sin\phi_\ell)^{\frac{1}{2}}} \qquad (6.21)$$

and

$$|\dot{F}_{r\ell}| = \frac{|\dot{F}_{c\ell}| Q_\ell^{\frac{1}{2}}}{\text{coshqg}\,(Q_\ell + Q_\ell^{-1} + 2\sin\phi_\ell)^{\frac{1}{2}}} \qquad (6.22)$$

### 6.4.6 Loss/area and the Parameter $Q_\ell$

The eddy-current loss per unit of surface area due to excitation from any one side is given by equation (5.43), which, using equation (6.21) and (6.16), becomes

$$\mathcal{P}_{y\ell d} = \frac{|\dot{F}_{c\ell}|^2 \cos\phi_\ell . \Delta_\ell . q\mu_o . \omega}{2\,\text{coshqg} . \sinh qg} \qquad (6.23)$$

where

$$\Delta_\ell = \frac{1}{Q_\ell + Q_\ell^{-1} + 2\sin\phi_\ell} \qquad (6.24)$$

Since $Q_\ell = 1$ is the condition for maximum loss, it is given by

$$\mathcal{P}_{y\ell dm} = \frac{|\dot{F}_{c\ell}|^2 \cos\phi_\ell . q\mu_o . \omega}{4(1+\sin\phi_\ell)\,\text{coshqg} . \sinh qg} \qquad (6.25)$$

The loss expressed at per unit of its maximum value is given from equations (6.24) and (6.25) as

$$\frac{\mathcal{P}_{y\ell d}}{\mathcal{P}_{y\ell dm}} = \frac{2+2\sin\phi_\ell}{Q_\ell + Q_\ell^{-1} + 2\sin\phi_\ell} \qquad (6.26)$$

The variations of $\Delta_\ell$ and the normalised loss (equation (6.26)) with the non-dimensional parameter $Q_\ell$ are shown in Figs. 6.1 and 6.2 respectively. Bowden also obtained similar expressions for loss and normalised loss as given in equations (6.23) and (6.26), although

his definition of $Q_\ell$ was independent of d.

In order to obtain the value of loss, the value of $Q_\ell$ has to be determined first, as is clear from equations (6.23) and (6.24). Since the loss expression (equation (6.23)) contains primary m.m.f. $|\dot{F}_{c\ell}|$, it would be helpful if a relation could be established between $Q_\ell$ and $|\dot{F}_{c\ell}|$. In fact it is possible to do so.

The expression for $Q_\ell$, given by equation (6.16), contains $\lambda$ which includes $\alpha_\ell$ (equation (5.29)) i.e. $|\dot{H}_{x\ell d}|$. Substituting for $|\dot{H}_{x\ell d}|$ from equation (6.21) the relation between $Q_\ell$ and $|\dot{F}_{c\ell}|$ is finally obtained. However, the resulting expression is lengthy and complicated and is not given here. Both sides of the resulting expression contains $Q_\ell$ with fractional indices and, as such, it is not possible to find the value of $Q_\ell$ except by some iteration process. This was computed using the Newton-Raphson method[63] and the variation of $Q_\ell$ with $|\dot{F}_{c\ell}|$ for various thicknesses of the plate is shown in Fig. 6.3.

Fig. 6.3 shows that the general nature of variation of $Q_\ell$ with $|\dot{F}_{c\ell}|$ is that $Q_\ell$ goes on increasing for the range of $|F_{c\ell}|$ plotted. This is true for all plate thicknesses. Thus, small values of $Q_\ell$ occur at low primary excitation, i.e. peak loss density in the plate is obtainable at small values of $|\dot{F}_{c\ell}|$ and as $|\dot{F}_{c\ell}|$

increases, the loss densities obtainable are progressively smaller proportions of the peak loss. This is, however, not strictly true about plates of very small thickness, where the loss densities obtainable are always quite high as indicated by small values of $Q_\ell$.

Fig. 6.3 has been obtained for one value of air-gap length and pole-pitch of excitation winding only, and a set of similar curves has to be obtained for any change in either or both of these quantities. For the same values of air-gap length and pole-pitch, Fig. 6.4 shows the variation of maximum loss against primary excitation (equation(6.25)). For a plate of given thickness and for a given value of primary m.m.f. $|\dot{F}_{c\ell}|$, the loss density may be obtained using Figs. 6.2, 6.3 and 6.4. For a plate of a given thickness the value of $Q_\ell$ may be obtained for any primary excitation from Fig. 6.2 and corresponding to this value of $Q_\ell$ the value of normalised loss may be obtained from Fig. 6.3. Having obtained the maximum loss from Fig. 6.4, the actual loss density may be calculated. This procedure, though lengthy, provides the value of $Q_\ell$ which may be used to find the values of other quantities and also to provide some idea of the proportion of obtainable loss that is being exploited. Furthermore, this procedure has an aspect of generality in that it utilises the normalised curve of Fig. 6.2 which is useful irrespective of the plate

thickness, the primary excitation and the machine dimensions. Alternately, however, all the above steps may be incorporated in the computer programme itself, so that loss values may be obtained straight as a function of $|\dot{F}_{c\ell}|$ as shown in Fig. 6.5.

6.4.7 Forces on the Surface of the Plate

The solid-iron plate, being subjected to magnetic fields, experiences forces of electromagnetic nature. At the surface of the plate, the x-component of force density is given by

$$F_{x\ell d} = -\frac{1}{2} \mathrm{Re}(\dot{J}_{z\ell d} \times B^{*}_{y\ell d}) \qquad (6.27a)$$

where $\dot{J}_{z\ell d}$ is the surface current density given by equation (5.37) and $B^{*}_{y\ell d}$ is the complex conjugate of $\dot{B}_{y\ell d} = -\mu_o \dot{T}_\ell \dot{H}_{x\ell d}$. Thus, from equations (6.12),

$$F_{x\ell d} = \frac{\hat{H}_{x\ell d}^{2} R_\ell^{2} \lambda^{4} q\rho}{8\omega d^{2}(\lambda-1)^{2}} \qquad (6.27)$$

Using equations (6.21) and (6.16), equation (6.27) finally becomes

$$F_{x\ell d} = \frac{\mu_o |\dot{F}_{c\ell}|^{2} q^{2} R_\ell \Delta_\ell \lambda^{2}}{4d(\lambda-1)\cosh qg \cdot \sinh qg} \qquad (6.28)$$

where $\Delta_\ell$ is given by equation (6.24).

At maximum loss $Q_\ell = 1$ and if the frequency is the same, this also represents the maximum force condition. The maximum force may be obtained from equation (6.28)

by putting $(2+2\sin\phi_\ell)^{-1}$ for $\Delta_\ell$, so that normalised force is also given by equation (6.26).

The y-component of force density at the surface of the plate is, likewise, given by

$$F_{y\ell d} = -\frac{1}{2}\,\mathrm{Re}(\dot{J}_{z\ell d} \times B^*_{x\ell d}) \qquad (6.29a)$$

where $B^*_{x\ell d}$ is the complex conjugate of $\dot{B}_{x\ell d} = \mu_o \dot{H}_{x\ell d}$. Thus

$$F_{y\ell d} = \frac{\mu_o \beta_\ell \lambda^2 \hat{H}^2_{x\ell d}}{4d(\lambda-1)} \qquad (6.29)$$

Using equations (6.21) and (6.16), this becomes

$$F_{y\ell d} = \frac{\mu_o^2 \omega \cos\phi_\ell q |F_{c\ell}|^2 \Delta_\ell}{2\rho \cosh qg \sinh qg} \qquad (6.30)$$

Thus the y-component of force density at the plate surface also has its maximum when $Q_\ell = 1$, provided frequency remains the same. The normalised force equation is also given by equation (6.26).

6.4.8 Flux/pole and $Q_\ell$

The mean flux density at the surface of the plate $B_{y\ell mn}$, is given by the equation

$$B_{y\ell mn} = \frac{2}{\pi}\left|\dot{B}_{y\ell d}\right| \qquad (6.31)$$

where $\dot{B}_{y\ell d} = -\mu_o \dot{T}_\ell \dot{H}_{x\ell d}$

The total flux per pole, $\Phi_{p\ell}$, is given by

$$\Phi_{p\ell} = B_{y\ell mn} \times \text{pole-area}$$

Thus, if L is the width of the plate in the z-direction, then using equations (6.12), (6.21) and (6.16), the total flux/pole is given by,

$$\Phi_{p\ell} = \frac{2\mu_o L|\dot{F}_{c\ell}|}{\sinh qg} \cdot \left[\frac{\Delta_\ell}{Q_\ell}\right]^{\frac{1}{2}} \qquad (6.32)$$

The effect of finite plate-thickness on the flux/pole is implicit in the expression $(\frac{\Delta_\ell}{Q_\ell})^{\frac{1}{2}}$ in equation (6.32). Three specific cases may be studied for this expression.

Case 1, $Q_\ell$ is large (i.e. $Q_\ell >> 1$)

In this case $\left[\frac{\Delta_\ell}{Q_\ell}\right]^{\frac{1}{2}} \to \frac{1}{Q_\ell}$, so that

$$\Phi_{p\ell}\Big]_{Q_\ell \text{ large}} \equiv \frac{2\mu_o L|\dot{F}_{c\ell}|}{Q_\ell \sinh qg} \qquad (6.33a)$$

Case 2, $Q_\ell$ is small (i.e. $Q_\ell << 1$)

In this case $\left[\frac{\Delta_\ell}{Q_\ell}\right]^{\frac{1}{2}} \to 1$ and

$$\Phi_{p\ell}\Big]_{Q_\ell \text{ small}} \equiv \frac{2\mu_o L|\dot{F}_{c\ell}|}{\sinh qg} \qquad (6.33b)$$

Case 3, $Q_\ell = 1$

In this case, equation (6.32) is given by

$$\Phi_{p\ell}\Big]_{Q_\ell=1} = \frac{\sqrt{2}\mu_o L|\dot{F}_{c\ell}|}{(1+\sin\phi_\ell)^{\frac{1}{2}} \sinh qg} \qquad (6.33c)$$

Thus, it is only when the value of $Q_\ell$ is large that the flux/pole is a function of $Q_\ell$ and hence of plate thickness (Fig. 6.3). For small values of $Q_\ell$ and for

$Q_\ell = 1$, the flux/pole is independent of plate-thickness. Also equation (6.33b) is independent of solid-iron parameters, so that for weak eddy-current reaction field the flux/pole is not influenced by either the thickness of the plate or the magnetisation curve of the material of the plate.

Equation (6.33c) gives the value of flux per pole when maximum loss occurs in the plate.

## 6.5 FIELD EQUATIONS AT PLATE SURFACE UNDER TRANSVERSE FLUX ARRANGEMENT

As before, the transverse flux arrangement is represented by a further suffix t with all quantities.

### 6.5.1 The Value of $\dot{T}_t$

Under this arrangement, the surface current density is given by equation (5.63a), so that the electric field intensity is obtained, using equation (3.4), and the reasoning of section 6.4.1, as

$$\hat{E}_{ztd} = - \rho(\beta_t + j\gamma_t)\left(\frac{2}{d} + \alpha_t\right)\dot{H}_{xtd} \qquad (6.34)$$

where $\dot{H}_{xtd} = \hat{H}_{xtd} \exp(-jqx)$ and is given by equation (6.7).

From equations (6.9) and (6.34), therefore,

$$\dot{T}_t = - \frac{q\rho}{\mu_o \omega}\left(\frac{2}{d} + \alpha_t\right)(\beta_t + j\gamma_t) \qquad (6.35)$$

The value of $\dot{T}_t$, given by equation (6.35), may now be used in obtaining the expressions of other electro-

magnetic field quantities at the surface of the plate.

6.5.2 Surface Magnetic Field Strength in Terms of Primary Excitation

Putting the value of $\dot{T}_t$ from equation (6.35) in equation (6.7) expression for the magnetic field strength, $|\dot{H}_{xtd}| = \hat{H}_{xtd}$ at the surface of the plate is obtained as

$$|\dot{H}_{xtd}| = \frac{\hat{K}_z}{\cosh qg\,(1+k_2{}^2 R_t{}^2+2k_2 R_t \sin\Phi_t)^{\frac{1}{2}}} \qquad (6.36)$$

where $R_t{}^2 = \beta_t{}^2 + \gamma_t{}^2$ and $k_2$ is given by

$$k_2 = \frac{q\rho}{\mu_o \omega}\cdot\left(\frac{2}{d} + \alpha_t\right)\tanh qg \qquad (6.37)$$

Equation (6.36), therefore, defines the magnetic field strength on the surface of the plate in terms of the primary excitation and its frequency, the machine dimensions, and the resistivity and the magnetisation curve of the material of the plate. It may be noted here that $k_2$ (equation (6.37)) contains two terms, of which the first term is prominent for small values of plate thickness and is independent of primary excitation, while the second term is prominent for large values of plate thickness.

$\dot{H}_{xtd}$ may also be obtained in terms of a dimensionless parameter $Q_t$ to be introduced in the next section.

6.5.3 The Dimensionless Parameter $Q_t$

As in Section 6.4.3, a non-dimensional parameter $Q_t$ may be defined in this case, as

$$Q_t = \frac{|\dot{Z}_{rytd}|}{|\dot{Z}_{ytd}|} \qquad (6.38)$$

where $|\dot{Z}_{ytd}|$ is the input impedance at the plate surface and is given by equation (5.69) and $|\dot{Z}_{rytd}|$ is the impedance at the surface due to the reaction field of eddy current and is given, as before, by equation (4.45). Substituting for $\dot{Z}_{rytd}$ and $\dot{Z}_{ytd}$,

$$Q_t = \frac{\mu_o \omega}{q\rho R_t (\frac{2}{d}+\alpha_t) \tanh qg} \qquad (6.39)$$

This expression is used to define the plate thickness for optimum loss in the following section. Equation (6.39) is also used in expressions of other electromagnetic field quantities at the surface of the plate.

6.5.4 Plate Thickness for Optimum Loss

Clearly $Q_t = 1$ represents maximum loss, so that a plate half-thickness $d_{tm}$ may be obtained for which the loss in the plate is maximum. Thus, from equation (6.39), by putting $Q_t = 1$,

$$|d_{tm}| = \frac{2q\rho R_t \tanh qg}{\mu_o \omega - q\rho R_t \alpha_t \tanh qg} \qquad (6.40)$$

Equation (6.40) shows that for a given set of values for (i) primary excitation (through $\alpha_t$) and its frequency, (ii) the machine dimensions and (iii) the resistivity and the magnetisation curve of the material, there exists a plate thickness for which the power loss

in the plate is a maximum. Conversely, for a given plate thickness, equation (6.40) may be used to define machine dimensions for maximum loss.

6.5.5 $|\dot{H}_{xtd}|$ and m.m.f. Expressions in Terms of $Q_t$

From equations (6.37) and (6.39)

$$R_t k_2 = \frac{1}{Q_t}$$

so that equation (6.36) becomes

$$|\dot{H}_{xtd}| = \frac{\hat{K}_z Q_t^{\frac{1}{2}}}{\text{coshqg}(Q_t + Q_t^{-1} + 2\sin\phi_t)^{\frac{1}{2}}} \qquad (6.41)$$

As has been shown in Appendix II, the eddy-current reaction m.m.f. in the plate $\dot{F}_{rt}$ is related to $|\dot{H}_{xtd}|$ by

$$|\dot{F}_{rt}| = \frac{|\dot{H}_{xtd}|}{q} \qquad (6.42)$$

and the primary m.m.f. $\dot{F}_{ct}$ is related to $\hat{K}_z$ by

$$|\dot{F}_{ct}| = \frac{|\hat{K}_z|}{q} \qquad (6.43)$$

From equations (6.41), (6.42) and (6.43), then

$$|\dot{H}_{xtd}| = \frac{q|\dot{F}_{ct}|Q_t^{\frac{1}{2}}}{\text{coshqg}(Q_t + Q_t^{-1} + 2\sin\phi_t)^{\frac{1}{2}}} \qquad (6.44)$$

and

$$|\dot{F}_{rt}| = \frac{|\dot{F}_{ct}|Q_t^{\frac{1}{2}}}{\text{coshqg}(Q_t + Q_t^{-1} + 2\sin\phi_t)^{\frac{1}{2}}} \qquad (6.45)$$

Equation (6.44) expresses the magnetic field

strength on the plate surface in terms of the primary mmf. and the effect of finite plate thickness is implicit in the definition of $Q_t$. $|\dot{H}_{xtd}|$, as given in equation (6.44), may be used in other equations in order to express them in terms of $|\dot{F}_{ct}|$.

6.5.6 Loss/area and the Parameter, $Q_t$

The eddy-current loss inside the plate per unit of its surface area due to excitation from any one of its sides is given by equation (5.72), which, using equations (6.44) and (6.39), becomes

$$\mathcal{P}_{ytd} = \frac{|\dot{F}_{ct}|^2 \cos\phi_t \Delta_t q \mu_o \omega}{2\sinh qg . \cosh qg} \qquad (6.46)$$

where

$$\Delta_t = \frac{1}{Q_t + Q_t^{-1} + 2\sin\phi_t} \qquad (6.47)$$

Since $Q_t = 1$ is the condition for maximum loss, from equations (6.46) and (6.47) the expression for maximum loss is obtained as

$$\mathcal{P}_{ytdm} = \frac{|\dot{F}_{ct}|^2 \cos\phi_t q \mu_o \omega}{4(1+\sin\phi_t)\sinh qg . \cosh qg} \qquad (6.48)$$

The normalised loss is obtained from equations (6.46), (6.47) and (6.48)

$$\frac{\mathcal{P}_{ytd}}{\mathcal{P}_{ytdm}} = \frac{2+2\sin\phi_t}{Q_t + Q_t^{-1} + 2\sin\phi_t} \qquad (6.49)$$

The variations of $\Delta_t$ and normalised loss with $Q_t$ are shown in Figs. 6.1 and 6.2 respectively. Equation (6.48) shows that maximum loss may be obtained in a plate irrespective of its thickness. Fig. 6.4 shows a plot of $\wp_{ytdm}$ against $|\dot{F}_{ct}|$.

In order to obtain the loss density in terms of the primary m.m.f., the non-dimensional parameter $Q_t$ should first be determined, as may be seen from equations (6.46) and (6.47). It is possible to obtain $Q_t$ as a function of primary m.m.f. $F_{ct}$ from equation (6.39) in which the value of $\alpha_t$ is obtained from equations (5.52) and (6.44). This gives

$$\frac{2Q_t}{d} + \left(\frac{\omega A}{2\rho}\right)^{\frac{1}{2}} \cdot \frac{q^{\frac{b-1}{2}} \cdot |\dot{F}_{ct}|^{\frac{b-1}{2}} \cdot Q_t^{\frac{b+3}{4}} \cdot \Delta_t^{\frac{b-1}{4}} \cdot k_{bt}}{\cosh^{\frac{b-1}{2}} qg} = \frac{\mu_o \omega}{q\rho R_t \tanh qg} \qquad (6.50)$$

Equation (6.50) gives the parameter $Q_t$ with fractional indices and hence it is not possible to obtain an algebraic solution. The value of $Q_t$ was computed for EN1A steel (i.e. for b = 0.112) using the iterative Newton-Raphson method[63]. Fig. 6.6 shows the variation of $Q_t$ against $|\dot{F}_{ct}|$ for various thicknesses of the plate.

The curves of Fig. 6.6 are similar to those obtained for the longitudinal flux arrangement (Fig. 6.3). Small values of $Q_t$ at low $|\dot{F}_{ct}|$ are indicative of the fact that optimum loss conditions are obtained at small values of $|\dot{F}_{ct}|$ and by increasing the primary excitation,

progressively smaller proportion of the peak loss is being obtained.

For a plate of given thickness, the value of $Q_t$ may be obtained from Fig. 6.6 for any primary excitation. Normalised loss value may be obtained from Fig. 6.2 corresponding to this value of $Q_t$, and from the knowledge of maximum loss,(Fig. 6.4), the actual loss may be obtained. This process, though lengthy, provides with the value of $Q_t$ which may be used in other expressions and which gives an idea of the proportion of obtainable loss that is being exploited. Also this procedure utilises the normalised curve of Fig. 6.2 which is useful at all values of primary excitations, plate thickness and machine dimensions.

Alternately, however, all the above steps may be incorporated in the computer programme, resulting in loss vs. primary excitation curves as shown in Fig. 6.7 .

6.5.7 Forces on the Surface of the Plate

Forces of electromagnetic origin act on the surface of the solid-iron plate. The x-component of force density on plate surface is given by

$$F_{xtd} = -\frac{1}{2} \mathrm{Re}(\dot{J}_{ztd} \times B^*_{ytd}) \qquad (6.51a)$$

where $\dot{J}_{ztd}$ is the surface current density and is given

by equation (5.63a) and $B^*_{ytd}$ is the complex conjugate of the y-component of flux density at the plate surface, $\dot{B}_{ytd}$, given by $-\mu_o \dot{T}_t \dot{H}_{xtd}$. Thus using equation (6.35), this becomes

$$F_{xtd} = \frac{\hat{H}_{xtd}^2 q \rho R_t^2 \left(\frac{2}{d} + \alpha_t\right)^2}{2\omega} \qquad (6.51)$$

Using equation (6.45) and (6.39) this finally becomes

$$F_{xtd} = \frac{\mu_o |\dot{F}_{ct}|^2 q^2 R_t \Delta_t \left(\frac{2}{d} + \alpha_t\right)}{2 \sinh qg . \cosh qg} \qquad (6.52)$$

The y-component of force density at the surface of the plate $F_{ytd}$, is, likewise, given by

$$F_{ytd} = -\frac{1}{2} \mathrm{Re}(\dot{J}_{ztd} \times B^*_{xtd}) \qquad (6.53a)$$

where $B^*_{xtd}$ is the complex conjugate of $\dot{B}_{xtd} = \mu_o \dot{H}_{xtd}$. Thus

$$F_{ytd} = \frac{\hat{H}_{xtd}^2}{2} \cdot \mu_o \beta_t \left(\frac{2}{d} + \alpha_t\right) \qquad (6.53)$$

Using equations (6.45) and (6.39), $F_{ytd}$ finally becomes

$$F_{ytd} = \frac{\mu_o^2 \omega |\dot{F}_{ct}|^2 \Delta_t \cos \phi_t}{2 \rho \sinh qg . \cosh qg} \qquad (6.54)$$

In both equations (6.52) and (6.54), $\Delta_t$ is given by equation (6.47). For maximum loss, $Q_t = 1$ and this applies for forces as well, so long as the frequency

remains the same. Thus in the force expressions above, the maximum force conditions would be obtained by replacing $\Delta_t$ with $(2 + 2\sin\phi_t)^{-1}$ and the normalised force density equations would also be given by equation (6.49).

6.5.8 Flux/pole and $Q_t$

The mean value of the flux density on the plate surface $B_{ytmn}$ is given by

$$B_{ytmn} = \frac{2}{\pi}|\dot{B}_{ytd}| \qquad (6.55)$$

where $\dot{B}_{ytd} = -\mu_o \dot{T}_t \dot{H}_{xtd}$

The flux/pole, $\Phi_{pt}$, is given by

$$\Phi_{pt} = B_{ytmn} \times \text{pole-area.}$$

Thus, using equations (6.44) and (6.35), the total flux/pole is given by

$$\Phi_{pt} = \frac{2\mu_o L|\dot{F}_{ct}|}{\sinh qg} \left[\frac{\Delta_t}{Q_t}\right]^{\frac{1}{2}} \qquad (6.56)$$

where L is the active width of the plate.

The effect of finite plate thickness is implicit in equation (6.56) in the expression $\left[\frac{\Delta_t}{Q_t}\right]^{\frac{1}{2}}$. However, it is only when $Q_t$ is large that finite plate thickness affects the flux/pole, as may be seen from the following study.

Case 1, $Q_t$ is large, ($Q_t >> 1$)

In this case $\left[\frac{\Delta_t}{Q_t}\right]^{\frac{1}{2}} \rightarrow \frac{1}{Q_t}$, so that

$$\Phi_{pt}\Big]_{Q_t \text{ large}} \equiv \frac{2\mu_o L|\dot{F}_{ct}|}{Q_t \sinh qg} \qquad (6.57a)$$

Case 2, $Q_t$ is small, ($Q_t << 1$)

In this case $\left[\frac{\Delta_t}{Q_t}\right]^{\frac{1}{2}} \rightarrow 1$, so that

$$\Phi_{pt}\Big]_{Q_t \text{ small}} \equiv \frac{2\mu_o L|\dot{F}_{ct}|}{\sinh qg} \qquad (6.57b)$$

Case 3, $Q_t = 1$

In this case

$$\Phi_{pt}\Big]_{Q_t = 1} = \frac{\sqrt{2}\mu_o L|\dot{F}_{ct}|}{(1+\sin\phi_t)^{\frac{1}{2}} \sinh qg} \qquad (6.57c)$$

Thus flux/pole, given by equation (6.57a), is a functicn of $Q_t$ and hence of plate thickness (Fig. 6.6). As in the longitudinal flux case, here also for weak eddy-current reaction field, the flux/pole is independent of plate-thickness and the magnetisation curve of the material of the plate. When $Q_t = 1$, the flux/pole is also independent of plate-thickness and equation (6.57c) gives the value of flux/pole for maximum power loss in the plate.

## 6.6 A DISCUSSION ON ELECTROMAGNETIC FIELD QUANTITIES ON THE PLATE SURFACE

### 6.6.1 General

In Chapter 5, one dimensional non-linear theories were developed for both longitudinal and transverse flux arrangements and so far in this chapter they have been correlated with the two-dimensional fields in the air-gap. Equations have been obtained for the various electromagnetic field quantities at the surface of the plate and in this section a discussion of these, including the model, is made.

### 6.6.2 The Arrangements in the Model

The model used in the analysis is that of Fig. 3.1 , except that the fields are one dimensional in the plate, i.e. the y-component of magnetic fields is neglected. In as much as a transverse flux arrangement implies that the flux passes through the plate, (especially when it is thin), it is, in a way, a misnomer, because of the one-dimensional nature of the problem. However, with a double-sided arrangement, both pole-arrangements are possible, and it is found convenient to retain the terms 'longitudinal' and 'transverse' flux, as was introduced with the two-dimensional linear theory of Chapter 3, to keep the continuity throughout the thesis.

It may be mentioned here that since by letting

the plate-thickness become very large, the present model corresponds to that of Bowden, some work on optimisation of loss in a plate with single-sided arrangement was carried out. High loss in the plate would result in increase in resistivity of the plate due to rise in temperature and a relation was obtained between normalised loss and normalised resistivity. The details of the work are given in Appendix III.

6.6.3 General Comments on Field Quantities

The non-linear theories developed in Chapter 5 depend for their solutionson the double function introduced in equation (5.17).

$$\hat{H}_x = \hat{H}_{xd} (1+hy')^r (1+fy')^s, \quad hy' < -1, \quad fy' < -1 \qquad (5.17)$$

The values of the constants h and f obtained for the two different pole-arrangements clearly show how these are affected by finite plate thickness. It has been mentioned in Chapter 5 (Sections 5.4.1 and 5.5.1) that by making the plate thickness very large, these constants are so modified that equation (5.17) always turns into a single function of the form

$$\hat{H}_x = \hat{H}_{xd} (1 + hy')^r \qquad (6.58)$$

which is of the same form of solution as was appropriately used by Bowden. This justifies the use of equation (5.17) as a solution to the differential equation (equation (5.14))

concerning $\hat{H}_x$ and y.

Having obtained a solution for the magnetic field strength in the solid iron, expressions for current density, impedance, loss, force and flux may be obtained relatively easily. It is seen that both magnetic field strength and current density inside the plate are confined to thin layers near the plate surfaces. It was found convenient to define a plate thick when its half-thickness was very much greater than $1/2\alpha_\ell$ in longitudinal flux arrangement and $2/\alpha_t$ in transverse flux arrangement.

For both pole-arrangements, the impedance angles are equal and are functions of the magnetisation curve of the material of the plate. It may be noted that for the linear case both become equal to $1/\sqrt{2}$.

The input impedance at the surface of the plate is generally higher in the longitudinal flux arrangement than in the transverse flux arrangement, for the same value of surface magnetic field strength. This suggests that eddy-current field is stronger for transverse flux arrangement than for longitudinal flux arrangement. Physically this is due to the currents being more uniformly distributed across the plate thickness in the transverse flux arrangement than in the longitudinal flux arrangement.

It was found convenient to carry on the analysis in terms of a dimensionless parameter, Q (i.e. $Q_\ell$ & $Q_t$)

defined as the ratio of wave impedances at the plate surface. Maximum loss and force conditions may be easily obtained by equating it to unity. The magnitude of this parameter represents the dominance or otherwise of the eddy-current field. It also indicates how much of the maximum possible loss is being obtained (Fig. 6.2). If optimisation of power loss in the plate is desired, the dimensions of the machine may be so chosen that Q tends to unity. Equations (6.17) and (6.40) may be used to select a plate of optimum thickness (i.e. Q = 1). It may be noted in these equations that for a given machine, there is always a plate-thickness which would give maximum loss; although these thicknesses are different for the two arrangements of poles. Conversely, for a plate of given thickness, these equations may be used to select machine dimensions such that maximum loss occurs.

Loss densities obtainable under the two different pole arrangements are shown plotted in Fig. 6.8 against the half thickness of the plate. The loss for the transverse flux arrangement is higher than that for the longitudinal flux arrangement, especially when the plate thickness is small. This agrees with similar observations made in connection with the linear theory (Section 4.3.4). Fig. 6.8 also includes a plot of the ratio of the losses under the two arrangements and this shows that the losses are not very much different. Thus, while for the non-linear case either arrangement of poles results in a high loss,

longitudinal flux arrangement is to be preferred for plates of large thickness and transverse flux arrangement may be preferred for plates of small thickness.

It may be mentioned here that while the non-dimensional parameters $Q_\ell$ and $Q_t$ are very helpful in the analysis and design, their values may not be obtained except by some iteration method on a digital computer. Thus in order to design a heating system using the model of Fig. 3.1, the values of $Q_\ell$ or $Q_t$ has to be obtained either from computation or from sets of curves of the nature shown in Figs. 6.3 and 6.6 .

## 6.7 CONCLUSION

In this chapter a general solution has been obtained for the electromagnetic field quantities at the surface of the plate by equating the solutions for electric field intensity from the present non-linear theory in the plate and the linear theory in the air-gap at the air/iron surface. Magnetic field strength on the plate surface was, thus, expressed in terms of the primary excitation which enabled the loss, the forces and the flux/pole to be expressed in terms of the same.

It was found convenient to carry out the analysis in terms of a non-dimensional parameter, Q (i.e. $Q_\ell$ or $Q_t$) defined as the ratio of input and output impedances at the plate surface when the eddy-current field was strong. Q = 1 represented the condition of maximum loss and forces. The relation between the surface magnetic

field strength and the primary excitation has been expressed in terms of Q so that the loss, the forces and the flux/pole have also been obtained in terms of this quantity.

A definition for $d_m$, the plate half-thickness for optimum loss, has been obtained from the definition of Q. $d_m$ (i.e. $d_{\ell m}$ or $d_{tm}$) has been expressed in terms of

(i) the magnitude and frequency of primary excitation,

(ii) the machine dimensions, and

(iii) the resistivity and the magnetisation curve of the material of the plate.

Thus for a given set of these values, there always existed a plate thickness when the loss in the plate would be a maximum.

A discussion of the field quantities under the two different pole arrangements concludes the work of this chapter. The use of a double function solution (equation 5.17) to the diffusion equation has been shown to be appropriate in order to account for the additional boundary condition at the centre of plate-thickness. Conditions have been obtained for defining a plate as thick and thin for both pole-arrangements. As in the linear case, the loss under TFA was markedly higher than that under LFA when the plate thickness was small.

# CHAPTER 7

# FINITE WIDTH EFFECTS FOR LONGITUDINAL FLUX ARRANGEMENT AND TRANSVERSE FLUX ARRANGEMENT

## 7.1 INTRODUCTION

The work in this chapter considers the effects of finite plate width (in the z-direction) on power loss and current-density distribution in a plate subjected to travelling magnetic fields from both sides.

In the analyses presented in Chapters 3 and 5, finite width effect was neglected so that current density in the plate was considered unidimensional. In a plate of finite width, however, current density in the plate will have components in all three dimensions, and, depending on the particular pole-arrangement, current densities will have preferred directions of flow in the end-region. Eddy-current power loss in the plate, likewise, will be different.

For a machine having constant-voltage excitation, the air-gap flux will be of approximately constant amplitude; the voltage induced in the plate, for sinusoidal flux, will be proportional to the flux and the resulting currents would be dependent on the plate impedance. These conditions may also be obtained in a machine having constant primary m.m.f. and weak eddy-current reaction in the plate (i.e. $Q < 1$).

The nature of the eddy-current reaction field (i.e. whether it is strong or weak) is determined to a great extent by the dimensions of the heater (e.g. pole-pitch, air-gap length, thickness of the plate) and the physical parameters of the material of the plate. Where the eddy-current reaction is weak, any change in the eddy-current reaction has little effect on flux/pole. This is seen from equations (6.33b) and (6.57b) which are independent of the physical parameters of the material of the plate.

Double-sided linear induction heaters are often weak eddy-current reaction devices; Jackson's[4] transverse flux slab heater is one such example. For machines having strong eddy-current reaction ($Q > 1$), three-dimensional analyses are necessary to account for the variation in the flux/pole and the air-gap flux density distribution. Bowden's[30] treatment of end-effects, for example, was concerned predominantly with machines having $Q > 1$. Thus, it was felt that in the present work, finite width effect would be considered in a heater having weak eddy-current reaction field; for such a case, the analysis is simpler than the three-dimensional analysis necessary for machines with strong eddy-current reaction.

If a heater has weak eddy-current reaction field, the current density and hence, the eddy-current loss, in a plate having low-resistivity end-strips would be higher than those in a plate without such end-strips. In the

present analysis a plate of finite thickness is considered as being subjected to double-sided excitation and in this chapter the effects of finite plate width on power loss and current-density distribution in the plate are studied.

The analysis presented in this chapter consists of a simple two-dimensional solution of current densities in the plate and in the end-strips. Current densities are assumed to be uniformly distributed in small depths near the plate surfaces and over the width of end-strips. Additional boundary conditions arise due to finite thickness of the plate. The analysis results in the definition of a finite width factor which is equal to the ratio of power loss in a plate with end-strips of finite resistivity to that in a plate having end-strips of zero resistivity. Both longitudinal and transverse flux arrangements are studied in detail.

The effect of magnetic non-linearity in the material of the plate is accounted for by defining an effective thickness for the assumed uniform current-density distributions; the non-linear theory of Chapter 5 is used for this purpose. The width for uniform distribution of end-region currents with and without end-strips is also defined. The nature of current-density distributions in the plate and their dependence, at the end of the active width, on the plate thickness and pole arrangements are also investigated.

In rotating electrical machines, the effect of finite rotor length or end-effect also arises and various attempts to account for this effect are found in published works[11,22,44,64-72]. A brief survey of some published literature precedes the solution presented in this chapter.

The chapter ends with a comparison of the present treatment with that of Woolley and Chalmers[66] and this includes a reference to the areas where new contributions are believed to have been made.

## 7.2 NATURE OF FINITE WIDTH EFFECT

The linear and the non-linear theories developed in earlier chapters (Chapters 3 and 5) assumed a machine* of infinite width (i.e. the machine was considered to extend to infinity in the z-direction, which is perpendicular to the direction of travel of the magnetic field) so that eddy currents flowing in the plate would close their paths only at infinity and thus have no effect on the electromagnetic field distribution within the boundaries of the model (Fig. 3.1); the current density in the plate could then be considered as purely z-directed.

---

* The word 'machine', used in this section, refers to the travelling-wave induction heating device being discussed throughout this thesis.

In a practical arrangement, however, the width of the machine would be finite and the currents in the plate would close their paths in the active as well as in the end regions. An infinitely wide machine can, nevertheless, be simulated by fitting low (ideally zero) resistivity end-strips (e.g. Copper) at the ends of active width of the plate,* as shown in Fig. 7.1a. The end-strips provide low resistivity paths for the end currents and these minimise end-region loss.. The resulting current density in the plate would be predominantly z-directed, $J_z$, since the use of end-strips would provide approximately equipotential surfaces at the interfaces between the active and end region, although current density in the x-direction, (i.e. in the direction of travel of magnetic field), $J_x$,

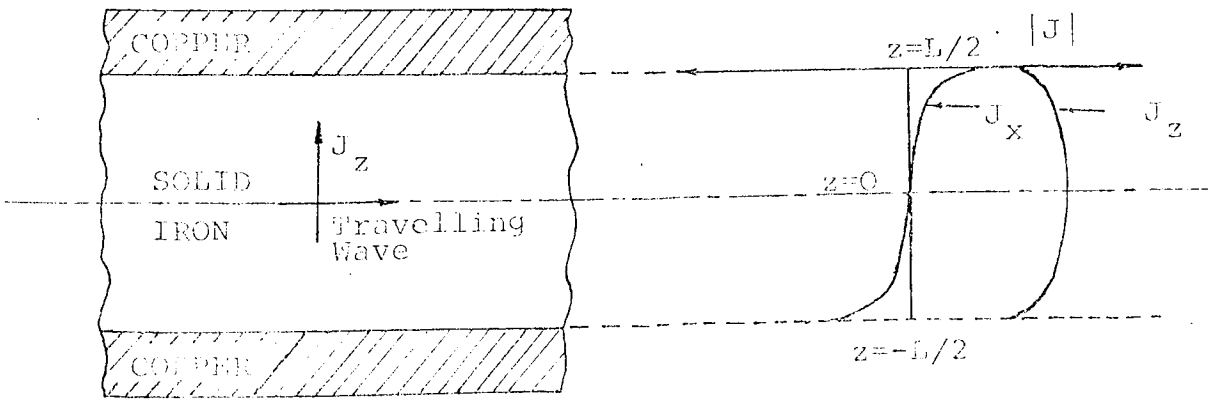


Fig.7.1a End-strip plate.

Fig.7.1b Assumed forms of distributions** of $J_z$ and $J_x$ over the active width of the plate

---

* This will be termed the 'end-strip plate' in this thesis.

** The actual distributions of $J_z$ and $J_x$ are obtained mathematically, for the given boundary conditions, in section 7.4.

would also exist. The assumed forms of distributions of $J_z$ and $J_x$ over the active width of the plate are shown in Figure 7.1b. It may be noted in Figure 7.1b that at the centre of the active width, i.e. at z=0, the current density in the plate is wholly z-directed and any correlation of electromagnetic field distribution with the theories developed in earlier chapters (Chapters 3 and 5) may be obtained only for values of $J_z$ at z=0.

In the absence of such low resistivity end-strips, the directional components of current density in the active width of the plate would have distributions similar to the current densities in an end-strip plate, but their relative magnitudes would be different. If the width of the plate is not greater than the active width of the primary, the currents are constrained to close their paths within the active region, and at the edges (i.e. at the ends of active width) of the plate, $J_z$ may not necessarily be greater than $J_x$.

In the present double-sided model with a plate of finite thickness, (Fig. 3.1), the dominance, or otherwise, of $J_z$ over $J_x$ depends on the pole arrangements on the two sides of the plate as well as on the plate-thickness. Figures 7.2a and 7.2b show the assumed distributions of end-currents in the plate for longitudinal and transverse flux arrangements, respectively. It may be noted in these figures that for the

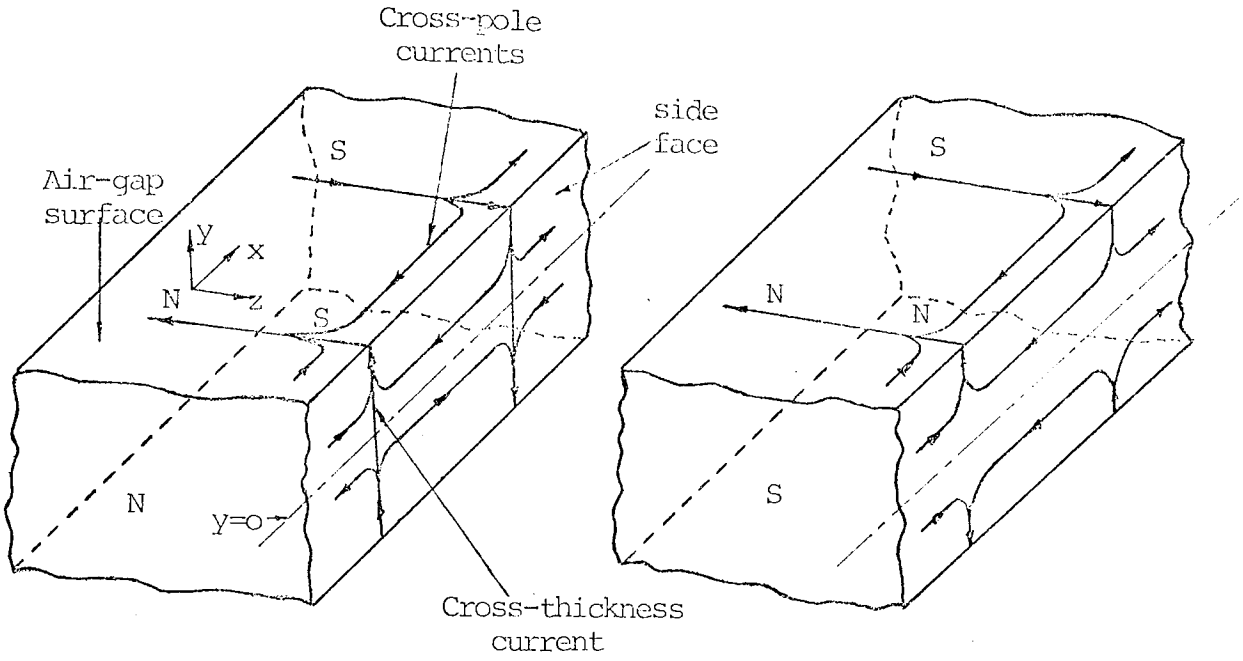


Fig.7.2a Idealised distribution of end-currents in the plate for longitudinal flux arrangement.

Fig.7.2b Idealised distribution of end-currents in the plate for transverse flux arrangement.

longitudinal flux arrangement (LFA), the end-currents are predominantly cross-thickness in nature, whereas for the transverse flux arrangement (TFA), the end-currents are cross-pole in nature. In the LFA, currents may flow from one air-gap face of the plate to the opposite air-gap face across the thickness, since they flow in opposite directions in the two faces. In the TFA, on the other hand, currents flow from one pole to the other within the same air-gap face or on the side face (Fig.7.2b), since they flow in the same direction in the two air-gap faces. In general, however, both x and y components (y is in the direction of plate-thickness) of currents will exist on the side faces in the end region. However, when the plate thickness is large, the electromagnetic fields in one half of the plate is independent of that in the other, so that

the end-currents would be cross-pole in nature.

As the magnitudes of the currents in a plate of finite width would be different from those obtained by the non-linear theory (Chapter 5), the air-gap flux density and its distribution over the active width would also be different. Changes in the magnitudes of current and flux densities are, however, governed by the machine dimensions and the nature of the eddy-current reaction.

For a given primary m.m.f., the expressions for the air-gap flux/pole are given by equations (6.32) and (6.56) for longitudinal and transverse flux arrangements respectively, and they apply approximately to the present machine with an end-strip plate (Fig.7.1a). For the weak eddy-current reaction, the expressions are modified to equations (6.33b) and (6.57b) respectively; which are seen to be independent of the parameters of the material of the plate ($\rho$, a and b). Thus so long as the reaction field is weak, the flux/pole is not greatly influenced by any change in the resistance and reactance in the eddy-current path due to finite plate width. Although it is realised that a three-dimensional analysis may result in a different expression for flux/pole, these equations predict that magnitudes of flux/pole for the

cases of a wide* and a narrow** plate, where the impedance to eddy-current path is higher than that in an end-strip plate, will be very little different from those obtained for the end-strip plate.

The nature of the eddy-current reaction field (i.e. whether it is strong or weak) is determined largely by machine dimensions such as the pole-pitch, the air-gap length and the thickness of the plate. These dimensions may be such that the magnitude of Q (equations (6.16) and (6.39)) is less than unity at all excitations, so that the machine may be said to have a weak eddy-current reaction field (see Section 7.1). In such a case, the eddy-current loss in the plate is proportional to the conductivity of the plate (c.f. for a strong reaction field, the loss is proportional to the resistivity of the plate). Physically this means that since the eddy-current reaction is weak, any change in the magnitude of eddy-current reaction has little effect on flux/pole. Thus, for a given primary m.m.f., the air-gap flux remains substantially constant irrespective of changes in plate impedance.

In addition to a weak eddy-current reaction field,

---

* A wide plate is one whose width is greater than the active width of the machine.

** A narrow plate is one whose width is the same as the active width of the machine.

the ratio of active width to pole-pitch influences the magnitude of air-gap flux/pole; the larger the ratio, the less the change in flux/pole for a given primary excitation.

In considering the distribution of the y-component of air-gap flux density (i.e. normal to the plate surface), it may be noted that in an end-strip plate, currents are virtually z-directed everywhere in the active region and close their paths in the end-strips, so that the y-component of air-gap flux density will be uniformly distributed along the z-direction, i.e. the active width. In the wide plate, currents can find an easy path (a path of minimum impedance between the poles) outside the active region and thus there should be little change in the y-component of air-gap flux density along the active width. The m.m.f. due to cross-pole currents within the active width, in the case of the narrow plate, does, however, affect the distribution of this flux density, but the effect is small since the circulation of eddy current within the active region is itself minimal, the eddy currents being forced by the primary m.m.f. to flow in the ends and side faces of the plate. The m.m.f. due to cross-pole currents is negligible in the longitudinal flux arrangement (Fig. 7.2a), since they flow in opposite directions in the two halves of the plate. It is only in the case of the transverse flux arrangement (Fig.7.2b) that the effects of the m.m.f.s due to cross-pole currents may be important; but if the reaction field is weak and the ratio of active width to pole-pitch is large, any

variation in eddy-current reaction will have little effect on flux/pole.

It may, therefore, be observed that irrespective of the type of plate used, for a given primary m.m.f., the air-gap flux, in a model of Fig.3.1 (but incorporating finite plate-width), remains substantially constant and the variation of the y-component of air-gap flux density along the active width is negligible so long as the machine dimensions are such that the eddy-current reaction is weak and the ratio of active plate width to pole-pitch is greater than unity.

For sinusoidal air-gap flux, the e.m.f. induced in the plate is directly proportional to the air-gap flux, so that for a given primary m.m.f., approximately equal voltages would be induced in the wide, narrow and the end-strip plates if the value of Q is less than unity. But in the wide and narrow plates, a part of this induced e.m.f. will be required to drive the currents in the end region and therefore, compared to the end-strip plate, there will be less e.m.f. available in the active region.

The reduction of e.m.f. in the active regions of the wide and the narrow plates results in lower current densities in the active regions and this, in turn, results in a reduction of eddy-current loss in the plates for a given primary excitation. This effect is termed as

'finite-width effect' in this thesis.

The effect of finite width on current and flux distributions and on eddy-current power loss is usually termed 'finite-length effect' or simply 'end-effect' in published works. Some of the attempts to account for this effect are discussed in the following section with a view to introducing the analytic method used in this thesis.

## 7.3 A BRIEF SURVEY OF LITERATURE*

The simplest and most direct method of accounting for the effect of finite width on eddy-current power loss is to introduce into the linear solutions either a 'resistivity multiplying factor'[11,64], a 'loss reduction factor'[65,66] or an 'impedance multiplying factor'[67], which accounts for the increased impedance of eddy-current paths and the change in power loss.

An early work incorporating a resistivity multiplying factor was that by Gibbs[11], who recognised that the currents in the secondary flowed not only in the air-gap surface, but also in the side faces and on the back (i.e. unexcited) face of the solid-iron section. He suggested a resistivity multiplying factor (> 1) on the assumption that the permeability and the thickness

---

* the word 'machine', used in this section, refers to a solid-secondary rotating machine.

of the end-region were the same as those of the active part of the machine. He also noted that the end-region currents should follow a path of minimum resistance. While such considerations of the distribution of end-currents are logical, the assumptions about end-region permeability and thickness need more justification.

In connection with his work on eddy-current coupling, James[68] offered a simpler treatment of end-effect than Gibbs's[11]. He considered the end-region as a thin conductive sheet of finite width with a potential distribution defined along the boundary between the end and the active regions. On the assumption that the currents were only resistance-limited, he obtained the ratio of end-region to active region loss; computed values for this ratio agreed well with experimental results.

Although James[68] considered the x and z-components of current density in the end region, the current density in the active region was assumed to be z-directed only. He did not define the width of the end region in the model, although he had shown that for a ratio of end-region width to pole-pitch greater than 0.4, the width of the end region may be considered as infinite. James's work showed that the use of copper end-rings would mean negligible loss in the end region.

To incorporate the effects of finite width, many

authors[30,67,69,70] have offered three-dimensional analyses. These analyses are the most complete solutions; but since it is impossible to include magnetic non-linearity in three-dimensional analyses, these treatments consider linear magnetisation only, although the effects of non-linearity are often included in the final solutions[30]. All three-dimensional analyses assume an idealised model for the machine under consideration. It is assumed in these theoretical models that the machine may be considered as one of an infinite array of machines, placed end-to-end, whose lengths were equal to the active length of the actual machine. Wood and Concordia[69], and later Angst[70], assumed that the z-directed current sheet on the primary flowed in one direction over the whole of the rotor length but reversed at the ends of the active length. The z-directed current sheet may, thus, be described by a Fourier series and a solution obtained in series form. However, in such treatments no account is taken of the primary end-region currents. Preston and Reece[22] suggested modification of the primary current sheet to allow for the end-region currents, when the secondary was wider than the stator (i.e. primary), by allowing the z-directed current to attenuate beyond the active length. However, in the active region, they assumed neither the x-component of current density nor any variation along the z-direction of the z-component of

current density. Bowden[30] proposed a more realistic approach of considering (like Gibbs[11]) the developed length (i.e. to include side faces and the back face of the secondary, rather than the active length of the air-gap surface only) of the secondary for the path of end currents. In his model, Bowden considered the z-directed current sheet to be constant only over a proportion of the developed length (i.e. over active length only) and the x-directed current sheet to be present where the z-directed current sheet ends. This resulted in the electromagnetic field quantities in the air-gap and in the solid-iron secondary to be attenuated beyond the active length of the secondary, thus showing the soundness of such assumptions. He obtained a finite-length factor from the consideration of losses in a machine with and without end-effects. Bowden also obtained the effect of finite length on flux/pole and included the effect of magnetic non-linearity on finite-length effect (Section 7.7.2). However, Bowden's solution applied to machines with strong eddy-current reaction field (i.e. $Q > 1$) only, as against the present treatment of weak eddy-current reaction field (i.e. $Q < 1$, Section 7.2).

Because of their three-dimensional nature, these analyses are the most accurate obtainable. However, since the idealised models consist of an array of machines placed end-to-end, these analyses imply that the electro-magnetic field quantities of any individual machine is

not affected by the presence of other electromagnetic fields in the immediate vicinity, which is an over-simplification. The models also imply that the end region of the primary contains high permeability iron, while in practice, the permeability is that of air. A yet more accurate model would incorporate the variations of both z and x-components of current densities within the active region.

Many authors[22,71,72] offer three-dimensional analyses, but do not compare the eddy-current loss in a machine having end-effect with that in a machine having no end-effect. Preston and Reece[22] obtained good agreement between their solutions and experimental results, but the solutions were complicated and failed to single out terms which show the effect of end-region currents. In Malti and Ramakumar's[71] analysis of eddy-current couplings, the end-effects were also implicit. But they assumed only z- and x-components of current flow and did not consider the y-component in the end region in their three-dimensional analysis. Also they did not consider the variation of permeability with depth. Thus their work did not consider magnetic non-linearity which has a considerable influence on finite-width effect. In Boldea, Rahman and Nasar's work[72], the end-effects were implicit; but they included the effect of finite thickness in addition to finite-width effect. They also considered the effects of magnetic non-linearity (Section 7.7.2). However,

their work had its limitations which may be summarised in their own words, "--- the theory is applicable to the case when the rotor has a finite thickness. If the rotor is considerably thick, the correlations between the measured and computed characteristics are not very good".

All three-dimensional analyses, so far discussed, obtain solutions in series form, which, because these analyses are complete, are the most accurate obtainable. However, the series form of solutions is complicated and lengthy, and the results may be obtained only by means of a computer. A non-series or closed form of solution, although it incorporates necessary approximations, does not require lengthy computation. Such solutions are sufficiently accurate in most applications and the expressions obtained are compact, simple and conceptually easier than the series form of solution.

In closed form, the solutions obtained by Yee[67], Russell and Norsworthy[65] and Woolley and Chalmers[66] are notable. Yee[67] assumed an axial (i.e. z-directed) current sheet of the primary excitation to be constant over the total axial length. He assumed that the axial component of eddy-current density decreased to zero at the ends of the axial length of the rotor (i.e. the secondary). In his linear analysis, Yee obtained two-dimensional current densities on the rotor surface. In order to account for end effects, he obtained an impedance multiplying factor

in closed form, since the air-gap impedance was calculated on the basis of radial (i.e. y-directed) component of flux density. He offered physical interpretations of his end-effect factor and showed that for large values of the ratio of active length to pole-pitch, this effect was small. Yee's solution is a rigorous one, but fails to predict the electromagnetic field components at the ends of the rotor.

Russell and Norsworthy[65] considered eddy currents induced in a thin conducting shell, placed in the air-gap of a screened-rotor induction motor. Since the thickness of the shell was considered to be small compared with the mean radius (of the cylindrical rotor), variation of current density over the shell-thickness was neglected, thus making the treatment two-dimensional. Assuming axially-constant radial air-gap flux density, they obtained correction factors for the reduction of power loss in the shell for both an open-ended shell and a shell with end-rings of zero resistance. Their work showed that the end-effect was very pronounced in the absence of such end-rings and that for large values of the ratio of active length to pole-pitch, this effect was small. In as much as they assumed axially-constant air-gap flux, considered no variation of their two-dimensional electromagnetic fields over the shell-thickness and considered continuity conditions at the boundary

between the active (i.e. region 1) and end (i.e. region 2) regions, Russell and Norsworthy's analysis resembles the present work (Section 7.4).

For the merits of being simple, straightforward, and yet accurate, the theory proposed by Woolley and Chalmers[66] is notable. They developed the solution for solid-iron rotor induction motor when the rotor was fitted with conducting end-rings, but included the case of no end-rings in their final solutions. By considering small equivalent thicknesses for the uniform flow of two-dimensional current densities both in the active as well as in the end regions, they proposed correction factors for the power loss in a solid-iron rotor. Their work has shown that unless the end-region has zero-resistivity end-rings, end-effects may be pronounced. Like other authors[65,67] Woolley and Chalmers also obtained that for large values of the ratio of active length to pole-pitch, end-effect was small. They extended their work to cover end-regions of arbitrary form and the sound theoretical basis of their work was shown by the fact that the rotor loss was obtained as being independent of the form of end region, as long as end-region was continuous through the rotor axis. The theoretical model assumed in the present treatment (Section 7.4.1) considers, like Woolley and Chalmers', a solid-iron body with conducting end-strips, no variation of air-gap flux density in the z-direction and small thicknesses near the surfaces for uniform current-

density distribution. There are, however, certain basic differences between the two treatments and these are discussed in Section 7.10.

In most of the literature referred to here, end-effects are considered in an infinitely thick secondary and eddy currents are due essentially to single-sided excitation. In this thesis a solid-iron plate of finite thickness is being considered and eddy currents are due to double-sided excitations and, in the following section, a solution is developed for finite-width effect (i.e. end-effect) which includes these constraints. The effect of magnetic non-linearity is included in Section 7.7.

## 7.4 A SOLUTION FOR FINITE WIDTH EFFECT

### 7.4.1 The Model

The model of Fig. 7.3a shows the cross-section of the plate in the y-z plane, together with two conducting end-strips at its ends. The plate has a resistivity, $\rho$, which is different from the resistivity, $\rho_e$, of the end-strips. The end-strips each have widths $d_e$ which are small compared with half-width of the plate, $L/2$.

The effectiveness of the end-strips depends on the resistivity and permeability of their material, their widths and also the nature of contact with the solid iron. Obviously, very low values of both resistivity and permeability are preferred and copper is

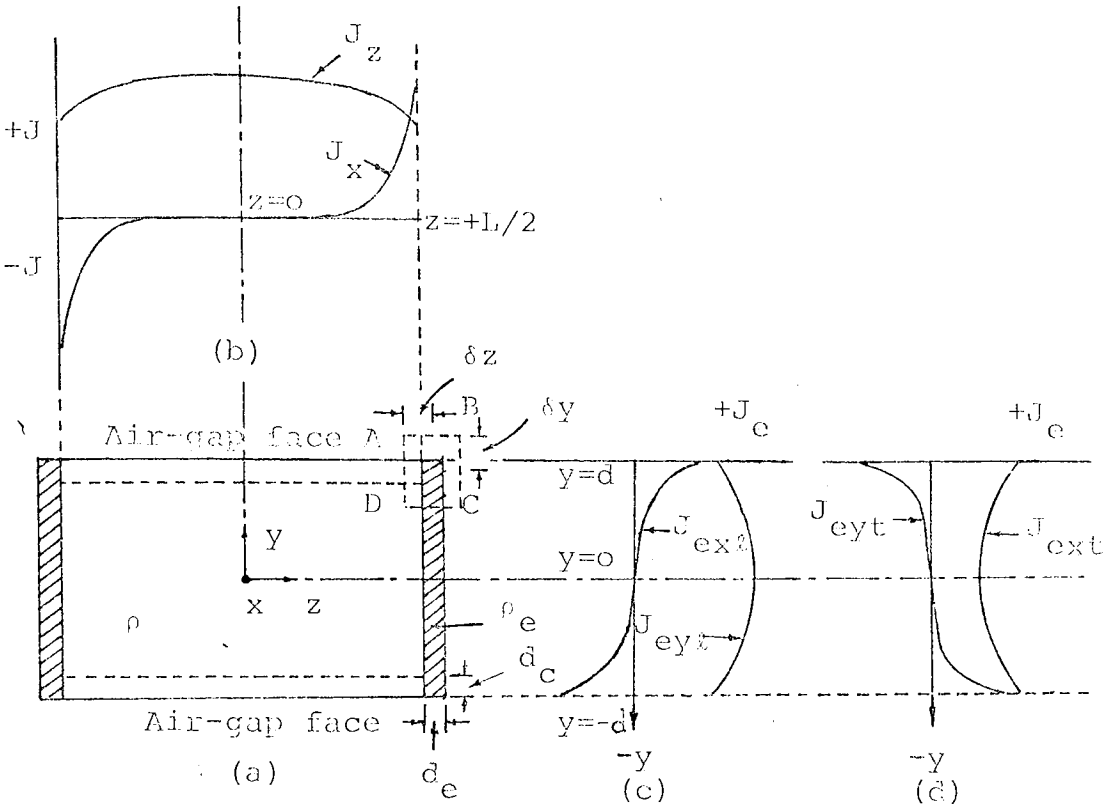


Fig. 7.3 The model considered to account for the finite width effect.

(a) Cross-section (in the y-z plane) of the solid-iron plate with conducting end-strips.

(b) Assumed distributions of $J_z$ and $J_x$ in the plate over the active width.

(c and d) Assumed distributions of $J_{ex}$ and $J_{ey}$ in the end-strips over the plate thickness for (c) longitudinal and (d) transverse flux arrangement.

a very good choice for this purpose[44,66,68]. While it is realised that in a practical arrangement of travelling wave heating, solid-iron plates are highly unlikely to be used in conjunction with conducting end-strips

as shown in Fig. 7.3a, this model will be retained for the sake of analysis. Once a solution for this model is obtained, the effects of the more likely case of not having conducting end-strips may be studied. This is discussed in detail in Section 7.8.3.

As has been mentioned in Section 7.2, the current densities in the active part of the plate will have both x and z-components. It is realised that at the centre of the plate width (i.e. at z=0), there will be no x-component of current density and only the z-component will be obtained. Towards the ends of the plate width (i.e. at $z \simeq \pm L/2$), however, the x-component of current density will increase. Fig. 7.3b shows the assumed distributions of current densities along the plate width.

In the end-strips (i.e. in the end region), the current densities are assumed to have x and y-components only. In order that the currents can flow into the end-strips, z-component of current density must also exist in the end-strips. However, if the width of the end-strips is small compared with both the active width and the pole-pitch of the primary, this component would be small compared with the x and y-components of current density. The loss produced by the z-component would, therefore, be insignificant compared with that due to the other two components. Thus the z-component of current density is neglected in the end-strips.

The x and y-components of current density will attenuate with depth from the surfaces of the end-strip and the assumed natures of their attenuations are given in Figs. 7.3c and 7.3d for longitudinal and transverse flux arrangements respectively. The symmetrical natures of their distributions about the y=0 plane is notable. (The electromagnetic field quantities in the end-strips are designated by a further suffix e, e.g. $J_{ex}$, $J_{ey}$, etc.).

For the purpose of analysis, the current density in the active part of the plate will be assumed to be uniformly distributed over a small thickness $d_c$ near the surface, where $d_c$ is small compared with the half-thickness, d, of the plate. Both the linear and non-linear theories presented earlier point out that the currents in the plate are, in fact, confined within a thin layer at the surface. Many previous authors[44,65,66] have retained this skin depth concept. In order to allow for the variation of current magnitudes along the z-direction, the current density itself is considered variable in the z-direction, so that the concept of small thicknesses having uniform current-density distribution may be retained. The concept of $d_c$ is, in reality, a concept of effective thickness in so far as it is not obtained as a 'skin depth' or a 'depth of penetration'. Only an effective value of this thickness $d_c$ may be obtained from the consideration of equivalence of some

other quantities, e.g. power loss invariance in the present work (Section 7.7.3).

Likewise, in the end-strips the currents are assumed distributed uniformly over the thickness $d_e$. The attenuations of currents from the air-gap surface to the inside of the end-strips are accounted for by the nature of the current density distribution, (Figs. 7.3c and 7.3d).

In this model, the positions of the primary windings have not been shown, because, it has been proved[65,66] that the loss in the secondary is independent of the end-region extension so long as it is continuous through the z-axis. However, it will be assumed in the above model that the active region of the plate extends to $\pm L/2$ and end-strips are beyond the active region.

In the above model, the air-gap flux density will be assumed to have no variation in the z-direction. It has been explained in Section 7.2 that the variation of the air-gap flux density in the z-direction is determined by the nature of the eddy-current reaction field in the plate. When the reaction field is weak, (and this is the case being considered) the variation of air-gap flux density along the z-direction is negligible. Many authors[11,65,66,72] have retained the concept of axially (i.e. along z-direction) constant air-gap flux density.

Apart from the condition of constant air-gap flux

density along the z-direction, weak eddy-current reaction field in the plate implies that the air-gap flux is approximately independent of the plate impedance. Thus, for a given primary excitation, the analysis may be carried out in terms of current-density distribution in the plate, since the e.m.f. induced in the eddy current paths is constant.

In the above model, it will also be assumed that no flux enters the end-strips. It is recognised that such an assumption neglects the fringing flux, but is, nevertheless, justified from experimental results[22]. Fringing flux is generally small and is neglected by many previous authors[65,66,68].

7.4.2 The Assumptions

The assumptions for the present solution of finite width effect have been discussed in Sections 7.2 and 7.4.1 in detail. However, they are summarised here for convenience. The assumptions are

(i) The current density in the solid-iron plate has x and z-components. $J_y=0$ in the plate.

(ii) The current density in the end-strips has x and y-components only. $J_{ez}=0$ in the end strips.

(iii) The current densities are distributed uniformly through a thickness $d_c$ near the surfaces in the solid-iron plate ($d_c << d$) and through a width $d_e$ of the end-strips ($d_e << L/2$).

(iv) The plate has a weak eddy-current reaction field, so that the machine acts as a constant-flux one for a given primary excitation.

(v) There is no variation of air-gap flux density in the z-direction. i.e. $\frac{dB_y}{dz} = 0$.

(vi) Negligible flux enters the end strips. i.e. $B_{ez} \to 0$.

(vii) The m.m.f. on the plate surface varies sinusoidally in space and time.

7.4.3 The Boundary Conditions

In the model of Fig. 7.3a, y=0 and z=0 may be recognised as axes of symmetry and the solution obtained will be subject to the boundary conditions at these axes. In addition, certain other boundary conditions need to be formulated at z=±L/2 and y=±d.

It is realised that the distribution of current density may be complex at the interfaces at z=±L/2. For this analysis, it will be assumed that the interface between solid-iron and end-strips is perfect and that the continuity condition for the e.m.f. is maintained. Applying Kirchoff's law at the rectangular section ABCD in Fig. 7.3a

$$d_c J_z \Big]_{z=(L/2)+(d_e/2)-\delta z} + d_e J_{ey} \Big]_{y=d-(d_c/2)-\delta y} = 0$$

It has been assumed that $(L/2) \gg d_e$ and $d \gg d_c$ and $\delta z$ and $\delta y$ may be made vanishingly small. Hence, in the

limit,

$$d_c J_z \Big]_{z=L/2} = - d_e J_{ey} \Big]_{y=d} \qquad (7.1)$$

Also at the rectangle ABCD,

$$\rho J_x \Big]_{z=(L/2)+(d_e/2)-\delta z} = \rho_e J_{ex} \Big]_{y=d-(d_c/2)-\delta y}$$

from which, in the limit,

$$\rho J_x \Big]_{z=L/2} = \rho_e J_{ex} \Big]_{y=d} \qquad (7.2)$$

Equations (7.1) and (7.2), therefore, define the boundary conditions at the interfaces at $z=\pm L/2$, as obtained on the surfaces ($y=\pm d$).

With reference to the assumed distributions of $J_x$ and $J_z$ in the plate in the z-direction (Fig.7.3b), $J_x(z) = -J_x(-z)$ and $J_z(z) = J_z(-z)$. Since the current densities are continuous along z, therefore, in the plate

$$J_x \Big]_{z=0} = 0 \qquad (7.3)$$

and

$$\frac{dJ_z}{dz} \Big]_{z=0} = 0 \qquad (7.4)$$

Equations (7.3) and (7.4) define the boundary conditions at the axis of symmetry, z=0.

In addition to these, two more boundary conditions will apply in the end region at the other axis of

symmetry y=0. These conditions, however, will be determined by the arrangements of poles on the two sides of the plate as shown by Figs. 7.3c and 7.3d.

Under longitudinal flux arrangement, the preferred direction of end-currents may be cross-thickness or y-directed[5] depending on the plate thickness. Cross-pole or x-directed currents will, however, exist. Fig. 7.3c shows the assumed variation of these components of current density and, as before, this arrangement of poles is designated by a further suffix $\ell$ with all electromagnetic field quantities. It may be seen that $J_{ex\ell}(y) = -J_{ex\ell}(-y)$ and $J_{ey\ell}(y) = J_{ey\ell}(-y)$. Thus

$$J_{ex\ell}\Big]_{y=0} = 0 \qquad (7.5)$$

and

$$\frac{dJ_{ey\ell}}{dy}\Big]_{y=0} = 0 \qquad (7.6)$$

Under transverse flux arrangement, the preferred direction of end-currents may be cross-pole or x-directed [5]. y-component of currents may, however, exist. Fig. 7.3d shows the assumed variation of these components of current density and, as before, this arrangement of poles is designated by a further suffix t with all electromagnetic field quantities. It may be seen in Fig. 7.3d that $J_{ext}(y) = J_{ext}(-y)$ and $J_{eyt}(y) = -J_{eyt}(-y)$ and thus

$$J_{eyt}\Big]_{y=0} = 0 \qquad (7.7)$$

and

$$\left.\frac{dJ_{ext}}{dy}\right]_{y=0} = 0 \qquad (7.8)$$

7.4.4 Expressions for Current Densities

7.4.4.1 General

The current densities in the model are assumed to have z and x-components in the solid iron and x and y-components in the end region. In this section, expressions will be obtained for these current densities subject to the assumptions and the boundary conditions outlined before. As in all previous chapters, the analysis here will be limited to y=+ve, i.e. the upper half of the plate only.

7.4.4.2 Current Densities in the Solid-iron Plate

When the plate is infinitely wide, only the z-component of current density will exist within the boundaries of the model. The case of an infinitely wide plate may be simulated by a plate with end-strips of zero resistivity. For such a plate and since the m.m.f. is assumed sinusoidally distributed in the x-direction,

$$\left.\begin{aligned} J_{zo} &= \hat{J}_z \cos qx \qquad (7.9) \\ \text{and} \qquad & \\ J_{xo} &= 0 \qquad (7.10) \end{aligned}\right\} \text{at all values of z}$$

where $q=\pi/\tau$ and $\tau$ = pole-pitch, $\hat{J}_z$ is the maximum amplitude of current density in the z-direction and $J_{zo}$ and $J_{xo}$ are the values of $J_z$ and $J_x$, respectively, when

end-strips have zero resistivity.

But when end-strips of finite resistivity are considered, the situation is different from those described by equations (7.9) and (7.10), and $J_x \neq 0$ except at z=0. However, the current densities in the plate must satisfy the condition div J=0, so that,

$$\frac{\partial J_x}{\partial x} + \frac{\partial J_z}{\partial z} = 0 \qquad (7.11)$$

Since the current densities in the plate are assumed uniformly distributed over a small thickness $d_c$ near the surface, there is no variation in the y-direction. Thus, from the condition curl $E = -\frac{\partial B}{\partial t}$,

$$\frac{\partial J_z}{\partial x} - \frac{\partial J_x}{\partial z} = \frac{1}{\rho}\frac{\partial B_y}{\partial t} \qquad (7.12)$$

Differentiating equation (7.12) with respect to z and using the assumption (v) of section 7.4.2,

$$\frac{\partial^2 J_z}{\partial x \partial z} - \frac{\partial^2 J_x}{\partial z^2} = 0 \qquad (7.13)$$

Differentiating equation (7.11) with respect to x, and subtracting from equation (7.13),

$$\frac{\partial^2 J_x}{\partial x^2} + \frac{\partial^2 J_x}{\partial z^2} = 0 \qquad (7.14)$$

Equation (7.14) is Laplace's equation in two dimensions and its solution for the present case is given by

$$J_x = \{A_1 \exp(qz) + B_1 \exp(-qz)\}\sin qx \qquad (7.15)$$

where $A_1$ and $B_1$ are the constants to be obtained from the boundary conditions. From the boundary condition of equation (7.3), $A_1 = -B_1$ and letting $A_1 = -B_1 = C_1/2$, equation (7.15) becomes

$$J_x = C_1 \sinh qz . \sin qx \qquad (7.16)$$

$C_1$ is a constant to be found from the boundary conditions at the interface of the plate and end-strips. However, it may be noted that when $\rho_e = 0$, $J_x = 0$ (equation 7.10), and therefore according to equation (7.16), $C_1 = 0$.

From equations (7.11) and (7.16), the expression $J_z$ may be obtained as

$$J_z = - C_1 \cosh qz . \cos qx + C_o \qquad (7.17a)$$

where the constant of integration, $C_o$, may be evaluated from the fact that when $\rho_e = 0$, $J_z = \hat{J}_z \cos qx$ and $C_1 = 0$. Thus

$$J_z = (\hat{J}_z - C_1 \cosh qz) \cos qx \qquad (7.17)$$

Equation (7.17) shows that when end-strips of finite resistivity are used, $J_z$ decreases towards the end of the active width due to the existence of predominantly cross-pole currents; although at the centre of active width i.e. at $z=0$, this decrement is a minimum.

7.4.4.3 Current Densities in the End-strips

In the end-strips, the current densities have x and y-components ($J_{ex}$ and $J_{ey}$, respectively) only, which

must satisfy the condition div J=0, and, hence,

$$\frac{\partial J_{ex}}{\partial x} + \frac{\partial J_{ey}}{\partial y} = 0 \qquad (7.18)$$

According to the assumption that negligible flux enters the end-strips, curl $E_e$=0 and since the currents are assumed distributed uniformly through $d_e$ and the z-component of current density is zero, therefore,

$$\frac{\partial J_{ex}}{\partial y} - \frac{\partial J_{ey}}{\partial x} = 0 \qquad (7.19)$$

From equations (7.18) and (7.19),

$$\frac{\partial^2 J_e}{\partial x^2} + \frac{\partial^2 J_e}{\partial y^2} = 0 \qquad (7.20)$$

Equation (7.20) shows that both the x and y-components of current densities in the end region satisfy the Laplace's equation in two dimensions. Their solutions for the stated conditions will be

$$J_{ex} = \{A_2\exp(qy)+B_2\exp(-qy)\} \sin qx \qquad (7.21)$$

and

$$J_{ey} = \{-A_2\exp(qy) + B_2\exp(-qy)\}\cos qx \qquad (7.22)$$

The constants $A_2$ and $B_2$ have, first, to be assessed with respect to the particular pole arrangements being considered and then, evaluated from boundary conditions at the interfaces.

In longitudinal flux arrangement, the relation between $A_2$ and $B_2$ may be obtained from equations (7.21)

and (7.5) (or alternately, from equations (7.22) and (7.6) ). Thus $A_{2\ell} = -B_{2\ell}$ (Further suffix $\ell$ denoting longitudinal flux arrangement) and letting $A_{2\ell} = -B_{2\ell} = C_{2\ell}/2$, the current densities are given by

$$J_{ex\ell} = C_{2\ell}.\sinh qy.\sin qx \qquad (7.23)$$

and

$$J_{ey\ell} = -C_{2\ell}.\cosh qy.\cos qx \qquad (7.24)$$

In transverse flux arrangement, the relation between the constants $A_{2t}$ and $B_{2t}$ (further suffix t denoting transverse flux arrangement) may be obtained from equations (7.21) and (7.7) (or alternately from equations (7.22) and (7.8) ). Thus $A_{2t} = B_{2t}$ and letting $A_{2t} = B_{2t} = C_{2t}/2$, the current densities are given by

$$J_{ext} = C_{2t}.\cosh qy.\sin qx \qquad (7.25)$$

and

$$J_{eyt} = -C_{2t}.\sinh qy.\cos qx \qquad (7.26)$$

The constants $C_1$ and $C_2$ will be evaluated in the following sections, where, from the considerations of power loss, finite width factors will be introduced.

## 7.5 FINITE WIDTH FACTOR FOR LONGITUDINAL FLUX ARRANGEMENT

### 7.5.1 Evaluation of constants $C_{1\ell}$ and $C_{2\ell}$

The constants $C_{1\ell}$ and $C_{2\ell}$ may be obtained by substituting the current density expressions, as obtained in section 7.4.4, into equations (7.1) and (7.2). After some manipulations, $C_{1\ell}$ and $C_{2\ell}$ are obtained as

$$C_{1\ell} = \frac{\hat{J}_{z\ell}}{\cosh q\frac{L}{2} + \eta_\ell . \sinh q\frac{L}{2} . \coth qd} \tag{7.27}$$

and

$$C_{2\ell} = \frac{\rho}{\rho_e} . \frac{\sinh q\frac{L}{2}}{\sinh qd} . \left[\frac{\hat{J}_{z\ell}}{\cosh q\frac{L}{2} + \eta_\ell . \sinh q\frac{L}{2} . \coth qd}\right] \tag{7.28}$$

where

$$\eta_\ell = \frac{\rho d_e}{\rho_e d_{c\ell}} \tag{7.29}$$

and $d_{c\ell}$ is the value of $d_c$ for longitudinal flux arrangement.

7.5.2 Loss in the Plate and in End-strips

The total loss in the plate and end-strips, $P_\ell$, is given by

$$P_\ell = P_{\ell c} + P_{\ell e} \tag{7.30}$$

where $P_{\ell c} = \int_\nu \rho |J_\ell|^2 d\nu$, is the loss in the plate and $P_{\ell e} = \int_\nu \rho |J_{e\ell}|^2 d\nu$, is the loss in end-strips. $|J_\ell|$ and $|J_{e\ell}|$ are the magnitudes of the resultant current density in the plate and in the end-strips respectively.

For a heater having 2p poles, each of pitch $\pi/q$, and of an active width of L and using the assumption of uniform current density distribution,

$$P_{\ell c} = \rho d_{c\ell} \int_{-p\pi/q}^{p\pi/q} \int_{-L/2}^{L/2} (J_{z\ell}^2 + J_{x\ell}^2) dz dx \tag{7.31}$$

where $J_{z\ell}$ and $J_{x\ell}$ are given by equations (7.17) and (7.16) respectively, together with equation (7.27).

For a plate of thickness 2d and using the assumption of uniform current density distribution,

$$P_{\ell e} = 2\rho_e d_e \int_{-p\pi/q}^{p\pi/q} \int_{o}^{d} (J_{ex\ell}{}^2 + J_{ey\ell}{}^2)\, dy\, dx \qquad (7.32)$$

where $J_{ex\ell}$ and $J_{ey\ell}$ are given by equations (7.23) and (7.24) respectively, together with equation (7.28).

Carrying out the integrations and using the results in equation (7.30),

$$P_\ell = \frac{p\pi}{q} \rho d_{c\ell} \left[ \hat{J}_{z\ell}{}^2 L - \frac{4\hat{J}_{z\ell} C_{1\ell}}{q} \cdot \sinh q \cdot \frac{L}{2} + \frac{C_{1\ell}{}^2}{q} \sinh qL + \frac{\rho_e d_e}{\rho d_{c\ell}} \cdot \frac{C_{2\ell}{}^2}{q} \cdot \sinh 2qd \right] \qquad (7.33)$$

The value of loss in an infinitely wide plate, i.e. in a plate with zero-resistivity end-strips, may be obtained from equation (7.33) by putting $\rho_e = 0$ and $C_{1\ell} = 0$. Thus if $P_{\ell O}$ gives the loss in the active width of an infinitely wide plate, then

$$P_{\ell O} = \frac{p\pi}{q} \cdot \rho d_{c\ell} \hat{J}_{z\ell}{}^2 L \qquad (7.34)$$

Equation (7.34) could, no doubt, be obtained by considering the flow of uniform current having an r.m.s. density of value $\hat{J}_{z\ell}/\sqrt{2}$ in the thickness $d_{c\ell}$ and over a length L.

Substituting the values of $C_{1\ell}$ and $C_{2\ell}$ from equations (7.27) and (7.28), respectively, into equation (7.33) and simplying, the expression for loss is finally given by

$$P_{\ell} = P_{\ell O}\left[1-\left(\frac{2}{qL}\right).\frac{\tanh q\frac{L}{2}}{1+\eta_{\ell}.\tanh q\frac{L}{2}.\coth qd}\right] \qquad (7.35)$$

where $P_{\ell O}$ is the loss in the active width of a plate having zero-resistivity end-strips and is given by equation (7.34), and $\eta_{\ell}$ is given by equation (7.29).

Equation (7.35) shows that the total loss in the plate and end-strips is less than the loss in the active width of a plate with zero-resistivity end-strips. Thus there is a reduction of power loss in the plate due to finite width effect; this is typical of constant flux machines.

7.5.3 Finite Width Factor

From equation (7.35), the effect of finite width on the power loss in the plate may be described by a finite width factor $K_{f\ell}$, given by

$$K_{f\ell} = \left[1-\left(\frac{2}{qL}\right).\frac{\tanh q\frac{L}{2}}{1+\eta_{\ell}.\tanh q\frac{L}{2}.\coth qd}\right] \qquad (7.36)$$

For plates with zero-resistivity end-strips $\eta_{\ell}\to\infty$, so that, from equation (7.36), $K_{f\ell}\to 1$ showing negligible finite width effect. For large values of plate thickness, $\coth qd\to 1$ and the finite-width factor, $K_{f\ell}$, becomes identical with those proposed by Woolley and Chalmers[66] and Russell and Norsworthy[65].

When the plate thickness is very small, $\coth qd$ becomes large and $K_{f\ell}$ tends to unity. This shows that the finite width effect is small in plates of small thickness

for the longitudinal flux arrangement. This could well have been logically deduced because in a practical arrangement, currents flowing along one surface may find an easy return path by flowing across the plate thickness.

Equation (7.36) shows that the finite width factor depends very much on the ratio of plate-width to pole-pitch. In order to reduce the finite width effect, therefore, the value of this ratio should be large.

In equation (7.36), $\eta_\ell$ incorporates the effects of varying $d_e$ and $d_{c\ell}$. It has different values for different plate thicknesses and plate and end-strip parameters, and to account for magnetic non-linearity; these will be discussed in detail later in this chapter. It may, however, be mentioned here that $\infty > \eta_\ell > 1$ and equation (7.36) shows that finite width effect is most pronounced for small values of $\eta_\ell$ and least pronounced for large values.

## 7.6 FINITE WIDTH FACTOR FOR TRANSVERSE FLUX ARRANGEMENT

### 7.6.1 Evaluation of Constants $C_{1t}$ and $C_{2t}$

Substituting equations (7.26) and (7.17) in equation (7.1) and equations (7.25) and (7.16) in equation (7.2), the values of the constants $C_{1t}$ and $C_{2t}$ may be obtained. Thus

$$C_{1t} = \frac{\hat{J}_{zt}}{\cosh q\frac{L}{2} + \eta_t \cdot \sinh q\frac{L}{2} \cdot \tanh qd} \qquad (7.37)$$

and

$$C_{2t} = \frac{\rho}{\rho_e} \cdot \frac{\sinh q\frac{L}{2}}{\cosh qd} \cdot \left[ \frac{\hat{J}_{zt}}{\cosh q\frac{L}{2} + \eta_t \cdot \sinh q\frac{L}{2} \cdot \tanh qd} \right] \quad (7.38)$$

where,

$$\eta_t = \frac{\rho d_e}{\rho_e d_{ct}} \quad (7.39)$$

and $d_{ct}$ is the value of $d_c$ for transverse flux arrangement.

The current density expressions in the plate are now given by equations (7.16) and (7.17) where $C_{1t}$ is given by equation (7.37) and the same in the end-strips are given by equations (7.25) and (7.26) where $C_{2t}$ is given by equation (7.38).

7.6.2 Loss in the Plate and in End-strips

The total loss in the plate and in the end-strips, $P_t$, is given by

$$P_t = P_{tc} + P_{te} \quad (7.40)$$

where, $P_{tc} = \int_v \rho |J_t|^2 dv$ is the loss in the plate, and

$P_{te} = \int_v \rho |J_{et}|^2 dv$ is the loss in the end-strips.

$|J_t|$ and $|J_{et}|$ are the magnitudes of the resultant current density in the plate and in the end-strips respectively.

For a heater of 2p poles, each of pitch $\pi/q$, and of active width L, and using the assumption of uniform current distribution through $d_{ct}$,

$$P_{tc} = \rho d_{ct} \int_{-p\pi/q}^{p\pi/q} \int_{-L/2}^{L/2} (J_{xt}^2 + J_{zt}^2) dz\, dx \qquad (7.41)$$

where $J_{xt}$ and $J_{zt}$ are given by equations (7.16) and (7.17) respectively, together with equation (7.37).

For a plate of thickness 2d and using the assumption of uniform current-density distribution through $d_e$,

$$P_{te} = 2\rho_e d_e \int_{-p\pi/q}^{p\pi/q} \int_{o}^{d} (J_{ext}^2 + J_{eyt}^2)\, dy\, dx \qquad (7.42)$$

where $J_{ext}$ and $J_{eyt}$ are given by equations (7.25) and (7.26) respectively, together with equation (7.38).

Carrying out the integrations and using the results in equation (7.40)

$$P_t = \frac{p\pi}{q} \cdot \rho d_{ct} \left[ \hat{J}_{zt}^2 L - \frac{4\hat{J}_{zt} C_{1t}}{q} \cdot \sinh q\frac{L}{2} + \frac{C_{1t}^2}{q} \cdot \sinh qL + \frac{\rho_e d_e}{\rho d_{ct}} \cdot \frac{C_{2t}^2}{q} \cdot \sinh 2qd \right] \qquad (7.43)$$

The value of loss in the active width of an infinitely wide plate, $P_{to}$, may be obtained from equation (7.43) by letting $\rho_e = 0$ and $C_{1t} = 0$. Thus

$$P_{to} = \frac{p\pi}{q} \cdot \rho d_{ct} \hat{J}_{zt}^2 L \qquad (7.44)$$

Equation (7.44) could also be obtained by considering the flow of uniform current having an r.m.s. density of value $\hat{J}_{zt}/\sqrt{2}$ in the thickness $d_{ct}$ and over a length L.

Substituting the values of $C_{1t}$ and $C_{2t}$ from equations (7.37) and (7.38) in equation (7.43) and carrying out the necessary simplifications, the expression for loss in the plate and in the end-strips is finally given by

$$P_t = P_{to}\left[1-\left(\frac{2}{qL}\right).\frac{\tanh q\frac{L}{2}}{1+\eta_t \tanh q\frac{L}{2}.\tanh qd}\right] \qquad (7.45)$$

where $P_{to}$ is the loss obtained in a plate having zero-resistivity end-strips, given by equation (7.44), and $\eta_t$ is given by equation (7.39).

### 7.6.3 Finite Width Factor

It may be seen in equation (7.45) that the effect of finite plate width is to reduce the loss in an infinitely wide plate by a finite width factor, $K_{ft}$, given by

$$K_{ft} = \left[1-\left(\frac{2}{qL}\right).\frac{\tanh q\frac{L}{2}}{1+\eta_t.\tanh\frac{L}{2}.\tanh qd}\right] \qquad (7.46)$$

The finite width factor $K_{ft}$ also accounts for the finite resistivity of end-strips, since, for end-strips of zero resistivity it reduces to unity. For large values of plate thickness $\tanh qd \to 1$ and the finite width factor, $K_{ft}$, becomes identical to those proposed by Woolley and Chalmers[66], and Russell and Norsworthy[65]. This similarity is natural, and perhaps necessary.

When the plate thickness is very small, $\tanh qd$

becomes very small and the factor approaches the form $\left[1 - \frac{\tanh q\frac{L}{2}}{q\frac{L}{2}}\right]$, which shows a marked finite width effect. This could also be logically deduced, because, when the plate thickness is small, the currents flowing across one air-gap surface do not find an easy return path (as in the case of longitudinal flux arrangement) and are constrained to follow the high resistance cross-pole path on the same air-gap surface.

Equation (7.46) shows that the finite width factor depends very much on the ratio of plate-width to pole-pitch; this ratio should be large in order to reduce the finite width effect.

Like $\eta_\ell$ in equation (7.36), $\eta_t$ is an important non-dimensional parameter in equation (7.46) and the observations made about $\eta_\ell$ in section 7.5.3 also apply here.

## 7.7 EFFECT OF MAGNETIC NON-LINEARITY

### 7.7.1 General

In the analysis so far, no account has been taken of the magnetic non-linearity of the material of the plate and the values $d_c$ and $d_e$ are yet to be obtained. The effect of magnetic non-linearity in plates of finite width may be accounted for by choosing a suitable value of $d_c$. Whereas the choice of $d_e$ has considerable influence on the power loss in the plate (Section 7.8),

magnetic non-linearity has very little effect on $d_e$ since end-strips are non-magnetic.

In the literature, various methods are suggested to account for the magnetic non-linearity in plates of finite width. In the following section, some of these methods will be discussed with a view to introducing the present treatment.

7.7.2 Methods of Accounting for Magnetic Non-linearity; a Brief Literature Survey

Combining the effects of magnetic non-linearity and finite width is analytically difficult because of the variation of permeability over the surface due to the variation of current densities. In the literature it is found that the effect of magnetic non-linearity is accounted for either by choosing a saturation flux density, $B_s$, or a value of effective permeability, $\mu_e$, for the iron.

Angst[70] and later Yee[67] used the rectangular B-H curve to account for magnetic non-linearity. However, both authors used the limiting non-linear theory for obtaining operational impedances which were multiplied by end-effect factors derived using linear theory. Yee and Wilson[73] accounted for the saturation of the flux due to the x-component of magnetic field strength only in the active region of the plate. However, they also used the limiting non-linear theory together with the linear analysis given by Yee[67] to account for the

end-effects. In the linear three-dimensional analysis of Boldea et al[72], the end-effects were implicit. However, in their analysis, non-linearity was included by the limiting non-linear theory 'in a special way'.

Bowden[30] accounted for magnetic non-linearity by introducing an equivalent constant permeability $\mu_e$ obtained from the consideration of invariance of the electromagnetic field, and therefore, of loss density, between the linear two-dimensional and the non-linear theories. In the opinion of the author, this is a logical step and while it offers accurate results, it avoids iterative solution. However, such equivalence of linear and non-linear solutions can only be truly obtained at the centre of the active width, i.e. at z=0.

Woolley and Chalmers[66] accounted for magnetic non-linearity by assigning an appropriate value to the small thickness near the surface over which current densities were assumed to be uniformly distributed, (i.e. $d_c$ of the present solution). However, they used the definition of the depth of flux penetration from the limiting non-linear theory in defining such thicknesses, but later modified it by a factor depending on finite width effect. In the present solution also, the effect of magnetic non-linearity will be accounted for by choosing an appropriate value for $d_c$, but, unlike the work of Woolley and Chalmers, the present model considers a plate of

finite thickness and two different pole arrangements, (i.e. LFA and TFA), so that any definition of $d_c$ must include the effects of these constraints in addition to the effect of magnetic non-linearity.

A convenient basis for the definition of $d_c$ would be to assume that for a given set of values of primary excitation, frequency and machine dimensions, the loss in the active width of an end-strip plate as obtained from the present solution may be equated to the loss obtained from the non-linear theory (Chapter 5) where finite-width effects were neglected. This is discussed further in the following section.

7.7.3 Definition of an Effective Value for $d_c$

Initially, the concept of $d_c$ was introduced as a means of making the problem amenable to analytic treatment. It is assumed that the current densities in the plate are uniformly distributed over a small thickness, $d_c$, (Section 7.4.1) and therefore, the z-component of current density at any depth within $d_c$ will also be the same as the z-component of current density on the surface of the plate.

In order to define an effective value for $d_c$, the surface value of the z-component of current density in a plate with zero-resistivity end-strips may be considered as that given by the present non-linear theory developed in Chapter 5. The total loss in the active region of a plate having zero-resistivity end-strips as obtained

from the solution of this chapter may then be equated to the loss (for the same active region) predicted by the present non-linear theory of Chapter 5 for the same surface current density.

Thus the choice of the effective value of $d_c$ is based on the assumptions that

(i) although the solution presented in this chapter (Section 7.4) considers two-dimensional fields for current density in the plate ($J_x$ and $J_z$), the non-linear one-dimensional theory may be used for the determination of $J_z$.

(ii) the current density $J_z$ obtained on the surface of a plate having negligible finite width effect and given by the present non-linear theory (Chapter 5) is the same as the current density on the surface of a plate having zero-resistivity end-strips and given by the present solution (Chapter 7), and

(iii) the loss in the active region of a plate having zero-resistivity end-strips (Sections 7.5.2 and 7.6.2) may be equated to the loss predicted by the non-linear theory (Sections 5.4.5 and 5.5.5).

The assumption (i) above tacitly implies that the theory predicting current densities in two dimensions is little affected by neglecting one. In fact, as will be shown in Section 7.9, the present analysis of finite width effect considering two-dimensional current densities

is very much one-dimensional in nature (i.e. $J_z >> J_x$), especially in the presence of end-strips, and as such, neglecting $J_x$ may be quite justified. In so far as a plate of finite width having zero-resistivity end-strips may be taken to simulate a plate of infinite width, assumption (iii) above is quite straightforward. Bowden[30] has also used a similar concept.

The choice of the value of $d_c$ will, of course, be influenced by the particular pole arrangements being considered. In the following sub-sections the values of $d_c$ will be obtained with regards to the longitudinal and transverse flux arrangements.

It may be mentioned here that when the plate is of a magnetically linear material, an effective value of $d_c$ may be obtained by equating the loss obtained from the linear two-dimensional theory (Chapter 3) to that obtained from the two-dimensional treatment of the present solution. The effective value for $d_c$ in that case is a function of the depth of penetration, $\delta (= 1/\alpha)$ and the thickness of the plate. This is discussed in detail in Appendix IV.

7.7.3.1 Effective Value of $d_{c\ell}$ for Longitudinal Flux Arrangement

The total loss per unit of surface area for this arrangement is given by equation (5.43). For a heater of active width L and having 2p poles, each of pitch $\tau/q$, the loss is obtained as

$$P_{y\ell d} = \frac{\hat{H}_{x\ell d}^{2}.\rho.\beta_{\ell}.\lambda^{2}}{4d(\lambda-1)} \cdot (2p\pi/q).L \qquad (7.47)$$

where $\lambda$ is given by equation (5.29).

For the same pole arrangement, the loss in the plate having zero-resistivity end-strips is given by equation (7.34), so that equating it to equation (7.47)

$$d_{c\ell} = \left(\frac{\hat{H}_{x\ell d}}{\hat{J}_{z\ell d}}\right)^{2} \cdot \frac{\beta_{\ell}.\lambda^{2}}{2d(\lambda-1)} \qquad (7.48a)$$

As mentioned in assumption (ii) of section 7.7.3, the value of $\hat{J}_{z\ell d}$ may be obtained, in this case, from equation (5.37), so that

$$d_{c\ell} = \frac{\beta_{\ell}}{R_{\ell}^{2}} \cdot \frac{2d(\lambda-1)}{\lambda^{2}} \qquad (7.48)$$

It may be seen in equation (7.48) that the value of $d_{c\ell}$ is always small compared with d and this applies irrespective of plate thickness, so that the assumption $d_{c\ell} << d$ is justified.

Using equations (7.48) and (7.29) in equation (7.36), the finite width factor for longitudinal flux arrangement, $K_{f\ell}$, including the effect of magnetic non-linearity, is given by

$$K_{f\ell} = 1 - \left(\frac{2}{qL}\right) \cdot \frac{\tanh q\frac{L}{2}}{1 + \frac{\rho d_e}{\rho_e d} \cdot \frac{R_\ell^2 \lambda^2}{2\beta_\ell(\lambda-1)} \tanh q\frac{L}{2} \cdot \coth qd} \qquad (7.49)$$

Equation (7.49) is the final form of expression for finite width factor and shows the effects of surface magnetic field strength (or in turn, primary excitation), frequency, finite plate thickness, the end-strip thickness, the resistivities $\rho$ and $\rho_e$ and the magnetisation curve of the material of the plate, in addition to the ratio of active width to pole-pitch. Fig. 7.4 shows the plot of $K_{f\ell}$ against $q\frac{L}{2}$ $(= \frac{\pi}{2} \cdot \frac{L}{\tau})$ for various values of plate-thickness and for given values of surface magnetic field strength, copper end-strip width and pole-pitch.

It may be seen from Fig. 7.4 and also from equation (7.49) that the finite width effect is quite pronounced for small values of the ratio of active width to pole-pitch and that the effect is quite negligible for higher values of this ratio. This applies at all plate thicknesses. Also evident from Fig. 7.4 is the fact that for plates of very small thickness, the effect of finite plate width is quite small at all values of the ratio of active width to pole-pitch. As already discussed in Section 7.5.3, this is to be expected in practice, since for small plate thickness, the end-currents find a low resistance return path across the plate thickness and, as such, the finite width effect is not pronounced in

this case.

7.7.3.2 Effective Value of $d_{ct}$ for Transverse Flux Arrangement

The total loss/area under this arrangement is given by equation (5.72) which, for 2p poles, each of pitch $\pi/q$, and for an active width of L, is given by

$$P_{ytd} = \frac{\hat{H}_{xtd}^2}{2} \cdot \rho\beta_t \cdot \left(\frac{2}{d} + \alpha_t\right) \cdot (2p\pi/q) \cdot L \qquad (7.50)$$

The loss in a plate of the same active width and having zero-resistivity end-strips is given, in this case, by equation (7.44). Thus, equating equation (7.50) to equation (7.44)

$$d_{ct} = \left(\frac{\hat{H}_{xtd}}{\hat{J}_{ztd}}\right)^2 \cdot \beta_t \cdot \left(\frac{2}{d} + \alpha_t\right) \qquad (7.51a)$$

In equation (7.51a), the expression for $\hat{J}_{ztd}$ may be obtained, according to the assumption (ii) of section 7.7.3, from equation (5.63), so that $d_{ct}$ is finally given by

$$d_{ct} = \frac{\beta_t}{R_t^2} \cdot \frac{1}{\left(\frac{2}{d} + \alpha_t\right)} \qquad (7.51)$$

It may be seen in equation (7.51) that $d_{ct}$ is small compared with d and this applies irrespective of the plate thickness and thus the assumption $d_{ct} << d$ is justified.

Using equation (7.51) and (7.39) in equation (7.46),

the finite width factor, including the effect of magnetic non-linearity, is given by

$$K_{ft} = 1 - \left(\frac{2}{qL}\right) \cdot \frac{\tanh q\frac{L}{2}}{1 + \frac{\rho d_e}{\rho_e d} \cdot \frac{R_t^2 (2+\alpha_t d)}{\beta_t} \tanh q\frac{L}{2} \cdot \tanh qd} \qquad (7.52)$$

Equation (7.52) is the final form of expression for finite width factor and shows the effects of surface magnetic field strength (i.e. primary excitation), frequency, finite plate thickness, the end-strip width, the resistivities $\rho$ and $\rho_e$, and the magnetisation curve of the material of the plate, in addition to the ratio of the active width to pole-pitch. Fig. 7.5 shows the plot of $K_{ft}$ against $q\frac{L}{2}$ for various values of half-thickness of the plate, d. The curves are drawn for a given value of surface magnetic field strength, copper end-strips of known width and a given pole-pitch.

It may be seen from Fig. 7.5, and also from equation (7.52), that the finite width effect is quite pronounced for small values of the ratio of active width to pole-pitch and less pronounced for large values of the same. Although this applies at all plate thicknesses, the finite width effect in this case is much higher than that in the longitudinal flux arrangement.

When the plate thickness is small, the finite width effect is quite large. As has been mentioned in Section

7.6.3, this is to be expected in practice, since the end-currents are, in this situation, constrained to flow in high resistance cross-pole paths. For large values of plate thickness, the end-currents are also cross-pole, but the resistance of their path is greatly reduced. This is shown in Fig. 7.5 where with an increase in plate thickness, the effect of finite width is seen to be reduced.

7.7.4 Influence of Pole Arrangements on $K_{f\ell}$ and $K_{ft}$

It is interesting to note that the curves of Fig. 7.4 and Fig. 7.5, are similar for large values of plate thickness, showing thereby, that the effect of the arrangement of poles on the two sides of the plate is negligible for thick plates. This is so because when the plate thickness is large, the electromagnetic field distributions in one half of the plate tend to be independent of the electromagnetic field distribution in the other half. With decrease in plate thickness, on the other hand, the curves of Fig. 7.4 and 7.5 diverge, showing thereby, the influence of pole arrangement on the finite width effect. The conclusion that, with decrease in plate thickness, the effect of finite width becomes less significant in the longitudinal flux arrangement and more significant in the transverse flux arrangement, is consistent with the physical interpretation of what happens in the plate itself. This is believed to show the strength of this

theory and provide its partial verification.

It may also be concluded that for higher loss in the plate, the longitudinal flux arrangement is preferred to the transverse flux arrangement.

## 7.8 CHOICE OF END-STRIP WIDTH, $d_e$

### 7.8.1 General

End-strip width $d_e$ was defined in Section 7.4.1 as the small width (compared with active width) over which the end-current densities were assumed uniformly distributed. The use of end-strips results in higher loss in the plate (for the kind of low Q heater being considered here) and the choice of the width of end-strips is always a compromise between high loss and the amount of end-strip material (e.g. Copper, which is expensive) required.

In this section two specific cases are considered,

(i) when the plate is fitted with end-strips, in which case the choice of $d_e$ is quite straightforward, and

(ii) when the plate is not fitted with end-strips, in which case an effective value of $d_e$ must be defined.

### 7.8.2 Choice of $d_e$ when the Plate is Fitted with End-strips

When the plate is fitted with end-strips, the width of such end-strips may be compared with the characteristic

depth of penetration $\delta_e \left(= \sqrt{\frac{2\rho_e}{\mu_o \mu_{en} \omega}}\right)$ * in the material of the end-strips. When the end-strip width is greater than (or equal to) $\delta_e$, the values of $\delta_e$ should be used for $d_e$[66], since the depth of penetration is electromagnetically equivalent to the depth over which the current density may be taken as being uniformly distributed. When the end-strip width is smaller than $\delta_e$, the value of end-strip width itself should be used for $d_e$.

However, the end-strip width should not be very small, because in that case currents may flow in the plate in parallel with the currents in the end-strips and much of the advantage of using the end-strips would be lost.

7.8.3 Effective Value of $d_e$ when the Plate is not Fitted with End-strips

If a plate is not fitted with low-resistivity end-strips, it does not mean that $d_e$=0, because currents in the end region have to find a return path within the plate itself, so that an effective value of $d_e$ may be defined. The absence of any low resistivity end-strips, however, means that there is no distinct interface at the end of the active width, and the currents have to flow within the same material, so that $\rho_e = \rho$. Since it is assumed that $d_e << L/2$ and only x and y-components of current densities are considered in the end-region, $d_e$

---

* $\mu_{en}$ is the relative permeability of the material of the end-strips.

is obtained at $z = \pm L/2$ whatever the actual width of the plate; this is in agreement with the conclusions of other authors[65,66].

So long as the currents close their paths in the end region, the boundary conditions formulated in Section 7.4.3 still apply. Thus, equation (7.2) becomes, with $\rho_e = \rho$,

$$J_x\Big]_{z=L/2} = J_{ex}\Big]_{y=d} \tag{7.53}$$

Equation (7.53) means that on the surface of the plate at $z = L/2$, the x-component of current density in the active region becomes equal to the x-component of current density in the end region. In other words, equation (7.53) holds good on the line of intersection of the planes $z = L/2$ and $y=d$.

Clearly, both x and y-components of current densities will arise in the end region and, of course, x and z-components of current densities will arise in the active region. Since the currents flowing to the end of the active region must find their paths partly in cross-pole (i.e. x-directed) and partly in cross-thickness (i.e. y-directed) directions, the condition to be satisfied on the same line of intersection of the planes $y=d$ and $z = L/2$ may be given as

$$\left[|J_z|^2 + |J_x|^2\right]_{z=L/2} = \left[|J_{ex}|^2 + |J_{ey}|^2\right]_{y=d} \tag{7.54}$$

Current densities in the active region have been assumed variable in the z-direction and those in the end region have been assumed variable in the y-direction, so that they assume particular values on the above line. Also since the currents are constrained to flow within the plate itself, their distribution along the above line must be governed by equation (7.54).

Using equation (7.53), equation (7.54) becomes

$$|J_z|^2\Big]_{z=L/2} = |J_{ey}|^2\Big]_{y=d} \tag{7.55}$$

The value of $|J_z|^2$ at $z = L/2$ may be obtained from equation (7.17) in conjunction with equations (7.27) and (7.37) for longitudinal and transverse flux arrangements respectively. The value of $|J_{ey}|^2$ at y=d may be obtained from equations (7.24) together with equation (7.28), for longitudinal flux arrangement and from equation (7.26) together with equation (7.39), for transverse flux arrangement. For both pole-arrangements this gives

$$\eta_\ell = \eta_t = 1 \tag{7.56}$$

And since $\rho = \rho_e$, this means

$$d_e = d_c \tag{7.57}$$

Thus, in the absence of conducting end-strips the effective value of end region width $d_e$ (over which end-currents are assumed uniformly distributed) may be taken to be the same as the effective value of the active region thickness $d_c$ (over which active region currents are assumed uniformly distributed). This applies irrespective of the pole-arrangements.

Using equation (7.56) in equations (7.36) and (7.46), the finite width factors in the absence of conducting end-strips may be obtained for longitudinal and transverse flux arrangements respectively. These factors are plotted against $q\frac{L}{2}$ for various values of half-thickness d (and for the same values of constants as in Figs.7.4 and 7.5) in Figures 7.6 and 7.7.

Comparing the curves of Fig. 7.6 with those of Fig. 7.4 for longitudinal flux arrangement (or the curves of Fig. 7.7 with those of Fig. 7.5 for transverse flux arrangement), it may be seen that in a given plate the finite width effect is, as expected, very much pronounced in the absence of end-strips. In a practical arrangement, this would mean that the end-currents no longer find the low resistivity return paths (as in an end-strip plate) and must flow in the high resistivity material of the plate itself to complete their paths. Thus a larger proportion of the induced e.m.f. in the plate would be required to drive them through the end

paths (cross-pole or cross-thickness), resulting in the induced e.m.f., and hence the eddy-current density, being reduced in the plate itself. The loss in the plate, which is proportional to the square of the current density, would be greatly reduced. This amounts to saying that the finite width effect would become more pronounced.

Figures 7.6 and 7.7 show the dependence of the finite width factors on the ratio of active width to pole-pitch and on the plate-thickness. Both figures show that with an increase in the ratio of active width to pole-pitch, the finite width effect is reduced and that with an increase in the plate-thickness, the finite width effect is increased under longitudinal flux arrangement and is decreased under transverse flux arrangement. For any plate thickness, therefore, the finite width effect is very much higher under transverse flux arrangement than under longitudinal one, so that if finite width effect is the only criterion, longitudinal flux arrangement of the poles should be chosen for higher loss.

## 7.9 ONE-DIMENSIONAL NATURE OF CURRENT DENSITY IN THE ACTIVE PART OF THE SOLID-IRON PLATE

### 7.9.1 General

As part of the analysis in this chapter, (i.e. finding the effects of finite plate width on loss), the components $J_x$ and $J_z$ of the current density in the plate were necessarily considered. However, as obtained in the

literature, $J_z$ is likely to be the dominant component of the two and a study of their relative magnitude reveals some interesting aspects about the two different pole-arrangements.

7.9.2 Current Densities at the End of Plate Width

At the centre of the plate width, z=0, and the x-component of current density, $J_x$, is zero (Fig. 7.16). Towards the ends of the active width, $J_x$ gradually increases and becomes significant at $z = \pm L/2$. $J_z$, on the other hand, has its highest value at the centre of the plate (i.e. at z=0) but decreases towards the ends of the active width (i.e. $z \simeq \pm L/2$). Therefore, the current densities at the end of the active width (i.e. at $z = \pm L/2$) only will be considered here in order to study their relative magnitudes.

The expressions for current densities $J_x$ and $J_z$ are given by equations (7.16) and (7.17), respectively, so that the ratio of their magnitudes at $z = \pm L/2$ is given by

$$\left|\frac{J_z}{J_x}\right|_{z=\pm L/2} = \frac{\hat{J}_z}{C_1 \sinh q\frac{L}{2}} - \coth q\frac{L}{2} \qquad (7.58)$$

The value of this ratio may now be obtained with particular regards to the arrangement of the poles.

7.9.3 One-dimensional Nature of Current Density in Longitudinal Flux Arrangement

In longitudinal flux arrangement, $C_1$ ($= C_{1\ell}$) is given by equation (7.27), so that using it in equation (7.58),

$$\left|\frac{J_{z\ell}}{J_{x\ell}}\right|_{z=\pm L/2} = \eta_\ell \coth qd \qquad (7.59)$$

Thus $|J_{z\ell}| > |J_{x\ell}|$ at $z = \pm L/2$ and, everywhere along the plate width. This applies irrespective of the plate thickness, since generally $\eta_\ell >> 1$. The dominance of the z-component of current density is maintained even in the absence of conducting end-strips.

It may be seen in equation (7.59) that when the plate is thin (i.e. $d << \frac{1}{q}$), then at the end of the active width (i.e. $z = \pm L/2$), the current density is almost wholly z-directed. With increase in the plate thickness, however, the x-component of current density becomes significant. Physically, this means that when the plate thickness is small, the currents reaching the end of the plate width tend to go across the thickness to complete their path and very little, if any, would tend to take the cross-pole path. When the plate thickness increases, more and more of the currents reaching the end of plate width tend to take the cross-pole path.

7.9.4 One-dimensional Nature of Current Density in Transverse Flux Arrangement

In transverse flux arrangement, $C_1 (=C_{1t})$ is given by equation (7.37), so that substituting this in equation (7.58),

$$\left[\frac{|J_{zt}|}{|J_{xt}|}\right]_{z=\pm L/2} = \eta_t \tanh qd \qquad (7.60)$$

Thus, for thick plates (i.e. $d >> \frac{1}{q}$), in this case, the z-component of current density may be taken to be the dominant one in the presence of end-strips. For plates of small thickness (i.e. $d << \frac{1}{q}$) and in the absence of conducting end-strips, the x-component of current density is dominant at the end of the active width. Physically, this implies that when the plate thickness is small, then, under this pole-arrangement, the end-currents are cross-pole. With an increase in plate thickness, although the end currents are still cross-pole in nature, the resistance of the end-path is greatly reduced. Finally, when the plate becomes infinitely thick, the pole arrangements lose their significance, since both the pole-arrangements reduce to studying finite width effect in an infinitely thick plate.

It may be noted in equations (7.59) and (7.60) that the presence or otherwise of conducting end-strips has a very pronounced effect in determining the relative

magnitudes of z and x-components of current density. In the presence of the end-strips $|J_{z\ell}| >> |J_{x\ell}|$ at all plate thicknesses, but $|J_{zt}|$ is not necessarily greater than $|J_{xt}|$ and the value of the ratio $|J_{zt}|/|J_{xt}|$ is very much dependent on the value of the plate thickness. In the absence of conducting end-strips, on the other hand, $|J_{z\ell}|$ is still greater than $|J_{x\ell}|$, while $|J_{zt}|$ is smaller than $|J_{xt}|$ and this applies at all plate thicknesses.

## 7.10 COMPARISON OF THE PRESENT WORK WITH THAT OF WOOLLEY AND CHALMERS[66]

### 7.10.1 General

It may be noted that the present treatment of finite width effect has followed closely the work done by Woolley and Chalmers[66]. There are, however, certain aspects of the present work which differ from their work. Also, in the present work, there are some areas where, it is believed, new contributions have been made.

### 7.10.2 Similarities

The most obvious similarity of the present work with that of Woolley and Chalmers[66] is the choice of the model in that they also consider low-resistivity end-rings (for their cylindrical machines), two resistivities and the concept of small thicknesses for uniform current flow. The natures of the current-density distributions in the active part of the solid-iron plate are similar. Some of the assumptions in the present work

are also the same as theirs and so are the boundary conditions at the interfaces of iron and end-strips. The mathematical approach to the problem is, likewise, similar and the resulting expressions for finite width factors are also of the similar nature.

7.10.3 Differences

The model used by Woolley and Chalmers[66], being that of an unlaminated cylindrical rotor, is necessarily a case of single-sided excitation. The present model, on the other hand, envisages a double-sided arrangement and the work is concerned with the effects of finite width in a solid-iron plate of finite thickness, 2d. The finite plate-thickness has been considered from the beginning of the analysis and the resulting expressions for finite width factors have been influenced by it. The two different arrangements of poles in the present work resulted in certain boundary conditions at the plane of symmetry, y=0, in the end-strips, which did not arise in their case. While the mathematical approach in the present work is similar to theirs, the present work was carried out in the widely used Cartesian co-ordinate system as against cylindrical co-ordinates in their work. (The cylindrical co-ordinate system was necessary in their work to account for the curvature of the small cylindrical rotor considered). The present work envisages travelling magnetic fields having linear travel along one

of the co-ordinates while their work envisaged a rotating magnetic field having angular motion along one of the co-ordinates.

The other basic difference with their work is in the choice of values for the thickness $d_c$, and also of $d_e$ in the absence of end-strips. For obtaining the value of $d_c$, the present work uses the non-linear theory presented in this thesis (Chapter 5), while they used the concept of the depth of flux penetration using the limiting non-linear theory.

Woolley and Chalmers considered the effective value of $d_e$, when end-strips were not fitted, to be proportional to the depth of flux penetration whereas the present work considers actual eddy-current fields at the end of active width for this purpose.

7.10.4 Areas of New Contributions

Although Woolley and Chalmers considered two-dimensional current densities in the end region (i.e. in end-rings), the currents were always cross-pole. In the present work, the end-currents have been shown to have preferred directions of flow in the end-strip and could be cross-thickness as well as cross-pole. The study of the relative magnitudes of currents at the end of plate width (Section 7.9) shows the variation in the nature of end-currents with plate thickness and pole arrangements.

The present work considers two different arrangements of poles (longitudinal and transverse flux) and as such, suggests two finite width factors. These factors, although similar in expression, reveal the characteristics typical of the particular pole arrangement. No previous work, it is believed, has done this.

The finite plate-thickness enters into the expressions for current density, loss and finite width factor; these expressions become identical to those of Woolley and Chalmers[66] when the thickness is made very large. This, together with the fact that identical finite width factors are obtained, when $2d \to \infty$, with both Cartesian and Cylindrical co-ordinate systems, implies that the finite width effect (or end-effect in a cylindrical rotor) is very little influenced by the effect of curvature.

The choice of the value of $d_c$ is not only different from Woolley and Chalmers' work, but it also provides a new approach to such a choice. The approach of the present work implies that the loss in a plate with zero resistivity end-strips is such that the current may be assumed to flow uniformly in the thickness $d_c$, the effective value of which may be obtained from a loss-invariance concept. It appears that the present suggestion holds.

## 7.11 CONCLUSIONS

In this chapter, the effects of finite plate width on loss and current density distribution have been studied in a plate fitted with conducting end-strips. Subject to certain assumptions and boundary conditions, a solution for loss in the plate has been obtained and from this, finite width factors have been defined as the ratio of the loss in a plate having finite-resistivity end-strips to that in a plate having zero-resistivity end-strips.

The finite width factors have been shown to depend on the ratio of active width to pole-pitch. In order to reduce the effect of finite plate width, this ratio should be large. This applies irrespective of pole arrangements and at all values of plate thicknesses.

The finite width effects are shown to depend also on the value of plate thickness. With decrease in plate thickness, the effect becomes small in longitudinal flux arrangement and becomes pronounced in transverse flux arrangement. This has been found to be consistent with the physical interpretation of actual current distributions in the plate. With large values of plate thickness, the factors become identical with those proposed by Woolley and Chalmers[66].

In addition to finite plate thickness, the effects of magnetic non-linearity in the plate have also been accounted for in the finite width factors. This has been

accomplished by obtaining an effective value for the thickness of uniform current flow in the plate from the present non-linear theory (Chapter 5) by a loss-invariance concept. It is believed to be a new approach for such a choice.

The study of the nature of currents at the ends of plate width shows the dependence of end-currents on plate thickness, and on the presence or otherwise of conducting end-strips. It shows distinctly that while with very thick plates, the finite width factors are independent of pole-arrangement, with plates of small thickness, they are not. With decrease in plate thickness, it is found that the cross-thickness nature of end-currents becomes prominent in longitudinal flux arrangement and the cross-pole nature of end-currents becomes prominent in transverse flux arrangement.

In the presence of conducting end-strips, the finite width factors are influenced by the primary excitation, its frequency, the resistivities of solid-iron plate and of end-strips, and the magnetisation curve of the material of the plate. In the absence of conducting end-strips, the finite width effects, as expected, are markedly more pronounced, but are seen to be little influenced by these quantities. The finite width factors, in the absence of end-strips, are such that unless the ratio of active width to pole-pitch is sufficiently high, the loss in

the plate would be very greatly reduced. Both in the presence and in the absence of conducting end-strips, it has been shown that, finite width effect being the only criterion, the longitudinal flux arrangement of poles must be chosen for higher loss in the plate.

# CHAPTER 8

# EXPERIMENTAL INVESTIGATIONS

## 8.1 INTRODUCTION

In Chapters 5 and 6, theories were developed for the electromagnetic field quantities in a magnetically non-linear plate subjected to travelling magnetic fields. In Chapter 7, the effect of finite plate width on power loss has been discussed in detail. It was shown in the above chapters (Chapters 5, 6, and 7), that the theories correlated with other published works[30,66]; nevertheless, these theories were verified through some carefully devised experimental investigations.

Measurements of power loss, flux/pole and surface current density were made on three EN1A steel plates subjected to travelling magnetic fields. Readings taken on the narrow plate (Section 8.2.2), were used for studying the finite width effects and the nature of the eddy-current distributions in the end regions.

In the following section, a description of the experimental rig* is given and in Section 8.3, preliminary tests for setting up the rig are described. This is followed by a description of the instrumentations and of the techniques used to measure the electromagnetic field quantities. Results obtained from the experiments are given together with theoretical values. The chapter ends

---

* To verify the theories of Chapter 7, the dimensions of the rig were so chosen that Q<1 (weak eddy-current reaction) for the range of excitation used in these experimental investigations.

with a discussion of the results of the experimental investigations.

## 8.2 DESCRIPTION OF THE EXPERIMENTAL RIG

### 8.2.1 General

The experimental rig was arranged so that a steel plate could be subjected to travelling magnetic fields from both sides. For this purpose, two identical primary members were used, the supply to these being taken from the same source. Each of the three plates (Section 8.2.2) used in the experiments, was instrumented for measuring the flux/pole, the flux/pole per cm. of the plate-width, the surface current density, and the temperature.

### 8.2.2 The Solid-iron Plates

For the purpose of the experimental investigations, three solid-iron plates of EN1A mild steel were used. One plate was so chosen that its length and breadth were greater than the corresponding dimensions of the active area. This plate was used for investigating the nature of end currents beyond the active region. This is referred to as the wide plate. A second plate was so chosen that its width was equal to the width of the active region. This was used to investigate the nature of eddy currents on the lateral side face (i.e. the x-y plane), (see Fig. 8.5), and also to investigate the finite width effects in the absence of any conducting end strips, (Section 7.8.3).

This is referred to as the narrow plate. The width of the third plate was the same as that of the active region, but it had copper end-strips brazed onto it at the ends of the active width. This plate was used to verify the present non-linear theories (Chapter 5), which neglected the finite width effects (Section 8.4.4). This is referred to as the end-strip plate.

All three plates were of the same thickness and were sliced out of one large steel plate; thus each had the same resistivity, $\rho$. The constants a and b in the parabolic B-H relation (equation (5.8)), were obtained from a log-log plot of the B-H curve of the material of the plates[30]. The dimensions and the parameters of the solid-iron plates are given in Table 8.1.

TABLE 8.1

DATA ON THE PLATES USED IN THE EXPERIMENTAL INVESTIGATIONS

| Plate | Length x cm | Width z cm | Thickness 2d cm | Parameters of the plate |
|---|---|---|---|---|
| Wide | 76.6 | 20.3 | 1.902 | $\rho = 1.9 \times 10^{-7}$ Ω.m |
| Narrow | 63.0 | 7.6 | 1.902 | a = 0.664 |
| End-strip* | 70.2 | 7.6 | 1.902 | b = 0.112 |

* The dimensions of the copper end-strips were:

Length = 70.5 cm, Width = 1.8 cm, Thickness = 1.902 cm

8.2.3 The Primary Members of the Heater

Two identical primary members were used for providing linear travelling magnetic fields. For this purpose two linear motor units were used. The linear motor units were chosen for two reasons:

(i) these were capable of providing high excitations, so that the verification of the theories could be extended over a wide range of excitation.

(ii) an examination of their dimensions showed that pronounced finite width effect would be obtained with these units, so that the proposed finite width factors (Chapter 7), could be verified.

The 3-phase windings of the linear motors were rated at 415V, 18.5A, and were star connected. The dimensions and the data of each of the units are given in Table 8.2. Although the rated current of the units was 18.5A, the experimental investigation was limited to 14A, because at higher currents, the rise in the temperature of the plate was very rapid. Table 8.3 shows the primary excitation in kA/m for the corresponding values of line current.

The surfaces of the linear motor units were covered with protective epoxy resin coatings. Since the coatings made it impossible to determine the air-gap length accurately, they were removed making sure that the teeth were not affected.

8.2.4 The Supplies

Because of the number of steel plates being used for both pole-arrangements, (i.e. LFA and TFA), the verification of the theory was limited to two frequencies only, namely, 50 Hz and 25 Hz. While investigations at other frequencies may be carried out as a part of further work, measurements taken at these two frequencies were believed sufficient to verify the present non-linear theories.

The 50 Hz supply was obtained from the 440V(L-L), 3-phase terminals of the a.c. mains and the 25 Hz supply was obtained from the output terminals of a 415/500V, 208A, 1000/1330 rev/min., variable speed, 3-phase alternator. The alternator was driven by an a.c. motor through an eddy-current coupling. By adjusting the speed of the alternator, variable frequency output could be obtained, the 25 Hz supply being obtained at 500 rev/min.

Both the 50 Hz and 25 Hz supplies were taken to a 42 kVA , 440V, 56A, 3-phase variable-output transformer, (Fig. 8.1), which provided variable excitation for the experiment. At 25 Hz, although the magnetising reactance of the transformer was low, the current limit of 56A was never exceeded during the experiments. The instruments used in the experiment were checked and found to be accurate to within $\pm$ 1% at both frequencies.

## 8.3 PRELIMINARY TESTS AND INSTRUMENTATION

### 8.3.1 Schematic Circuit Diagram

Fig. 8.1 shows the circuit diagram (partly schematic) used in the experiments. The 3-phase a.c. supply (both 50 Hz and 25 Hz) was connected to the circuit through a 3-phase transformer and an isolating switch (T in Fig. 8.1). Ammeters and polyphase wattmeters (together with current transformers), were used to measure the total current and power inputs to the two primaries as well as those to the individual primaries. This provided a check on the power and the currents being measured for each of the two primaries.

A slight unbalance in the current to the individual primaries was noted; but this was always less than $\pm$ 7% of the reading of the ammeter A2, (taking A2 as reference), the extent of unbalance becoming less with decreasing excitation. Attempts to eliminate this unbalance by the use of resistances were abandoned because over the range of excitation, considerable adjustments of these resistances were required which was found impracticable, since readings had to be taken quickly to avoid a significant rise in the temperature of the plate. The effect of this unbalance on the power loss in the plate was found to be negligible, since the readings obtained from the wattmeters W2 and W3 were nearly equal and the reading of W1 was obtained as the sum of the above two;

the actual power loss in each primary being taken as half of the reading of W1. The readings of the voltmeters V1, V2 and V3 were balanced.

8.3.2 Preliminary Tests for Identifying the Locations for Longitudinal and Transverse Flux Arrangements

For the experimental investigations one primary member was mounted on top of the other (Photoplate 8.1), and it was necessary to rearrange the rig frequently for longitudinal and transverse flux arrangements. Before the start of the experiments, therefore, locations had to be marked to identify both the pole-arrangements for easy and accurate reference. Some preliminary tests were made for this purpose.

A clamping arrangement was used for mounting one primary member on top of the other. The lower primary member was fixed to the table and was immobile. The upper primary member, when mounted on the clamping arrangement, had its z-axis coincident with that of the lower one; no movement of the upper primary was possible in the z-direction, although it could be slid in the x-direction and raised or lowered in the y-direction.

For identifying locations of the pole-arrangements, two full-pitch search coils (single turn), were placed and secured in identical positions on the surfaces of the two primaries. The upper primary was then mounted on the clamp so that the two primary surfaces were

separated by an air-gap of about 1 cm. The search coil leads were twisted and taken out to a selector switch where they were connected in series, the two end-terminals being taken to an oscilloscope.

Both primaries were excited (about 4A in each phase), and the position of minimum search coil voltage was obtained by sliding the top primary along the x-axis. The relative positions of the two primaries then corresponded to Fig. 8.2a, which was the longitudinal flux arrangement, where the corresponding poles of the two primaries were of the same polarity. This position was marked as a reference point on the top primary member.

When the top primary was slid one pole-pitch from the position of Fig. 8.2a, the search coil voltage was a maximum. The relative positions of the two primaries then corresponded to Fig. 8.2b, which was the transverse flux arrangement, where the poles were of opposite polarity. However, this left a portion of both the primaries uncovered at the ends of the active length,

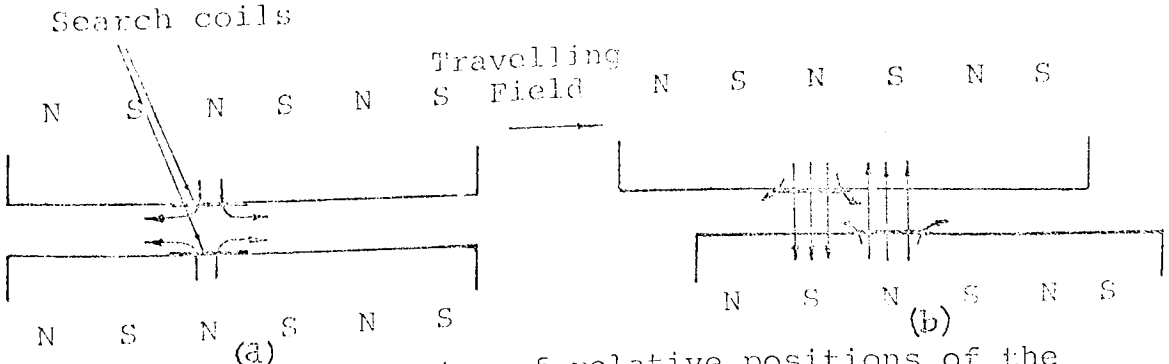


Fig. 8.2 Determination of relative positions of the two primary members for the longitudinal and the transverse flux arrangements.

resulting in unequal reluctances for the end windings. To avoid this, the top primary was rotated horizontally through $180^{o}$ from the position of Fig. 8.2a, and making sure that the directions of travel of both the magnetic fields were the same, the positions of maximum search coil voltage was obtained. This position was marked as a reference for the transverse flux arrangement.

In the transverse flux arrangement, the attractive force between the two primary members was naturally strong and considerable physical force was needed to move the top primary member. In the longitudinal flux arrangement the attractive force between them was weak and only slight physical force was needed to move the top primary member. This acted as a cross-check for the respective positions and could be felt physically.

8.3.3 Instrumentation of the Solid-iron Plates

As part of the verification of the present non-linear theories, measurements of flux/pole and current density were made on the surfaces of the plates (Section 8.1). In addition to these, air-gap flux-density distribution along the z-direction and the temperature of the plate were measured on the plate surfaces. For these purposes, the plates were fitted with search coils, current-density probes and thermocouples.

8.3.3.1 The Search Coils

For measuring the flux/pole, full-pitch search coils were placed and secured on the surfaces of each

of the plates. For this purpose a single-turn search coil of 0.08 mm.diameter, 44 SWG, copper wire was used. The width of the search coils was the same as that of the active region of the plate.

The search coils were secured to the plate surfaces by an adhesive liquid and a non-magnetic cementing material. The latter also provided thermal and additional electrical insulations for the wire. The ends of the coil were twisted, (so that the effects of voltages induced due to fringing fluxes were negligible) and taken to a selector switch.

Fig. 8.3 shows the location of the full-pitch search coil on the surface of the wide plate (terminal a), while the search coils for the narrow and the end-strip plates are shown in Figs. 8.5 and 8.6 respectively. Also shown in Fig. 8.3 are the locations of full-pitch search coils of width 0.5 cm, numbered 1 to 11. These search coils were used to measure the flux/pole per cm. of plate width.

Knowing the areas of the search coils, it was possible to obtain the distribution of air-gap flux density in the z-direction. In order to obtain the areas of all the search coils, the coils configuration was projected, magnified 10 times, by a Shadowgraph on a large tracing paper from which the areas were measured by means of a planimeter.

As shown in Fig. 8.3, one end of all the search coils was joined to a single common wire (terminal b); with this search coil configuration, any two terminals could be used as a search coil and therefore readings could be taken even when one coil was broken. The other ends of the array of search coils (shown as arrow heads) were carefully twisted and connected to the selector switch.

8.3.3.2 The Current-density Probes

For measuring the surface current-density, current-density probes were attached to the plates. These probes consisted of two insulated constantan wires, each 0.1 mm in diameter, spot-welded onto the cleaned plate surface. Constantan wire was used instead of copper wire because of the latter's dissimilar melting point with respect to the solid-iron plate.

The spot welding was done by passing a high energy pulse from a capacitor discharge unit through one end of one wire and the plate, so that the wire was welded at the desired spot on the surface. One end of the other Constantan wire was also spot-welded 0.5 cm apart and the two wires together formed a J-probe*; the voltage between these two wires was equal to the voltage drop due to the current density in the plate surface, provided the area covered by the J-probe was vanishingly small. The two J-probe leads were carefully twisted and secured on the plate surface, and the two terminals were

* For the purpose of abbreviation, the term 'J-probe' is used for current-density probe.

finally connected to the selector switch.

Fig. 8.4 shows the arrays of the current-density probes for the wide plate, while those for the narrow and end-strip plates are shown in Figs. 8.5 and 8.6. In these figures the J-probes are marked by the letters Z and X, implying thereby that they were fitted along the z and x-axes respectively. They are also numbered for convenience. In Figs. 8.5 and 8.6, the end region J-probes are marked as XE and Y; XE is for measuring the current density in the x-direction and Y for measuring the current density in the y-direction. (Y's appear only on the lateral surface of the narrow plate).

As shown in Fig. 8.4, an array of J-probes was fitted in the central part of the plate (i.e. near x=0). A second array was fitted at a distance of one pole-pitch and a third array was fitted at a distance of one and a half pole-pitch from the central array. These two arrays provided a check on the readings of the first array. The J-probes were attached over one half of the plate width (i.e. between z=0 and z=+L/2), although some J-probes were also attached over the other half (i.e. between z=0 and z=-L/2) for providing a check on the readings.

Because of the similarity of the readings from the J-probes on the surface of the wide plate, the number of J-probes for the narrow and the end-strip plates were

reduced, although a duplicate array of the J-probes was always used. On the lateral surface of the narrow plate (Fig. 8.5), J-probes were fitted to measure both x and y- components of current density.

8.3.3.3 The Thermocouples

Three thermocouples were placed on the surface of each of the plates to record the rise in their temperatures. The thermocouples consisted of insulated copper and constantan wires fused at one end and spot-welded on the plate surface. The other ends were taken to a digital thermometer which displayed the temperature. One thermocouple was attached at the central part of the plate, while two more thermocouples were attached at distances of one and one-and-a-half pole-pitch. The locations of some thermocouples are shown in Figs. 8.3, 8.5 and 8.6 for the wide, narrow and end-strip plates respectively.

8.3.4 Location of the Two Primaries

In all experimental investigations, an air-gap of 1.5 mm. was used; pieces of especially compressed paper (commercially known as 'elephant hide'), each 1.5 mm. thick, were placed between the plate and the primary surfaces. These compressed papers were good electrical insulators, non-magnetic and could stand high temperatures (above 200$^{o}$C). The coefficient of thermal expansion of the compressed papers was small, so that the air-gap remained

sufficiently constant over the range of excitation used.

In addition to providing the air-gap, these compressed papers provided positive spacing for the J-probes, the search coils and the thermocouples between the plate and the top primary number. With particular regard to the axes of symmetry (viz. x=0 and z=0 lines), the top primary was placed in the proper position and the whole rig was tightened so that uniform air-gap was obtained and the vibration of the plate under excitation was minimised. The total height of each constituent region was compared with the height at which the top primary member was placed. Two air-blowers were used for cooling the plate; these were positioned for minimum effect on the J-probes, etc., on the plate surface.

Photoplate 8.1 shows the wide plate in position between the two primary members for the longitudinal flux arrangement.

## 8.4 EXPERIMENTAL MEASUREMENTS

### 8.4.1 General

Initially, it was necessary to investigate the effects of the rise in the temperature of the plate under excitation, of entry and exit edges and of finite plate width on experimental measurements; these effects are discussed in the following sections. Methods of measuring the power loss, the flux/pole and the surface

current density are described in Section 8.4.5 through 8.4.7. This is followed by the description of the additional investigations undertaken.

8.4.2 Effect of Temperature

The rise in the temperature of the plate during the experiments affected its resistivity and permeability. However, no provision for changes in temperature was made in the non-linear theories. (Reference to this has been made in Chapter 9). Consequently, the experimental results would show some deviation from the theoretical values, especially at higher excitations when the rise in temperature was more rapid.

In order to allow approximately for the rise in the temperature of the plate, theoretical curves were also obtained for higher values of resistivity. Table 8.4 shows the increase in the resistivity of EN1A steel with

TABLE 8.4

VARIATION OF RESISTIVITY OF EN1A STEEL WITH TEMPERATURE[74]

| TEMPERATURE, $^{o}C$ | 100 | 200 | 300 | 400 |
|---|---|---|---|---|
| Electrical Resistivity, $\mu\Omega.cm.$ | 20.6 | 27.2 | 35.6 | 45.8 |

temperature (Ref. 74). Allowing for the rise in the temperature of the plate, therefore, theoretical results for various electromagnetic field quantities were obtained

at resistivity values of 25, 30 and 40 $\mu\Omega$.cm. in addition to the measured value. Correlation of measured values of certain quantities (e.g. the surface current density) would be sought with theoretical results obtained using a higher value of resistivity.

With an increase in the temperature, the permeability of the plate also increases[75], although at Curie point it drops to a low value. However, the change in permeability was not very significant and above the knee of the B-H curve, the variation of permeability was small; thus no approximate allowance was made for the increase in permeability at higher temperatures. At higher excitations due to rapid rise in the temperature of the plate, the experimental values of flux/pole may be expected to be somewhat less than the theoretical value.

During experimental measurement, every effort was made to take readings with the least possible variation of the temperature of the plate. These included:

(i) The plate was continuously cooled by means of air-blowers.

(ii) Between two sets of readings considerable time was allowed to pass, so that the plate could cool down, and

(iii) Each set of readings was taken as quickly as possible.

8.4.3 Entry and Exit Edge Effect

In the flat, linear configuration of the rig, the air-gap for the primary windings near the ends of the active length (i.e. in the x-direction), was larger than that for the winding at the centre of the active length, although its effect was minimised by using intermediate and end coils (Table 8.2). Due to the fringing flux and the flow of current between the pole-centre and the edge of the plate, the flux and the current densities at the end of the active length were less than those at the centre of the active length. Measurement of current density near the ends of the active length showed a decrease of between 25% and 30% (current density at the centre of the active length as base).

However, since this effect occurred at the extreme ends of the active length, its effect on current density measurement was avoided by limiting the measurements to the central part of the plate. Also since the area affected by entry and exit edge effects was less than 10% of the total active area, the total active area could be considered for loss density calculations. (Reference to this effect has been made in Chapter 9).

8.4.4 Effect of Finite Plate Width

Effects of finite plate width on loss and current density distribution were discussed in Section 7.2.

Accordingly, the readings obtained from the narrow and wide plate would be influenced by the finite plate width.

On the surface of the end-strip plate, the voltage induced in the 0.5 cm. wide full-pitch coils was compared with the voltage of the J-probes which were also 0.5 cm. long. It was found that the voltage of the search coils was nearly twice the voltage of the J-probes, thus showing that the voltage induced in the search coil was the same as that due to the flow of the current density on the surface of the plate. The end-strip plate may, therefore, be considered as approximately simulating the condition of an infinitely wide plate. The readings of power loss, flux/pole and surface current density obtained from the end-strip plate would, therefore, be compared with the theoretical values obtained from Chapters 5 and 6 where finite width effects were neglected.

8.4.5 Measurement of Power Loss

The power loss in the plates was measured by the use of polyphase wattmeters. For this purpose the losses in the individual primary members were measured under no-load condition, i.e. without having the plate in position and with the members removed so far apart that the magnetic circuits were independent of each other. At any excitation, half of the total loss in the two primary members was taken as the no-load loss in

each. As a cross-check, losses were measured in the individual primary members (Fig.8.1) and were found to be in close agreement with the value obtained above. Readings of no-load loss were taken over the range of experimental excitation values and for the frequencies used.

With the plate in position between the two primary members the total loss in both primary members was measured using the same wattmeter; half of it was taken to be occurring in each of them. Once again, losses were measured in the individual primary members as shown in the circuit diagram of Fig. 8.1, and was found to be within 4% of the mean value measured above. Readings of load loss were taken over the same range of excitation and frequency values as with the no-load test.

For each value of excitation, the no-load losses were subtracted from the measured load loss to obtain the power loss in the plate. Loss density (in $kW/m^2$) was obtained by dividing the power loss in the plate with the surface area of the active region.

The loss densities obtained are plotted in Figs.8.7 and 8.8 for the longitudinal and transverse flux arrangements respectively. Loss densities obtained for all three plates are plotted together with the theoretical curves.

Discussion of the results from these experiments are made in Section 8.5.2.

8.4.6 Measurement of Flux/pole

For measuring the flux/pole, a full-pitch, single turn search coil having a width equal to that of the active area, (Section 8.3.3.1), was used. When the primary members are excited, the magnetic flux passing through a search coil induces a voltage in it. If $v_1$ is the voltage induced in the search coil, then the flux/pole, $\phi_p$, is given by

$$\phi_p = \int_0^t v_1 dt \qquad (8.1)$$

where t represents time.

The output from the search coil was fed to an integrator circuit, shown in Fig. 8.9. The operational amplifier A used for this purpose was a plug-in unit of a TETRANIX oscilloscope, and was first calibrated using a signal generator.

For an input voltage of $v_1$, the output voltage $v_2$

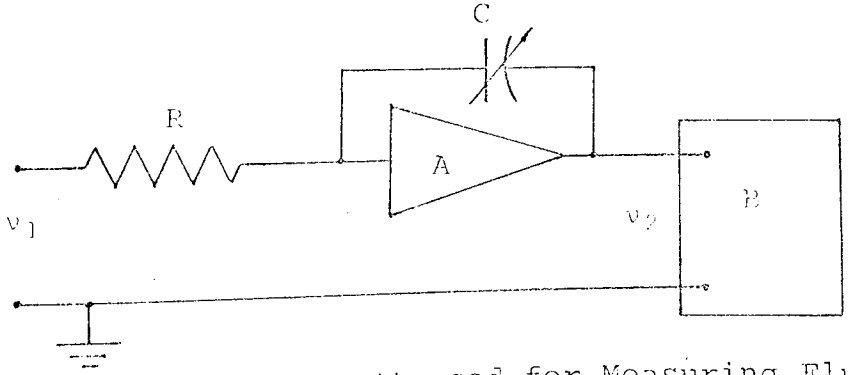


Fig. 8.9 Integrator Circuit used for Measuring Flux

A = Operational Amplifier
B = Electronic Voltmeter, Wave Analyser and Oscilloscope
R = 0.01 MΩ, C = 1.0μF

of the integrator circuit is given by

$$v_2 = \frac{1}{RC} \int_0^t v_1 dt \qquad (8.2)$$

where R and C are the resistance and capacitance, respectively, of the integrator circuit. Using equations (8.1) and (8.2), the flux/pole, $\phi_p$ is given by

$$\phi_p = RCv_2 \qquad (8.3)$$

The values of the resistance and the capacitance used in the experiments were 0.01 MΩ and 1.0 μF respectively. The voltage $v_2$ was read on an electronic voltmeter. Further amplification of the search coil voltage was not necessary because the search coil voltage was high and the input impedances of the integrator circuit and the voltmeter were high as well.

When the voltage output of the search coil is sinusoidal, then from equation (8.1), the peak flux is given by

$$|\phi_p| = \frac{V_1}{\omega} \qquad (8.4)$$

where $V_1$ is the amplitude of the sinusoidal induced voltage and $\omega=2\pi x$ (frequency of the primary excitation). For the sinusoidal output voltage from the search coil, the magnitude of the search coil voltage was read directly on the electronic voltmeter and the flux was obtained by dividing it with the angular frequency. This acted as a cross-check on the readings obtained using the integrator circuit.

For obtaining the fundamental flux/pole, a wave analyser* was used. Since the voltage induced in the search coil was sinusoidal except at very high excitations, higher order harmonics were found to be of very small percentage (less than 5%), of the fundamental component over the range of excitation used.

Figs. 8.10 and 8.11 show the measured fundamental component of flux/pole for the end-strip plate in longitudinal and transverse flux arrangements respectively. Readings were taken for both 50 Hz and 25 Hz, and the figures also show the curves predicted from the present non-linear theories.

Discussion of these results is made in Section 8.5.4.

8.4.7 Measurement of Surface Current Density

For the measurement of current density on the surfaces of the plates, the current-density probes attached to the surface (Section 8.3.3.2) were used. The output terminals of the current-density probes were fed to an amplifier and then taken to the electronic voltmeter and the wave analyser. The same operational amplifier as in Fig. 8.9 was used, except that the capacitance was replaced by a resistance, $R_1$. Photoplate 8.2 shows the experimental rig and the measuring instruments used.

If $v_p$ is the fundamental of the voltage reading obtained from the current-density probes, placed a distance $L_p$ apart, then the fundamental component of the current

* The wave analyser was first calibrated using a signal generator.

density on the surface of the plate, $J_1$, is given by

$$J_1 = \frac{v_p}{\rho L_p} \qquad (8.5)$$

where $\rho$ is the resistivity of the plate (Table 8.1).

Equation (8.5) applies for both the z and x-components of current density. Throughout the experiment $L_p$ was 0.5 cm; this was believed to be the smallest permissible distance between the ends of a J-probe for half of the active width used (= 38mm). Figs. 8.12 and 8.13 show the plots of the surface current density $J_{z1}$ for the end-strip plate for the longitudinal and transverse flux arrangements respectively. Experimental points for both 50 Hz and 25 Hz are plotted together with the theoretical curves.

Discussion of the results obtained is made in Section 8.5.5.

8.4.8 Additional Investigations

In addition to the experimental measurements described so far, investigations were also undertaken to verify the validity of certain assumptions. These included the measurement of the variation of air-gap flux density in the z-direction, the theoretical and the experimental investigations of some finite-width effects, the oscillograms of wave shapes from the search coils and the current-density probes and the measurement of the temperature of the plates.

8.4.9 Measurement of the Variation of the Air-gap Flux Density in the z-direction

For the measurement of the variation of the air-gap flux density in the z-direction, full-pitch, single-turn search coils of width 0.5 cm. were fitted on the surface of the wide plate (Fig. 8.3)*. These coils are numbered from 1 to 11 and the flux was measured using the integrator circuit shown in Fig. 8.9. The flux density obtained from each of these search coils was taken to be that occurring at the centre of the area covered by the coil. The measured values of the flux density along the z-direction are plotted in Figs. 8.14 and 8.15 for the longitudinal and the transverse flux arrangements respectively. Various excitation values and the two frequencies, 25 Hz and 50 Hz, were used.

Observations from these figures are made in Section 8.5.6.

8.4.10 Theoretical and Experimental Investigations of some Finite-width Effects

8.4.10.1 Theoretical Investigations concerning $d_{c\ell}$ and $d_{ct}$

While for the purpose of analysis, the thickness for assumed uniform current-density distributions in the

* Such arrays of search coils were also fitted on the surfaces of the narrow and end-strip plates, but are not shown in Figs. 8.5 and 8.6 for clarity.

plate, $d_c$ (i.e. $d_{c\ell}$ or $d_{ct}$), was considered to be small compared with the half-thickness of the plate, d, (Section 7.4.1), the effective value of $d_c$ was obtained from a new loss-invariance concept (Section 7.7.3). It was, therefore, necessary to investigate whether the value of $d_c$, so obtained, was small compared with d (since otherwise the analysis would not be valid). Theoretical calculations were therefore undertaken for the end-strip plate for both pole-arrangements and frequencies, over the range of excitation used and the results obtained are given in Table 8.5.

It may be observed in Table 8.5 that the effective values of $d_c$ obtained for both pole-arrangements were small (less than 9%), compared with the half-thickness of the plate, thus verifying that the assumption of $d_c << d$ holds, despite the new loss-invariance concept used in obtaining $d_c$.

8.4.10.2 Experimental Investigations of End-current Distributions

It was mentioned in Chapter 7 (Sections 7.8 and 7.9) that the current-density distribution on the line of the intersection of the planes z=L/2 and y=d was given by equation (7.54), and the ratio of the current-density distributions at z=L/2 was given by equation (7.58). Tests were made on the narrow plate to verify these observations.

Since for the narrow plate, $J_z$ at z=L/2 could not be obtained, the readings of the J-probes nearest to z=L/2 (namely, Z21 and X21, Fig. 8.5), were used to represent the surface current densities at the end of the active width. For the same reason readings of the J-probes on the lateral surface nearest to y=d (namely, XE6 and Y3, Fig. 8.5), were used to represent the current densities at y=d. Since the current density is directly proportional to the J-probe reading, the J-probe readings were used for verifying the equations and the results are given in Tables 8.6 and 8.7 for longitudinal and transverse flux arrangements respectively.

To obtain the ratios of end-currents, the readings for $J_x$ (i.e. $J_{x\ell}$ or $J_{xt}$) were obtained from the J-probe attached to the narrow plate at the end of the active width, (namely, XE5 of Fig. 8.5) and the readings for $J_{z\ell}$ were obtained from the J-probe nearest to the end of the active width on the surface of the narrow plate (namely, Z21 of Fig. 8.3). For the transverse flux arrangement, however, $J_{zt}$ was obtained from the mean of the readings of the J-probes on the surface and on the lateral side face nearest to the end of active width (i.e. Z21 and Y3 of Fig. 8.5). This was necessary because $J_{zt}$ at z=0 was not only impossible to obtain but was also difficult to predict from the variations of the readings of these two J-probes, and the mean value was taken as a compromise. Since only the ratios of current densities

were of concern, readings as obtained from the J-probes were used and the results are given in Tables 8.8 and 8.9 for the longitudinal and the transverse flux arrangements respectively.

In all the above measurements, the fundamental components of the J-probe readings were always obtained. Observations and discussions of these results are given in Section 8.5.7.

8.4.11 Oscillograms of Voltage from Current-density Probes and Search Coils

Oscillograms of voltages from current-density probes were taken to study the natures of current-density and flux distributions on the surfaces of the plates for both pole-arrangements. These are shown in Figs. 8.16 through 8.25.

Figs. 8.16 and 8.17 show that oscillograms of voltages from the J-probes and the search coil array, respectively, on the surface of the wide plate. Figs. 8.18 through 8.22 show the oscillograms of voltages from the current-density probes on the surface of the narrow plate; Fig. 8.22 showing those on the lateral side face. Oscillograms of voltages from the current-density probes on the surface of the end-strip plate are shown in Figs. 8.23 through 8.25; Fig.8.25 also includes an oscillogram of voltages from the full-pitch search coil.

Observations about the oscillograms are made in

Section 8.5.8.

8.4.12 Measurement of the Temperature of the Plate

Each of the three plates were fitted with thermo-couple probes to monitor the rise in their temperatures when subjected to the travelling magnetic fields. Slight difference in the temperature in the three locations on the plate surface was noted, and could be due to the contact of the weld points. However, the difference was not large, (less than $\pm$ 10% of the reading of the thermo-couple at the centre), and the mean of the temperature readings of the three locations was taken.

Figs. 8.26 and 8.27 show the plots of the rise in the temperatures of all three plates for 50 Hz and 25 Hz respectively.

These will be discussed in Section 8.5.9.

8.5 DISCUSSION OF TEST RESULTS

8.5.1 General

Experimental investigations on the end-strip plate to verify the non-linear theories of Chapters 5 and 6 and on the plates without end-strips to determine the effects of finite width on power loss and current-density distributions, have been described in Section 8.4. The results of these experiments were presented in tabular and graphical forms and, in this section, these results are discussed, and compared with the calculated values.

8.5.2 Eddy-current Power Loss

The experimental values of power loss density in the plates are plotted, together with the graphs of calculated values, as a function of the primary excitation in Figs. 8.7 and 8.8 for the longitudinal and the transverse flux arrangements, respectively, for both 50 Hz and 25 Hz.

The experimental values of loss density obtained from the end-strip plate agree well with the theoretical values at low excitations. In general, experimental values of loss density obtained from the end-strip plate are slightly greater than the theoretical values (varying between 3% and 13%, calculated value as base), over the whole range of excitation. The reasons for the difference between the theoretical and experimental values could be

(i) probable imperfections in the copper-iron interfaces causing an uneven distribution of current in the plate, and

(ii) the iron loss in the teeth of the primary member under load condition which were included in the measured values.

During the tests, the power loss caused an increase in the temperature of the plate, and hence an increase in the resistivity of the material of the plate. Theoretical values of loss density obtained using a higer value of resistivity would be less than those shown in Figs.

8.7 and 8.8 (for all three plates, Q < 1). Thus the agreement with theoretical values is better in the above figures than would be obtained for higher values of resistivity. Nevertheless the results of Fig. 8.7 and 8.8 are considered to verify the solutions obtained for loss density.

Several other observations may be made from Figs. 8.7 and 8.8. It may be observed that the loss in the end-strip plate is greater than that in both the wide and the narrow plates; this is to be expected because of the negligible loss in the end strips and because additional e.m.f. is required to drive the currents in the end region in the narrow and the wide plates. It may also be seen in Figs. 8.7 and 8.8 that the difference between the measured loss values of the end-strip plate and the narrow (or wide) plate is higher for the transverse flux arrangement (TFA) than for the longitudinal flux arrangement (LFA); this shows that the effect of finite width is more pronounced in the TFA than in the LFA due to predominantly cross-pole currents at the end of the active width.

Also notable in the above figures is the fact that the loss values obtained for the wide plate are only slightly higher (maximum 5%), than those obtained for the narrow plate, so that only slight reduction in the effects of finite plate width on loss is achieved

by the use of a plate much wider than the width of the active area. This shows that the effective end-region width, $d_e$, for the narrow and the wide plates may be considered equal and that the loss due to the z-component of current density in the end region may be neglected.

8.5.3 Finite Width Factors in the Absence of Conducting End-strips

The power loss obtained in the end-strip plate may be assumed to represent approximately the power loss in an infinitely wide plate (Section 8.4.4), so that finite width factors for plates having no conducting end-strips may be obtained approximately as the ratio of the power loss in the narrow plate to that in the end-strip plate.

Table 8.10 shows the values of the finite-width factors obtained for the narrow plate for both the LFA and the TFA, the calculated values being obtained from equations (7.36) and (7.46), respectively, with n=1. Fairly good agreement is obtained between the calculated and measured finite-width factors, although the measured values are slightly greater than the calculated values. The difference between the calculated and experimental values varies between - 0.2% and +21%, (calculated value as base), the maximum difference occurring at the highest excitation for the TFA at 50 Hz. The difference between the calculated and the measured values of finite width factors is consistent with the difference between the

calculated and measured values of loss density (Section 8.5.2). In general, better agreement with the calculated values is obtained at 25 Hz where the increase in the temperature of the plate was not very great (Fig. 8.27).

It may also be noted in Table 8.10 that the finite width effect is more pronounced for the TFA than for the LFA due to the predominantly cross-pole currents.

8.5.4 Flux Per Pole

The variations of the calculated and the experimental values of the fundamental components of the flux/pole with the primary excitation for the end-strip plate are shown in Figs. 8.10 and 8.11 for the LFA and the TFA respectively. Agreement between the calculated and measured values of flux/pole is fairly good at low excitations; the difference between the experimental and the calculated values of flux/pole varies between 0% and -12% (calculated value as base). The maximum difference occurs at the highest primary excitation for the LFA at 50 Hz. The difference between the calculated and experimental values occurs because the actual resistivity of the plate was greater (due to the increase in the temperature of the plate) than the value used in calculations; the calculated values, thus, under-estimating the eddy-current reaction.

The flux/pole was also measured on the narrow and the wide plates and the values obtained were slightly

less that those for the end-strip plate; the difference was between -5% and -18% (flux/pole on the end-strip plate as base). The small difference in the air-gap flux/pole for all three plates indicates that the flux/pole is relatively unaffected by the paths of eddy currents in the end region of the plate when the eddy-current reaction field is weak. This confirms the observations made in Section 7.2 in connection with the nature of finite width effect. However, the experimental values of flux/pole for the narrow and the wide plate are not plotted in Figs. 8.10 and 8.11 for clarity.*

Fig. 8.25c shows a typical oscillogram of the voltage from the full-pitch search coil (proportional to flux/pole) for the end-strip plate.

### 8.5.5 Surface Current Density

#### 8.5.5.1 Current Density on the Surface of the End-strip Plate

The experimental values of the fundamental components of current density along the z-direction on the surface of the end-strip plate are plotted, together with the theoretical curves, in Figs. 8.12 and 8.13 for the LFA

---

* Other researchers[30,44] obtained much higher differences (over 200% in ref. 30) between measured values of flux/pole in solid-iron rotors with and without copper end-rings; this is typical for machines with strong eddy-current reaction ($Q > 1$).

and the TFA respectively; good agreement was obtained between the calculated and the experimental values at low values of primary excitation. With increase in the primary excitation, the experimental values of current density deviate increasingly from the calculated values, the difference being higher for the TFA (Fig. 8.13) than for the LFA (Fig. 8.12). The difference ranges from 0% to -24% (calculated value as base), the maximum difference occurring at the current-density value for the TFA at the highest primary excitation. Two reasons may be given for this difference:

(i) At higher excitations, the temperature of the plate increased and so did its resitivity (Section 8.4.2); this caused a decrease in the surface current density. Better agreement between the calculated and experimental values of current density at higher excitations may be obtained by using a higher resistivity value in calculations. However, this would cause greater error at lower excitations and a compromise value of resistivity is difficult to obtain.

In order to determine whether the use of a higher resistivity in calculations gives closer agreement between the experimental and theoretical values of current density, theoretical curves were obtained for $\rho$ = 40 $\mu\Omega$.cm. for 50 Hz and

$\rho$ = 30$\mu\Omega$.cm. for 25 Hz cases, (Table 8.4), and are shown in dotted lines in Figs. 8.12 and 8.13. It may be noted that the experimental points and the dotted curves converge at higher excitations.

(ii) The z-component of the current density on the surface of the plate for the TFA is less than that in the LFA; this shows that the difference is partly due to the existence of the cross-pole currents in the TFA within the active region, (oscillograms of Figs. 8.24 and 8.25), as well as in the end-strips.

8.5.5.2 Current Densities on the Surfaces of the Narrow and the Wide Plates

The z and x-components of current density were also measured on the surfaces of the narrow and the wide plates. The z-component of current density for these plates was always much smaller than the corresponding values for the end-strip plate, while the x-component of current density for these plates was generally more significant (oscillograms of Figs. 8.16, 8.18 and 8.21). Thus the assumption of the z-component of current density being always the dominant component was not strictly true for the wide and the narrow plates, and the values of $J_z$ for these plates were not plotted in Figs.8.12 and 8.13. The reason for lower surface current density values and significant x-component of

the surface current density in the cases of the wide and the narrow plates was the increased impedance to the eddy current paths because of the absence of low-resistivity end-strips.

The measured z-component of the surface current density values for the narrow and the wide plates are approximately 20% lower than those for the end-strip plate at higher excitations; at lower excitations the difference is less.

8.5.6 Variation of the Air-gap Flux Density Along the z-direction

The variation of the air-gap flux density along the z-direction was measured using the arrays of search coils placed on the surfaces of the plates. The results obtained for the wide plate are plotted in Figs. 8.14 and 8.15 for the LFA and the TFA respectively. Similar results were also obtained for the narrow and the end-strip plates.

Figs. 8.14 and 8.15 show that for both pole-arrangements and for both the frequencies used, the air-gap flux density for the wide plate is substantially constant along the active width over the range of the excitation used. This observation is also substantiated by the oscillograms of Fig. 8.17.

At the end of the active width, i.e. at z=L/2 (=38 mm.), the flux density could not be measured

because the search coils on either side of the line $z = L/2$ measured flux densities inside and outside the active region respectively. The measured flux density at 35.5 mm from the centre ($z = 0$) was less than that at the centre, indicating that the flux density decreases near the end of the active width.

The results of the flux density measurement show that the air-gap flux density does not vary along the z-direction for the heater with low eddy-current reaction ($Q<1$), thus verifying the assumption (v) of section 7.4.2.

### 8.5.7 End-Current Distributions For the Narrow Plate

For investigating the nature of end-current distributions, the narrow plate was fitted with J-probes on the line of intersection of the planes $z = L/2$ and $y=d$ and also on the lateral side face (Fig. 8.5) in addition to those in the active region. Tables 8.6 and 8.7 show the measured magnitudes proportional to the current densities at $z = L/2$ and $y=d$ , while Tables 8.8 and 8.9 give the ratio of the current density components at the end of the active width.

#### 8.5.7.1 Verification For the Continuity Condition (equation (7.54)) Between the Active and the End-Regions

Equation (7.54) was given in section 7.8.3 as the equation governing the distribution of current densities on the line of intersection of the planes $z=L/2$ and $y=d$

and was an important condition in determining the effective end-region width, especially in the absence of end-strips.

It was, however, difficult to obtain both $J_z$ at z=L/2 (section 8.4.10.2), and $J_{ey}$ at y=d and J-probes nearest to both z=L/2 and y=d lines (namely, Z21 and Y3, Fig. 8.5 ), were used for this purpose. The x-components of current densities were, likewise, obtained from the J-probes nearest to both z=L/2 and y=d lines (namely, X21 and XE6, Fig. 8.5).

It can be seen in Tables 8.6 and 8.7 that the magnitudes proportional to the current density obtained on the air-gap surface of the narrow plate (J-probes Z21 and X21) are approximately equal to those obtained on the lateral side face (J-probes Y3 and XE6). This applies for both pole-arrangements and frequencies. The slight difference could be due to the distance of the respective J-probes from the line of intersection of z=L/2 and y=d planes. The results obtained from the J-probes are, nevertheless, considered sufficient to verify equation (7.54).

In addition to verifying equation (7.54), Tables 8.6 and 8.7 show the different natures of end-current distributions for the LFA and the TFA. This can be obtained by comparing the readings obtained from the J-probes on the air-gap surface of the narrow plate nearest to the end of the active width (Z21 and X21, Fig. 8.5) and on the lateral side face nearest to the air-gap surface (Y3 and XE6, Fig. 8.5).

For example, the readings obtained for the x-component of current density on the lateral side face (J-probe XE6, Fig. 8.5) near the air-gap surface show the predominance of the cross-pole current for the TFA.

8.5.7.2 Verification for the Ratio of the Directional Components of Current Densities at the End of the Active Width (Equations (7.59) and (7.60))

The ratios of the z and x-components of current densities at the end of the active width are given by equations (7.59) and (7.60) for the LFA and the TFA respectively. The ratio of these two components of current density at z=L/2 is obtained for the narrow plate ($\eta$=1) from the readings of J-probes fitted nearest to the end of the active width (Z21, XE5 and Y3, Fig. 8.5).

Tables 8.8 and 8.9 show that the ratios of the end current densities obtained from experimental measurements bear good agreement with the calculated values; agreement is better for the LFA than for the TFA. The difference between the calculated and the measured values of the ratio varies for the LFA between -14% and +12% (calculated value as base) and for the TFA between 9% and 40%. The reason for this difference is that $J_z$ could not be obtained exactly at z=L/2 and measurements were approximate. In the TFA, the difference was due to a further approximation in obtaining $J_{zt}$ at z=L/2 (section 8.4.10.2).

The results of the Tables 8.8 and 8.9 are, however, considered sufficient to suggest the validity of equations (7.59) and (7.60), respectively, for a plate without end-strips. The results of these Tables also act as a verification for the method of obtaining the end-region width and, in particular, equation (7.56) (i.e. $\eta_\ell=\eta_t=1$).

### 8.5.8 Oscillograms of Voltages from the J-probes and Search Coils

#### 8.5.8.1 Oscillograms for the Wide Plate

Figs.8.16 and 8.17 show the oscillograms of voltages from the J-probes and the search coils, respectively, on the surface of the wide plate. While the oscillograms of Figs. 8.16 and 8.17 are for the LFA and the TFA respectively, similar oscillograms were also obtained for opposite pole-arrangements.

Fig. 8.16a for the LFA shows that while the change in the magnitude of the z-component of current density within the active width of the plate is small, the decrease in its magnitude beyond the active width is pronounced. In Fig. 8.16b, on the other hand, the x-component of current density is shown to be increasing from the centre towards the end of the active width. In particular, the wave-shape marked d beyond the active region (at z=43 mm.) clearly suggests that the end currents flow beyond the active region

rather than within it.

Since the areas of the search coils (marked 1 to 11 in Fig. 8.3) on the surface of the wide plate were approximately equal, the oscillograms of Fig. 8.17 for the TFA clearly show that there was negligible variation of the air-gap flux density along the z-directions within the active width. This substantiates the information obtained from Figs. 8.14 and 8.15.

The invariance of air-gap flux density along the active width was also obtained from the oscillograms of the search coils on the surfaces of the narrow and the end-strip plates.

8.5.8.2 Oscillograms for the Narrow Plate

Oscillograms of voltages from the current-density probes on the air-gap surface and the lateral side face of the narrow plate (Fig. 8.5) are shown in Figs. 8.18 through 8.22 for the two different pole-arrangements.

Figs. 8.18 and 8.19 show the relative magnitudes proportional to $J_z$'s and the $J_x$'s at particular locations for the LFA, while Figs. 8.21 and 8.22 show those for the TFA. An examination of these figures shows that while the z-component of current density is the dominant one at the centre (z=0) of the plate, the x-component of the current density becomes significant towards the end of the active width of the plate. Towards the end of the active width,

the x-component of current density is much more significant in the TFA (Fig. 8.21c) compared with that in the LFA (Fig. 8.19a).

Oscillograms of Figs. 8.19b, 8.19c and of Figs. 8.22a and 8.22b show the cross-pole and the cross-thickness natures of end-currents for the two different pole-arrangements. Fig. 8.19c for the LFA shows that on the lateral side face (i.e. the x-y plane) of the narrow plate, the y-component of current density (wave shape a) is much greater than the x-component of current density (wave shape b), while in Fig. 8.22a for the TFA the converse is true. Similar observation may also be made for the oscillograms of Figs. 8.19b and 8.22b. This strongly substantiates the view (expressed in Chapter 7) that in the end region, currents flow predominantly across the thickness of the plate in the LFA and from pole-to-pole in the same half of the plate in the TFA.

### 8.5.8.3 Oscillograms for the End-Strip Plate

Figs. 8.23 through 8.25 show the oscillograms of voltages from the current-density probes and the full-pitch search coil on the surface of the end-strip plate (Fig. 8.6). Comparing the voltages of the oscillograms (for the LFA) of Fig. 8.23a for the end-strip plate with those of Fig. 8.18a for the narrow plate, it may be observed that although both are of the similar form, the wave-shapes of Fig. 8.23a are

more sharp-peaked. Harmonic analysis of these oscillograms shows that the fundamental magnitudes in Fig. 8.23a are upto 20% less than those in Fig. 8.18a. This shows that the presence of the low-resisitivity end-strips causes the x-component of the current density in the active region on the surface of the plate to be decreased.

Figs. 8.23, 8.24 and 8.25 also show the relative magnitudes of the z and the x components of current densities at various locations on the plate surface. Comparing the wave shapes in Figs. 8.23 and 8.24, it may be seen that the z-component of the current density is generally the dominant one. However, for the TFA, the x-component of current density can be significant at the end of the active width (Fig. 8.25b).

Fig. 8.25c shows the voltage from the full-pitch search coil on the surface of the plate and the output of the same voltage from the integrator circuit for the TFA. (Similar oscillograms of search coil voltage were also obtained for the other pole-arrangement and for the other plates.). The phase shift of $\pi/2$ between them may be noted, as also the sinusoidal natures of both voltage wave shapes. The ratio of the amplitudes of the wave shapes in Fig. 8.25c is 3.176 (ideally, it should be equal to $\pi$).

### 8.5.9 Temperature-Time Curves

The curves of Figs. 8.26 and 8.27 show the rise in the

temperature on the surfaces of the plates with time for 50 Hz and 25 Hz supplies respectively.

The curves of Fig. 8.26 are higher than those of Fig. 8.27 showing thereby that the use of higher frequency is advisable for heating purposes. In both figures it may be seen that the rise in the temperature is higher for the LFA than for the TFA. This suggests that the LFA produces more power loss in the plate than the TFA, which is true for weak eddy-current reaction ($Q<1$).

The lower curves of Figs.8.26 and 8.27 refer to the wide plate, where, because of the greater plate area, the rise in the temperature of the plate was less rapid.

# CHAPTER 9

# GENERAL CONCLUSIONS AND FURTHER WORK

## 9.1 GENERAL CONCLUSIONS

This thesis is concerned with the study of the electromagnetic fields in the solid-iron plate in a travelling wave induction heater where the plate is subjected to travelling magnetic fields on both sides. The study is divided into two parallel developments; one for a heater in which the corresponding poles on the opposite sides of the plate are of the same instantaneous polarity, called the longitudinal flux arrangement (LFA), and the other for a heater in which the corresponding poles are of the opposite instantaneous polarity, called the transverse flux arrangement (TFA).

The linear two-dimensional solutions (Chapters 3 and 4) concerning the penetration of electromagnetic fields into the solid-iron plate show that the expressions for the electromagnetic field quantities, the eddy-current power loss and the forces of electromagnetic origin are all functions of the thickness of the plate. For both pole-arrangements, the plate may be considered electromagnetically thick if its half-thickness is greater than $\pi/4$ times the depth of penetration in the material of the plate. In the LFA, the plate may be considered thick if its half-thickness is greater than $1/\pi$ times the pole-pitch of the excitation current sheet (section 3.4.6), while in the TFA, the plate may be considered thick if its half-thickness is greater than $\pi/2$ times the quotient (depth of penetration)$^2$/(pole-pitch) (section 3.5.6.). In electromagnetically thick plates,

the expressions for electromagnetic field quantities are the same for both pole-arrangements whereas in thin plates these expressions exhibit characteristics particular to the pole-arrangement (section 4.3). For thin plates the power loss in the TFA is many times greater than that in the LFA, while for thick plates, the power loss is the same in both pole-arrangements.

The study of the eddy-current reaction field inside the plate shows that it is a function of the plate-thickness in addition to the relative permeability of the plate and the air-gap length (sections 4.2.2. and 4.2.3). The magnetic field strengths on the surface of the plate for either pole-arrangement, $\hat{H}_{x\ell d}$ or $\hat{H}_{xtd}$, (equations (4.13) or (4.31)) cannot be considered the same as the primary excitation $\hat{K}_z$, even for small values of the ratio of air-gap length to pole-pitch, since the expressions for these quantities are functions of plate thickness. This, it is believed, has not been considered before.

Irrespective of the finite thickness of the plate, the magnetic field strength in the plate is predominantly one dimensional for both pole-arrangements (sections 3.4.7. and 3.5.7.) if $2\alpha^2 > q^2$; no previous study, it is believed, has shown this for a machine of this form.

The non-linear theories consider one-dimensional magnetic field strength in the plate for both pole-arrangements; a new double-function (equation (5.17)) is introduced as a solution to the diffusion equation in order to account for

the additional boundary conditions at the centre of the thickness of the plate. It is shown that in transition from electromagnetically thin to thick plates, not only does the loss density in the plate decrease, but the exponent of the surface magnetic field strength in the loss expression reduces also from approximately 2 to (b+3)/2 (sections 5.4.5 and 5.5.5). By defining a dimensionless parameter Q as the ratio of the input impedances at the surface of the plate (section 6.4.3 and 6.5.3), the dominance or otherwise of the eddy-current reaction field is determined according as whether Q is very large or small compared with unity. Q=1 represents the condition for maximum loss in the plate (from the principle of impedance matching). It is shown that for a given set of values for (i) the magnitude and the frequency of the primary excitation, (ii) the dimensions of the heater, and (iii) the parameters of the material of the plate ($\rho$, a and b), a plate thickness exists at which maximum loss would occur in the plate (equations (6.17) and (6.40)). The air-gap flux/pole is obtained as being independent of the solid-iron parameters when the eddy-current reaction was weak i.e. Q<1 (sections 6.4.8 and 6.5.8).

The nature of the distribution of end-current in a plate of finite width (in addition to finite thickness) affects the power loss in the plate. An investigation into the effects of finite width on the power loss in the plate shows that, for weak eddy-current reaction, the power loss is reduced compared with the same in a plate having negligible finite width effect (equations (7.35) and (7.45)). The

reduction in the power loss in the plate due to finite width effect depends on the ratio of active width to pole-pitch; this ratio ought to be large in order to minimise such a reduction. In addition, the finite width effect depends on the plate-thickness, the parameters of the material of the plate and the pole-arrangement. With a decrease in the plate thickness, the effect of finite width becomes less significant in the LFA and more significant in the TFA (section 7.7.4). This was found to be consistent with the actual eddy-current distribution in the plate; in the LFA, the end currents are predominantly cross-thickness in nature, whereas in the TFA, the end currents are cross-pole in nature (Fig. 7.2). The consideration of the ratios of the directional components of surface current densities in the plate at the end of the active width (sections 7.9.2 and 8.5.7.2) substantiates this observation and shows how the distribution of end current modifies with the variation in the thickness of the plate. In so far as the effect of finite width on loss in concerned, the LFA is to be preferred for obtaining higher eddy-current power loss in the plate.

The experimental investigations undertaken (Chapter 8) verify the proposed non-linear theories and the effects of finite width on power loss and current-density distributions in the plate; the investigations show that the increase in the temperature of the plate has considerable influence on the experimental results.

In a travelling wave induction heater, the eddy-current

power loss in the plate would have to be as high as possible. If solid-iron plates of a given thickness would be used, either pole-arrangement may be utilised and the use of equation (6.17) or (6.40) for optimum plate thickness is recommended for the design of the heater. If solid-iron plates of various thicknesses would be used, the utilisation of the transverse flux arrangement is recommended for thin plates and the utilisation of the longitudinal flux arrangement is recommended for thick plates. With the provision of one of the two primary members being movable, the same heating device may be used for both pole-arrangements. It is highly recommended that a travelling wave induction heater should be multipole and have large ratios of active width to pole-pitch, plate thickness to pole-pitch and small ratio of air-gap length to pole-pitch, although the last condition may not be practicable.

The aim of this work was to study the electromagnetic fields produced in a solid-iron plate when it is subjected to travelling magnetic fields on both sides. It is considered that this thesis presents a thorough study of the electromagnetic field quantities in the plate under the constraints of finite plate-thickness, magnetic non-linearity and of finite active width. It is believed that the aim was accomplished and that this work provides a good foundation for further work.

## 9.2 FURTHER WORK

The work of this thesis was concerned with a new kind of induction heater; extensive theoretical work was necessary for providing a sound basis for future work. In this work, only those experiments considered necessary to verify the theory were carried out and consequently, scope exists for extensive experimental investigations. For example, plates of various thicknesses may be considered in the investigations, particularly in verifying optimum plate-thickness (i.e. for which maximum loss occurs). Experiments may also be devised to measure the forces developed on the plate, which were not considered in the present work.

The linear arrangement of Fig. 3.1 (which is considered throughout this thesis) gives rise to the entry and exit phenomena on the plate resulting in lower current and flux densities at the ends of the active length. This affects the overall power loss calculations, which assumes uniform current density over the whole of the active length. Although for multipole heaters, entry and exit effects have little influence on power loss, in 2-pole heaters, they may be singificant. Further work may be carried out on this aspect, providing, perhaps, a finite length factor, which would show the effects of entry and exit phenomena on the power loss and the electromagnetic field distributions in the plate.

The power loss in the plate causes a substantial increase in the temperature of the solid-iron plate. A travelling-wave heating system being the aim of the future development of this

work, a high power loss and hence a rapid rise in the temperature of the plate to very high values (upto 1000$^{o}$C) is to be envisaged. The rise in the temperature of the plate brings about an increase in the resistivity of its material and also a change in the air-gap length. While the variation in the air-gap length in the linear arrangement considered here may be kept to a minimum at all temperatures, the effects of the variation in the resistivity need to be taken into account. This necessitates the solution of heat transfer equation together with the diffusion equation for electromagnetic field quantities. This was attempted by Jackson [6] in connection with his work on eddy-current couplings. For the present model, extensive work may be carried out to incorporate the effects of the rise in the temperature of the plate especially at high excitation, resulting, perhaps in predicted temperature vs. power loss and time curves.

The theories presented in this thesis predict the penetration of the magnetic flux from the air-gap surface to the inside of the plate. The two different pole-arrangements give rise to the different natures of flux penetration and also to special boundary conditions at the plane of symmetry, y=0. Both flux and current density penetration tests may be carried out by splitting the plate as shown in Fig. 9.1a and putting on search coils and current-density probes on the mating surfaces as shown in Fig. 9.1b and using copper end-strips to bridge the split faces. The effects of the split on the electromagnetic fields have

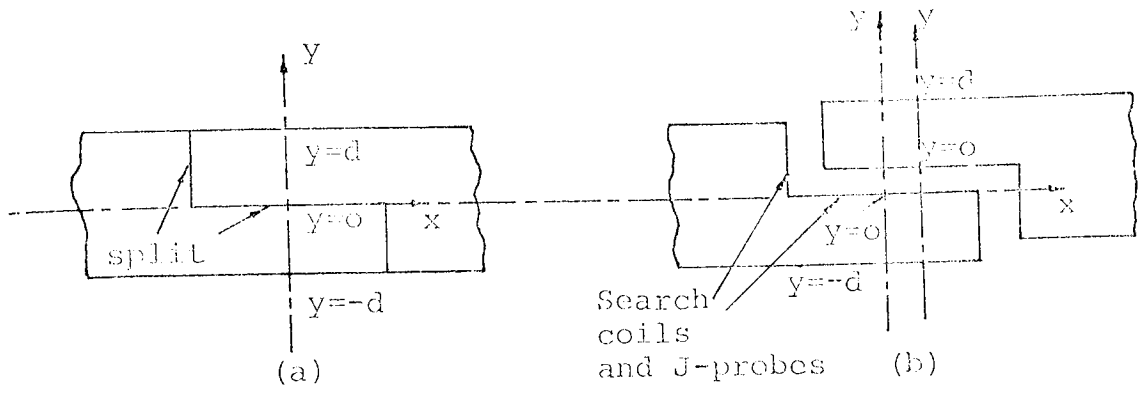


Fig. 9.1: The x-y plane of the plate: (a) the plate with faces for split. (b) Split faces exaggerated to show the locations of search coils and J-probes.

been dealt with in detail in Bowden's work.[30]

While experimenting, vibrations were noticed in the plate at certain values of excitation and frequency. Although in the work of this thesis vibrations were minimised by the clamping arrangement, investigations may be made in future on the nature and the extent of the electromechanical effects of such vibrations. One effect of considerable influence may be the loss of symmetry (about y=0 and z=0 planes) due to vibration.

In this thesis the analysis was carried out in terms of field theory, whilst eventually an equivalent circuit approach may be easier to use. Thus an equivalent circuit for the present system may be obtained from the work presented in this thesis.

In future work, attempts may be made to obtain the normalised loss as a function of normalised plate thickness

(i.e. plate thickness/optimum plate thickness) with normalised resistivity (resistivity/resisitivity at maximum loss) as a parameter. This will increase the scope of application of the present work.

Finite-difference and finite-element solutions were mentioned only briefly in this thesis. Elaborate work may be carried out in these lines in future, so that more accurate results may be obtained from computation. However, it is believed that this would be mainly an academic exercise.

# APPENDIX 1

## AN APPROXIMATE ALLOWANCE FOR THE EFFECT OF HYSTERESIS

### A1.1 GENERAL

Hysteresis complicates the eddy-current problems further. In general, however, the effect of hysteresis on loss and force is small and as such, more often than not, hysteresis is neglected. Some finite difference approaches[53,54] already discussed have also shown that the eddy-current loss calculated using B-H curve alone accounts for a considerable part of the hysteresis loss. In the works of this thesis, hysteresis is neglected. However, an attempt is made in this appendix to include hysteresis approximately in the analysis.

Pohl's[49] is an excellent attempt to include the effect of hysteresis on loss and field distribution. He introduces a multiplying factor (greater than one) by which the attenuation of the field quantities is accelerated and the eddy-current loss is reduced. The total loss due to eddy-current and hysteresis is, however, increased by this factor. Bowden[30] also accounted for hysteresis in the similar fashion.

Attempts have been made in the past to represent the magnetic hysteresis by rectangular B-H loop[57,58], but the representation by an idealised elliptical B-H loop, as shown in Fig. A1.1, remains a popular approach[13,59-61]. O'Kelly[59-61] has done extensive work

using elliptical B-H loop.

Elliptical B-H loop is a very simple and logical approach for representing hysteresis. For the actual B-H loop it is a good approximation. Moreover, this is

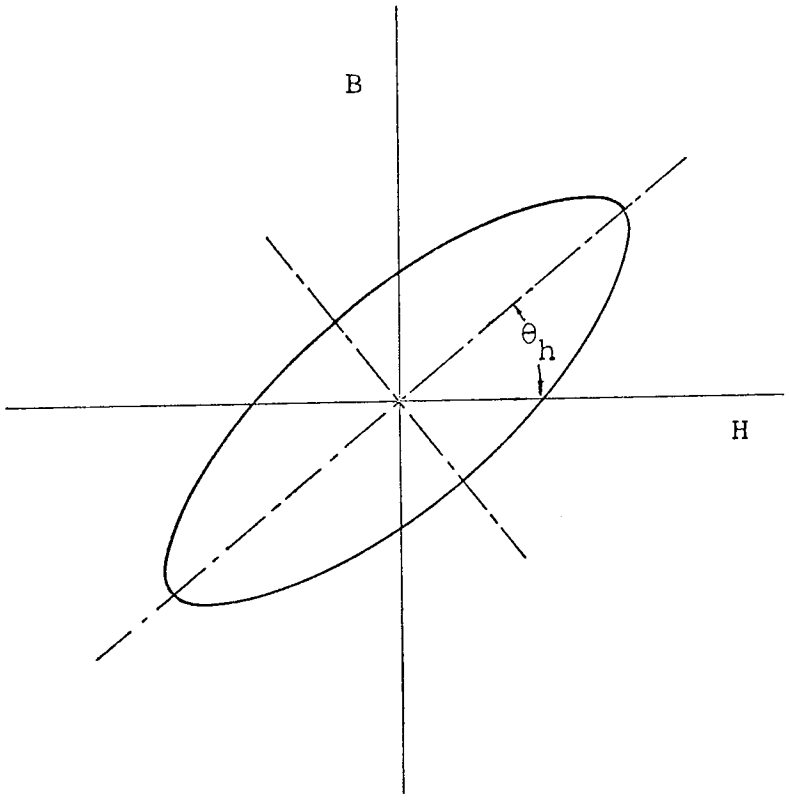


Fig. A1.1 Elliptical B-H Loop.

a good choice for the effect of hysteresis to be amenable to analytic treatment. In this thesis, therefore, an elliptical B-H loop, as shown in Fig. A1.1, is considered and its effect on expressions for electromagnetic field quantities already obtained in Chapter 3 is studied.

## A1.2 INCORPORATING THE EFFECT OF HYSTERESIS

### A1.2.1 Modification in Laplace's Equation

In its simplest form, hysteresis introduces an angle

so that,

$$k_h = (1 + j)\alpha_h$$

i.e.

$$k_h = (c_1 + jc_2)\alpha \qquad \text{(A1.6)}$$

where,

$$c_1 = \sqrt{2}\cos\{(\pi/4) - (\theta_h/2)\} \qquad \text{(A1.7)}$$

and

$$c_2 = \sqrt{2}\sin\{(\pi/4) - (\theta_h/2)\} \qquad \text{(A1.8)}$$

The field components deduced in the following sections

y

Please swap the following two pages while reading.

Author

In the absence of hysteresis, the equations ---

magnetic field components and current density, under longitudinal flux arrangement , are given by equation (3.38) through (3.40). On consideration of hysteresis these are modified as given below

$$\dot{H}_{x\ell h} = \frac{-2\hat{K}_z(c_1+jc_2)}{\dot{M}_{\ell h}}\left[\cosh\alpha(c_1+jc_2)y\right]\exp(-jqx) \qquad \text{(A1.9)}$$

$$\dot{H}_{y\ell h} = \frac{-j2\hat{K}_z q}{\alpha\dot{M}_{\ell h}}\left[\sinh\alpha(c_1+jc_2)y\right]\exp(-jqx) \qquad \text{(A1.10)}$$

so that,

$$k_h = (1 + j)\alpha_h$$

i.e.

$$k_h = (c_1 + jc_2)\alpha \qquad \text{(A1.6)}$$

where,

$$c_1 = \sqrt{2} \cos \{(\pi/4) - (\theta_h/2)\} \qquad \text{(A1.7)}$$

and

$$c_2 = \sqrt{2} \sin \{(\pi/4) - (\theta_h/2)\} \qquad \text{(A1.8)}$$

The field components deduced in the following sections pertains, as before, to the model of Fig. 3.1 and are given for the two different pole arrangements. The primary members in Fig. 3.1 are assumed to have infinite permeability and the field components are represented by a further subscript, h, to show the effect of hysteresis.

A1.2.2 Field Components and Loss and Force Equations Under Longitudinal Flux Arrangements.

In the absence of hysteresis, the equations for magnetic field components and current density, under longitudinal flux arrangement , are given by equation (3.38) through (3.40). On consideration of hysteresis these are modified as given below

$$\dot{H}_{x\ell h} = \frac{-2\hat{K}_z (c_1+jc_2)}{\dot{M}_{\ell h}} \left[\cosh\alpha(c_1+jc_2)y\right] \exp(-jqx) \qquad \text{(A1.9)}$$

$$\dot{H}_{y\ell h} = \frac{-j2\hat{K}_z q}{\alpha \dot{M}_{\ell h}} \left[\sinh\alpha(c_1+jc_2)y\right] \exp(-jqx) \qquad \text{(A1.10)}$$

of lag for the flux density, B, with respect to the magnetic field strength, H, and this angle is termed hysteresis angle. Neglecting the harmonics introduced by saturation, the hysteresis loop may be considered as an ellipse with the major axis making an angle $\theta_h$ with the H-axis (Fig. A1.1). A complex permeability, $\mu_h$, due to hysteresis may then be defined as,

$$\mu_h = \frac{B}{H}\cdot\exp(-j\theta_h) = \mu_r\mu_o\exp(-j\theta_h) \qquad \text{(A1.1)}$$

Laplace's equation in two dimensions, equation (3.18), is thus modified to

$$\frac{\partial^2 A}{\partial x^2} + \frac{\partial^2 A}{\partial y^2} = \alpha_h^2(1+j)^2 A \qquad \text{(A1.2)}$$

where A is the vector potential, defined in equation (3.8), and

$$\alpha_h = \left(\frac{\mu_r\mu_o\omega}{2\rho}\right)^{\frac{1}{2}} \exp(-j\theta_h/2) \qquad \text{(A1.3)}$$

The solution of equation (A1.2) is still given by equation (3.20), but the value of k, equation (3.21), is modified to, say, $k_h$, where,

$$k_h^2 = q^2 + j2\alpha_h^2 \qquad \text{(A1.4)}$$

Under the usual assumption of $2\alpha^2 >> q^2$, it is obvious that $2\alpha_h^2 >> q^2$, since, from equation (A1.3), $|\alpha_h| = |\alpha|$. The use of this assumption was justified in Sections 3.4.4 and 3.5.4 and will be taken to hold here. Thus in equation (A1.4)

$$2\alpha_h^2 >> q^2 \qquad \text{(A1.5)}$$

and

$$\dot{J}_{z\ell h} = \frac{j4\hat{K}_z\alpha}{\dot{M}_{\ell h}} \cdot [\sinh\alpha(c_1+jc_2)y] \exp(-jqx) \qquad \text{(A1.11)}$$

where

$$\dot{M}_{\ell h} = -2\cosh qg\cosh c_1\alpha d.\cos c_2\alpha d\Big[\{(m\tanh qg - c_2\tan c_2\alpha d)\tanh c_1\alpha d + c_1\} +$$

$$j\{(m\tanh qg + c_1\tanh c_1\alpha d)\ \tan c_2\alpha d + c_2\}\Big] \qquad \text{(A1.12)}$$

i.e. magnitudically,

$$|\dot{M}_{\ell h}| = \sqrt{2}\cosh qg\{m^2.\tanh^2 qg(\cosh 2c_1\alpha d - \cos 2c_2\alpha d) +$$

$$2m.\tanh qg(c_1\sinh 2c_1\alpha d + c_2\sin 2c_2\alpha d) + 2(\cosh 2c_1\alpha d +$$

$$\cos 2c_2\alpha d)\}^{\frac{1}{2}} \qquad \text{(A1.13)}$$

The values of the electromagnetic field components at the surface of the plate may be obtained from equations (A1.9) through (A1.11) with the substitution of y = d. After some calculations, this gives

$$H_{x\ell dh} = \frac{-2\hat{K}_z}{|\dot{M}_{\ell h}|}\left[\cosh 2c_1\alpha d + \cos 2c_2\alpha d\right]^{\frac{1}{2}} \exp(-jqx)\underline{/H_{x\ell dh}} \qquad \text{(A1.14)}$$

$$H_{y\ell dh} = \frac{-\sqrt{2}\hat{K}_z q}{\alpha.|\dot{M}_{\ell h}|}\left[\cosh 2c_1\alpha d - \cos 2c_2\alpha d\right]^{\frac{1}{2}} \exp(-jqx)\ \underline{/H_{y\ell dh}} \qquad \text{(A1.15)}$$

and

$$J_{z\ell dh} = \frac{2\sqrt{2}\hat{K}_z\alpha}{|\dot{M}_{\ell h}|}\left[\cosh 2c_1\alpha d - \cos 2c_2\alpha d\right]^{\frac{1}{2}} \exp(-jqx)\underline{/-H_{y\ell dh}} \qquad \text{(A1.16)}$$

where $|\dot{M}_{\ell h}|$ is given by equation (A1.13) and,

$$\angle H_{x\ell dh} = \tan^{-1}\left[\frac{m\tanh qg\left(\frac{c_2}{c_1}\sinh 2c_1\alpha d - \sin 2c_2\alpha d\right)}{m\tanh qg.\left(\sinh 2c_1\alpha d + \frac{c_2}{c_1}\sin 2c_2\alpha d\right) + (c_1+c_2)(\cosh 2c_1\alpha d + \cos 2c_2\alpha d)}\right] \qquad (A1.17)$$

and

$$\angle H_{y\ell dh} = \tan^{-1}\left[\frac{m\tanh qg\,(\cosh 2c_1\alpha d - \cos 2c_2\alpha d) + (c_1\sinh 2c_1\alpha d + c_2\sin 2c_2\alpha d)}{(c_2\sinh 2c_1\alpha d - c_1\sin 2c_2\alpha d)}\right] \qquad (A1.18)$$

Equations (A1.14) through (A1.18) may be compared with equations (3.44) through (3.48), respectively, in order to see the effect of hysteresis.

The total loss/area, given by equation (3.55), is now modified to

$$P_{y\ell dh} = \frac{2\hat{K}_z^2\alpha\rho}{|\dot{M}_{\ell h}|^2}\,(c_2\sinh 2c_1\alpha d - c_1\sin 2c_2\alpha d) \qquad (A1.19)$$

The force equations given by equations (3.60) and (3.61) are, likewise, modified to

$$F_{x\ell h} = \frac{2\mu_o\mu_r\hat{K}_z^2 q}{|\dot{M}_{\ell h}|^2}\,(\cosh 2c_1\alpha y - \cos 2c_2\alpha y) \qquad (A1.20)$$

and

$$F_{y\ell h} = \frac{2\mu_o\mu_r\hat{K}_z^2\alpha}{|\dot{M}_{\ell h}|^2}\,(c_2\sinh 2c_1\alpha y - c_1\sin 2c_2\alpha y) \qquad (A1.21)$$

$|\dot{M}_{\ell h}|$ in equation (A1.19) through (A1.21) is given by equation (A1.13).

A1.2.3 Field Components and Loss and Force Equations Under Transverse Flux Arrangement

Under transverse flux arrangement, the field components, in the absence of hysteresis, are given by equations (3.74) through (3.76). When hysteresis is considered, these equations are modified to the forms:

$$\dot{H}_{xth} = \frac{2\hat{K}_z(c_1+jc_2)}{\dot{M}_{th}} \cdot [\sinh\alpha(c_1+jc_2)y]\exp(-jqx) \quad (A1.22)$$

$$\dot{H}_{yth} = \frac{j2\hat{K}_z q}{\alpha\dot{M}_{th}} \cdot [\cosh\alpha(c_1+jc_2)y]\exp(-jqx) \quad (A1.23)$$

and

$$\dot{J}_{zth} = \frac{-j4\hat{K}_z\alpha}{\dot{M}_{th}} \cdot [\cosh\alpha(c_1+jc_2)y]\exp(-jqx) \quad (A1.24)$$

where ,

$$\dot{M}_{th} = 2\cosh qg\cosh c_1\alpha d\cos c_2\alpha d\left[\{m\tanh qg + c_1\tanh c_1\alpha d - c_2\tan c_2\alpha d\} + j\{(m\tanh qg\tanh c_1\alpha d + c_1)\tan c_2\alpha d + c_2\tanh c_1\alpha d\}\right] \quad (A1.25)$$

i.e. magnitudically,

$$|\dot{M}_{th}| = \sqrt{2}\cosh qg\left[m^2\tanh^2 qg(\cosh 2c_1\alpha d + \cos 2c_2\alpha d) + 2m\tanh qg(c_1\sinh 2c_1\alpha d - c_2\sin 2c_2\alpha d) + 2(\cosh 2c_1\alpha d - \cos 2c_2\alpha d)\right]^{\frac{1}{2}} \quad (A1.26)$$

The surface values of the above quantities may be obtained by substituting y = d in the above equations. After some calculations, this gives

$$H_{xtdh} = \frac{2\hat{K}_z}{|\dot{M}_{th}|}\left[\cosh 2c_1\alpha d - \cos 2c_2\alpha d\right]^{\frac{1}{2}} \exp(-jqx) \; \underline{/H_{xtdh}} \qquad \text{(A1.27)}$$

$$H_{ytdh} = \frac{\sqrt{2}\hat{K}_z q}{\alpha|\dot{M}_{th}|}\left[\cosh 2c_1\alpha d + \cos 2c_2\alpha d\right]^{\frac{1}{2}} \exp(-jqx) \; \underline{/H_{ytdh}} \qquad \text{(A1.28)}$$

and

$$J_{ztdh} = \frac{2\sqrt{2}\alpha\hat{K}_z}{|\dot{M}_{th}|}\left[\cosh 2c_1\alpha d + \cos 2c_2\alpha d\right]^{\frac{1}{2}} \exp(-jqx) \; \underline{/-H_{ytdh}} \qquad \text{(A1.29)}$$

where $|\dot{M}_{th}|$ is given by equation (A1.26), and,

$$\underline{/H_{xtdh}} = \tan^{-1}\left[\frac{m\tanh qg\left(\frac{c_2}{c_1}\sinh 2c_1\alpha d + \sin 2c_2\alpha d\right)}{m\tanh qg\left(\sinh 2c_1\alpha d - \frac{c_2}{c_1}\sin 2c_2\alpha d\right) + (c_1+c_2)(\cosh 2c_1\alpha d - \cos 2c_2\alpha d)}\right] \qquad \text{(A1.30)}$$

and

$$\underline{/H_{ytdh}} = \tan^{-1}\left[\frac{m\tanh qg(\cosh 2c_1\alpha d + \cos 2c_2\alpha d) + (c_1\sinh 2c_1\alpha d - c_2\sin 2c_2\alpha d)}{(c_2\sinh 2c_1\alpha d + c_1\sin 2c_2\alpha d)}\right] \qquad \text{(A1.31)}$$

The above equations may be compared with equations (3.79) through (3.83), which were obtained neglecting hysteresis.

The total loss/area, given by equation (3.90), is now modified to

$$P_{ytdh} = \frac{2\hat{K}_z^2\alpha\rho}{|\dot{M}_{th}|^2}\cdot(c_2\sinh 2c_1\alpha d + c_1\sin 2c_2\alpha d) \qquad \text{(A1.32)}$$

The force equations, given by equations (3.95) and (3.96), are now modified to

$$F_{xth} = \frac{2\mu_r\mu_o q\hat{K}_z^2}{|\dot{M}_{th}|^2} (\cosh 2c_1\alpha y + \cos 2c_2\alpha y) \qquad (A1.33)$$

and

$$F_{yth} = \frac{2\mu_r\mu_o \alpha\hat{K}_z^2}{|\dot{M}_{th}|^2} (c_2 \sinh 2c_1\alpha y + c_1 \sin 2c_2\alpha y) \qquad (A1.34)$$

In the above equations $|\dot{M}_{th}|$ is given by equation (A1.26).

## A1.3 COMMENT

In the above two sections, equations for electromagnetic field components and for loss and force densities have been obtained, for both longitudinal and transverse flux arrangements, including the effect of hysteresis. The effect of hysteresis is embodied in the different expressions through the constants $c_1$ and $c_2$. These equations may be readily verified against those obtained in Chapter 3, where hysteresis was neglected.

In the absence of hysteresis $\theta_h = 0$ and both the constants $c_1$ and $c_2$ become unity, i.e.

$$c_1 = c_2 = 1 \qquad (A1.35)$$

Substituting equation (A1.35) in the above expressions, each reduces to its corresponding form in Chapter 3.

It is believed that no published work that deals with the model of Fig. 3.1, has allowed for hysteresis in this way.

# APPENDIX II

## THE M.M.F. EQUATIONS AND APPROXIMATE RELATIONS BETWEEN $|\dot{H}_{xd}|$ AND $|\dot{F}_c|$

### A2.1 THE M.M.F. EQUATIONS

Fig. A2.1 shows the model (as Fig. 3.1) considered throughout this thesis. The m.m.f equation concerning the primary current sheet $\hat{K}_z$ and the x-component of

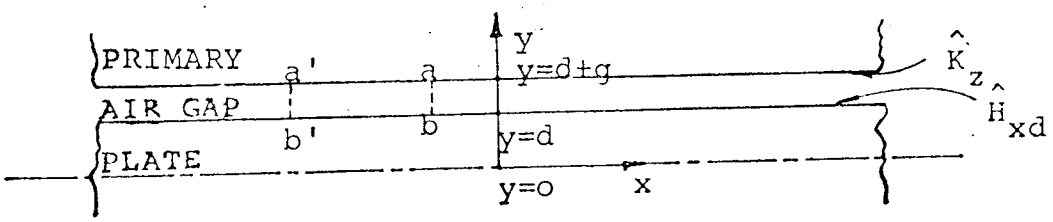


Figure A2.1

magnetic field strength on the plate surface, $\dot{H}_{xd}$ may be obtained by considering the path aa'b'b in this figure. Note that the path includes the primary current sheet but no secondary currents.

Applying Ampere's circuital law around this path,

$$\dot{F}_g = \dot{F}_c + \dot{F}_r \qquad \text{(A2.1)}$$

where,

$\dot{F}_g$ is the resultant m.m.f. of the air-gap region

$\dot{F}_c = \int \hat{K}_z dx$ is the m.m.f. of the primary current sheet

and $\dot{F}_r = \int \dot{H}_{xd} dx$ is the m.m.f. of the eddy current reaction field in the plate.

However, $\dot{F}_r$ represents the m.m.f. of the eddy current reaction field if $\mu_r \tanh qg \tanh qd >> 1$, (equation 4.13).

This condition holds for moderate values of qg and qd.

Now, the integrals may be solved from considering $\dot{K}_z = \hat{K}_z \exp(-jqx)$ and $\dot{H}_{xd} = \hat{H}_{xd} \exp(-jqx)$, so that

$$\dot{F}_c = \frac{j\hat{K}_z}{q} \qquad \text{(A2.2)}$$

and

$$\dot{F}_r = \frac{j\dot{H}_{xd}}{q} \qquad \text{(A2.3)}$$

Equation (A2.1) is now given by

$$\dot{F}_g = \frac{j}{q}(\hat{K}_z + \dot{H}_{xd}) \qquad \text{(A2.4)}$$

$\dot{H}_{xd}$ may be obtained from equation (6.7) and using equation (6.12) and (6.35) the resultant air-gap m.m.f. may be obtained for longitudinal and transverse flux arrangements respectively.

## A2.2 APPROXIMATE RELATIONS BETWEEN $|\dot{H}_{xd}|$ AND $|\dot{F}_c|$

The relation between the surface magnetic field strength, $|\dot{H}_{xd}|$, and the primary m.m.f. $|\dot{F}_c|$ is given by equations (6.21) and (6.16) for longitudinal flux arrangement and by equations (6.44) and (6.39) for transverse flux arrangement. An approximate relation between them may be obtained when the non-dimensional parameter Q (i.e. $Q_t$ or $Q_\ell$ ) is large. Equation (6.44), for example, becomes, when $Q_t >> 1$

$$|\dot{H}_{xtd}| \equiv \frac{q|\dot{F}_{ct}|}{\cosh qg} \equiv q|\dot{F}_{ct}| \qquad \text{(A2.5)}$$

since, as seen from equation (6.39), for a given plate and primary excitation, large values of $Q_t$ are always associated with small values of qg. Similarly, for longitudinal flux arrangement,

$$\left|\dot{H}_{x\ell d}\right| \equiv \frac{q\left|\dot{F}_{c\ell}\right|}{\cosh qg} \equiv q\left|\dot{F}_{c\ell}\right| \qquad \text{(A2.6)}$$

## APPENDIX III

## CALCULATIONS FOR OPTIMUM LOSS ON A SINGLE-SIDED ARRANGEMENT

Although this thesis considers a double-sided arrangement as shown in Fig. 3.1, some work was done at the outset of this project, on the optimisation of loss in a semi-infinite plate with excitation from only one side. For this purpose, expressions were used from Bowden's thesis, and it is believed to be an extension of his work.

The loss/area, $P_n$, is given by (equation 6.27 of Ref.30)

$$P_n = \frac{|\dot{F}_c|^2 \mu_o \omega q \cos\phi_n \Delta_n}{2\sinh qg . \cosh qg} \qquad \text{(A3.1)}$$

where $\phi_n = \phi_t$, given by equation (5.65) of this thesis and

$$\Delta_n = \frac{1}{Q_n + Q_n^{-1} + 2\sin\phi_n} \qquad \text{(A3.2)}$$

and $Q_n = Q_{t\infty}$, given by equation (6.39) when $d \gg \frac{2}{\alpha_t}$

With increase in loss inside the plate, its temperature rises and so does its resistivity along with a variation in air-gap length. To obtain very high losses (of the order of $MW/m^2$), the air-gap length should be sufficiently large (e.g. 1 cm or more), so that any small change would be negligible. Alternately, provisions may be made to keep the air-gap reasonably constant in the

flat arrangement being considered. Thus, it was decided to investigate the variation in loss with variation in resistivity alone.

For given values of primary excitation and frequency, Figure A3.1 shows the variation of loss against resistivity in an EN1A steel plate for various values of pole-pitch and for an air-gap of 1 cm. Similar curves may be obtained for any change in these values. Fig. A3.1 shows the very definite pattern that, for any pole-pitch, there is always a value of resistivity when the loss in the plate is a maximum. With reasonable values of pole-pitch, (e.g. varying between, say, 12 cm and 25 cm), such resistivity values may, in fact, be attained with rise in temperature. Also to be noted in the figure is the fact that the curves are flat-topped, so that losses near to peak may be obtained relatively easily.

On the basis of the findings of Figure A3.1, it was decided to investigate the relation between generalised loss and resistivity. The maximum loss, $P_{nm}$, may be obtained from equations (A3.1) and (A3.2) by putting $Q_n = 1$, so that

$$\frac{P_n}{P_{nm}} = \frac{2+2\sin\phi_n}{Q_n+Q_n^{-1}+2\sin\phi_n} \qquad \text{(A3.3)}$$

Since $\phi_n$ is constant, it is necessary to calculate $Q_n$

only in equation (A3.3).

In terms of machine parameters and primary excitation $Q_n$ is given by equations (6.34) and (6.35) of Bowden's work, as

$$N_\Delta = \frac{2\mu_o^2\omega|\dot{F}_c|^{(1-b)}\cosh^{(b-1)}qg}{q^{(1+b)}\rho R_n^2 k_b A\tanh^2 qg} \qquad (A3.4)$$

where

$$N_\Delta = Q_n^{\frac{b+3}{2}}\Delta_n^{\frac{b-1}{2}} \qquad (A3.5)$$

($R_n = R_t$, given by equation (5.64) of this thesis, $k_b = k_{bt}$, given by equation (5.54) of this thesis and A = 1.25a.)

If $\rho = \rho_m$ at maximum loss, then this applies when $Q_n = 1$. If $N_{\Delta m}$ represents the value of $N_\Delta$ when $\rho = \rho_m$ i.e. at maximum loss, then for a particular machine with given primary excitation and frequency, equation (A3.4) gives

$$\frac{N_{\Delta m}}{N_\Delta} = \frac{\rho}{\rho_m} \qquad (A3.6)$$

But from equation (A3.5) and (A3.2)

$$\frac{N_{\Delta m}}{N_\Delta} = \frac{(2+2\sin\phi_n)^{\frac{(1-b)}{2}}}{Q_n^{\frac{b+3}{2}}(Q_n+Q_n^{-1}+2\sin\phi_n)^{\frac{(1-b)}{2}}} \qquad (A3.7)$$

From equations (A3.6) and (A3.7), therefore

$$\frac{\rho}{\rho_m} = \frac{1}{Q_n^{\frac{b+3}{2}}}\left[\frac{2+2\sin\phi_n}{Q_n+Q_n^{-1}+2\sin\phi_n}\right]^{\frac{(1-b)}{2}} \qquad (A3.8)$$

From equations (A3.3) and (A3.8), then

$$\frac{P}{P_{nm}} = Q_n^{\frac{b+3}{1-b}} \left(\frac{\rho}{\rho_m}\right)^{\frac{2}{1-b}} \qquad \text{(A3.9)}$$

Equation (A3.9) is the final form of the relation between generalised loss and resistivity and shows that it is necessary to obtain $Q_n$ for this relationship. $Q_n$ may be obtained as a function of $\rho/\rho_m$ from equation (A3.8) and since $P_{nm}$ may be obtained from equation (A3.1), the generalised loss may be obtained from equation (A3.9) or (A3.3).

Fig. A3.2 shows the plots of $Q_n$ and $P_n/P_{nm}$ against $\rho/\rho_m$. These curves, being generalised in nature, apply to all machine parameters and excitation values.

It may be noted in Fig. A3.2 that the variation of $P_n/P_{nm}$ is not symmetrical about $(\rho/\rho_m) = 1$. For example, the value of $P_n/P_{nm}$ at $(\rho/\rho_m) = 0.1$ is about 30% higher than that at $(\rho/\rho_m) = 10$. This is useful in optimising the loss, because almost invariably, $(\rho/\rho_m) << 1$ and one is working on the higher loss side. A close examination of Fig. A3.2 also reveals that for values of $\rho/\rho_m$ between 0.1 and 0.5, $P_n/P_{nm}$ varies between 0.6 and 0.95. It may be possible, in some cases, to increase the resistivity to within this range at sufficiently high temperatures (below Curie point). Small values of $Q_n$ (between 3.8 and 1.54) are indicative of the fact that obtainable loss values are to a large extent exploited. At other ranges of $\rho/\rho_m$, loss values are either

not high or the cost of obtaining such losses does not justify the advantages gained. $(\rho/\rho_m) = 0.22$ is a fairly good choice, because at this value, which may not be very difficult to obtain, the loss in the plate is as high as 80% of the peak loss.

# APPENDIX IV

## CHOICE OF THE VALUE OF $d_c$ FOR LINEAR CASE

### A4.1 GENERAL

As mentioned in Section 7.7.3, the value of $d_c$ for a magnetically linear material may be chosen in the same manner as for the non-linear case. The loss calculated from the linear theory for an infinitely wide plate may be equated to the loss calculated assuming the presence of zero-resistivity end-strips. In so far as having zero-resistivity end-strips simulates the condition of an infinitely wide plate, such an equation seems to be a logical step. It may, however, be remembered that the linear theory (Chapter 3) considers only one component, viz. $J_z$ in the plate and the theory for finite width effect (Chapter 7) considers both $J_z$ and $J_x$ in the plate. Such an equation, therefore, implies that the loss calculated on the basis of two-dimensional current-density in the plate is little affected by neglecting one. This may be possible, since it has been shown in Section 7.9 that in the presence of low resistivity end-strips, the current density in the plate is one-dimensional in nature.

The values of $d_c$ will, therefore, be obtained for both longitudinal and transverse flux arrangements by equating the loss in an infinitely wide plate to that in a plate fitted with zero-resistivity end-strips at its ends.

## A4.2 VALUE OF $d_{c\ell}$ FOR LONGITUDINAL FLUX ARRANGEMENT

The loss/area under longitudinal flux arrangement may be obtained from equation (3.54). Therefore, total loss for a heater of 2p poles, each of pitch $\pi/q$, and of active width L, is given by

$$P_{y\ell o} = (2p\pi/q).L.\frac{2\hat{K}_z^2.\rho\alpha}{|M_\ell|^2}.(\sinh 2\alpha d - \sin 2\alpha d) \qquad (A4.1)$$

The total loss in the plate fitted with zero-resistivity end-strips is given by equation (7.34) so that equating it to equation (A4.1),

$$d_{c\ell} = \left(\frac{\hat{K}_z}{\hat{J}_{z\ell}}\right)^2 . \frac{4\alpha}{|M_\ell|^2} .(\sinh 2\alpha d - \sin 2\alpha d) \qquad (A4.2)$$

$\hat{J}_{z\ell}$ in equations (A4.2) was assumed distributed uniformly over the thickness $d_{c\ell}$ and hence is also its value at the plate surface. Thus, using assumption (ii) of section 7.7.3, the value of $\hat{J}_{z\ell}(= \hat{J}_{z\ell d})$ may be obtained, in this case, from the linear theory, equation (3.46), and equation (A4.2) finally becomes

$$d_{c\ell} = \frac{1}{2\alpha} \cdot \left[\frac{\sinh 2\alpha d - \sin 2\alpha d}{\cosh 2\alpha d - \cos 2\alpha d}\right] \qquad (A4.3)$$

This value of $d_{c\ell}$ may be used in the expression for $\eta_\ell$, (equation 7.29) for using in the finite width factor. Such a substitution, once again, shows that the finite width effect is most pronounced in plates of large thickness

and least pronounced in plates of small thickness.

A4.3 VALUE OF $d_{ct}$ FOR TRANSVERSE FLUX ARRANGEMENT

The total loss/area in this case is given by equation (3.89). Thus, the total loss for a heater of 2p poles, each of pitch $\pi/q$, and of active width L, is given by

$$P_{yto} = \frac{2p\pi}{q}.L.\frac{2\hat{K}_z^{\,2}\rho\alpha}{|M_t|^2}.(\sin 2\alpha d + \sin 2\alpha d) \qquad (A4.4)$$

The total loss in a plate fitted with zero-resistivity end-strips is given by equation (7.44), so that equating it to equation (A4.4),

$$d_{ct} = \left(\frac{\hat{K}_z}{\hat{J}_{zt}}\right)^2 \cdot \frac{4\alpha}{|M_t|^2} \cdot (\sinh 2\alpha d + \sin 2\alpha d) \qquad (A4.5)$$

$\hat{J}_{zt}$ in equation (A4.5) was assumed distributed uniformly over the thickness $d_{ct}$ and hence, is also its value at the plate surface. Thus, using assumption (ii) of Section 7.7.3, the value of $\hat{J}_{zt}(=\hat{J}_{ztd})$ may be obtained, in this case from the linear theory, equation (3.81), and equation (A4.5) finally becomes

$$d_{ct} = \frac{1}{2\alpha} \cdot \left[\frac{\sinh 2\alpha d + \sin 2\alpha d}{\cosh 2\alpha d + \cos 2\alpha d}\right] \qquad (A4.6)$$

The value of $d_{ct}$, given by equation (A4.6), may be substituted in the expression of $\eta_t$, equation (7.39), for

using in finite width factor. Such a substitution, once again, shows that the finite width effect is most pronounced in plates of small thickness and least pronounced in plates of large thickness.

For an infinitely thick plate, in the linear case, the end-effect factors for longitudinal and transverse flux arrangements are exactly equal instead of being approximately so as in the non-linear case.

## REFERENCES


1. SHARPLES, J.J.: 'Electrical Heating Methods'. Process Engineering Technique Evaluation - Heat Transfer. Morgan-Grampion Books Ltd, 1970.
2. Dictionary of Science and Technology, 'Heating, Electric'. McGraw-Hill Book Co., 1971.
3. ROSS, N.V.: 'A System for Induction Heating of Large Steel Slabs' Trans. IEEE., 1970, IGA-6, 5, pp. 449..
4. JACKSON, W.B.: 'Transverse Flux Induction Heating of Flat Metal Products'. International Congress on Electro-heat. Warsaw 1972.
5. DAVIES, E.J., and BOWDEN, A.L.: 'Travelling Wave Induction Heaters'. Universities Power Conference. University of Aston in Birmingham. 1975.
6. JACKSON, P.N.: 'High Speed Eddy-current Coupling and Dynamometers'. Ph.D. Thesis. University of Aston in Birmingham. 1975.
7. THOMSON, J. J.: 'On the Heat Produced by Eddy-currents in an Iron Plate exposed to an Alternating Magnetic Field'. The Electrician, 8th April, 1892. pp. 599.
8. RUDENBERG, R.: 'The Energy of Eddy-currents' (in German). Sammlung Elektrotechnischer Vortraege (a yearbook), F. Enke, Stuttgart, Germany, 1906.

9. ROSENBERG, E.: 'Eddy-current in Iron Masses'. The Electrician, 23rd August, 1923, pp. 188.

10. BURCH, R.C., and DAVIS, N.R.: 'An Introduction to the theory of Eddy-current Heating'. (Book). Earnst Benn Ltd., 1st Ed., London.1928.

11. GIBBS, W.J.: 'Theory and Design of Eddy-current slip Coupling I, II, III', The Beama Journal, 1946, 53, pp. 5, 123, 172, 219.

12. BEATSON, C.: 'Search Coils peer deep into difficult Magnetic Circuits'. The Engineer, 30th September, 1971, pp. 36.

13. STOLL, R. L.: 'The Analysis of Eddy-currents' (Book), 1st ed., Claredon Press, 1974.

14. BAKER, R.M.: 'Transverse Flux Induction Heating' Trans AIEE, 1950, 69, II, pp. 711.

15. GIBSON, R.C., JACKSON, W.B., and WAGGOTT, R.: 'Some Practical Experience of Transverse Flux Induction Heating and the Correlation with Theoretical Analysis'. Universities Power Conference, University Of Aston. 1975.

16. LACKNER, R.V.: 'Continuous Flash Annealing Produces Fine Grained Aluminium Sheet'. Modern Metals, September, 1960, pp. 62.

17. LAITHWAITE, E.R.: 'Linear Induction Motors'. Proc. IEE, 1957, 104A, pp. 461.

18. LAITHWAITE, E.R., TIPPING, D., and HESMONDALGH, D.E.: 'The Application of Linear Induction Motors to Conveyors'. Proc. IEE, 1960, 107A, pp. 284.

19. LAITHWAITE, E.R.: 'Induction Machines for Special Purposes' (Book), 1st ed., George Newnes, 1966.

20. NASAR, S.A.: 'Electromagnetic Fields and Forces in a Linear Induction Motor, taking into account Edge Effects'. Proc. IEE, 1969, 116, (4). pp. 605

21. BOLTON, H.: 'Transverse Edge Effect in Sheet Rotor Induction Motors'. Proc. IEE, 1969, 116, (5), pp. 725.

22. PRESTON, T.W., and REECE, A.B.J.: 'Transverse Edge Effects in Linear Induction Motors' Proc. IEE, 1969, 116, (6), pp. 973. Corrigenda: Proc. IEE, 1970, 117, (9), pp. 1808. Correspondence: Proc. IEE, 1971, 118, (12), pp. 1820.

23. GLAZENKO, T.A.: 'Some Design Problems of an Asynchronous Clutch with a Solid Mass Rotor'. (In Russian). Arotomatika i Telemekhanita, 1958, 19, (8), pp. 800.

24. CONCORDIA, C., and PORITSKY, H.: 'Synchronous Machine with Solid Cylindrical Rotor'. Trans. IEEE, 1937, 56, pp. 49.

25. KUYPER, W.W.: 'Pole-face Losses in Solid-rotor Turbine Generators'. Trans. AIEE, 1943, 62, pp. 827.

26. MUKHERJI, K.C.: 'Certain Approaches to Electromagnetic Field Problems Pertaining to Dynamo Electric Machines'. Proc. IEE, 1961, 108C, pp. 405.

27. MUKHERJI, K.C.: 'Reaction of Eddy-currents Induced in a Ferromagnetic Medium on the Inducing Field'. ibid, 1965, 112, (2), pp. 444.

28. STOLL, R.L., and HAMMOND, P.: 'Calculation of the Magnetic Field of Rotating Machines. Part 4: Approximate Determination of the Field and the Losses Associated with Eddy-current in Conducting Surfaces'. ibid, 1965, 112, (11), pp. 2083.

29. LAMMERANER, J., and STAFL, M.: 'Eddy-currents' (Book), 2nd Ed. Illife Books Ltd., 1966.

30. BOWDEN, A.L.: 'A Study of Magnetic Non-linearity and Finite Length Effect in Solid Iron Subjected to Travelling mmf Wave'. Ph.D. Thesis. University of Aston in Birmingham. 1972.

31. HABERLAND, G., and HABERLAND, F.: 'The Alternating Field in Saturated Solid Iron'. (In German). Archiv Für Elektrotechnik, 1936, 30, pp. 126.

32. McCONNELL, H.M.: 'Eddy-current Phenomena in Ferromagnetic Materials'. Trans. AIEE, (Communication and Electronics), 1954, 73, pp. 226.

33. MacLEAN, W.: 'Theory of Strong Electromagnetic Waves in Massive Iron'. J. Appl. Phys., 1954, 25, (10), pp. 1267.

34. AGARWAL, P.D.: 'Eddy-current Losses in Solid and Laminated Iron'. Trans. IEEE, 1959, 78, (1), pp. 169.

35. ELLETT, R.C.: 'Induction Heating of Mild Steel Vessels in a Pulsating Field'. M.Phil. Thesis, University of Aston in Birmingham. 1974.

36. DAVIES, E.J., and BOWDEN, A.L.: 'Direct Resistance Heating of Ferromagnetic Billets'. International Congress on Electroheat. Warsaw. 1972.

37. FISHER, J., and MOSER, H.: 'The Representation of the Magnetisation Curve by Simple Algebraic and Transcendental Functions'. (In German), Archiv Elektrotechnick, 1956, 42, pp. 286.

38. NEJMAN, L.R.: 'Skin Effect in Ferromagnetic Bodies'. (In Russian). Gosenergoizdat., Leningrad, 1949.

39. LASOCINSKI, J.: 'Electromagnetic Field in the Air-gap of an Infinitely Long Machine with Solid Ferromagnetic Rotor'. (In Polish).

39 (con't.) Rozprawy Elektrotechniczne, 1965, 11, (4), pp. 743.

40. DAVIES, E.J.: 'An Experimental and Theoretical Study of Eddy-current Couplings and Brake'. Trans. IEEE, 1963, PAS-67, pp. 401.

41. DAVIES, E.J.: 'General Theory of Eddy-current Couplings and Brakes'. Proc. IEE , 1966, 113, (5), pp. 825.

42. PILLAI, K.P.P.: 'Fundamental Frequency Eddy-current Loss due to Rotating Magnetic Field. Part 1.: Eddy-current Loss in Solid Rotors'. ibid, 1969, 116, (3), pp. 407.

43. PILLAI, K.P.P.: 'Fundamental Frequency Eddy-current Loss due to Rotating Magnetic Field. Part 2.: Eddy-current Loss in Hollow Rotors'. ibid, 1969, 116, (3), pp. 411.

44. DAVIES, E.J., JAMES, B., and WRIGHT, M.T.: 'Experimental Verification of the Generalised Theory of Eddy-current Couplings'. ibid, 1975, 122, (1), pp. 67.

45. WOOLLEY, I.: 'Unlaminated Rotors for a.c. Machines with Special Reference to some new Designs'. Ph.D. Thesis, University of Manchester Institute of Science and Technology, 1971.

46. CHALMERS, B.J., and WOOLLEY, I.: 'General Theory of Solid-rotor Induction Machines'. Proc. IEE, 1972, 119, (9), pp. 1301.

47. OLLENDORF, F.: 'The Penetration of Electromagnetic Waves into Highly Saturated Iron'. (In German), Z. Tech. Phys., 1931, 12, pp. 39.

48. GONEN, D., and STRICKER, S.: 'Analysis of an Eddy-current Brake'. Trans. AIEE, 1965, 84, pp. 357.

49. POHL, R.: 'Electromagnetic and Mechanical Effects in Solid Iron due to an Alternating or Rotating Magnetic Field'. Proc. IEE, 1944, 91, pt. II, pp. 239.

50. KESAVAMURTHY, N., RAJAGOPALAN, P.K., and RAO, V.S.: 'Effects of Saturation on Core Loss of Thin Ferromagnetic Plates subjected to Alternating Magnetic Flux'. ibid, 1963, 110, pp. 459.

51. KESAVAMURTHY, N., and RAJAGOPALAN, P.K.: 'Eddy-currents in Solid Iron due to an Alternating Magnetic Flux'. ibid, 1959, 105C, pp. 207.

52. BINNS, K.J., JABBAR, M.A., and BARNARD, W.R.: 'Computation of the Magnetic Field of Permanent Magnets in Iron Cores'. Proc. IEE, 1975, 122, (12), pp. 1377.

53. GILLOT, D.H., and CALVERT, J.F.: 'Eddy-current Losses in Saturated Solid Magnetic Plates, Rods and Conductors'. Trans. IEEE, 1965, Magnetics, 1, pp. 126.

54. GILLOT, D.H., and ABRAMS, M.D.: 'Numerical Analysis of Hysteresis and Eddy-current Losses in Solid Cylindrical Rods of No. 1010 Steel'. Trans. IEEE, 1967, PAS-86, (9), pp. 1077.

55. LIM, K.K., and HAMMOND, P.: 'Universal Loss Charts for the Calculation of Eddy-current Losses in Thick Steel Plates'. Proc. IEE, 1970, 117, (4), pp. 857.

56. LIM, K.K., and HAMMOND, P.: 'Numerical Method for Determining the Electromagnetic Field in Saturated Steel Plates'. Proc. IEE., 1972, 119, (11), pp. 1667.

57. COPELAND, M.A., and SLEMON, G.R.: 'An Analysis of Hysteresis Motor. Pt. 1'. Trans. IEEE, 1963, PAS-82, pp. 34.

58. JACKSON, R.D.: 'Digital Simulation of the Hysteresis Motor'. Proc. IEE, 1973, 120, (12), pp. 1533.

59. O'KELLY, D.: 'Flux Penetration in a Ferromagnetic Material Including Hysteresis and Eddy-current Effects'. J. Phys. D., 1972, 5, pp. 203.

60. O'KELLY, D.: 'Hysteresis and Eddy-current Losses in Steel Plates with Non-linear Magnetisation Characteristics'. Proc. IEE, 1972, 119, 11, pp. 1675.

61. O'KELLY, D.: 'Theory and Performance of Solid-Rotor Induction and Hysteresis Motor'. Proc. IEE, 1976, 123,(5), pp. 421.

62. DORAIRAJ, K.R., and KRISHNAMURTHY, M.R.: 'Polyphase Induction Machines with a Slitted Ferromagnetic Rotor'. Trans. IEEE, 1967, PAS-86, (7), pp. 844. (Pt. II).

63. McCRACKEN, D.D.: 'A Guide to Fortran IV Programming'. (Book), 2nd Ed., Wiley, 1965.

64. GIBBS, W.J.: 'Induction and Synchronous Motors with Unlaminated Rotor'. Proc. IEE, 1948, 95, (2), pp. 411.

65. RUSSELL, R.L., and NORSWORTHY, K.H.: Eddy-current and Wall Losses in Screened-rotor Induction Motors'. ibid, 1958, 105A, pp. 163.

66. WOOLLEY, I., and CHALMERS, B.J.: 'End Effects in Unlaminated-rotor Induction Machines'. ibid, 1973, 120, (6), pp. 641.

67. YEE, H.: 'Effects of Finite Length in Solid-Rotor Induction Machines'. ibid, 1971, 118, (8), pp. 1025.

68. JAMES, B.: 'Eddy Current Couplings with and Without End Rings'. M.Sc. Thesis. University of Aston in Birmingham, 1969.

69. WOOD, A.J., and CONCORDIA, C.: 'An Analysis of Solid Rotor Machines, Pt. III, Finite Length Effects'. Trans. IEEE, 1960, PAS-79, pp. 21.

70. ANGST, G.: 'Polyphase Induction Motor with Solid Rotor; Effects of Saturation and Finite Length'. ibid, 1962, 80, pp. 902.

71. MALTI, M.G., and RAMAKUMAR, R.: 'Three Dimensional Theory of Eddy Current Couplings'. ibid, 1963, PAS-82, pp. 793.

72. BOLDEA, I., RAHMAN, A., and NASAR, S.A.: 'Finite-width, Finite-thickness, and Saturation Effects in Solid-rotor Induction Machines'. ibid. 1975, PAS-94, (5), pp. 1500.

73. YEE, H., and WILSON, T.: 'Saturation and Finite-length Effects in Solid-rotor Induction Machines'. Proc. IEE, 1972, 119, pp. 877.

74. WOOLMAN, J., and MOTTRAM, A.I.M.: 'The Mechanical and Physical Properties of the British Standard EN Steels'. (Book), Vol. 1, 1st Ed., Pergamon Press, 1964.

75. BOZORTH, R.M.: 'Ferromagnetism'. (Book), 8th Ed., D. Van Nostrand Company, 1964.

TABLE 8.2

DATA OF THE IDENTICAL PRIMARY UNITS (S100, LINTROL LINEAR MOTORS)

Dimensions are the same on both primary units.

| | | |
|---|---|---|
| No. of phases | | 3 |
| Nature of connection | | Y (star) |
| No. of poles | 2p | 6 |
| No. of slots | | 18 |
| Width of slot (= Width of tooth) | | 1.25 cm. |
| Rated current/phase | | 18.5A |
| Rated Supply | | 415V (L-L) |
| Synchronous linear speed (50 Hz) | | 7.5 m/s |
| Force developed | | 450N |
| Pole pitch | $\tau$ | 7.5 cm. |
| Active width | L | 7.6 cm. |
| Total number of coils (full-pitch) | | 17 |
| No. of intermediate[1] coils | | 2 |
| No. of end[1] coils | | 2 |
| No. of turns in a coil | | 52 |
| No. of turns in series per phase N | | 104 |

---

(1) The intermediate and end coils are short-pitched and are used for reducing the effects of unbalancing.

TABLE 8.3

PRIMARY EXCITATION OF EACH OF THE PRIMARY MEMBERS

$q = \frac{\pi}{\tau} = 41.88791\ m^{-1}$

| Primary line current Amps. | Primary m.m.f. $\lvert\dot{F}_{c\ell}\rvert = \lvert\dot{F}_{ct}\rvert = \lvert\dot{F}_{c}\rvert$ At/pole | Primary Current Sheet $\tilde{K}_z = q\lvert\dot{F}_{c}\rvert$, kA/m |
|---|---|---|
| 1.5 | 210.8 | 8.8 |
| 2.0 | 280.8 | 11.8 |
| 3.0 | 421.2 | 17.6 |
| 4.0 | 561.6 | 23.5 |
| 5.0 | 702.0 | 29.4 |
| 6.0 | 842.4 | 35.3 |
| 7.0 | 982.4 | 41.2 |
| 8.0 | 1123.2 | 47.0 |
| 9.0 | 1263.6 | 52.9 |
| 10.0 | 1404.0 | 58.8 |
| 11.0 | 1544.4 | 64.7 |
| 12.0 | 1684.8 | 70.6 |
| 13.0 | 1825.2 | 76.5 |
| 14.0 | 1965.6 | 82.3 |

TABLE 8.5

THEORETICAL VALUES OF EQUIVALENT THICKNESSES $d_{c\ell}$ AND $d_{ct}$ AND THE FINITE WIDTH FACTORS $K_{f\ell}$ AND $K_{ft}$ FOR THE END-STRIP PLATE

Half-thickness of the plate, d = 0.951 cm.

| Frequcncy Hz | Excitation m.m.f. At/pole | LONGITUDINAL FLUX ARRANGEMENT | | TRANVERSE FLUX ARRANGEMENT | |
|---|---|---|---|---|---|
| | | Effective thickness $d_{c\ell}$ cm. | Finite width factor $K_{f\ell}$ | Effective thickness $d_{ct}$ cm. | Finite Width factor $K_{ft}$ |
| 50 | 200 | 0.022 | 0.9995 | 0.038 | 0.9941 |
| | 400 | 0.032 | 0.9993 | 0.050 | 0.9922 |
| | 600 | 0.039 | 0.9991 | 0.057 | 0.9911 |
| | 800 | 0.045 | 0.9990 | 0.062 | 0.9903 |
| | 1000 | 0.049 | 0.9989 | 0.066 | 0.9896 |
| | 1200 | 0.053 | 0.9988 | 0.070 | 0.9891 |
| | 1400 | 0.056 | 0.9987 | 0.072 | 0.9887 |
| | 1600 | 0.059 | 0.9987 | 0.075 | 0.9884 |
| | 1800 | 0.061 | 0.9986 | 0.077 | 0.9881 |
| | 2000 | 0.063 | 0.9986 | 0.079 | 0.9878 |
| 25 | 200 | 0.024 | 0.9996 | 0.041 | 0.9955 |
| | 400 | 0.035 | 0.9994 | 0.053 | 0.9941 |
| | 600 | 0.043 | 0.9993 | 0.061 | 0.9932 |
| | 800 | 0.049 | 0.9992 | 0.066 | 0.9926 |
| | 1000 | 0.054 | 0.9991 | 0.071 | 0.9922 |
| | 1200 | 0.057 | 0.9991 | 0.074 | 0.9918 |
| | 1400 | 0.061 | 0.9990 | 0.079 | 0.9913 |
| | 1600 | 0.063 | 0.9990 | 0.079 | 0.9913 |
| | 1800 | 0.066 | 0.9989 | 0.081 | 0.9910 |
| | 2000 | 0.068 | 0.9989 | 0.083 | 0.9909 |

TABLE 8.6

MEASURED MAGNITUDES PROPORTIONAL TO CURRENT DENSITY AT $z \simeq L/2$ AND $y \simeq d$ FOR THE NARROW PLATE UNDER LONGITUDINAL FLUX ARRANGEMENT. (VERIFICATION FOR EQUATION (7.54) ).

| Frequency Hz | Excitation kA/m | Fundamental of the J-probe readings in mV ( $\propto$ current density) at locations of * | | | | Measured magnitudes proportional to approximately | |
|---|---|---|---|---|---|---|---|
| | | Z21 $\propto J_{z\ell}\rceil_{z\simeq L/2}$ | X21 $\propto J_{x\ell}\rceil_{z\simeq L/2}$ | XE6 $\propto J_{ex\ell}\rceil_{y\simeq d}$ | Y3 $\propto J_{ey\ell}\rceil_{y\simeq d}$ | $\{J_{z\ell}^2+J_{x\ell}^2\}^{\frac{1}{2}}$ at $z\simeq L/2$ | $\{J_{ex\ell}^2+J_{ey\ell}^2\}^{\frac{1}{2}}$ at $y\simeq d$ |
| 50 | 11.8 | 4.95 | 1.2 | 1.6 | 4.4 | 5.093 | 4.682 |
| | 23.5 | 9.5 | 2.0 | 3.1 | 8.1 | 9.708 | 8.673 |
| | 35.3 | 13.3 | 2.8 | 4.5 | 11.5 | 13.592 | 12.349 |
| | 47.0 | 15.5 | 3.3 | 5.6 | 14.0 | 15.847 | 15.078 |
| | 58.5 | 17.5 | 3.75 | 6.3 | 15.5 | 17.897 | 16.731 |
| | 70.6 | 18.5 | 4.2 | 6.9 | 17.0 | 18.971 | 18.347 |
| | 82.3 | 19.5 | 4.8 | 7.3 | 18.0 | 20.082 | 19.424 |
| 25 | 11.8 | 2.3 | 0.8 | 0.95 | 2.4 | 2.435 | 2.581 |
| | 23.5 | 5.0 | 1.47 | 1.95 | 4.8 | 5.212 | 5.181 |
| | 35.3 | 6.8 | 2.0 | 2.75 | 6.8 | 7.088 | 7.335 |
| | 47.0 | 8.2 | 2.5 | 3.45 | 8.3 | 8.573 | 8.988 |
| | 58.8 | 9.3 | 2.75 | 3.85 | 9.5 | 9.698 | 10.25 |
| | 70.6 | 10.2 | 3.1 | 4.15 | 10.8 | 10.661 | 11.57 |
| | 82.3 | 11.0 | 3.3 | 4.35 | 11.5 | 11.484 | 12.295 |

* The locations of these J-probes are shown in Fig. 8.5

TABLE 8.7

MEASURED MAGNITUDES PROPORTIONAL TO CURRENT DENSITY AT $z \simeq L/2$ AND $y \simeq d$ FOR THE NARROW PLATE UNDER TRANSVERSE FLUX ARRANGEMENT

(Verification for equation (7.54))

| Frequency | Excitation | Fundamental of the J-probe readings in mV ($\propto$ current density) at locations of * | | | | Measured magnitudes proportional to approximately | |
|---|---|---|---|---|---|---|---|
| | | Z21 | X21 | XE6 | Y3 | | |
| Hz | kA/m | $\propto J_{zt}]_{z\simeq L/2}$ | $\propto J_{xt}]_{z\simeq L/2}$ | $\propto J_{ext}]_{y\simeq d}$ | $\propto J_{eyt}]_{y\simeq d}$ | $\{J_{zt}^2+J_{xt}^2\}^{\frac{1}{2}}$ at $z\simeq L/2$ | $\{J_{ext}+J_{eyt}^2\}^{\frac{1}{2}}$ at $y\simeq d$ |
| 50 | 11.8 | 4.5 | 3.65 | 4.7 | 1.2 | 5.794 | 4.851 |
| | 23.5 | 7.5 | 7.2 | 9.5 | 2.45 | 10.397 | 9.811 |
| | 35.3 | 10.5 | 11.9 | 14.9 | 3.65 | 15.279 | 15.341 |
| | 47.0 | 12.6 | 15.0 | 19.5 | 4.55 | 19.590 | 20.024 |
| | 58.8 | 13.8 | 18.0 | 23.0 | 5.0 | 22.681 | 23.537 |
| | 70.6 | 14.5 | 20.5 | 26.0 | 5.4 | 25.110 | 26.555 |
| | 82.3 | 15.0 | 22.0 | 27.0 | 5.6 | 26.627 | 27.575 |
| 25 | 11.8 | 2.6 | 2.1 | 2.8 | 0.9 | 3.342 | 2.941 |
| | 23.5 | 4.85 | 4.1 | 5.7 | 1.8 | 6.351 | 6.307 |
| | 35.3 | 6.9 | 6.4 | 8.7 | 2.7 | 9.411 | 9.109 |
| | 47.0 | 8.6 | 8.4 | 11.8 | 3.55 | 12.022 | 12.322 |
| | 58.8 | 9.8 | 10.0 | 13.8 | 4.0 | 14.001 | 14.368 |
| | 70.6 | 10.8 | 11.3 | 15.2 | 4.4 | 15.631 | 15.824 |
| | 82.3 | 11.8 | 12.5 | 17.5 | 4.7 | 17.19 | 18.120 |

* Locations of these J-probes are shown in Fig. 8.5.

TABLE 8.8

MEASURED AND CALCULATED VALUES OF THE RATIO OF END CURRENT DENSITIES UNDER LONGITUDINAL FLUX ARRANGEMENT (EQUATION (7.59)) FOR THE NARROW PLATE

$\tau$ = 7.5 cm. $q = \pi/\tau$ 2d = 1.902 cm

| Frequency Hz | Primary Excitation kA/m | Fundamental of J-Probe readings in mV (∝current density) at locations of * | | Measured ratio of end current-density | Calculated ratio of end current density |
|---|---|---|---|---|---|
| | | XE5 $\propto J_{x\ell}\big]_{z=L/2}$ | Z21 $\propto J_{z\ell}\big]_{z\simeq L/2}$ | $\frac{J_{z\ell}}{J_{x\ell}}\big]_{z\simeq L/2}$ | $\frac{J_{z\ell}}{J_{x\ell}}\big]_{z=L/2}$ = cothqd |
| 50 | 11.8 | 1.85 | 4.95 | 2.273 | 2.6417 |
| | 23.5 | 3.52 | 9.5 | 2.692 | 2.6417 |
| | 35.3 | 4.8 | 13.3 | 2.771 | 2.6417 |
| | 47.0 | 5.15 | 15.5 | 3.000 | 2.6417 |
| | 58.8 | 5.85 | 17.5 | 3.000 | 2.6417 |
| | 70.6 | 6.28 | 18.5 | 2.947 | 2.6417 |
| | 82.3 | 6.6 | 19.5 | 2.959 | 2.6417 |
| 25 | 11.8 | 0.9 | 2.3 | 2.556 | 2.6417 |
| | 23.5 | 1.75 | 5.0 | 2.857 | 2.6417 |
| | 35.3 | 2.3 | 6.8 | 2.957 | 2.6417 |
| | 47.0 | 2.9 | 8.2 | 2.828 | 2.6417 |
| | 58.8 | 3.35 | 9.3 | 2.776 | 2.6417 |
| | 70.6 | 3.6 | 10.2 | 2.833 | 2.6417 |
| | 82.3 | 3.8 | 11.0 | 2.895 | 2.6417 |

* The locations of these J-probes are shown in Fig. 8.5.

TABLE 8.9

MEASURED AND CALCULATED VALUES OF THE RATIO OF END-CURRENT DENSITIES UNDER TRANSVERSE FLUX ARRANGEMENT (EQUATION (7.60)) FOR THE NARROW PLATE

$\tau$ = 7.5 cm. $q = \pi/\tau$. 2d = 1.902 cm.

| Frequency Hz | Primary Excitation kA/m | Fundamental of J-probe readings in mV ($\propto$ current density) at location of * | | Measured ratio of end-current density $\left[\frac{J_{zt}}{J_{xt}}\right]_{z\simeq L/2}$ | Calculated ratio of end-current density $\left[\frac{J_{zt}}{J_{xt}}\right]_{z=L/2} = \tanh qd$ |
|---|---|---|---|---|---|
| | | XE5 $\propto J_{xt}]_{z\simeq L/2}$ | $\frac{1}{2}$(Z21+Y3) $\propto J_{zt}]_{z\simeq L/2}$ | | |
| 50 | 11.8 | 4.45 | 2.85 | 0.64 | 0.379 |
| | 23.5 | 8.6 | 4.975 | 0.578 | 0.379 |
| | 35.3 | 13.4 | 7.075 | 0.528 | 0.379 |
| | 47.0 | 17.5 | 8.575 | 0.49 | 0.379 |
| | 58.8 | 20.8 | 9.4 | 0.451 | 0.379 |
| | 70.6 | 23.5 | 10.15 | 0.432 | 0.379 |
| | 82.3 | 25.0 | 10.3 | 0.412 | 0.379 |
| 25 | 11.8 | 2.7 | 1.75 | 0.647 | 0.379 |
| | 23.5 | 5.3 | 3.325 | 0.627 | 0.379 |
| | 35.3 | 8.1 | 4.8 | 0.593 | 0.379 |
| | 47.0 | 10.8 | 6.075 | 0.562 | 0.379 |
| | 58.8 | 12.8 | 6.9 | 0.538 | 0.379 |
| | 70.6 | 14.0 | 7.65 | 0.546 | 0.379 |
| | 82.3 | 15.0 | 8.25 | 0.55 | 0.379 |

* The locations of these J-probes are shown in Fig. 8.5.

TABLE 8.10

MEASURED AND CALCULATED VALUES OF FINITE WIDTH FACTORS FOR THE NARROW PLATE

| Frequency Hz | Primary Excitation kA/m | LONGITUDINAL FLUX ARRANGEMENT | | | | TRANSVERSE FLUX ARRANGEMENT | | | |
|---|---|---|---|---|---|---|---|---|---|
| | | Measured loss for the narrow plate. kW | Measured loss for the end-strip plate. kW | Measured finite-width factor $K_{f\ell}$ | Calculated finite-width factor $K_{f\ell}$ | Measured loss for the narrow plate kW | Measured loss for end-strip plate kW | Measured finite-width factor $K_{ft}$ | Calculated finite-width factor $K_{ft}$ |
| 50 | 11.8 | 0.041 | 0.048 | 0.854 | 0.8315 | 0.027 | 0.043 | 0.628 | 0.5712 |
| | 23.5 | 0.168 | 0.200 | 0.840 | 0.8315 | 0.138 | 0.214 | 0.645 | 0.5712 |
| | 35.3 | 0.384 | 0.430 | 0.893 | 0.8315 | 0.349 | 0.536 | 0.651 | 0.5712 |
| | 47.0 | 0.644 | 0.743 | 0.867 | 0.8315 | 0.682 | 1.022 | 0.668 | 0.5712 |
| | 58.8 | 1.098 | 1.214 | 0.906 | 0.8315 | 1.057 | 1.575 | 0.671 | 0.5712 |
| | 70.6 | 1.598 | 1.787 | 0.895 | 0.8315 | 1.548 | 2.275 | 0.680 | 0.5712 |
| | 82.3 | 2.208 | 2.420 | 0.920 | 0.8315 | 2.012 | 2.915 | 0.690 | 0.5712 |
| 25 | 11.8 | 0.0178 | 0.021 | 0.845 | 0.8315 | 0.0183 | 0.030 | 0.610 | 0.5712 |
| | 23.5 | 0.0565 | 0.068 | 0.830 | 0.8315 | 0.057 | 0.094 | 0.606 | 0.5712 |
| | 35.3 | 0.129 | 0.150 | 0.867 | 0.8315 | 0.129 | 0.210 | 0.624 | 0.5712 |
| | 47.0 | 0.247 | 0.282 | 0.879 | 0.8315 | 0.248 | 0.380 | 0.653 | 0.5712 |
| | 58.8 | 0.384 | 0.451 | 0.851 | 0.8315 | 0.397 | 0.621 | 0.642 | 0.5712 |
| | 70.6 | 0.568 | 0.655 | 0.867 | 0.8315 | 0.586 | 0.900 | 0.651 | 0.5712 |
| | 82.3 | 0.785 | 0.902 | 0.870 | 0.8315 | 0.797 | 1.207 | 0.665 | 0.5712 |

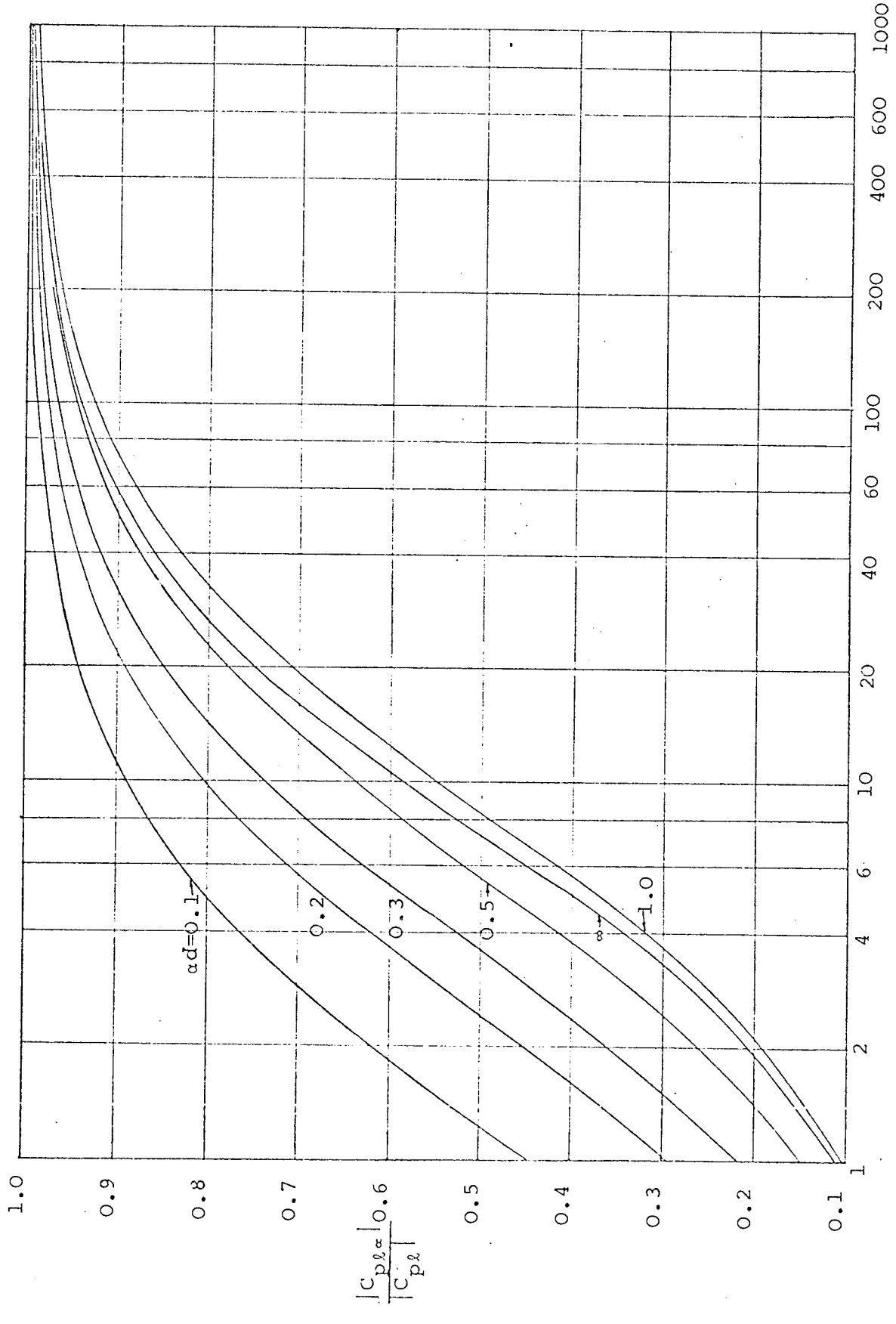


Fig. 3.2 Variation of the ratio $|C_{pl\alpha}|/|C_{pl}|$ with primary relative permeability, $\mu_1$, for various values of half-thickness of the plate. $\mu_r = 1000$, $g = 1.0$ mm. $\tau = 25$ cm, $\omega = 100\pi$.

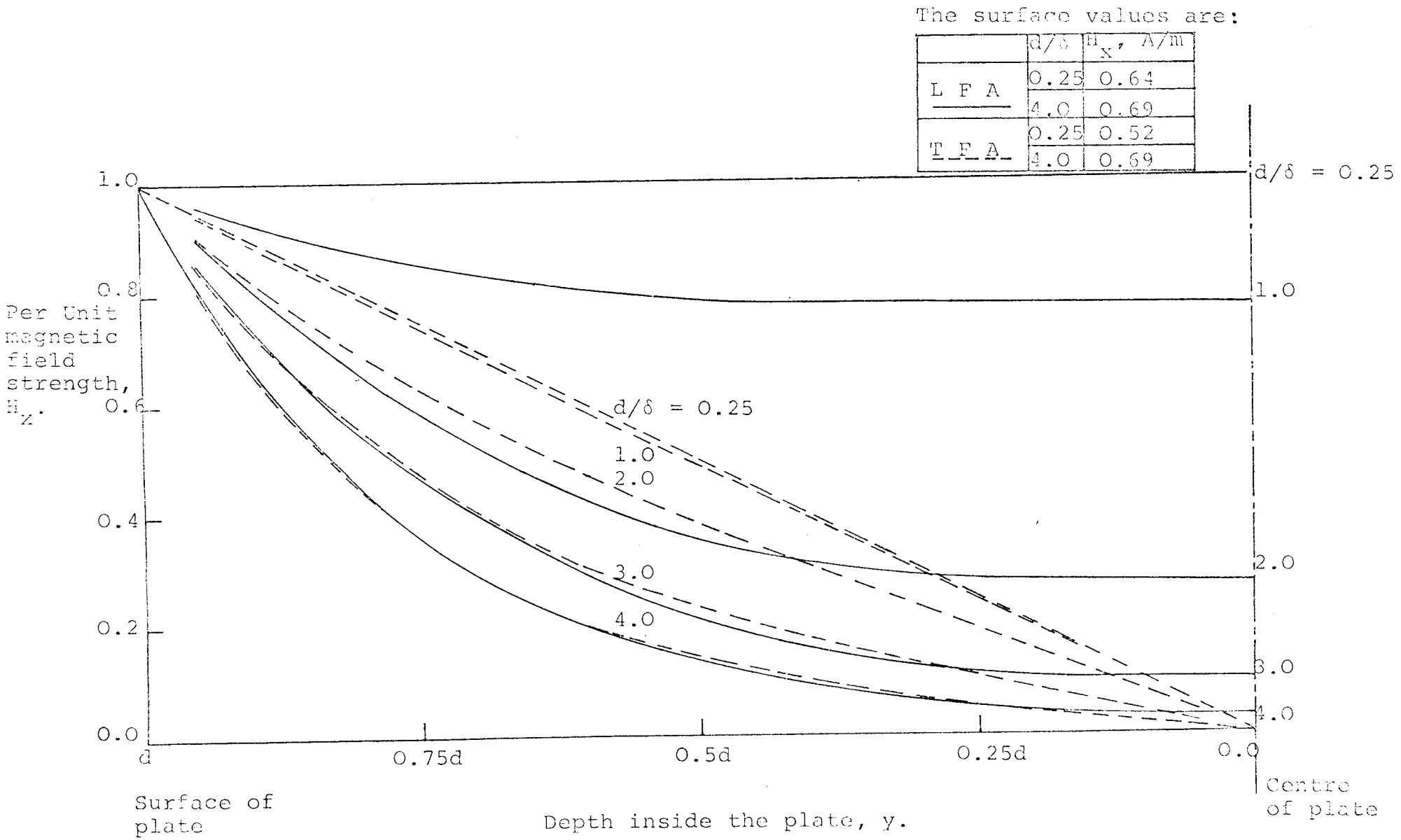


Fig. 3.3 Attenuation of per unit magnetic field strength, $H_x$, with depth inside the plate, y, for various ratios of d/δ. Firm lines indicate LFA and and dotted lines TFA. Unit values of $H_x$ are given in the table. $K_z$ = 1.0 A/m, δ = 1.0mm, g = 5.0 mm, g/τ = 0.02, ω = 100π, $\mu_r$ = 1000.

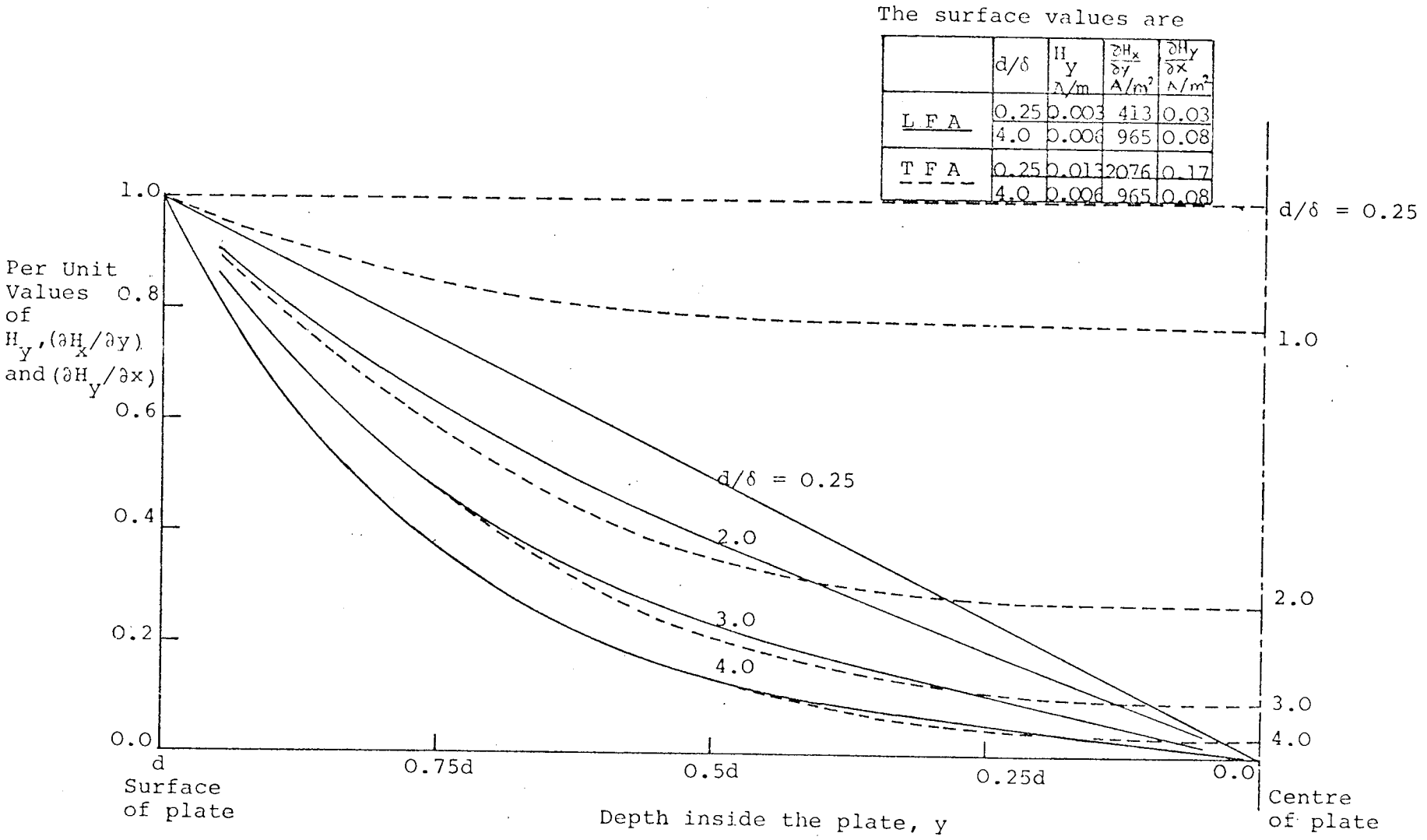


Fig. 3.4 Attenuation of per unit values of $H_y$, $(\partial H_x/\partial y)$ and $(\partial H_y/\partial x)$ with depth inside the plate, y, for various ratios of $d/\delta$ for both LFA (firm lines) and TFA (dotted lines). Unit values are given in the table. $K_z = 1.0 A/m$, $\delta = 1.0$ mm, $g = 5.0$ mm, $g/\tau = 0.02$, $\omega = 100\pi$, $\mu_r = 1000$.

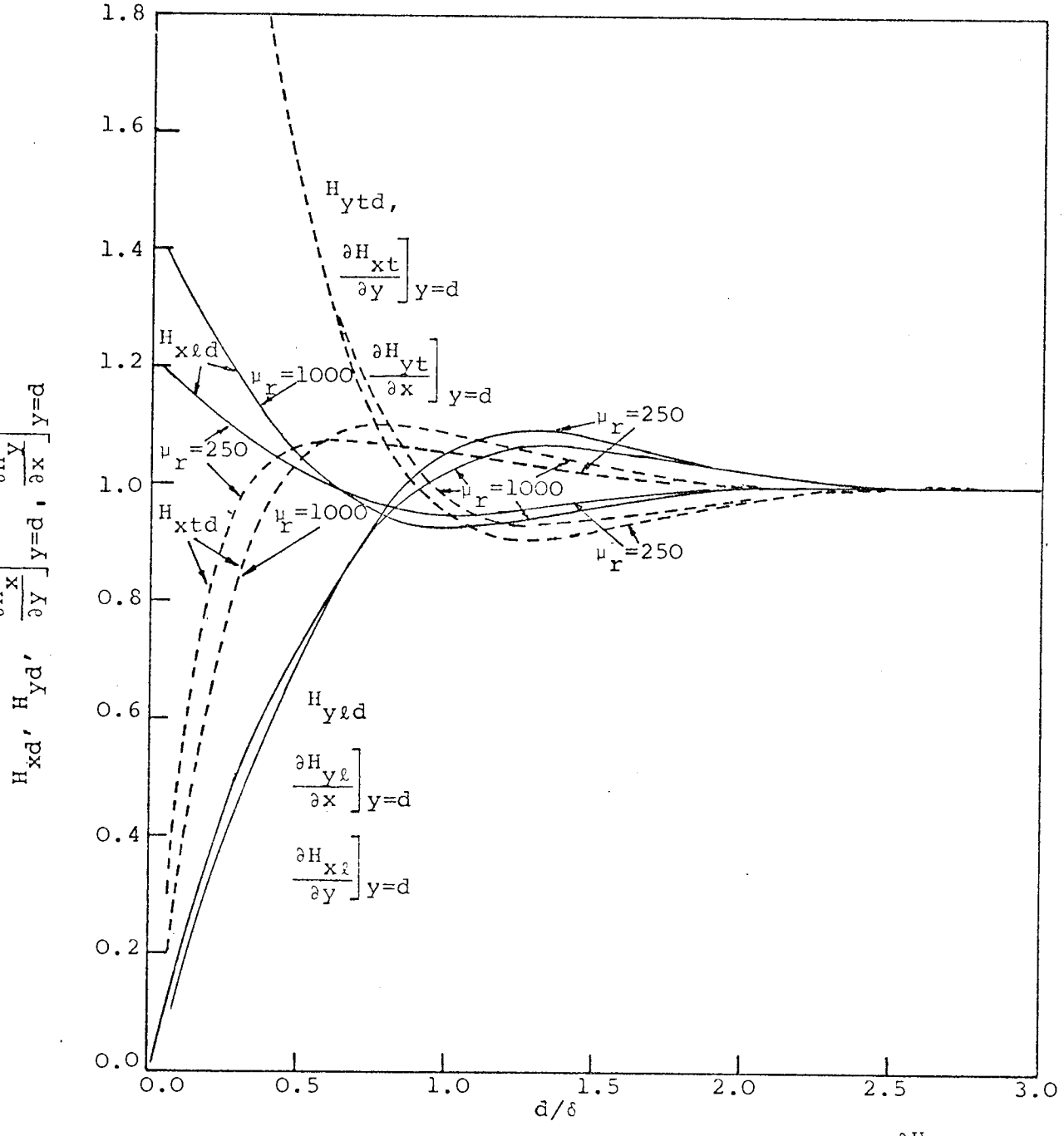


Fig. 3.5 Variation of surface values of $H_x$, $H_y$, $\frac{\partial H_x}{\partial y}$ and $\frac{\partial H_y}{\partial x}$ with the ratio of $d/\delta$ for two values of $\mu_r$ under both longitudinal (firm lines) and transverse (dotted lines) flux arrangements. g = 5 mm. $g/\tau$ = 0.02, $\omega = 100\pi$.

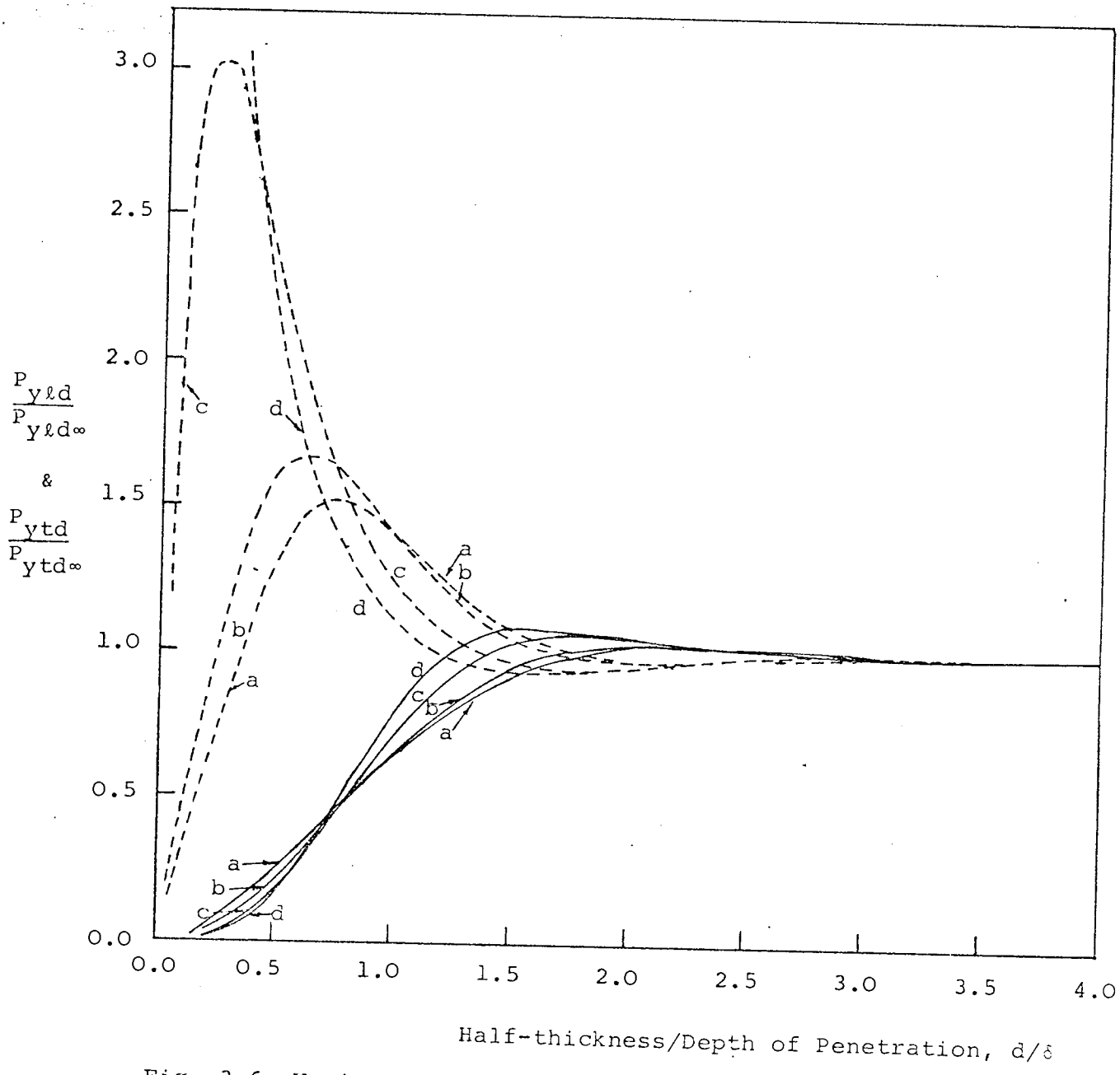


Fig. 3.6 Variation of power loss in the plate for longitudinal flux arrangement, $P_{y\ell d}$, (firm lines) and for transverse flux arrangement, $P_{ytd}$, (dotted lines), per unit of their values for thick plate, with the ratio d/δ. $\mu_r$ = 1000, $\delta/\tau$ = 0.005, $\omega = 100\pi$. $g/\tau$ ratio: (a) 0.1, (b) 0.05, (c) 0.01, (d) 0.001.

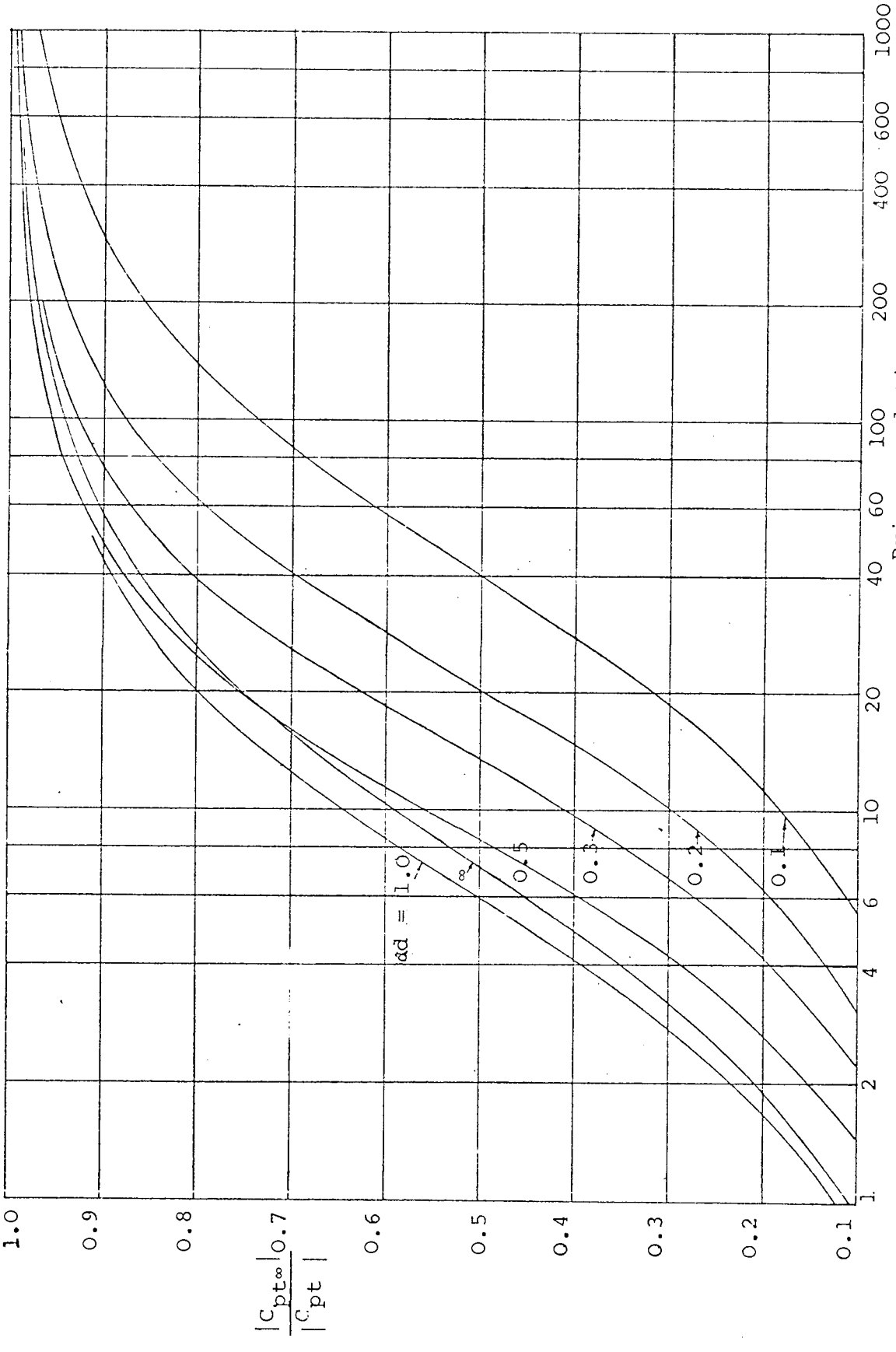


Fig. 3.7 Variation of the ratio $|C_{pt\infty}|/|C_{pt}|$ with primary relative permeability, $\mu_1$, for various values of half-thickness of the plate. $\mu_r$ = 1000, g = 1.0 mm, $\tau$ = 25 cm, $\omega = 100\pi$.

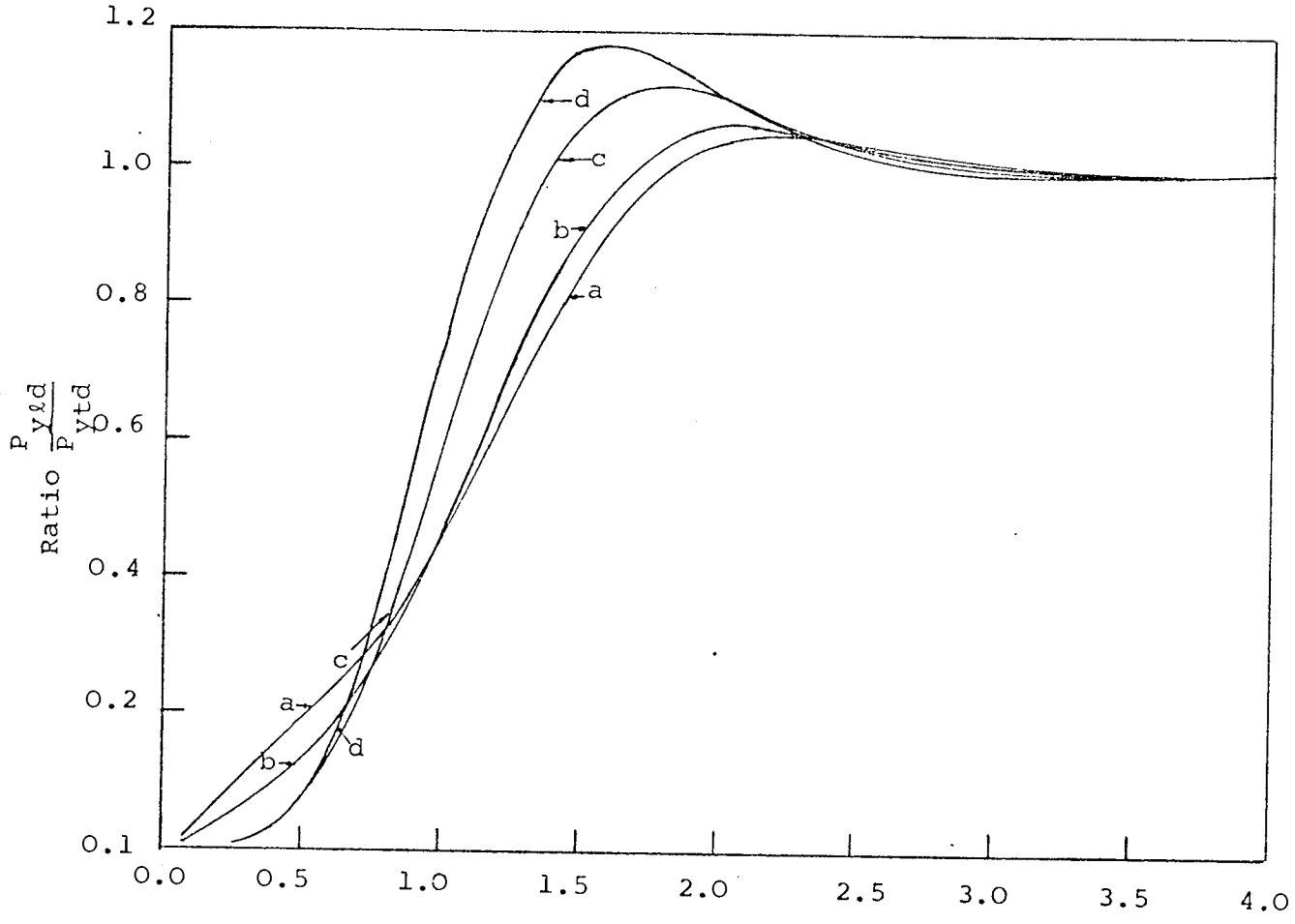


Fig. 4.1 Variation of the ratio of power loss in longitudinal flux arrangement to that in transverse flux arrangement with the ratio of d/δ for various ratios of g/τ.
$\mu_r$ = 1000. δ/τ = 0.005, ω = 100π.
Airgap to pole-pitch ratio, g/τ.
(a) 0.1, (b) 0.05, (c) 0.01, (d) 0.001.

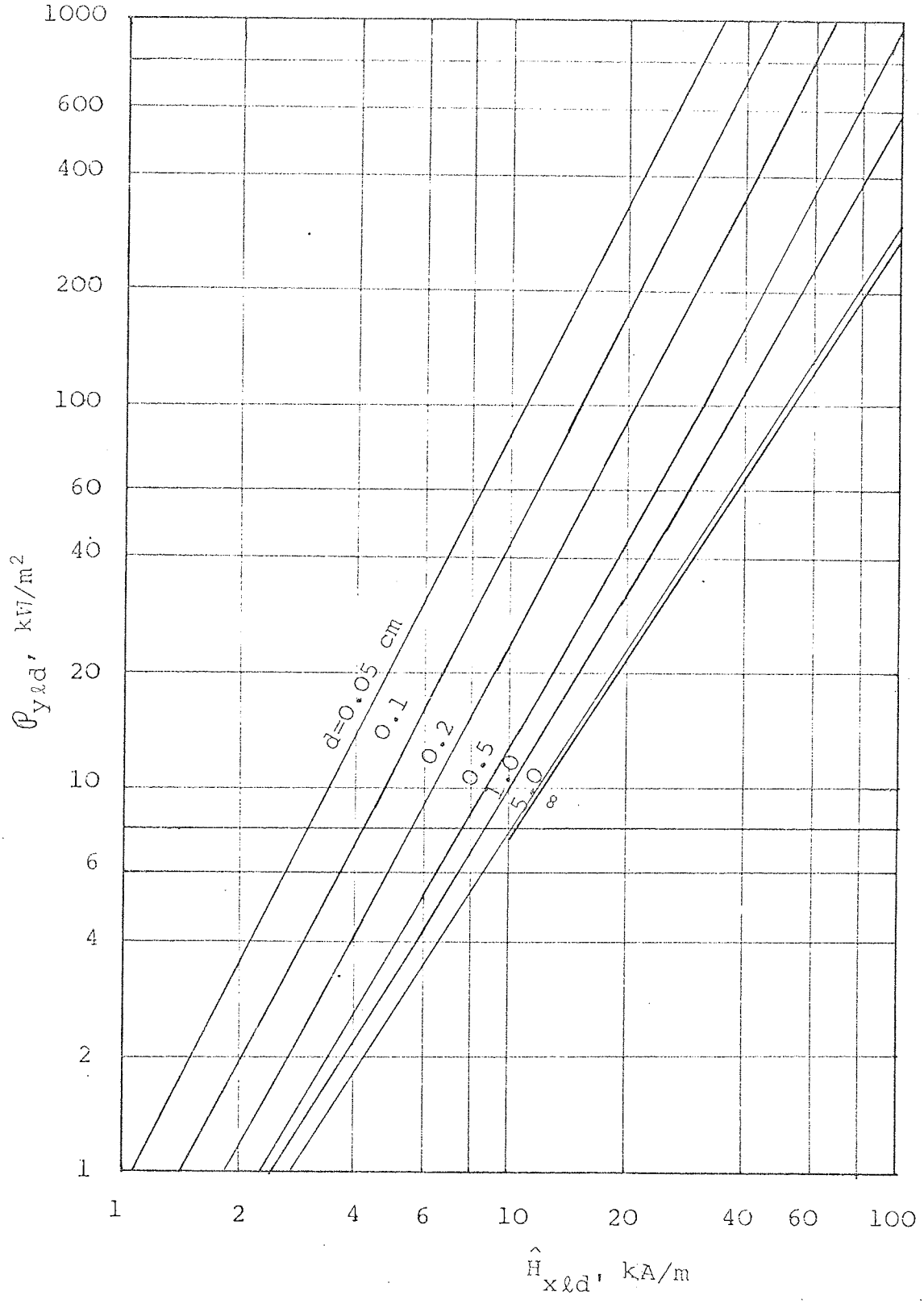


Figure 5.3: Variation of loss density in the plate with surface magnetic field strength for various half-thicknesses of the plate. Equation (5.43). Frequency = 50 Hz.

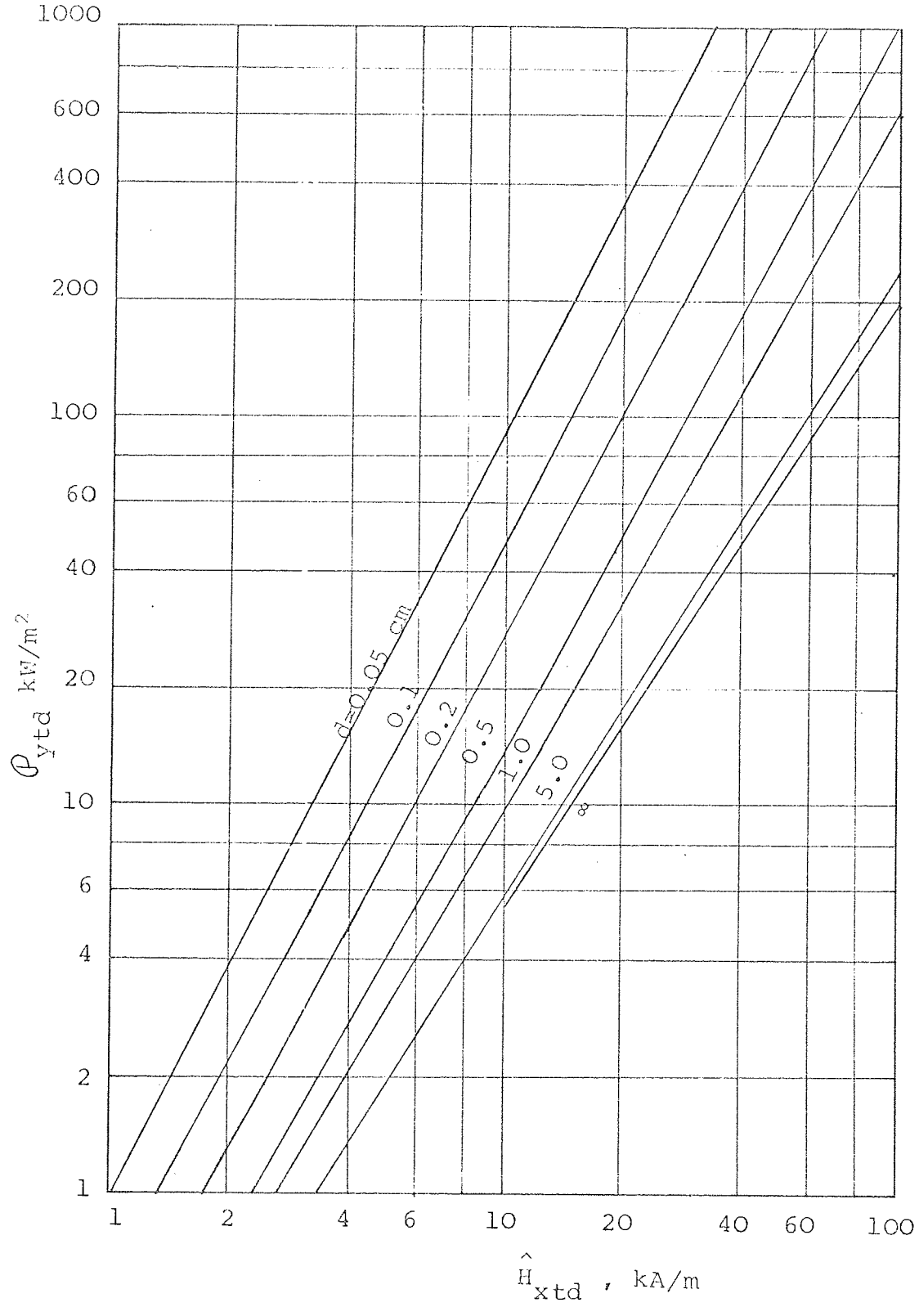


Figure 5.4: Variation of loss density in the plate with surface magnetic field strength for various half-thicknesses of the plate. Equation (5.72). Frequency = 50 Hz.

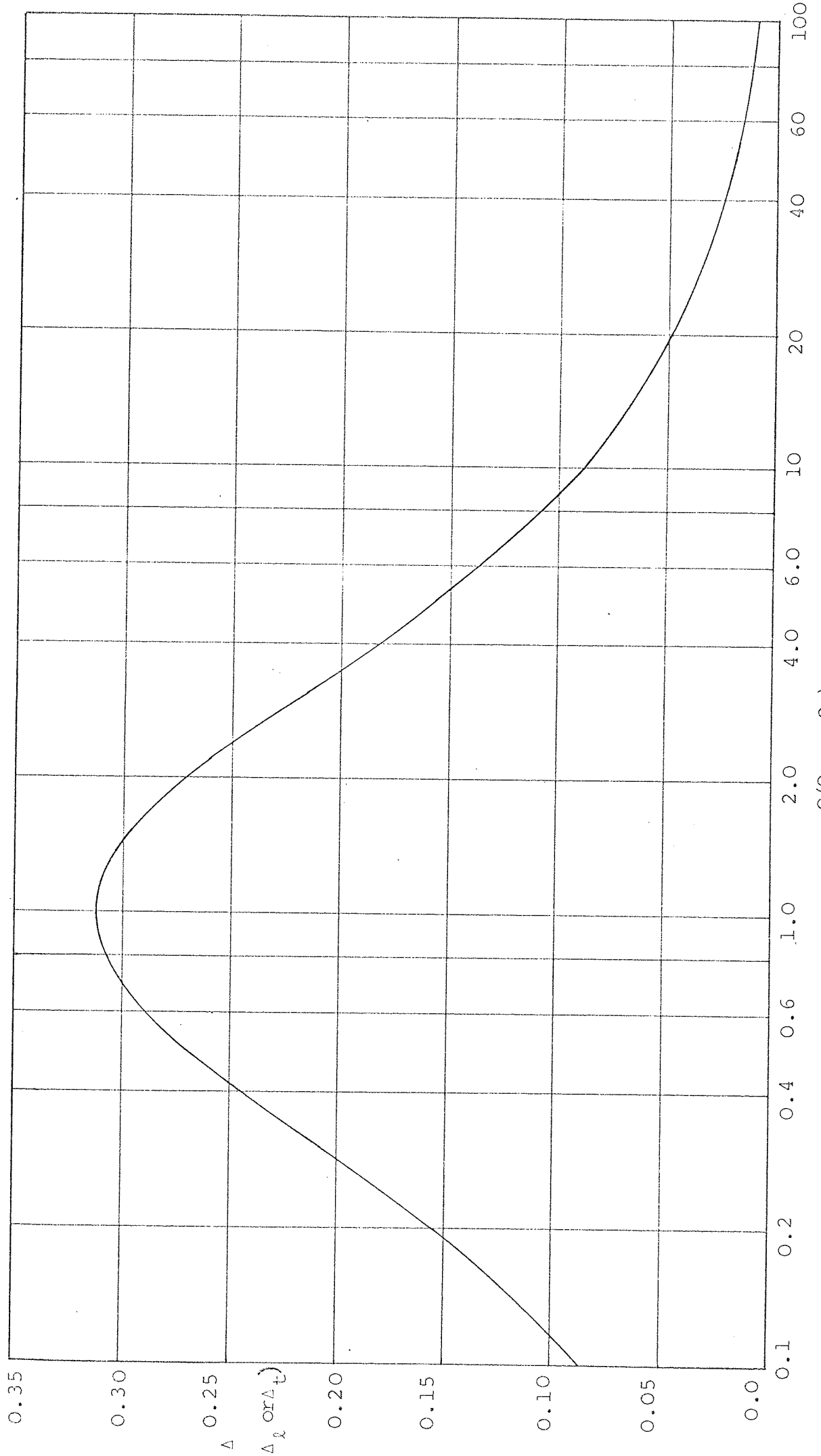


Fig. 6.1 Variation of $\Delta(\Delta_\ell$ or $\Delta_t)$ with $Q(Q_\ell$ or $Q_t)$; Equation (6.24) or (6.47). $b = 0.112$. Note that the curve is symmetrical about $Q = 1$.

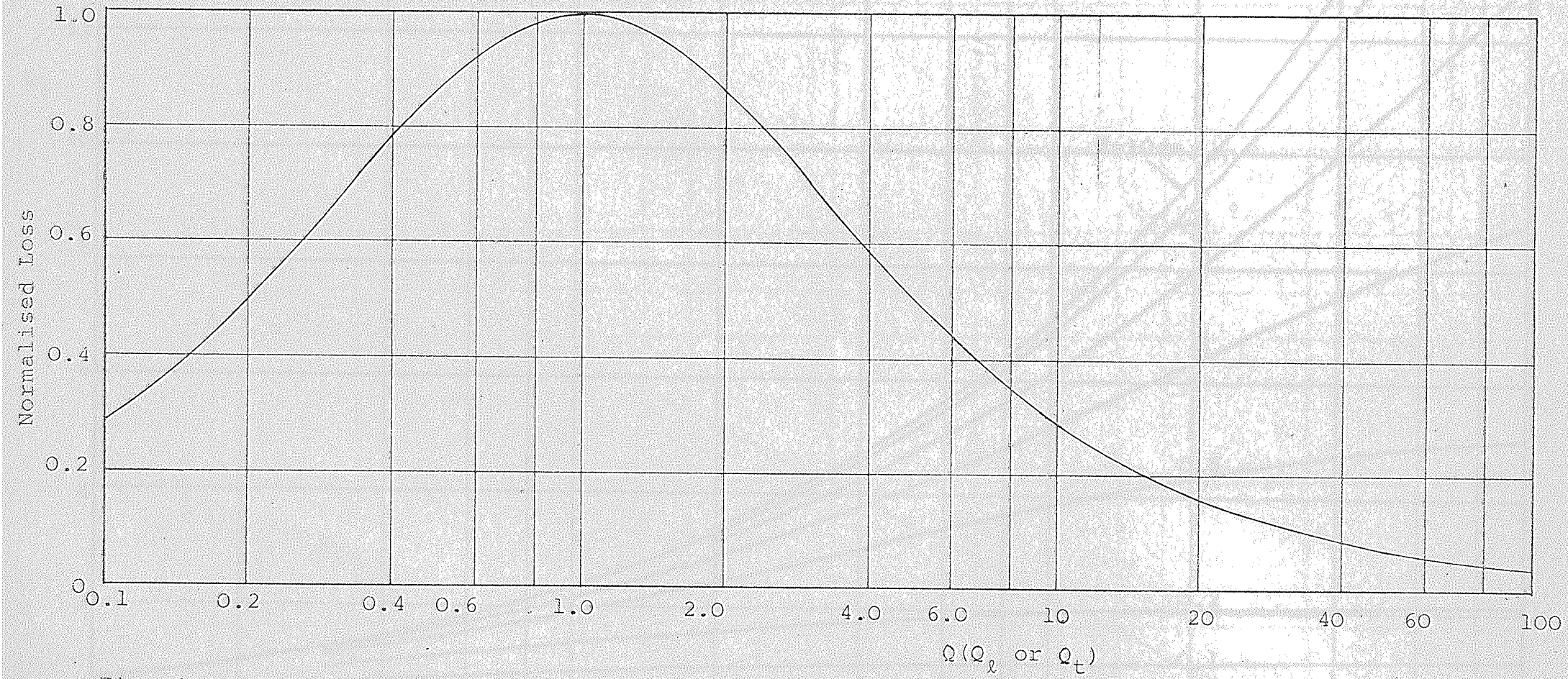


Fig. 6.2 Variation of normalised loss (or force) with $\Omega(Q_\ell$ or $Q_t)$. Equations (6.26) and (6.49). b = 0.112.

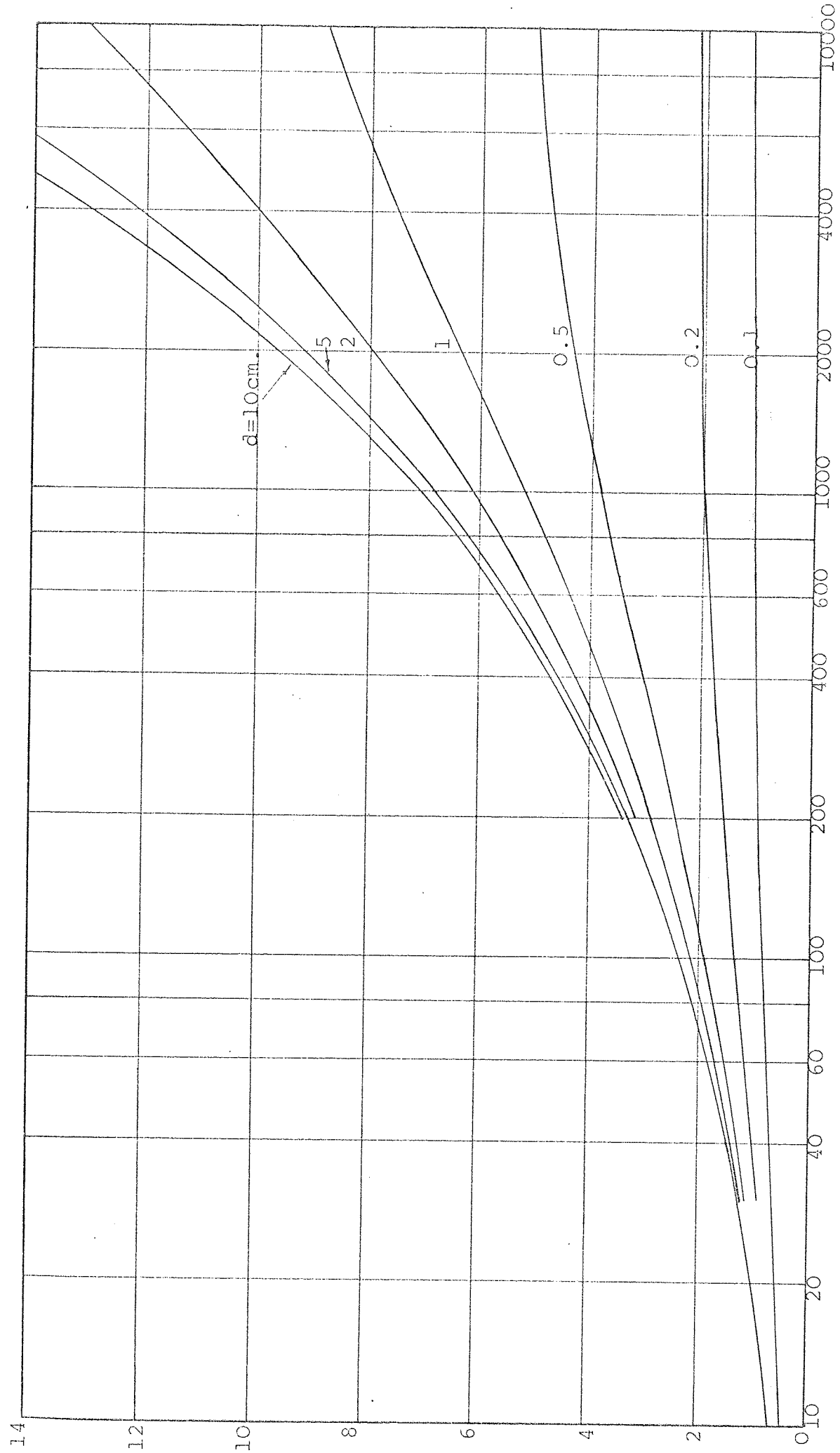


Fig. 6.3 Plot of the dimensionless parameter, $Q_\ell$, against the primary m.m.f. $|F_{c\ell}|$, for various half-thicknesses of the plate. g=1 mm, $\tau$ = 18 cm., $\omega$ = 100$\pi$, b = 0.5$\ell$12 and A = 1.25a (= 0.83) for ENIA steel plate.

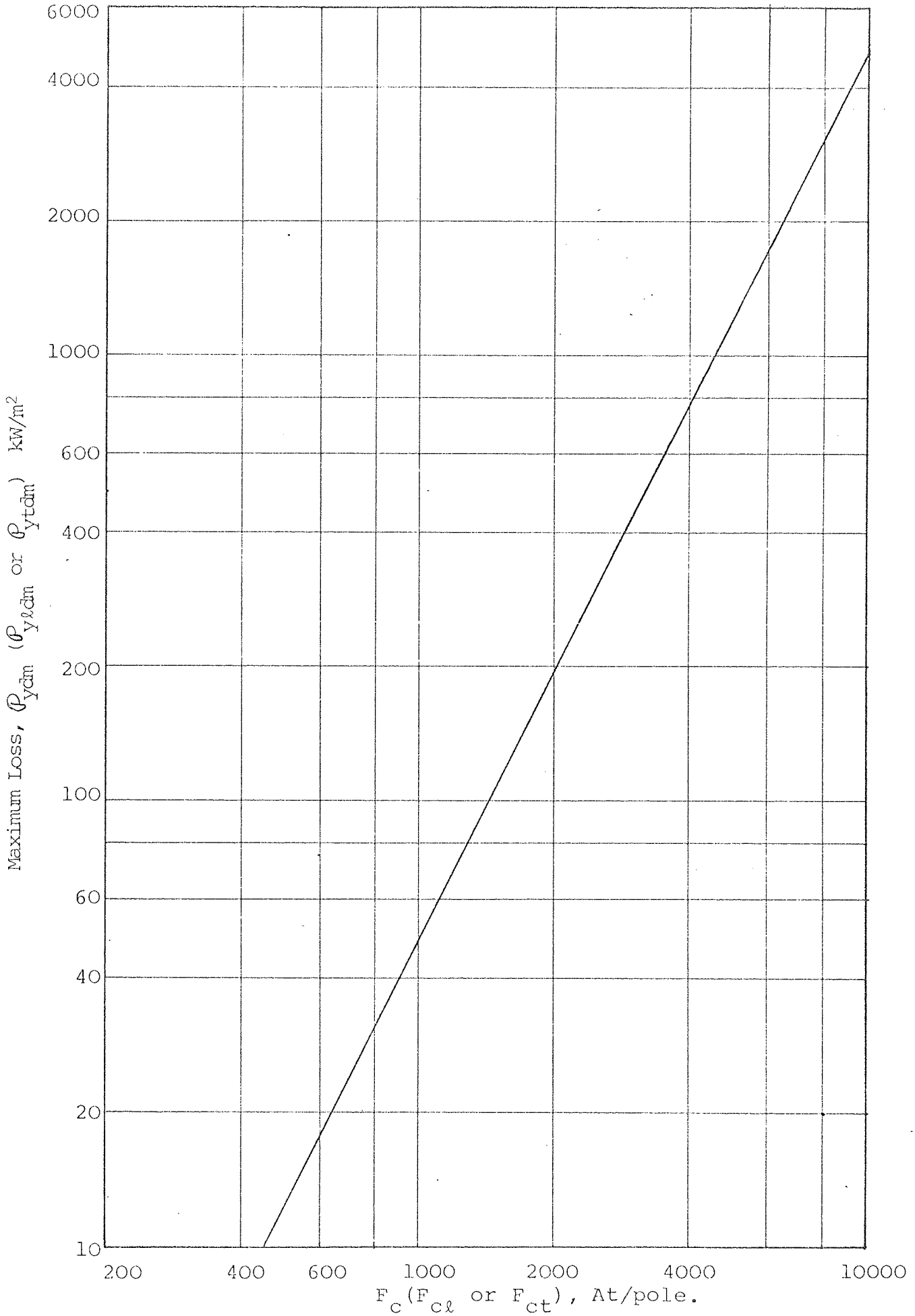


Fig. 6.4 Plot of maximum power loss, equation (6.25) or (6.48), against primary m.m.f. g = 1 mm, r = 18 cm. $\omega = 100\pi$.

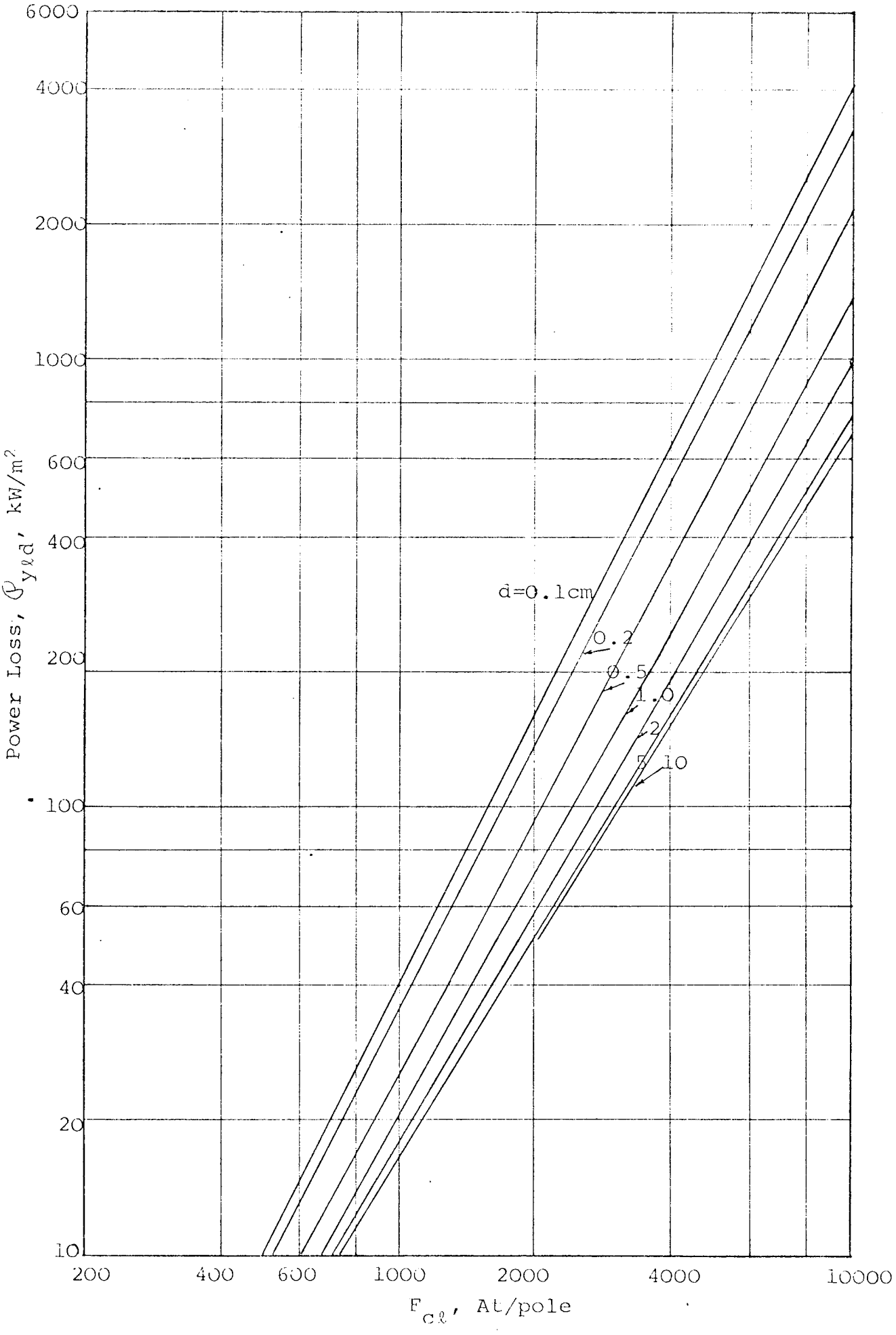


Fig. 6.5 Plot of power loss against primary m.m.f. for various half-thicknesses of the plate for longitudinal flux arrangement. $g$ = 1 mm, $\tau$ = 18 cm.

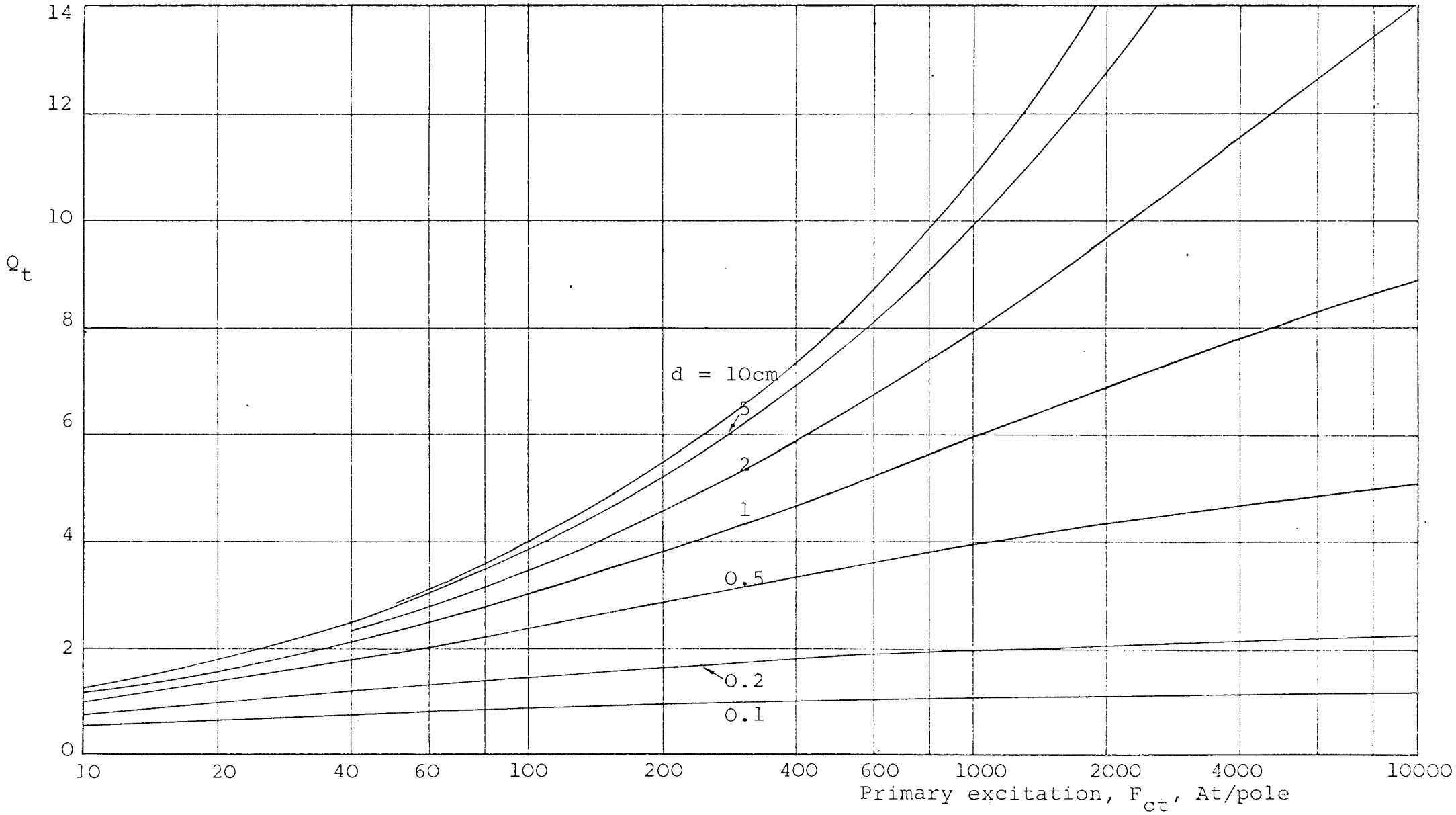


Fig. 6.6 Plot of $Q_t$ against primary excitation, $F_{ct}$, equation (6.50), for various plate thicknesses. Transverse flux arrangement. g = 1 mm, $\tau$ = 18 cm, $\omega = 100\pi$.

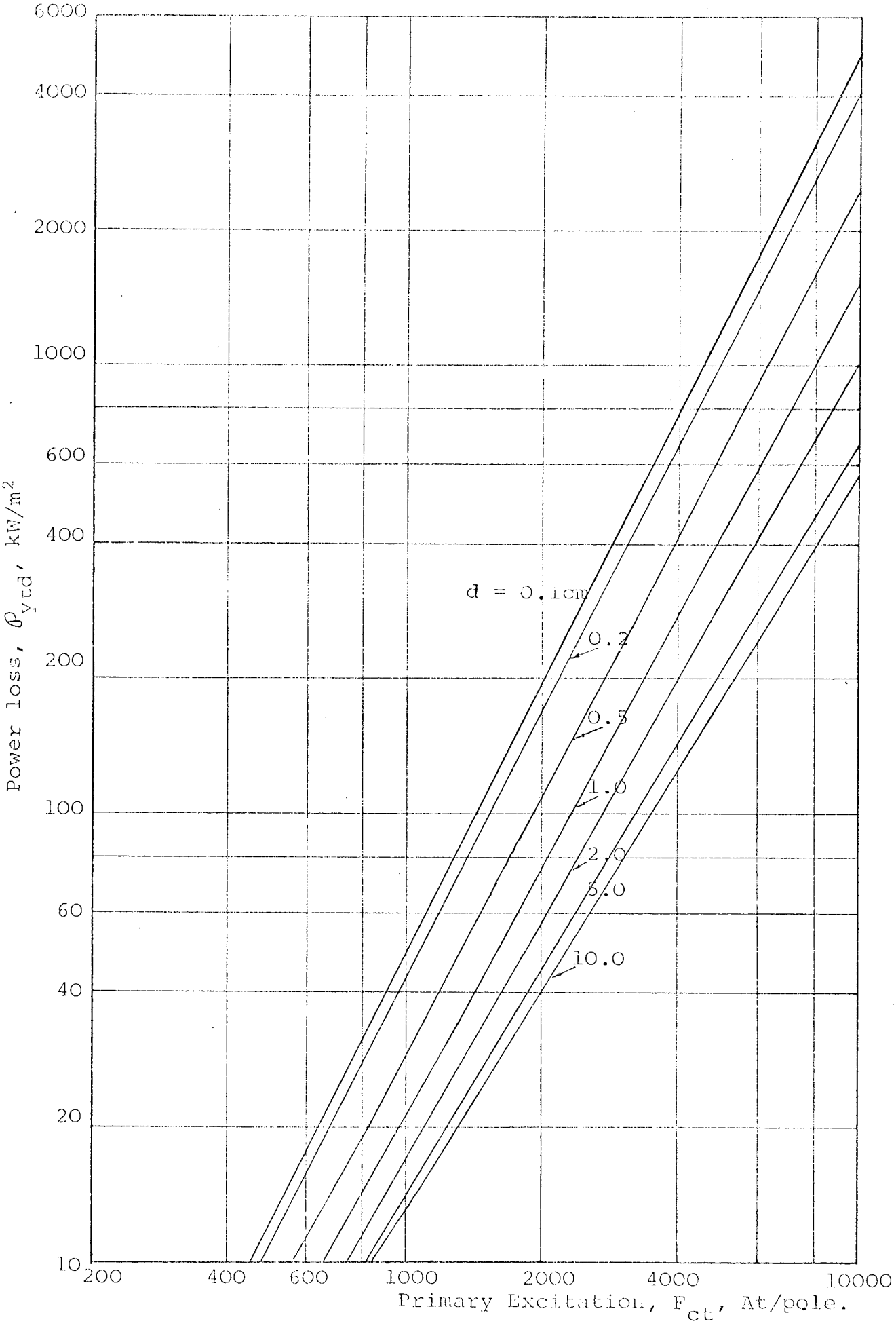


Fig. 6.7 Plot of power loss against primary m.m.f. $F_{ct}$, for various plate thicknesses under transverse flux arrangement, g = 1 mm, $\tau$ = 18 cm, $\omega$ = 100$\pi$.

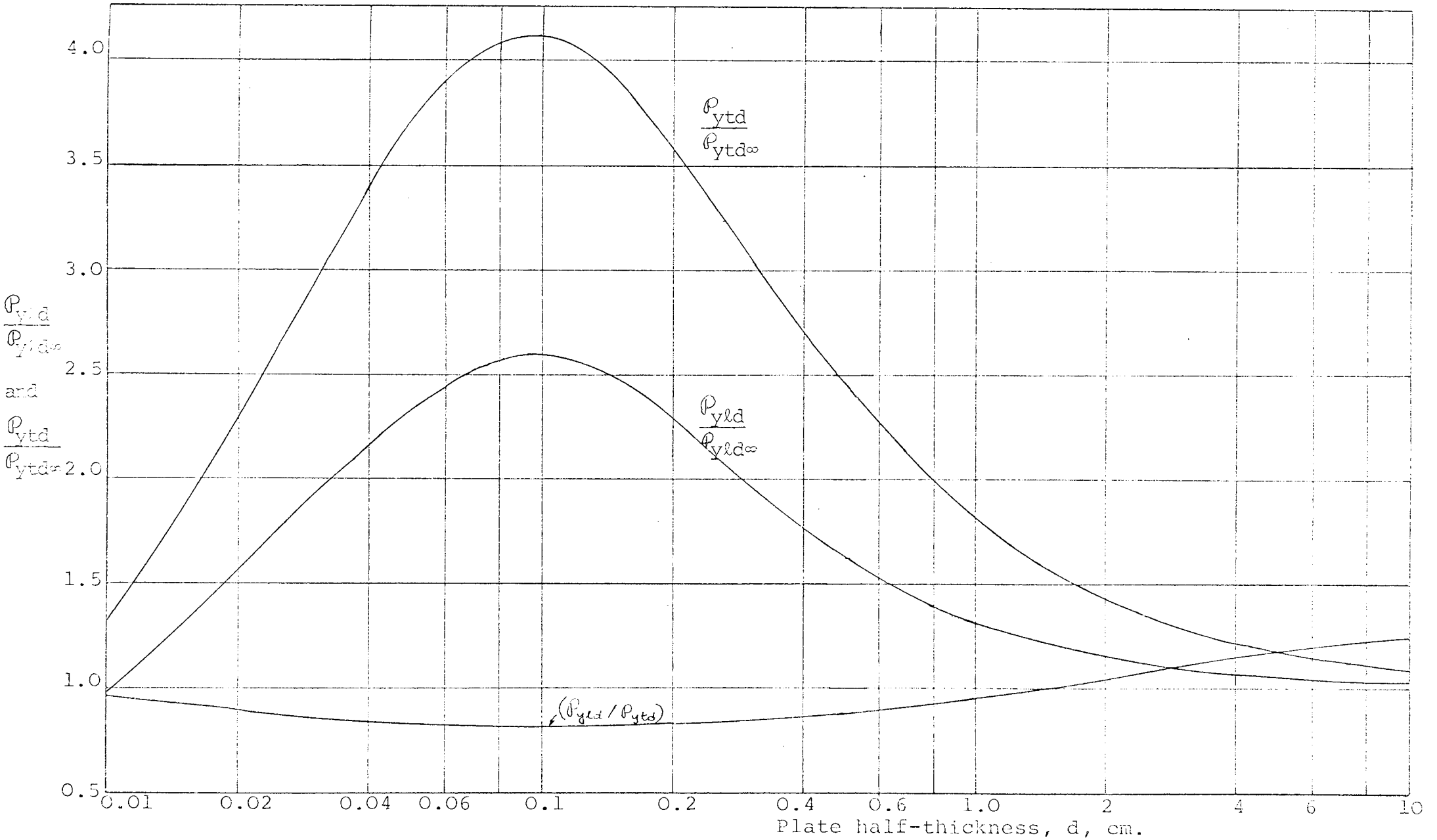


Fig. 6.8 Plot of the ratios $\rho_{yld}/\rho_{yld\infty}$ and $\rho_{ytd}/\rho_{ytd\infty}$ against half-thickness of the plate, d. $|E_c|$ = 1000 At/pole, g = 1 mm, $\tau$ = 18 cm, $\omega = 100\pi$.

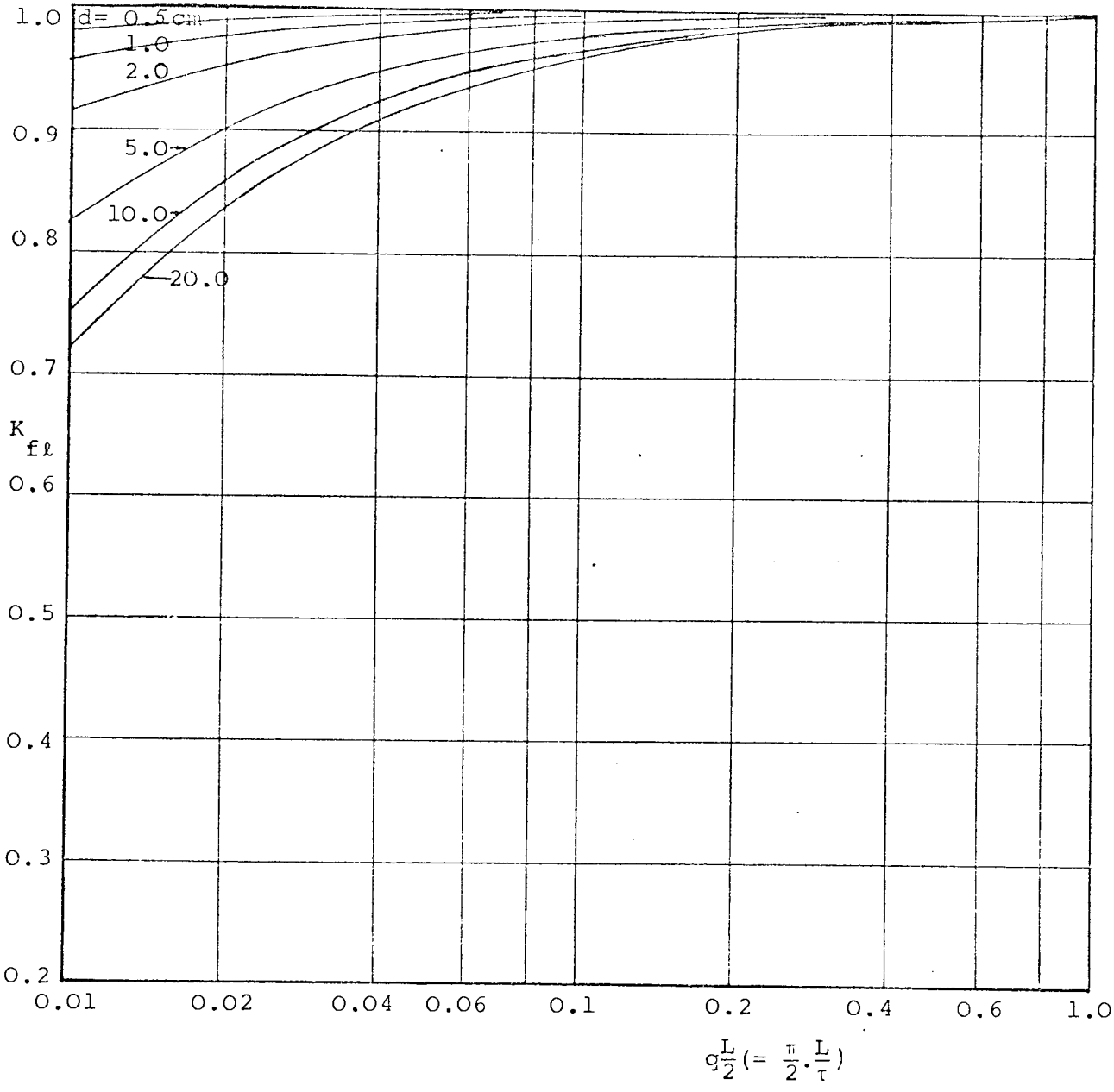


Fig. 7.4 Variation of finite-width factor for longitudinal flux arrangement, $K_{f\ell}$, with $(qL/2)$ ($\propto$ ratio of active width to pole-pitch), for various plate thicknesses in the presence of copper end-strips. $H_{x\ell d}$ = 1 kA/m, $\tau$ = 25 cm, $d_e$ = 0.5 cm.

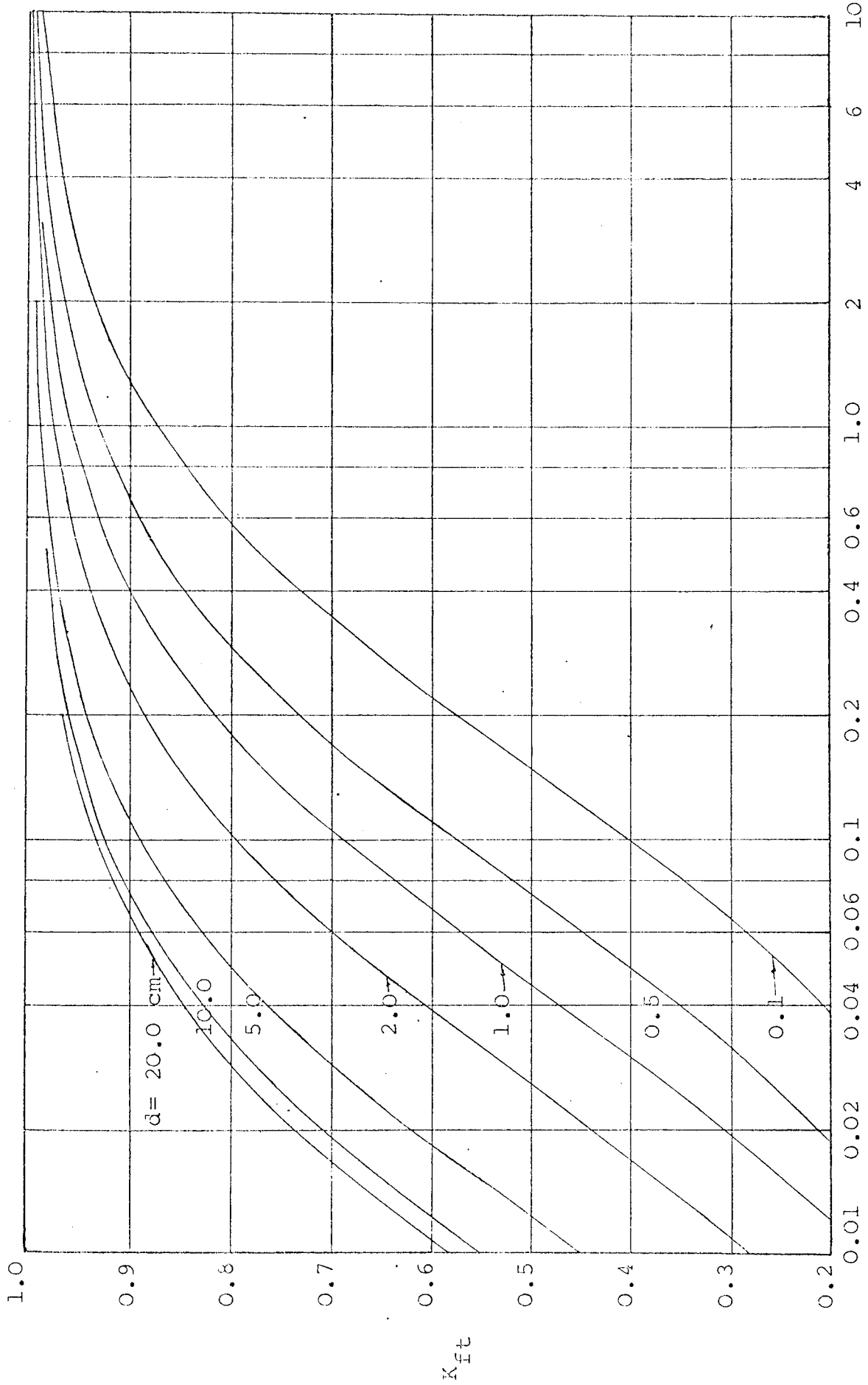


Fig. 7.5 Variation of finite width factor, $K_{ft}$, for transverse flux arrangement, equation (7.52) with $(qL/2)$ (= ratio of active width to pole-pitch) for various values of plate thickness in the presence of copper end-strips. $H_{xtd}$ = 1 kA/m, $\tau$ = 25 cm., $d_e$ = 0.5 cm.

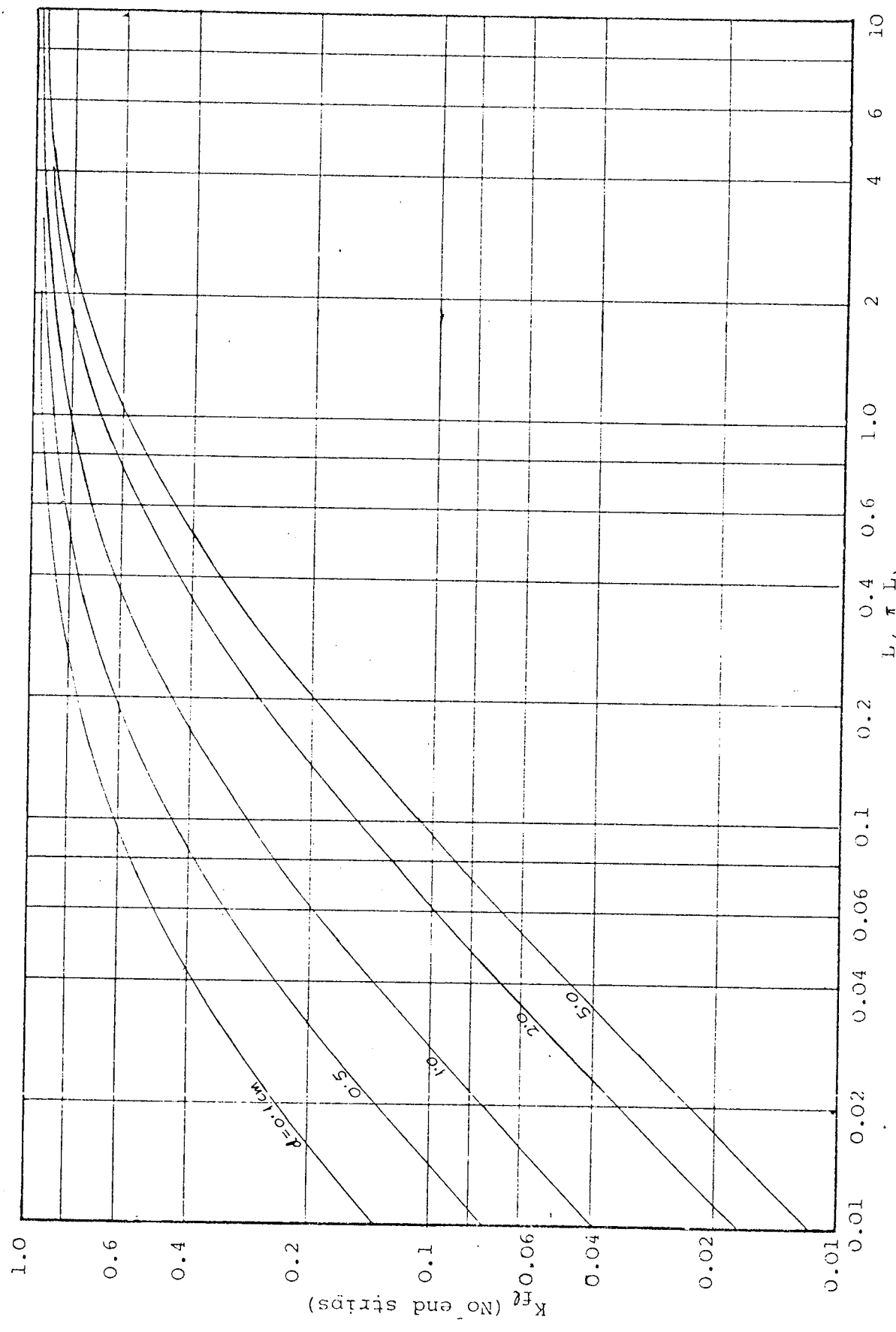


Fig. 7.6 Variation of finite-width factor for longitudinal flux arrangement, $K_{f\ell}$, with $(q\frac{L}{2})$ ("ratio of active width to pole-pitch) for various plate thicknesses in the absence of conducting end-strips. $H_{xtd}$ = 1 kA/m, $\tau$ = 25 cm, $\omega$ = 100$\pi$.

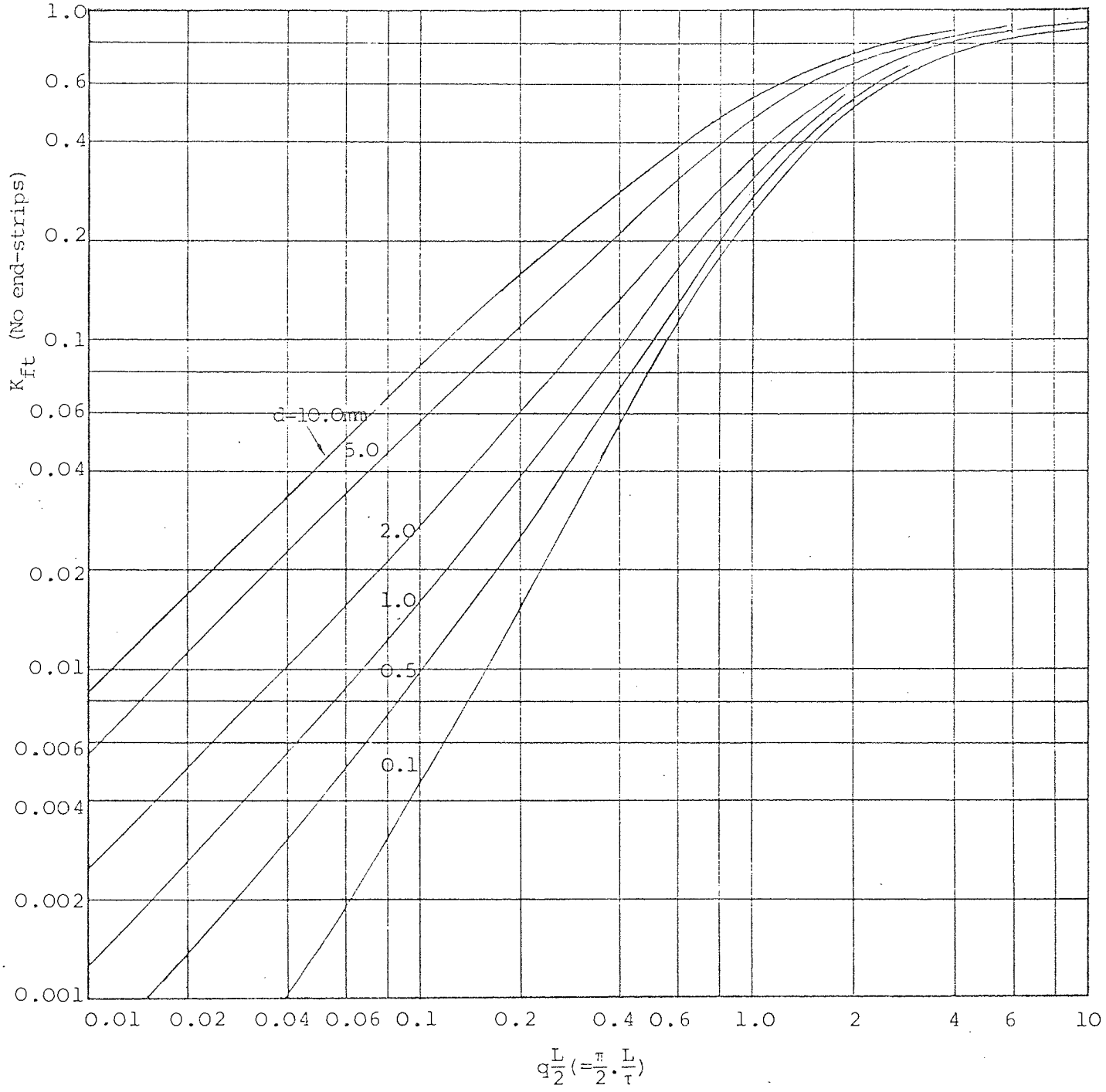


Fig. 7.7 Variation of finite-width factor for transverse flux arrangement, $K_{ft}$, with $(qL/2)$ (= ratio of active width to pole-pitch) for various plate thicknesses in the absence of low resistivity end-strips. $H_{xtd}$ = 1kA/m, $\tau$ = 25 cm., $\omega = 100\pi$.

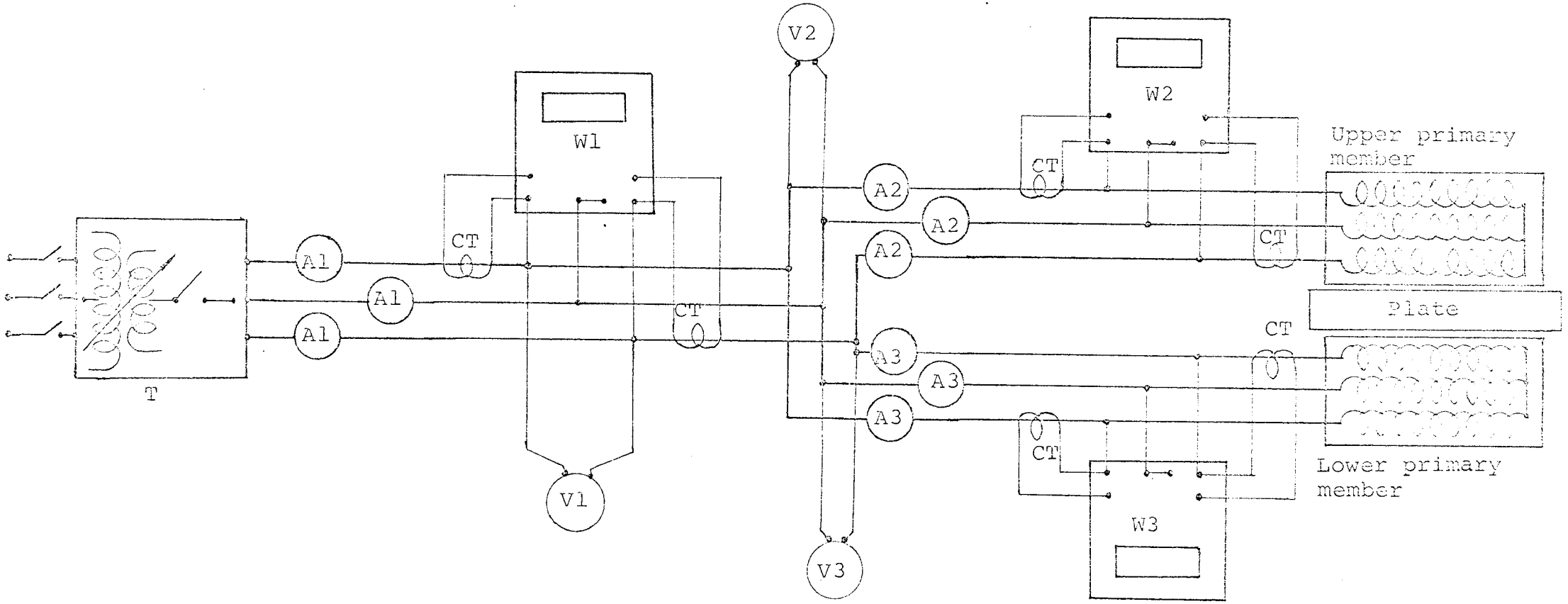


Fig. 8.1 Circuit diagram used in experiments.

T = Three-phase transformer with isolating switch.
A1, A2, A3, = Ammeters.
CT = Current transformer.
W1, W2, W3 = Three-phase wattmeters.
V1, V2, V3 = Digital voltmeters.

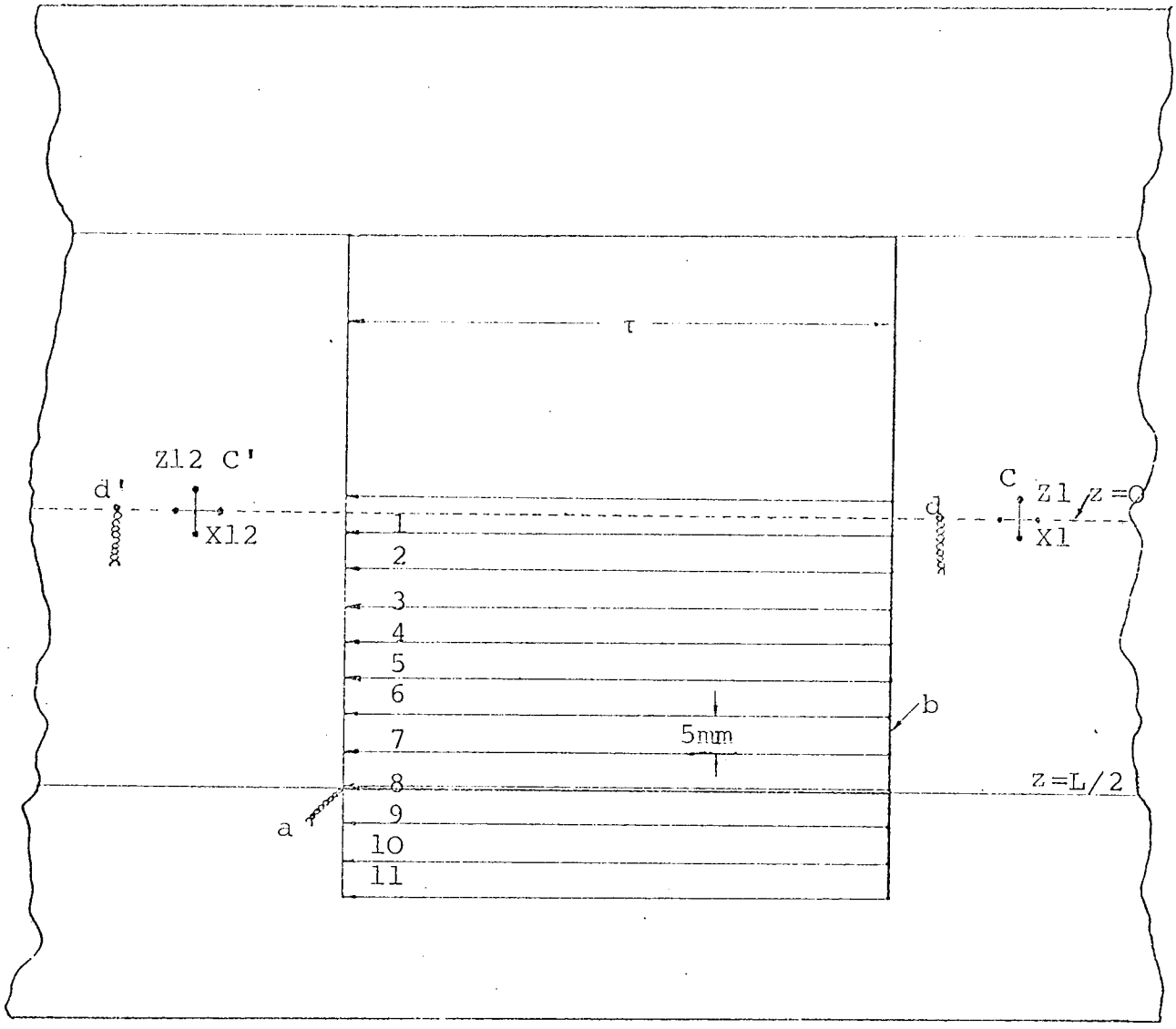


Fig. 8.3 Location of full-pitch search coil for measuring flux/pole and other search coils each 5 mm wide on the surface of wide plate.

a : Full-pitch search coil ends twisted and taken to selector switch.
b : One end of all search coils joined on this wire.
C & C' : Location of J-probes, Fig. 8.4.
d & d' : Location of thermocouples. There was another thermocouple to the right of d (outside this fig.) at equal distance.
1,2,3,--- : Search coil numbers; coil formed by wires on immediate top and bottom of the numbers.
The ends of the search coils marked by arrows were twisted and taken to selector switch.

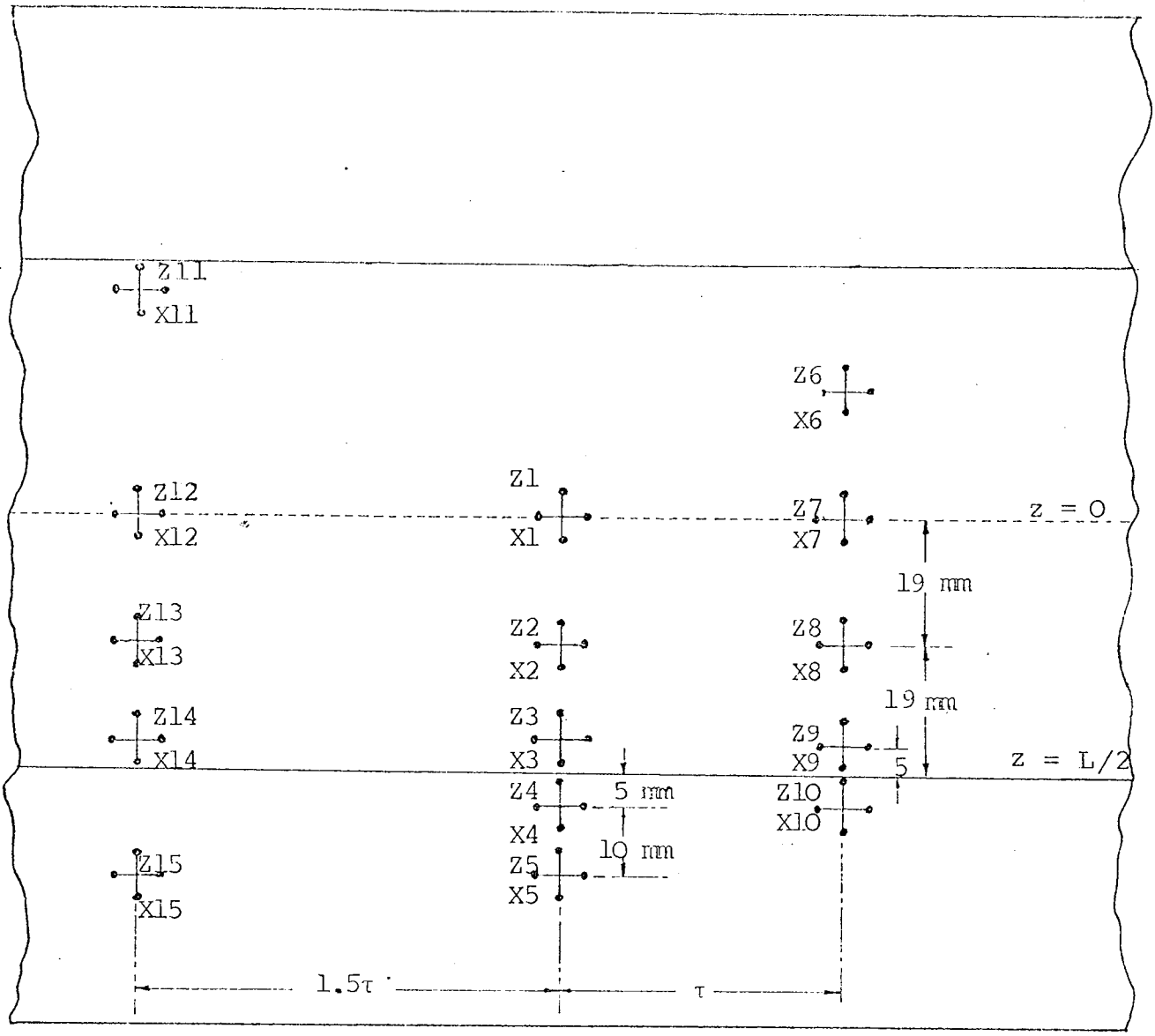


Fig. 8.4 Location of current-density probes on the surface of the wide plate. J-probes marked by Z's are along the z-axis and measure $J_z$'s and the J-probes marked by X's are along the x-axis and measure $J_x$'s. Two more sets of J-probes were placed on z = 0 line at ½ pole-pitch from the ends of active length. (Not shown in this figure).

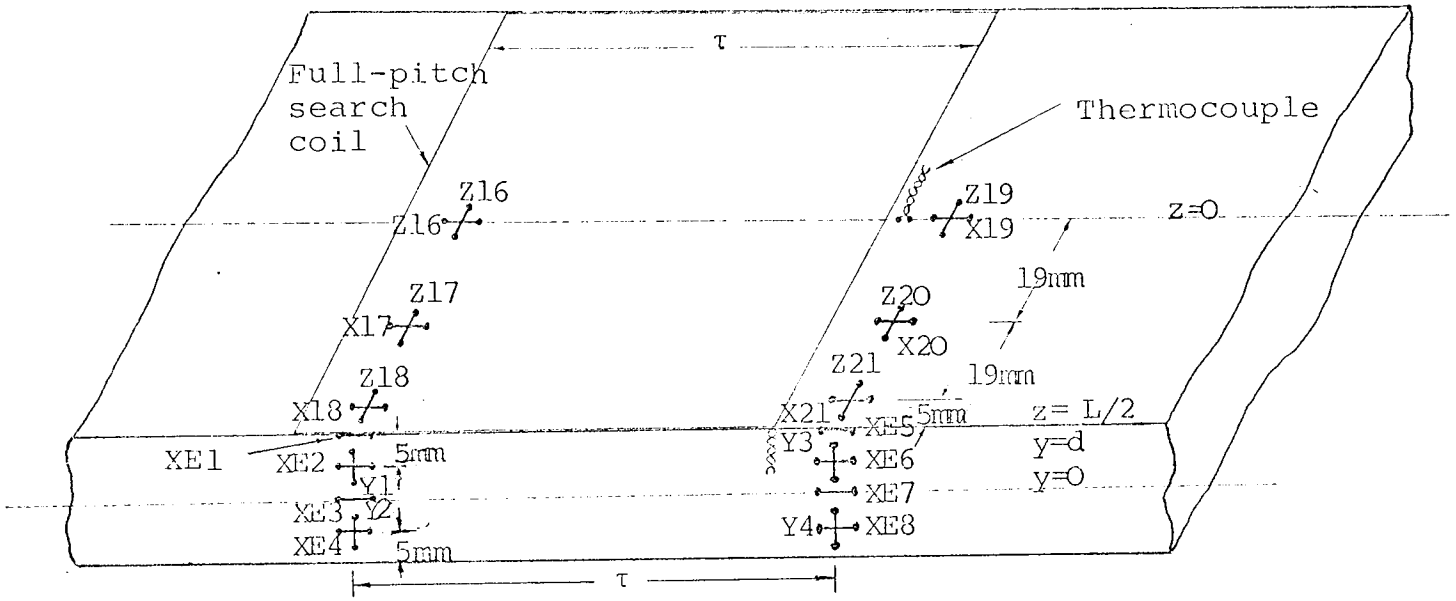


Fig. 8.5 Location of full-pitch search coil and the current-density probes on the surface and lateral side face of the narrow plate. Location of a thermocouple probe is also shown.

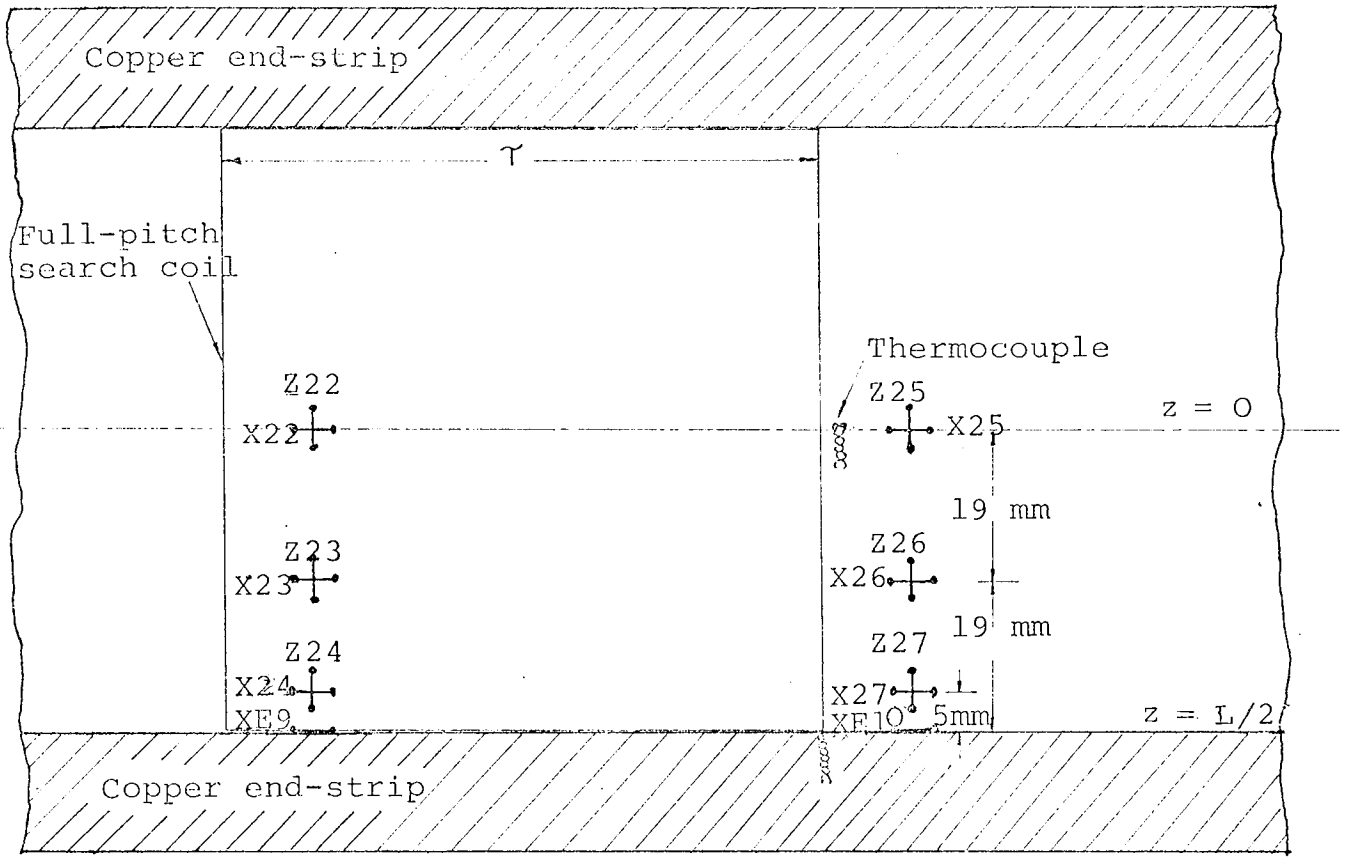


Fig. 8.6 Location of full-pitch coil and current-density probes on the surface of the end-strip plate. Location of a thermocouple probe is also shown.

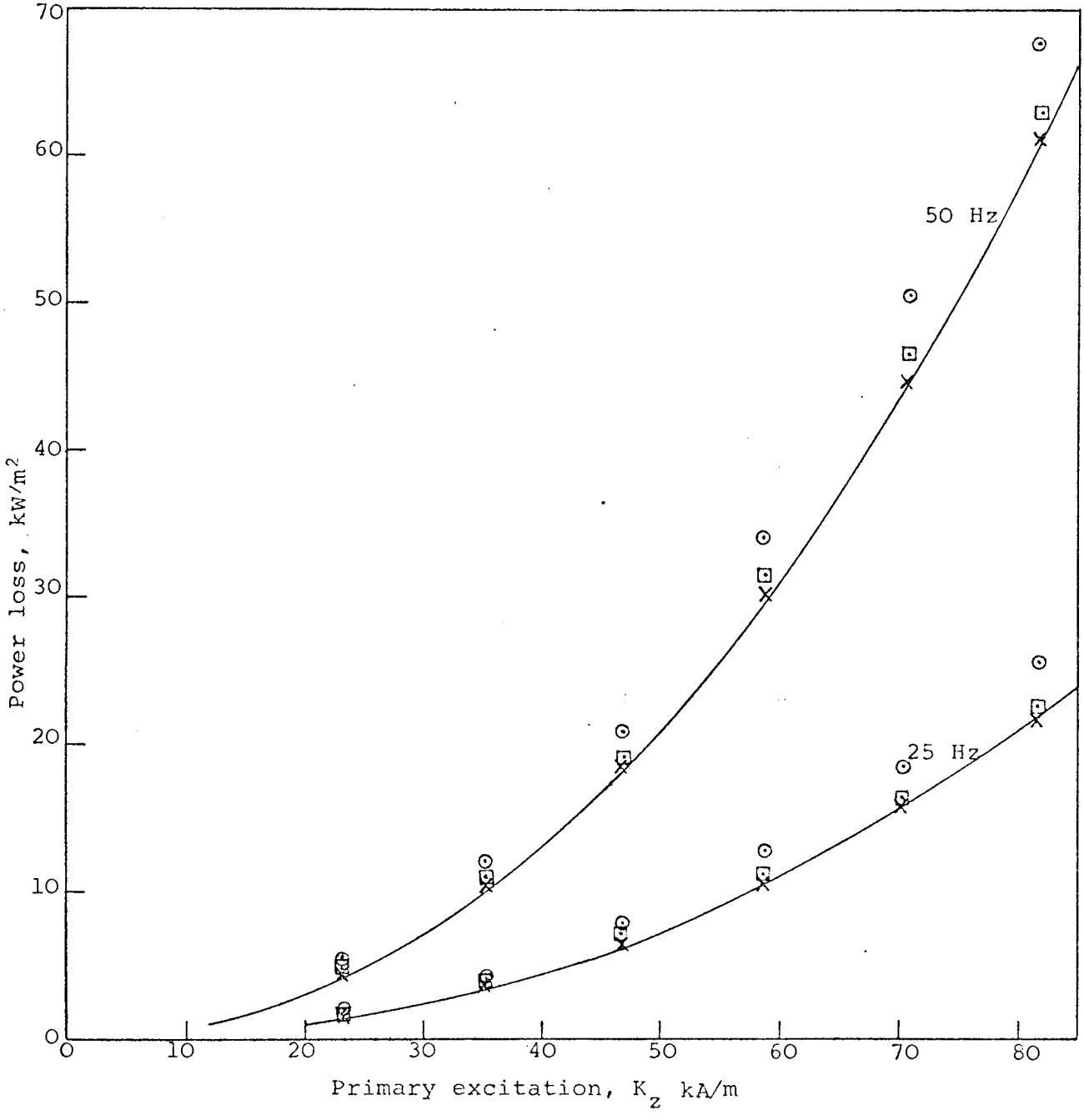


Fig. 8.7 Measured and calculated values of loss/area against excitation for longitudinal flux arrangement at both 25 Hz. and 50 Hz.

Measured: ⊙ : End-strip plate. ⊡ : Wide plate. X : Narrow plate.
——— : Calculated, equation (6.23).

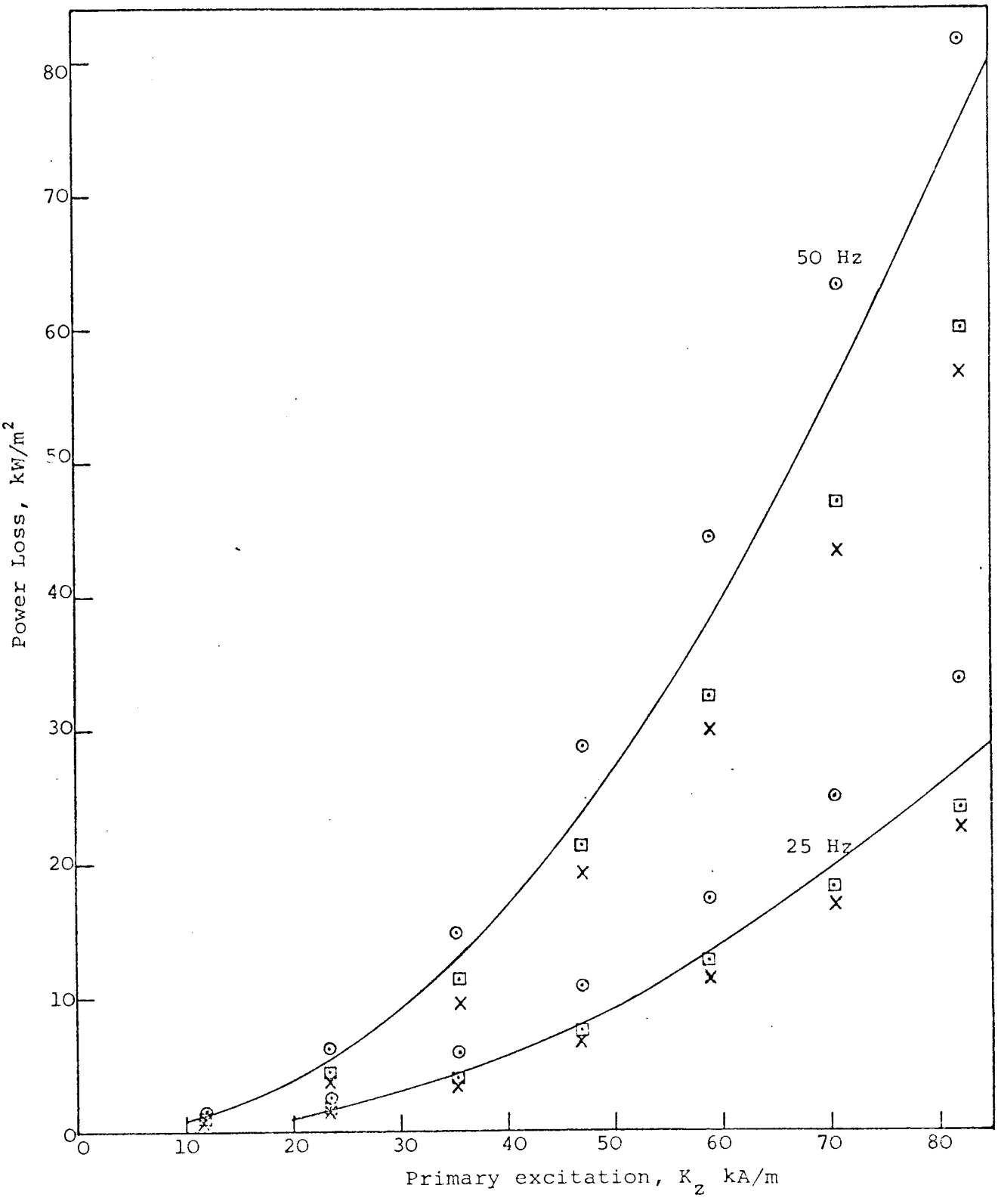


Fig. 8.8 Measured and calculated values of loss/area against excitation for transverse flux arrangement at both 25 Hz and 50 Hz.

Measured ⊙ : End-strip plate. ⊡ : Wide plate.
× : Narrow plate.

Calculated : ——— , Equation (6.46)

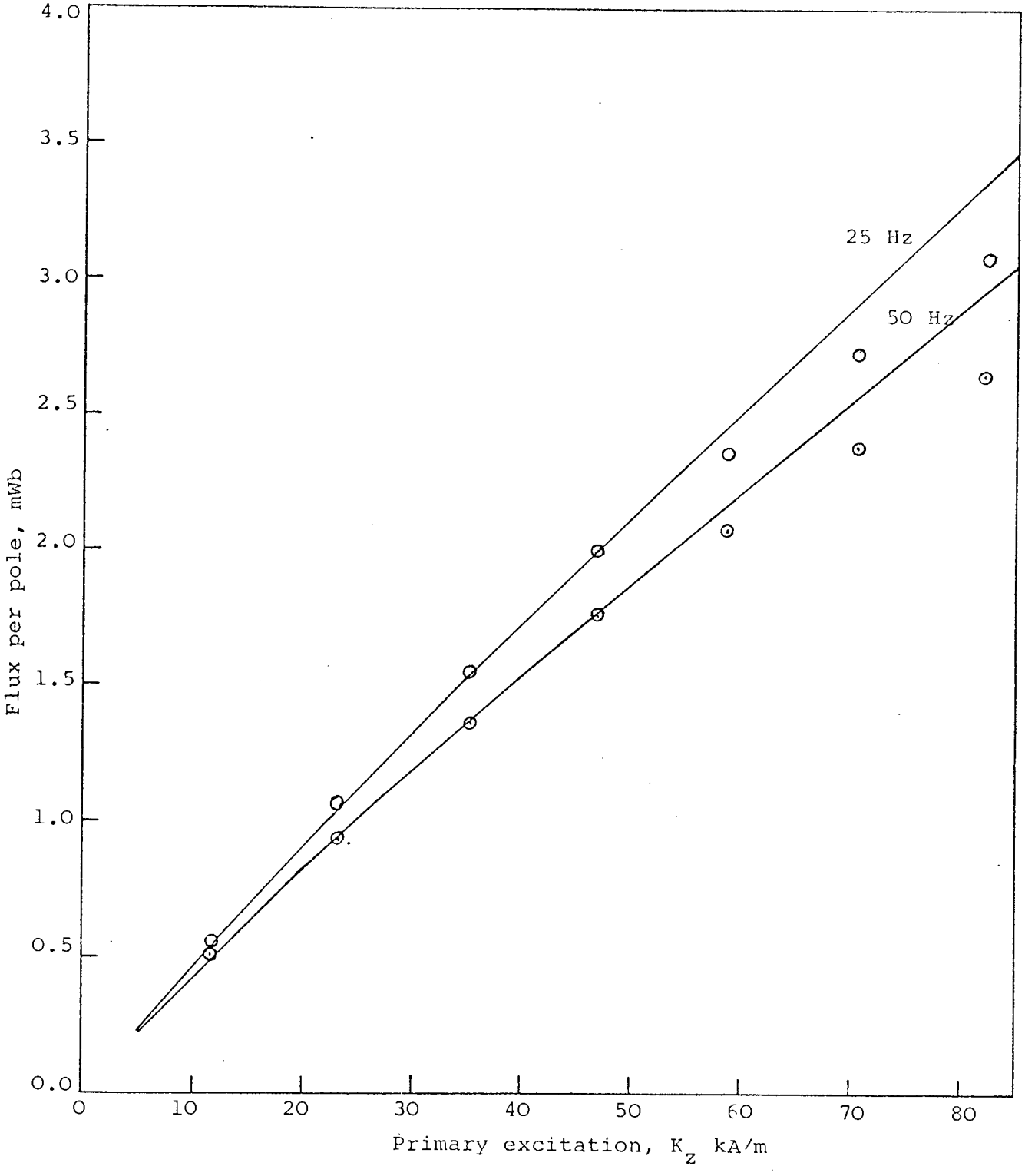


Fig. 8.10 Variation of measured and calculated values of flux/pole with excitation under longitudinal flux arrangement for the end-strip plate at both frequencies.

○ : Measured at 25 Hz
⊙ : Measured at 50 Hz
——— : Calculated, Equation (6.32)

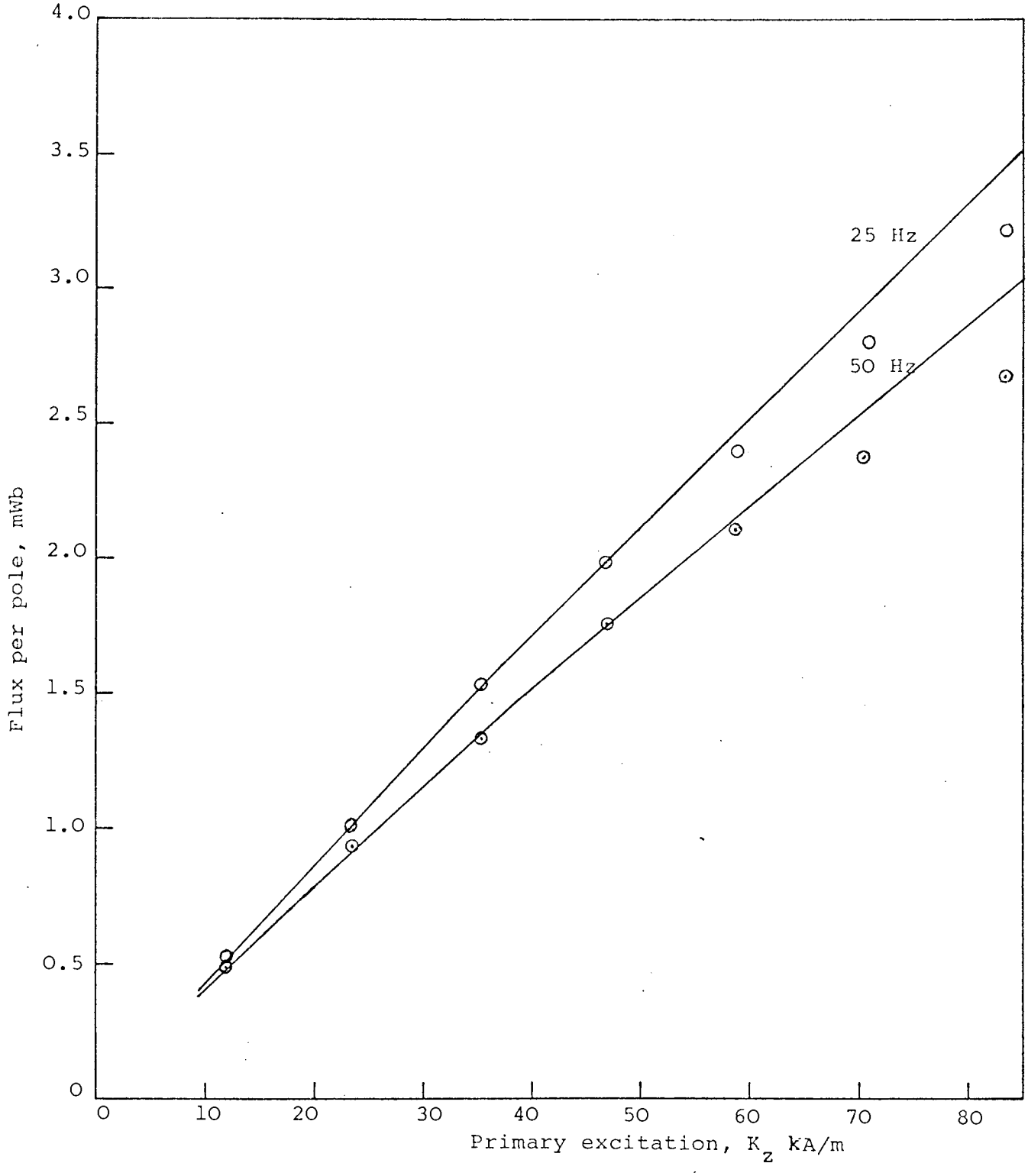


Fig. 8.11 Variation of measured and calculated values of flux/pole with excitation under transverse flux arrangement for the end-strip plate at both frequencies.

O : Measured at 25 Hz
⊙ : Measured at 50 Hz
——— : Calculated, Equation (6.56)

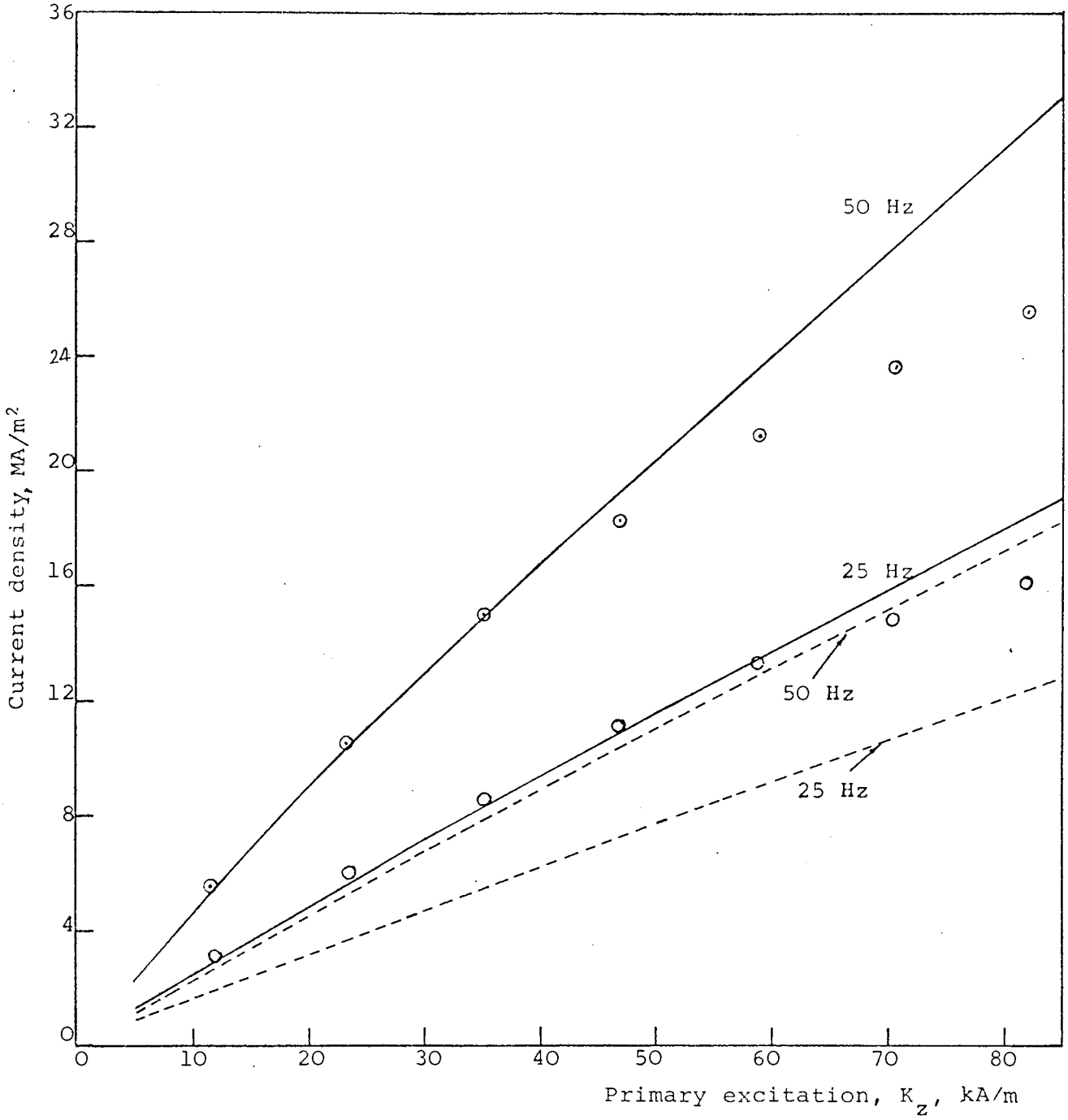


Fig. 8.12 Variation of measured and calculated values of current density on the surface of the end-strip plate with excitation for longitudinal flux arrangement at both frequencies. The dotted curves are calculated surface current density values for a higher restivity (40 μΩ-cm. for 50 Hz and 30 μΩ-cm. for 25 Hz).

○ : Measured at 25 Hz
⊙ : Measured at 50 Hz
——— : Calculated, equations (5·37) and (6.18).
------

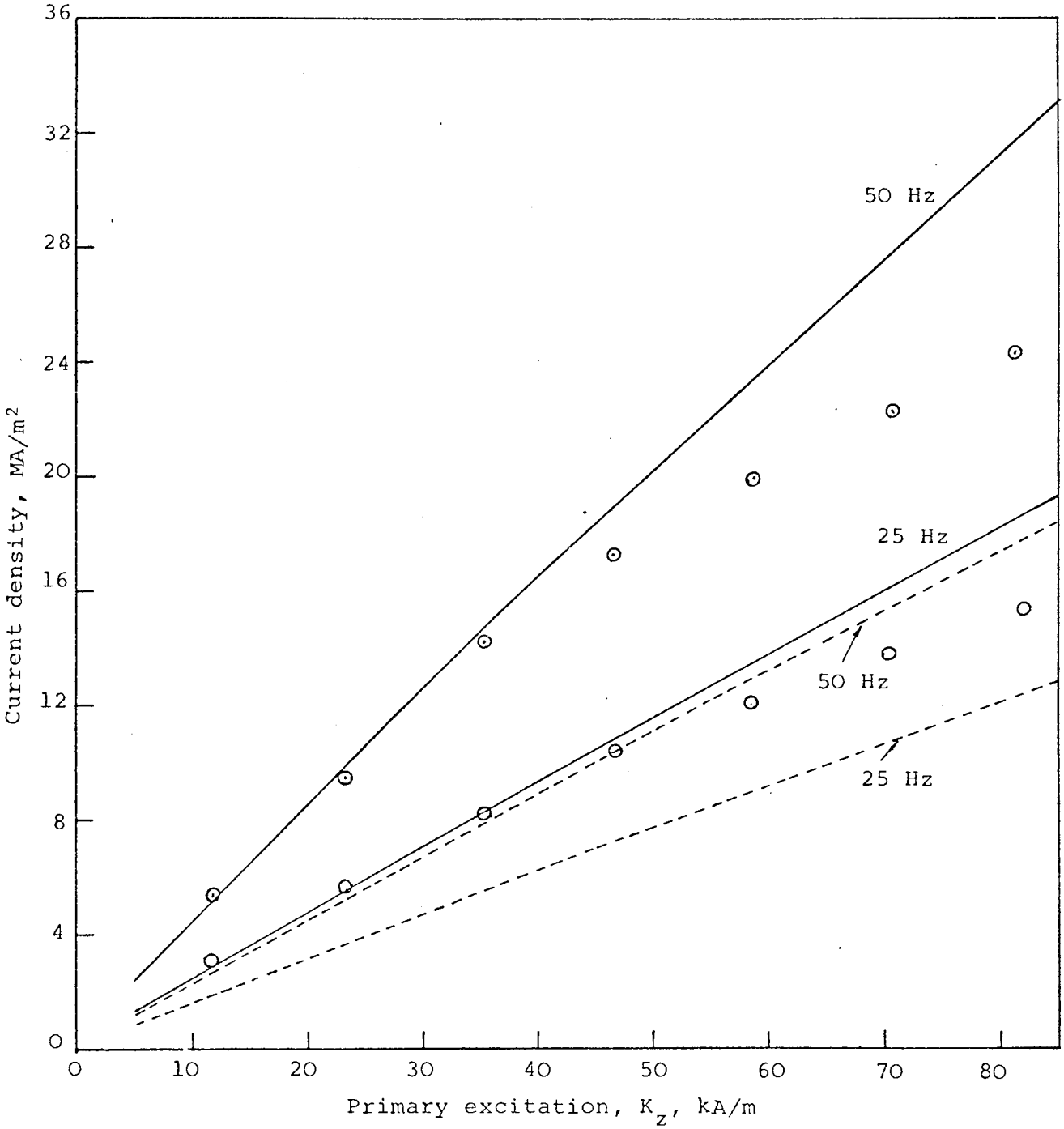


Fig. 8.13 Variation of measured and calculated values of current density on the surface of the end-strip plate with excitation for transverse flux arrangement at both frequencies. The dotted curves are calculated surface current density values for a higher resistivity (4.0 μΩ-cm. for 50 Hz and 30 μΩ-cm. for 25 Hz).

O : Measured at 25 Hz
⊙ : Measured at 50 Hz
——— : Calculated, equations (5.63) and (6.41)

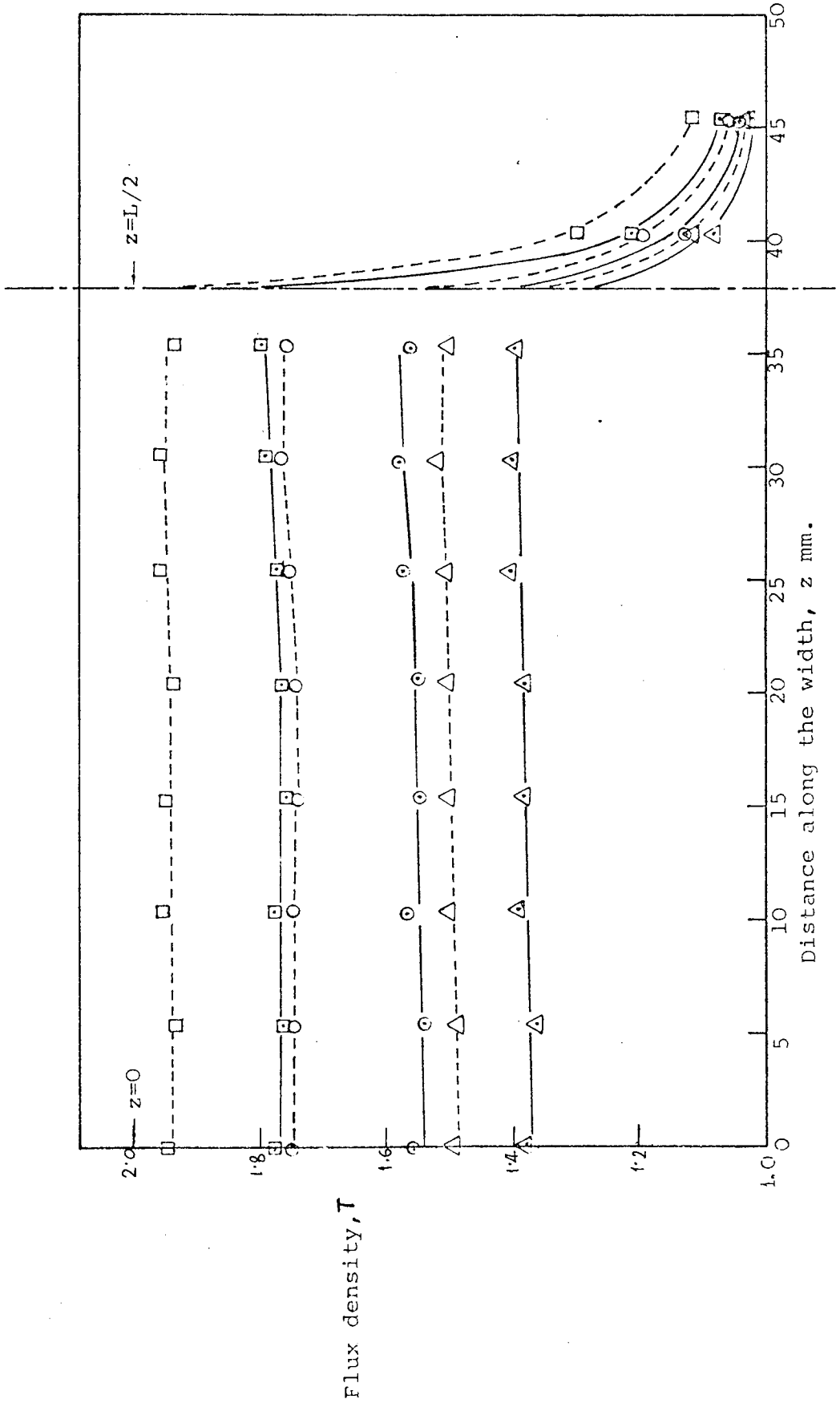


Fig. 8.14 Variation of measured air-gap flux density along the width of the active region of the wide plate for longitudinal flux arrangement at various excitations. Dotted lines are for 25 Hz and firm lines for 50 Hz.

25 Hz

□ : 82.3 kA/m
○ : 58.8 kA/m
△ : 35.3 kA/m

50 Hz

⊡ : 82.3 kA/m
⊙ : 58.8 kA/m
⧋ : 35.3 kA/m

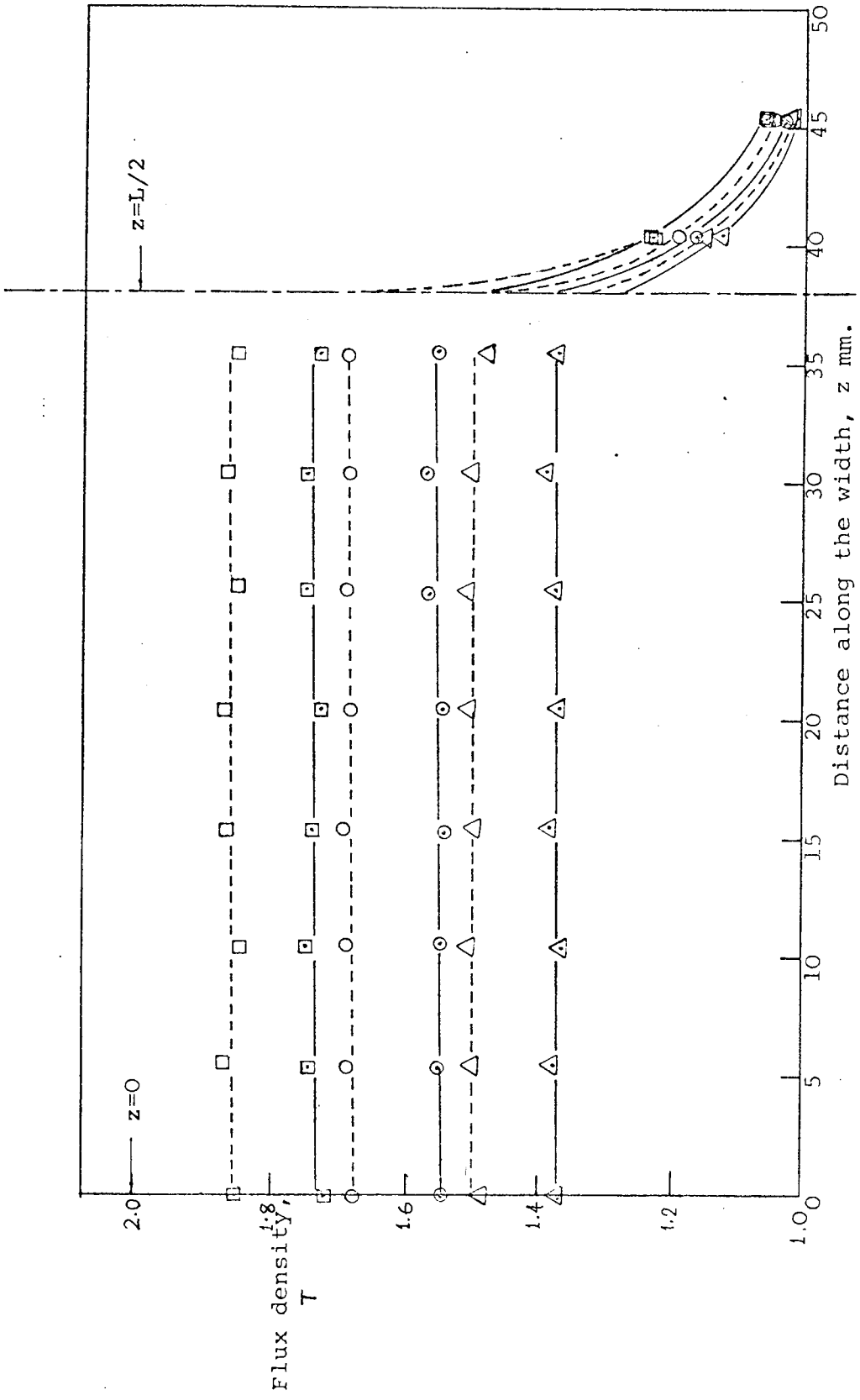


Fig. 8.15 Variation of measured air-gap flux density along the width of the active region of the wide plate for transverse flux arrangement for various excitations. Dotted lines are for 25 Hz and firm lines for 50 Hz.

25 Hz

□ : 76.5 kA/m
○ : 58.8 kA/m
△ : 35.3 kA/m

50 Hz

□ : 82.3 kA/m
⊙ : 58.8 kA/m
△ : 35.3 kA/m

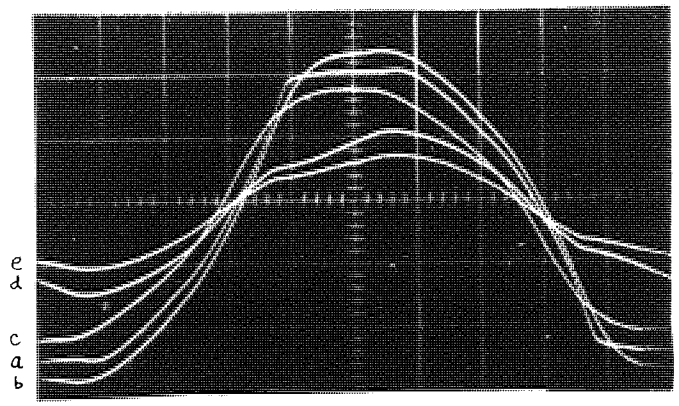


Fig. 8.16a

Voltages proportional to $J_z$

| Wave-Shape | : | J-probe |
|---|---|---|
| a | : | Z1 |
| b | : | Z2 |
| c | : | Z3 |
| d | : | Z4 |
| e | : | Z5 |

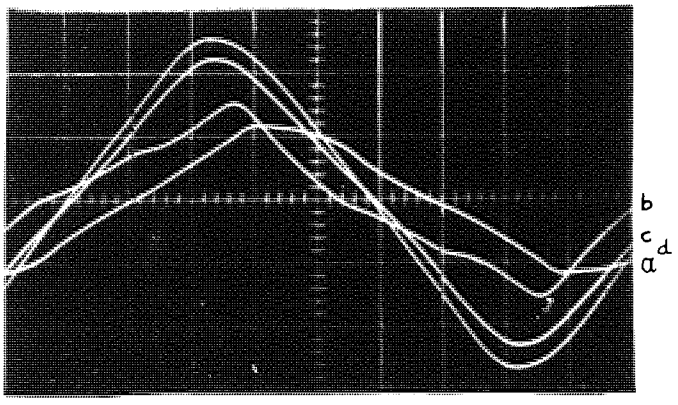


Fig. 8.16b

Voltages proportional to $J_x$

| Wave-Shape | : | J-probe |
|---|---|---|
| a | : | X1 |
| b | : | X2 |
| c | : | X3 |
| d | : | X4 |

Fig. 8.16 : Oscillograms of voltages from current-density probes on the surface of the wide plate for longitudinal flux arrangement.

| | | |
|---|---|---|
| Excitation | = 58.8 kA/m | 0.5 V/cm |
| Frequency | = 50 Hz | 2 ms /cm |
| Amplification | = 100 | |

Locations of the J-probes are shown in Fig. 8.4.

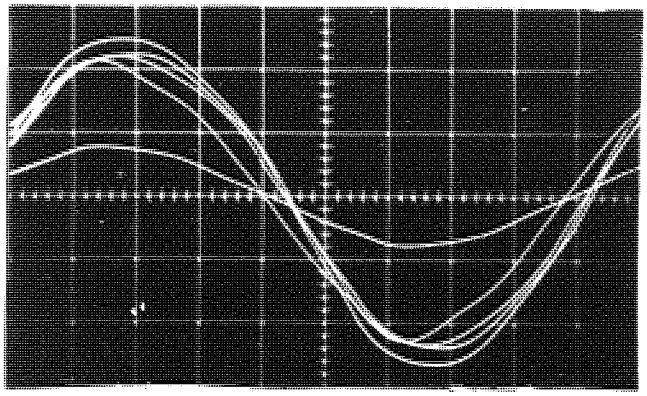

Fig. 8.17a

Voltages from the array of search coils ($\propto B_y$).

| Wave-Shape | : | Coil Number |
|---|---|---|
| a | : | 1 |
| b | : | 3 |
| c | : | 5 |
| d | : | 7 |
| e | : | 9 |

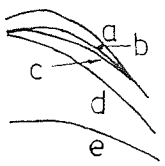


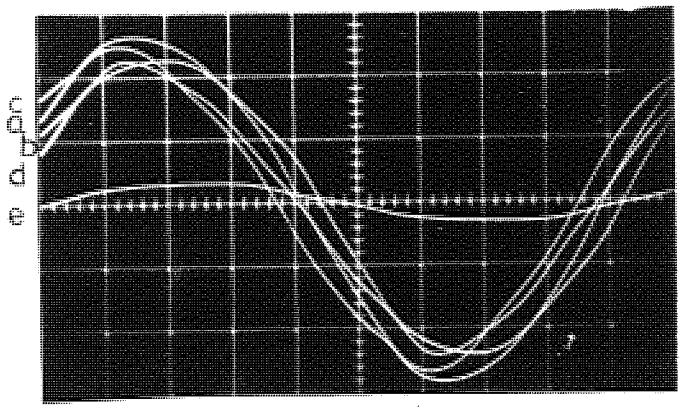


Fig. 8.17b

Voltages from the array of search coils ($\propto B_y$).

| Wave-Shape | : | Coil Number |
|---|---|---|
| a | : | 1 |
| b | : | 4 |
| c | : | 6 |
| d | : | 8 |
| e | : | 10 |

Fig. 8.17: Oscillograms illustrating the variation of air-gap flux-density on the surface of the wide plate along z-direction for transverse flux arrangement

Excitation = 58.8 kA/m
Frequency = 50 Hz 0.5 V/cm
Amplification = 100 2 ms /cm

Locations of the search coils are shown in Fig. 8.3.

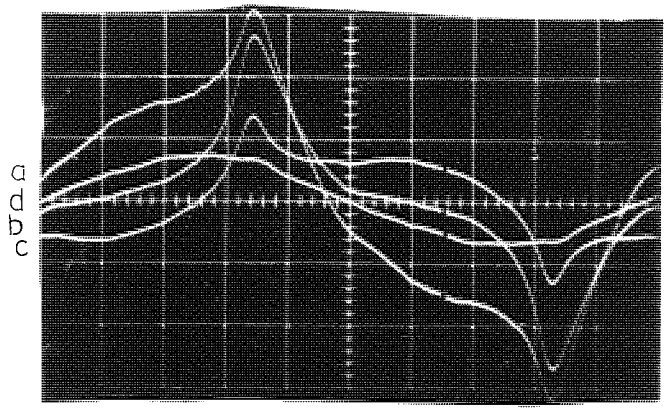


Fig. 8.18a

Voltages proportional to Jx's

Wave Shape : J-probe

a : XE5
b : X21
c : X20
d : X19

0.2 V/cm

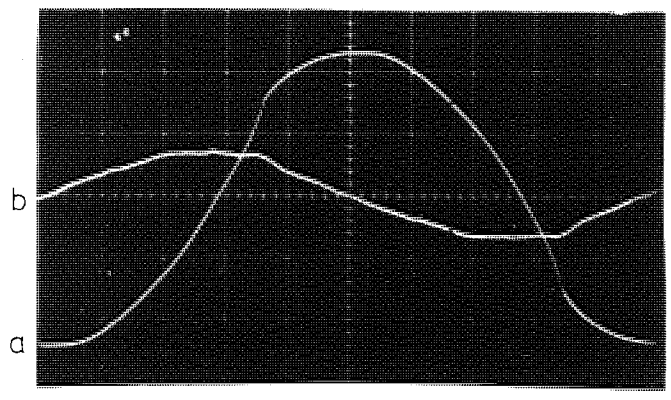


Fig. 8.18b

Wave Shape : J-probe

a : Z19
b : X19

a : 0.5 V/cm
b : 0.2 V/cm

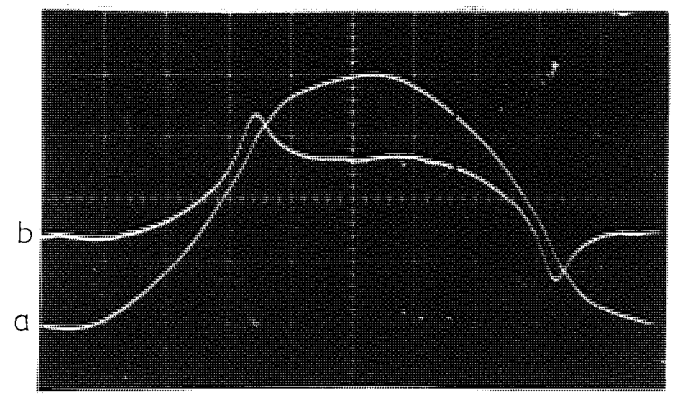


Fig. 8.18c

Wave Shape : J-probe

a : Z20
b : X20

a : 0.5 V/cm
b : 0.2 V/cm

Fig. 8.18: Oscillograms of voltages from the current-density probes on the surface of the narrow plate for longitudinal flux arrangement.

Excitation = 47 kA/m
Frequency = 50 Hz
Amplification = 100

Locations of the J-probes are shown in Fig. 8.5.

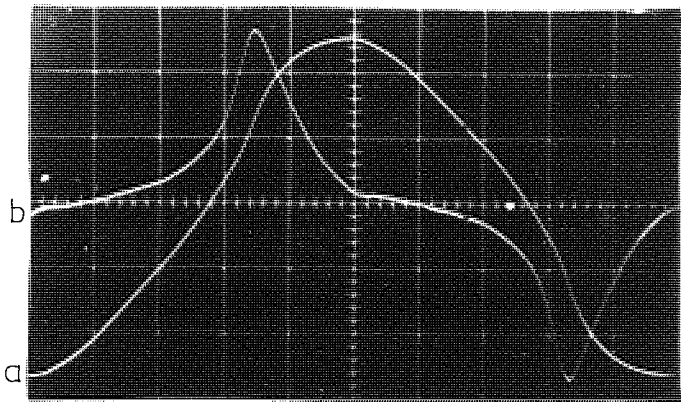


Fig. 8.19a

Wave Shape: J-probe

a : Z21

b : X21

a : 0.5 V/cm

b : 0.2 V/cm

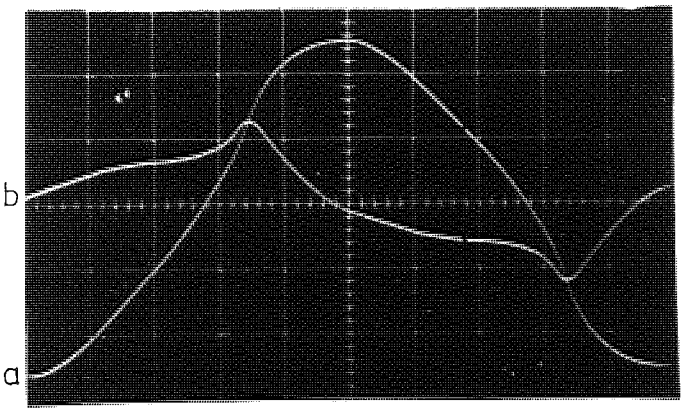


Fig. 8.19b

Wave Shape : J-probe

a : Z21

b : XE5

a : 0.5 V/cm

b : 0.2 V/cm

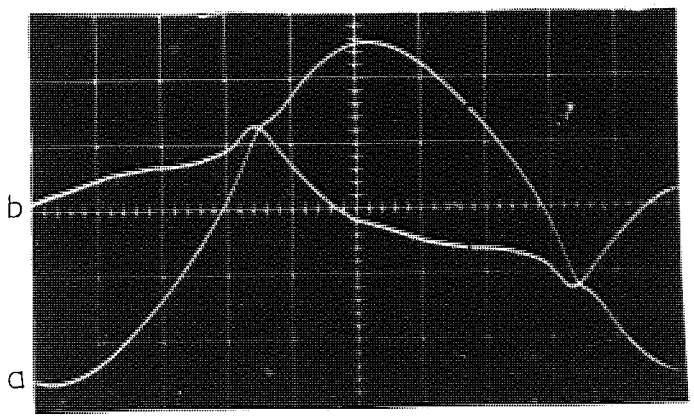


Fig. 8.19c

Wave Shape : J-probe

a : Y3

b : XE5

a : 0.5 V/cm

b : 0.2 V/cm

Fig. 8.19: Oscillograms comparing the voltages from the current-density probes on the surface and lateral side face of the narrow plate for longitudinal flux arrangement.

Excitation = 47 kA/m.
Frequency = 50 Hz
Amplification = 100

Locations of the J-probes are shown in Fig. 8.5.

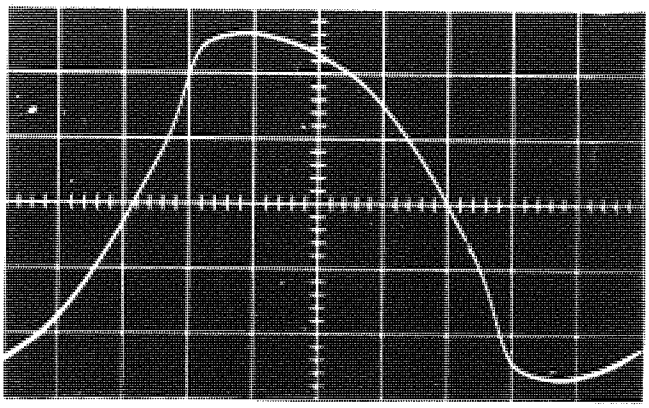

Fig. 8.20a:

Voltage from a current-density probe.

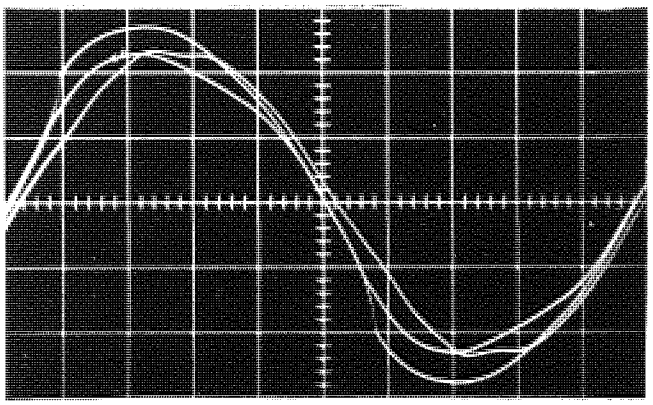

Fig. 8.20b:

Voltages proportional to $J_z$.

| Wave-Shape | : | J-probe |
|---|---|---|
| a | : | Z19 |
| b | : | Z20 |
| c | : | Z21 |

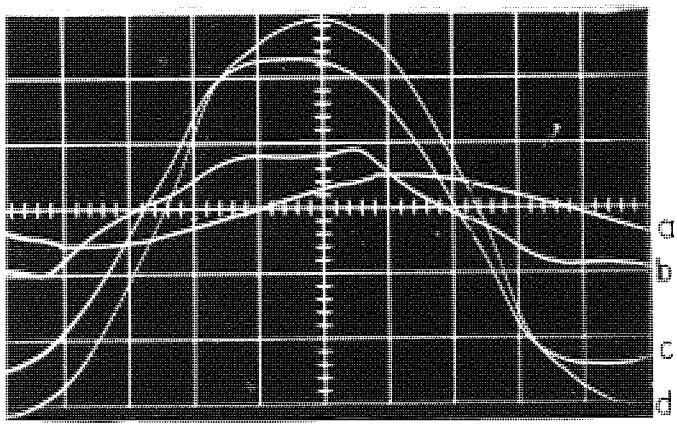


Fig. 8.20c:

Voltages proportional to $J_x$.

| Wave-Shape | : | J-probe |
|---|---|---|
| a | : | X19 |
| b | : | X20 |
| c | : | X21 |
| d | : | XE5 |

Figure 8.20: Oscillograms of voltages from current-density probes on the surface of the narrow plate for transverse flux arrangement.

| | | |
|---|---|---|
| Excitation | = 47 kA/m | 0.5 V/cm |
| Frequency | = 50 Hz | 2 ms /cm |
| Amplification | = 100 | |

Locations of the J-probes are shown in Fig. 8.5.

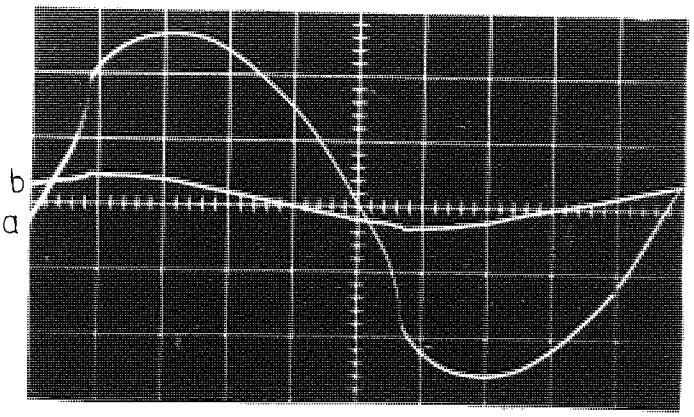


Fig. 8.21a:

Wave-Shape: J-probe

a : Z19

b : X19

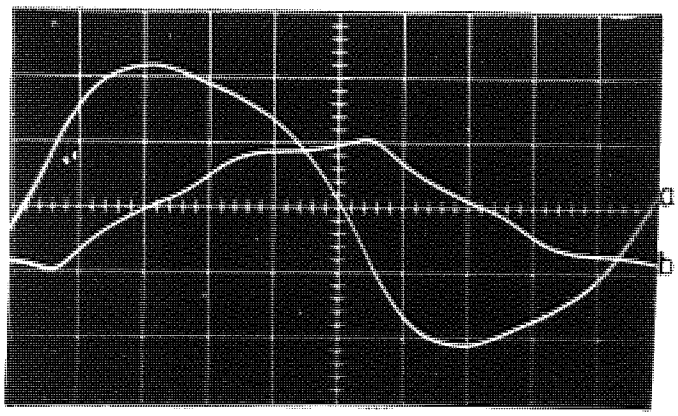


Fig. 8.21b:

Wave-Shape: J-probe

a : Z20

b : X20

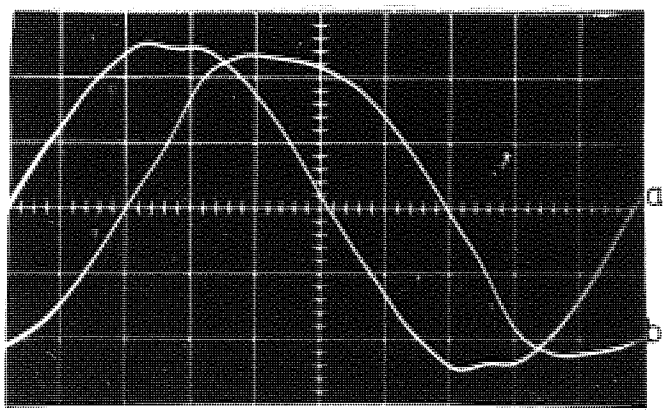


Fig. 8.21c:

Wave-Shape: J-probe

a : Z21

b : X21

Figure 8.21: Oscillograms of voltages from current-density probes comparing the magnitudes of $J_z$'s and $J_x$'s on the surface of the narrow plate for transverse flux arrangement.

Excitation = 47 kA/m 0.5 V/cm
Frequency = 50 Hz 2 ms /cm
Amplification = 100

Locations of the J-probes are shown in Fig. 8.5.

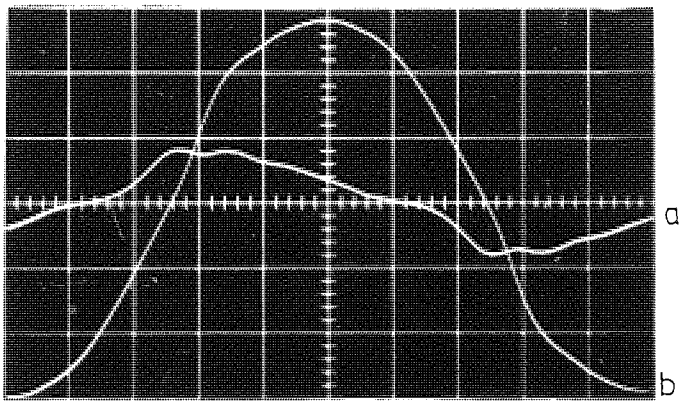


Fig. 8.22a

Wave-Shape : J-probe

a : Y3

b : XE5

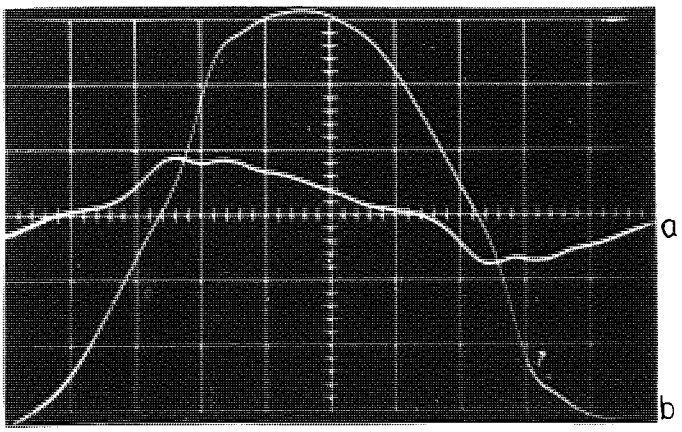


Fig. 8.22b

Wave-Shape : J-probe

a : Y3

b : XE6

Fig. 8.22 : Oscillograms of voltages from current-density probes comparing the magnitudes of $J_y$'s and $J_x$'s on the surface and lateral side face of the narrow plate for transverse flux arrangement.

| | | |
|---|---|---|
| Excitation | = 47 kA/cm | 0.5 V/cm |
| Frequency | = 50 Hz | 2 ms /cm |
| Amplification | = 100 | |

Locations of the J-probes are shown in Fig. 8.5.

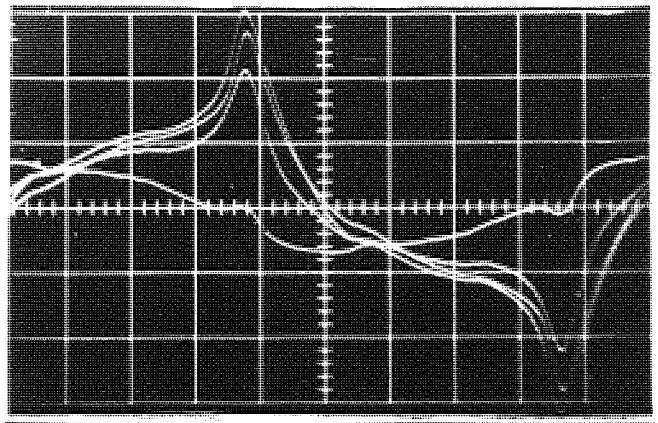

Fig. 8.23a

Voltages proportional to $J_x$

Wave-Shape : J-probe

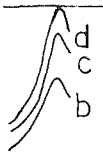


a : X25
b : X26
c : X27
d : XE10

0.2 V/cm

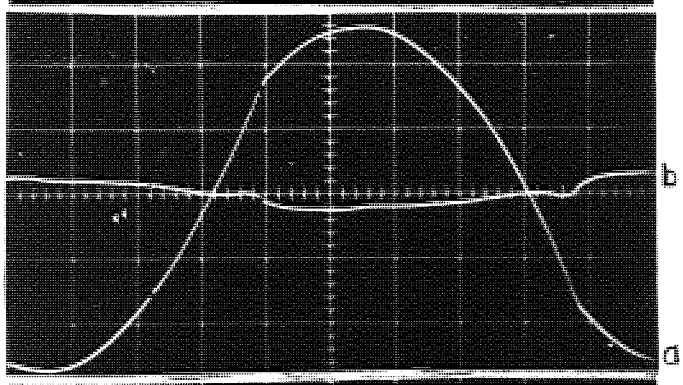


Fig. 8.23b

Wave-Shape : J-probe

a : Z25
b : X25

0.5 V/cm

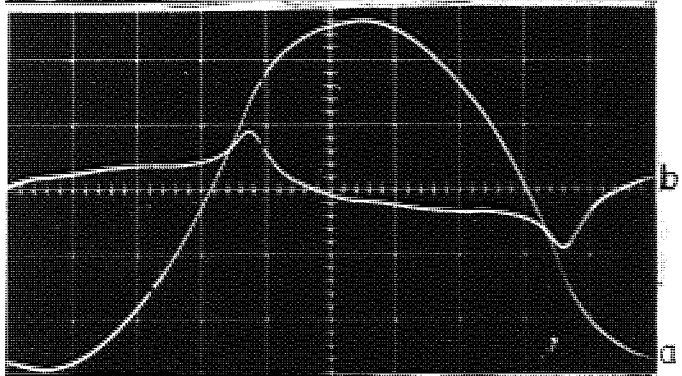


Fig. 8.23c

Wave-Shape : J-probe

a : Z26
b : X26

0.5 V/cm

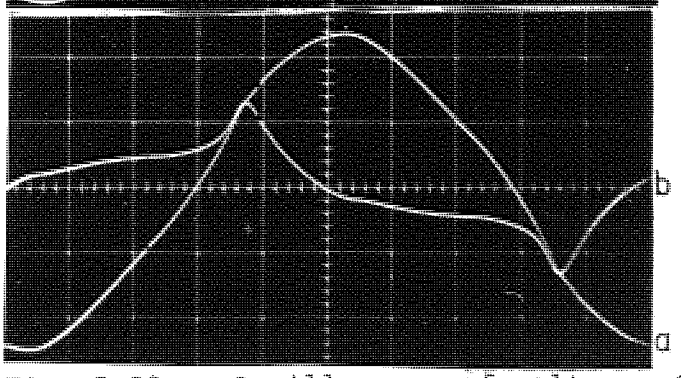


Fig. 8.23d

Wave-Shape : J-probe

a : Z27
b : X27

0.5 V/cm

Fig. 8.23 : Oscillograms of voltages from current-density probes on the surface of end-strip plate for longitudinal flux arrangement.

Excitation = 47 kA/m
Frequency = 50 Hz
Amplification = 100

Location of the J-probes are shown in Fig. 8.6.

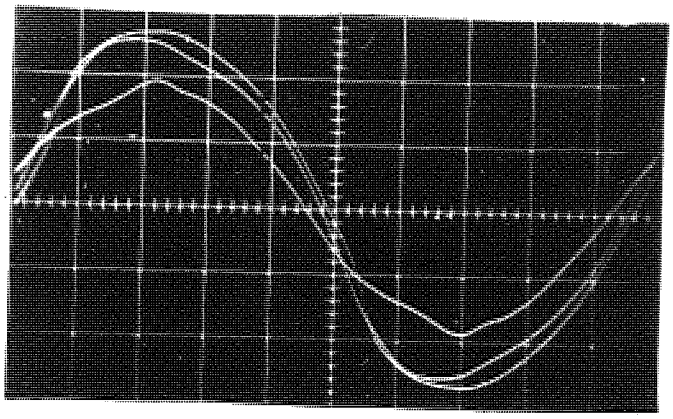

Fig. 8.24a

Voltages proportional to $J_z$

| Wave-Shape | : | J-probe |
|---|---|---|
| a | : | Z25 |
| b | : | Z26 |
| c | : | Z27 |

0.5 V/cm

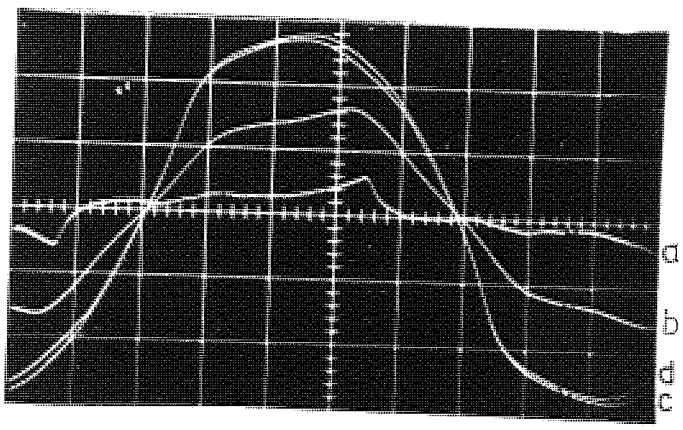

Fig. 8.24b

Voltages proportional to $J_x$

| Wave-Shape | : | J-probe |
|---|---|---|
| a | : | X25 |
| b | : | X26 |
| c | : | X27 |
| d | : | XE10 |

a : 0.2 V/cm
b,c,d : 0.5 V/cm

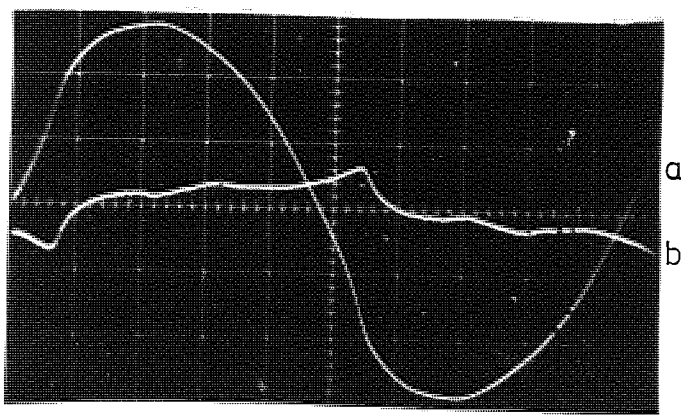

Fig. 8.24c

| Wave-Shape | : | J-probe |
|---|---|---|
| a | : | Z25 |
| b | : | X25 |

a : 0.5 V/cm
b : 0.2 V/cm

Fig. 8.24: Oscillograms of voltages from the current-density probes on the surface of the end-strip plate for transverse flux arrangement.

Excitation = 47 kA/m
Frequency = 50 Hz
Amplification = 100

Locations of the J-probes are shown in Fig. 8.6.

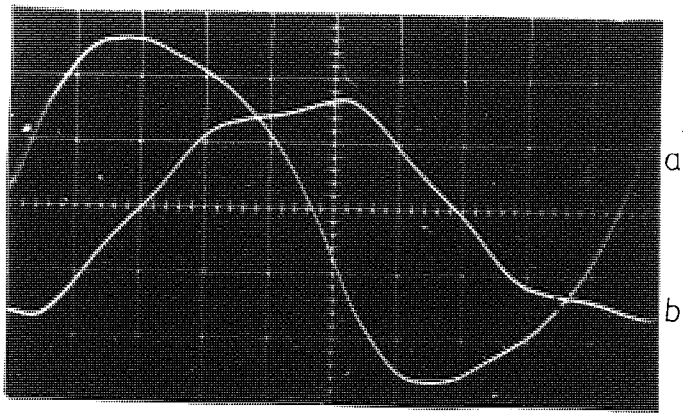


Fig. 8.25a

Wave-Shape : J-probe

a : Z26

b : X26

Amplification = 100

0.5 V/cm

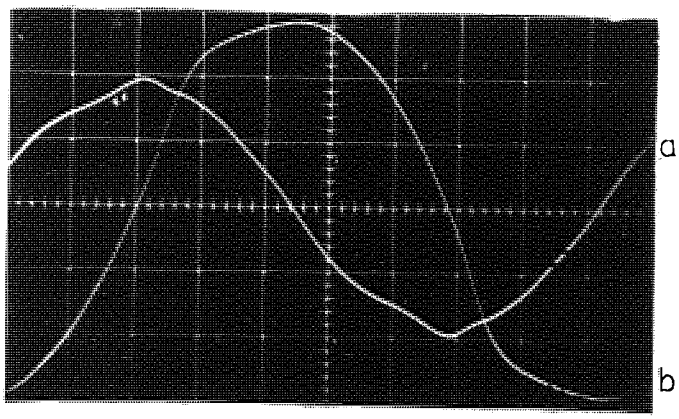


Fig. 8.25b

Wave-Shape : J-probe

a : Z27

b : X27

Amplification = 100

0.5 V/cm

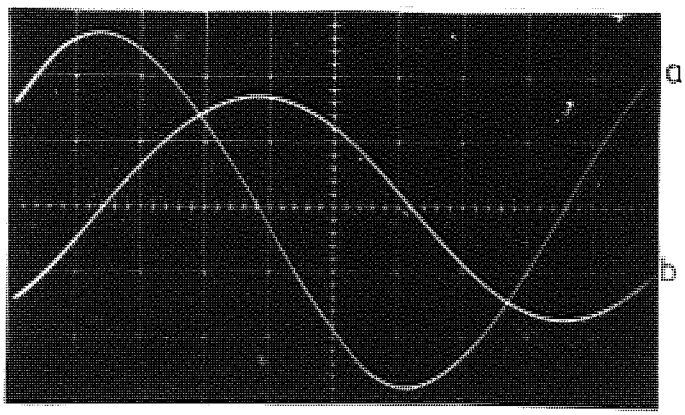


Fig. 8.25c

Voltages from full-pitch search coil.

a : Search-coil voltage
b : Integrated voltage from search coil

Amplification = 1

a : 0.2 V/cm
b : 0.1 V/cm

Fig. 8.25: Oscillograms of voltages from current-density probes and full-pitch search coil on the surface of the end-strip plate for the transverse flux arrangement.

Excitation = 47 kA/m
Frequency = 50 Hz

Location of J-probes and search coil are shown in Fig. 8.6.

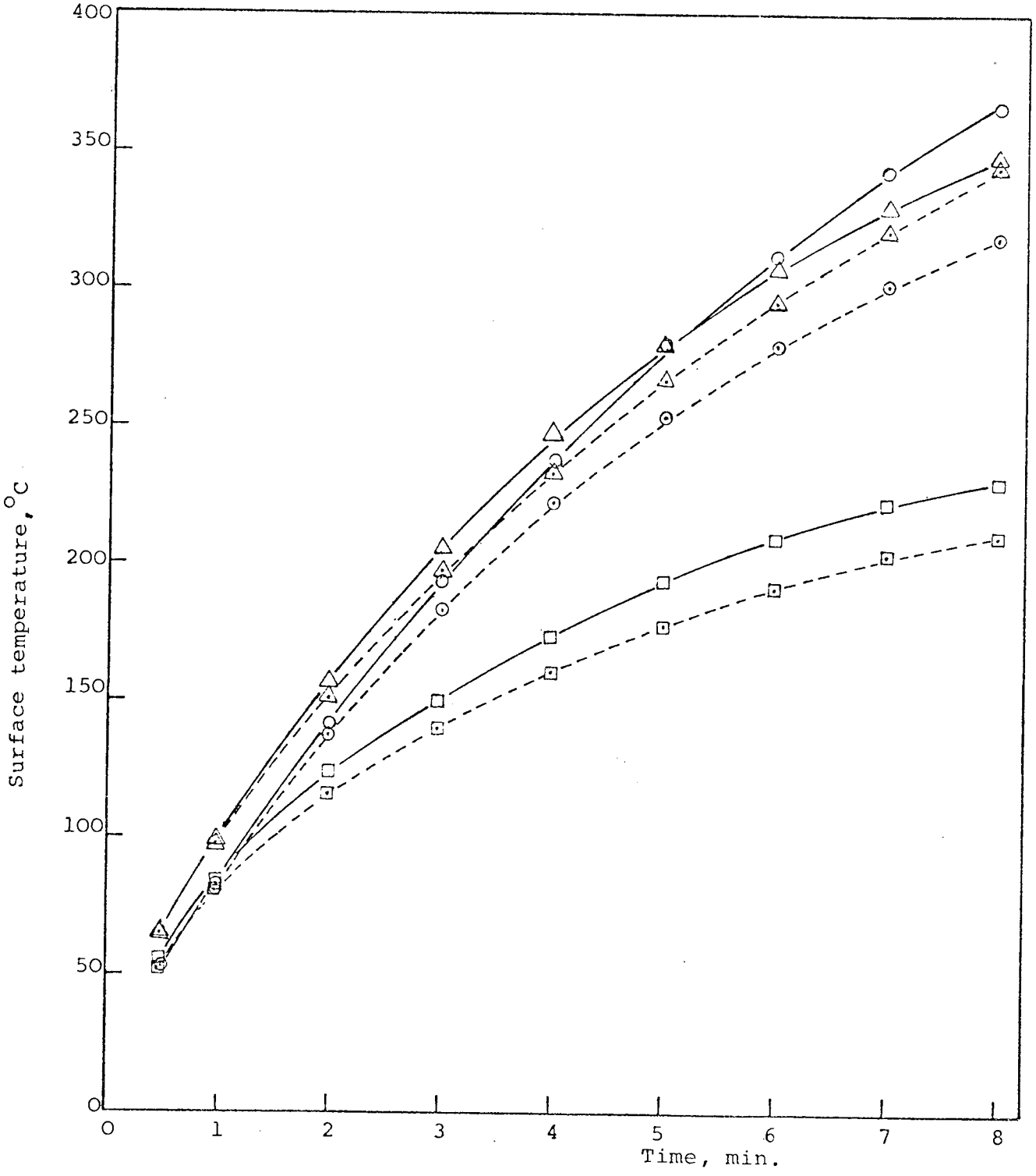


Fig. 8.26 : Measured temperature-time curves for the three different plates at 50 Hz for an excitation of 58.8 kA/m. Firm lines are for longitudinal flux arrangement and the dotted lines are for transverse flux arrangement.

| LFA | | TFA | |
|---|---|---|---|
| □ | : Wide plate | ⊡ | : Wide plate |
| △ | : Narrow plate | △ | : Narrow plate |
| ○ | : End-strip plate | ⊙ | : End-strip plate |

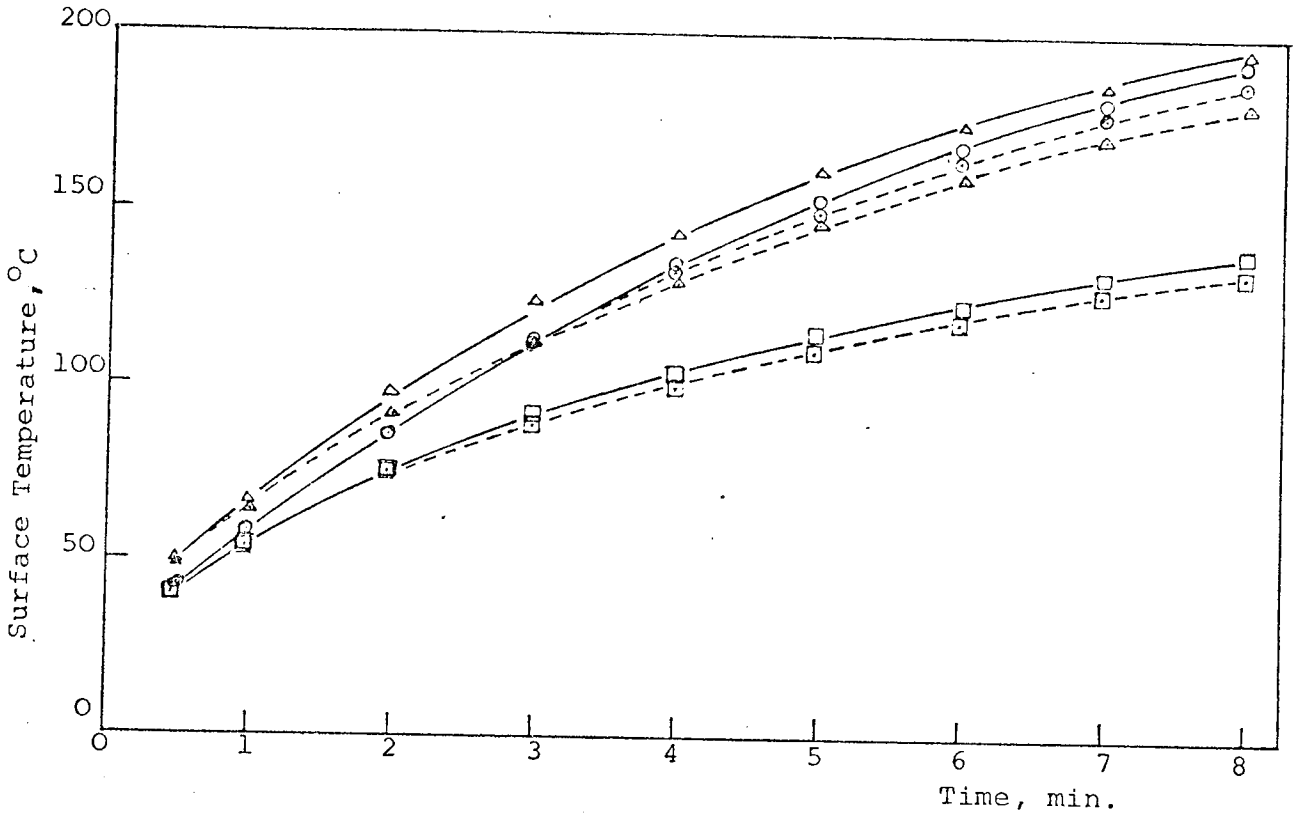


Fig. 8.27 : Measured temperature-time curves for the three different plates at 25 Hz for an excitation of 64.7 kA/m. Firm lines are for longitudinal flux arrangement and the dotted lines are for transverse flux arrangement.

| LFA | | TFA | |
|---|---|---|---|
| □ | : Wide Plate | ⊡ | : Wide Plate |
| △ | : Narrow Plate | ◬ | : Narrow Plate |
| ○ | : End-strip Plate | ⊙ | : End-strip Plate |

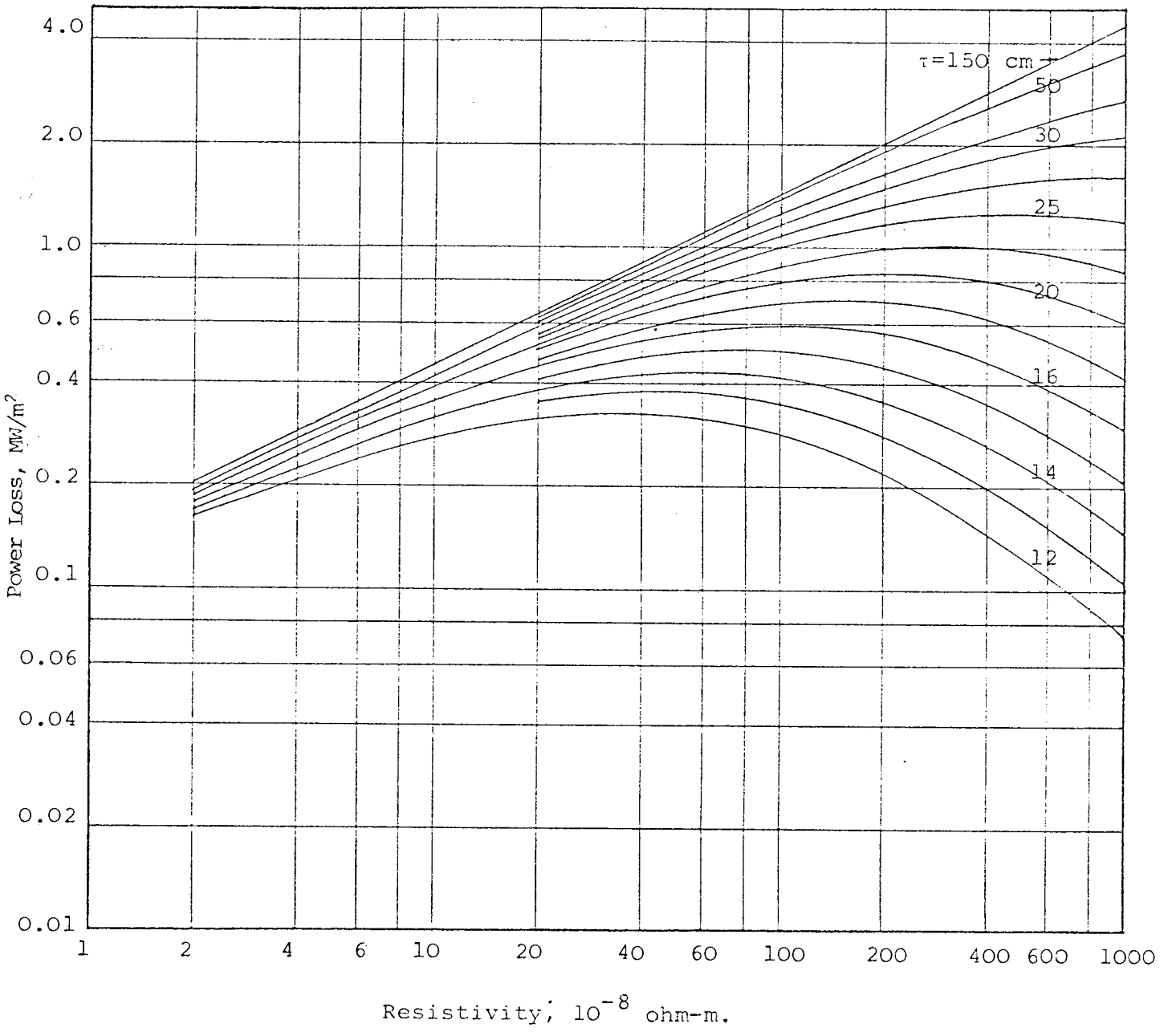


Fig. A3.1 Variation of power loss with resistivity for various pole-pitches in a semi-infinite plate for a single-sided arrangement. Surface magnetic field strength = 210 kA/m.. Air-gap length = 1.0 cm. Frequency = 50 Hz.

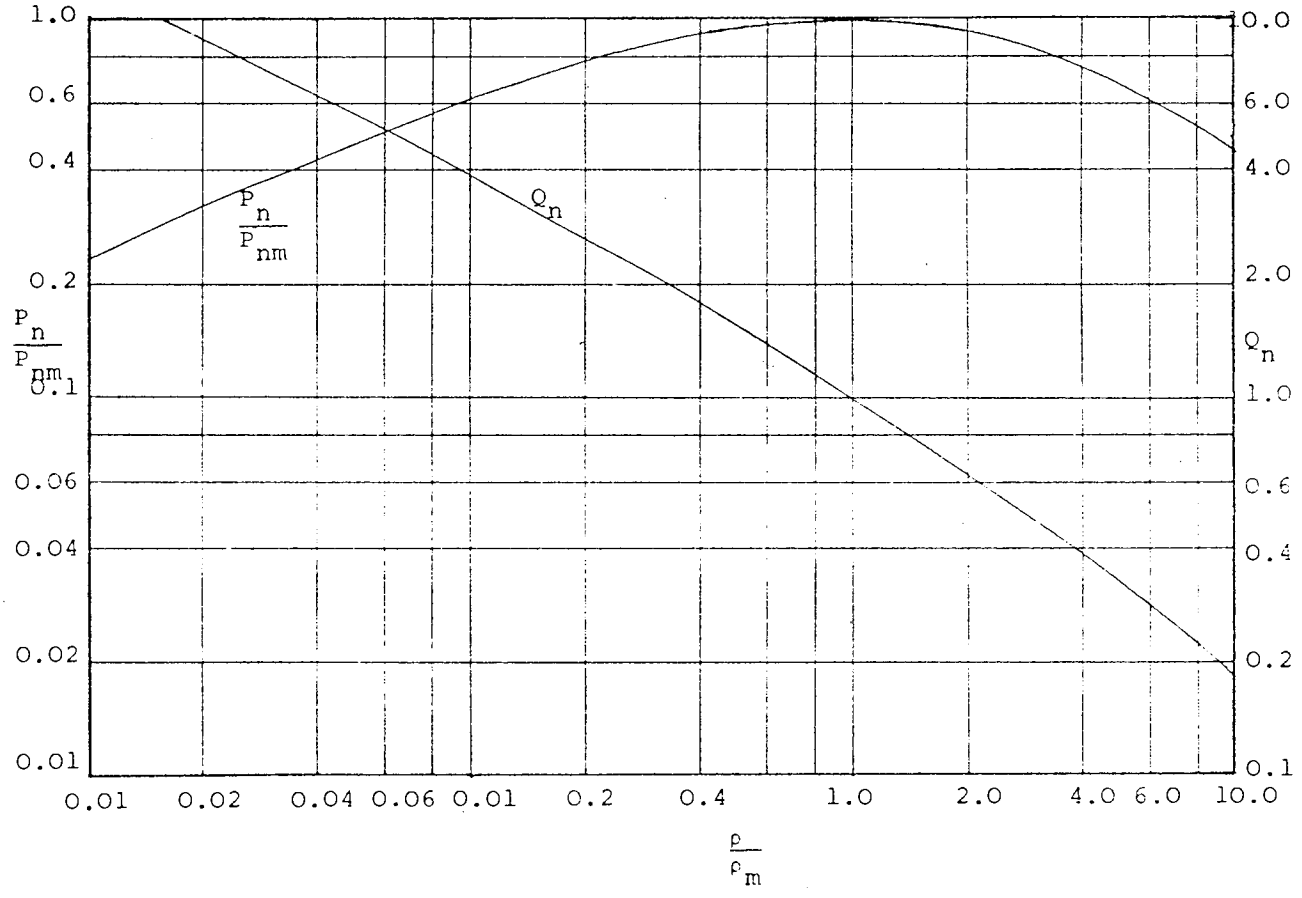


Fig. A3.2 Variation of generalised power loss, $P_n/P_{nm}$, and the parameter $Q_n$, with resistivity expressed as per-unit of its value at maximum loss $b = 0.112$. Note that the $P_n/P_{nm}$ curve is not symmetrical about $(\rho/\rho_m) = 1$.

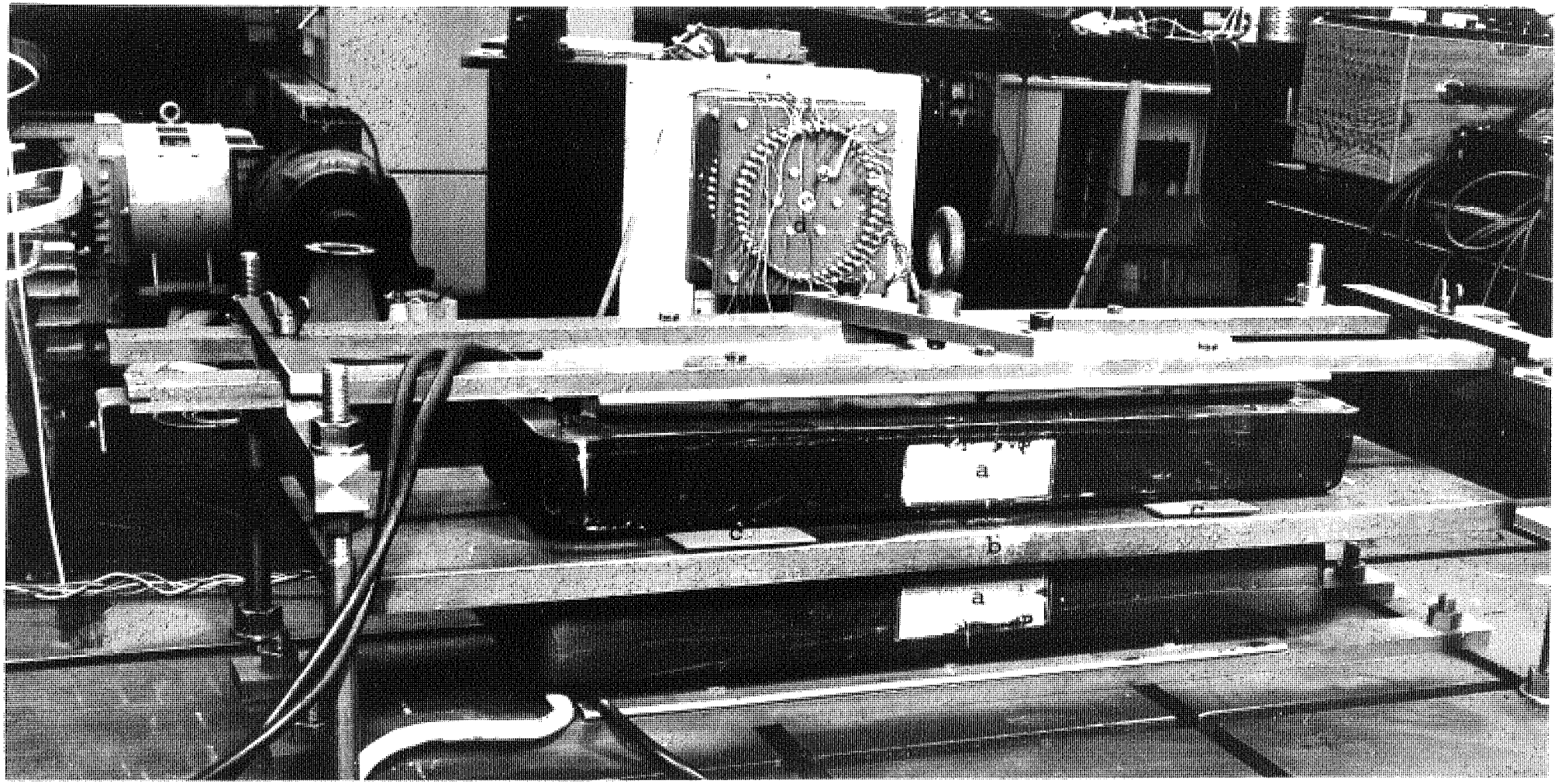


Photoplate 8.1: The wide plate in position between the two primary members.

(a) The primary members
(b) The wide plate
(c) Elephant-hide pieces (used for providing air-gap)
(d) The selector switch.

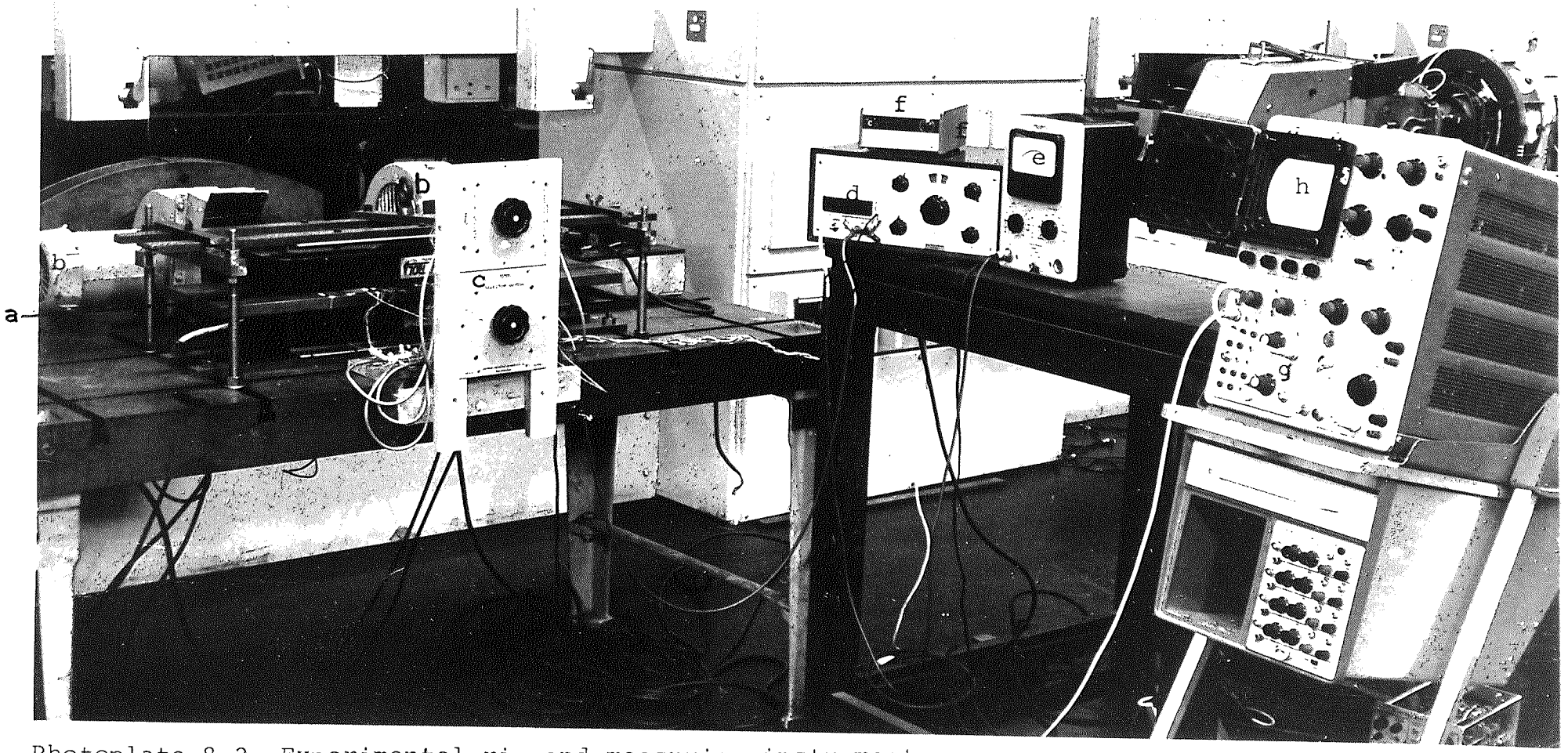


Photoplate 8.2: Experimental rig and measuring instruments.

(a) The experimental rig.

(b) The air blowers

(c) The selector switches

(d) The wave analyser (Muirhead, model K-134-A)

(e) The electronic voltmeter (Bruel and Kjaer, type 2409)

(f) 10-way digital thermometer (Comark 3000)

(g) The operational amplifier (type O plug-in unit)

(h) The oscilloscope (Tetronix, type 533A)